Two-dimensional discontinuous Galerkin model for flow and mixing within emergent vegetation

Xitong Sun

Supervised by:

Dr. Georges Kesserwani

Prof. Virginia Stovin

A thesis submitted in partial fulfilment of the requirements for the degree of Doctor of Philosophy

Department of Civil and Structural Engineering

The University of Sheffield

March 2024

Declaration

I, Xitong Sun, confirm that the thesis is my own work. I am aware of the University's Guidance on the Use of Unfair Means (www.sheffield.ac.uk/ssid/unfair-means). This work has not previously been presented for an award at this, or any other, university.

Xitong Sun

March, 2024

Abstract

Simulating laminar to low-turbulence flows and mixing within cylinder arrays is vital for predicting pollutant transport within emergent vegetation and thus designing vegetated water bodies to treat pollutants. However, viscous turbulence models with the equations integrating the kinematic and eddy viscosity terms suffer from excessive computational costs and are not practical for large-scale applications. Therefore, this PhD research aims to develop a sufficiently efficient and accurate numerical tool that provides detailed flow fields around the cylinders to simulate solute transport within the cylinder array.

A second-order discontinuous Galerkin (DG2) numerical solver to the two-dimensional depth-averaged inviscid Shallow Water Equations (SWE) which exclude the kinematic and eddy viscosity terms can produce high-quality and fast-converged flow fields, even on coarse grid resolution. This is attributed to the numerical complexity within the DG2 formulation which helps it accurately capture advective fluxes. This PhD project explored the suitability of the inviscid DG2-SWE solver in the context of laminar to low-turbulence wakes past cylinders. It was found that the DG2-SWE solver can efficiently simulate accurate wake formations that resemble experimental measurements and those produced by more complex turbulence models. However, using the DG2-SWE solver is limited to choosing an unusually coarse grid resolution of 0.25 times cylinder diameter, in which the numerical error dissipation mimics the mechanics of viscous turbulent models.

With a successful simulation of flow fields using the DG2-SWE solver, a solute transport model linked to the DG2-SWE solver for modelling mixing within an array of cylinders was also developed in this project. Given its good capability in treating advective fluxes, a DG2 solver is applied to solve the advection diffusion equation (ADE), taking the flow fields and explicitly generated turbulent diffusivity from the DG2-SWE simulation results as the inputs. The feasibility of this newly developed DG2-ADE solver in simulating solute transport within cylinder arrays is assessed by comparison with laboratory-scale experiments under laminar, transitional and low-turbulence regimes. Due to the absence of viscosity fluxes, the DG2-SWE solver tends to overestimate the magnitude of turbulent diffusivity fields. Calibrated DG2-SWE simulations are used based on increased Manning's coefficients, n_M, to ensure physically acceptable ranges for turbulent diffusivity fields required for the DG2-ADE simulations. The results show that applying the DG2-ADE solver provides an acceptable way to effectively predict the solute movement and accurately quantify the mixing process. The implication of this is that the newly developed numerical tool that links the DG2-SWE solver to the DG2-ADE solver can accurately model flow and mixing past a large number of cylinders at affordable computational costs - total GPU runtimes are around 32 hours for laminar regime and 6 hours for transitional and low-turbulence regimes.

Acknowledgements

First and foremost, I would like to deeply thank my supervisors, Dr. Georges Kesserwani and Prof. Virginia Stovin, for their kind support and patient guidance during my PhD journey. It is my honour to have their quick, informative and constructive feedback. My sincere thanks also go to SEAMLESS-WAVE group members: Dr James Shaw, Dr Mohammad Kazem Sharifian, Dr Mahya Hajihassanpour, Dr Janice Lynn Ayog, Dr Mohammad Shirvani, and Alovya Ahmed Chowdhury. Thanks for their discussion and suggestions which helped me address questions.

I greatly appreciate the collaboration with Dr. J Leonardo Corredor-Garcia and Dr. Fred Sonnenwald, who generously supported me and helped me understand the experimental data. I am indebted to all good friends I met in the Department of Civil and Strucutral Engineering in the University of Sheffield: Dr. Zhangjie Peng, Dr. Weijiang Yu, Dr. Menglin Dai and Dr. Shiyao Wang. All of you make my life and research experience memorable.

I owe my deepest gratitude to my girl friend, Zhihui Wang. I am extremely lucky to meet you and have your accompanies throughout my PhD journey and our future life. Last but not least, to my mother, Jie Wang. Many thanks for your support and unconditional love.

List of Content

List of Figures

List of Tables

List of symbols

Symbol	Name	Units
Δt	Time step	(s)
Δx	Spatial grid size in *x*-direction	(m)
Δy	Spatial grid size in *y*-direction	(m)
ν_k	kinematic viscosity	(m^2/s)
ν_t	Turbulence/eddy viscosity	(m^2/s)
$\bar{t}$	Solute travel time	(s)
$\bar{u}$	Time-averaged longitudinal velocity	(m/s)
$\bar{v}$	Time-averaged transverse velocity	(m/s)
∂	Partial derivatives operator	(-)
∂_t	Partial derivatives of time	(-)
∂_x	Partial derivatives in the *x*-direction	(-)
∂_y	Partial derivatives in the *y*-direction	(-)
ϕ	Solid volume fraction	(-)
$\mathbf{F(U)}$	*x*-directional spatial flux vector	(-)
$\mathbf{G(U)}$	*y*-directional spatial flux vector	(-)
$\mathbf{S_b(U)}$	Source term vector representing bed slope/topography	(-)
$\mathbf{S_f(U)}$	Source term vector representing friction effects	(-)
$\mathbf{U}$	Vector of flow variables	(-)
$\mathbf{U}^0$	Average coefficient of flow variables	(-)
$\mathbf{U}^{1x}$	*x*-directional slope coefficient of flow variables	(-)
$\mathbf{U}^{1y}$	*y*-directional slope coefficient of flow variables	(-)
$\mathbf{U}_\mathrm{h}$	DG2 approximation of the state (or flow) variables	(-)
2D	Two-dimensional	(-)
3D	Three-dimensional	(-)
ADE	Advection diffusion equation	(-)
CFL	Courant-Friedrichs- Lewy	(-)
DEM	Digital Elevation Model	(-)
DG2	Second-order Discontinuous Galerkin	(-)
DG	Discontinuous Galerkin	(-)
DNS	Direct Numerical Simulation	(-)

FV2	Second-order finite volume	(-)
FV	Finite volume	(-)
GPU	Graphics processing unit	(-)
LES	Large Eddy Simulation	(-)
MUSCL	Monotonic Upstream-centred Scheme for Conservation Laws	(-)
RANS	Reynolds-Averaged Navier-Stokes	(-)
RI	Relevance index	(-)
SPIV	Surface particle image velocimetry	(-)
SWE	Shallow water equations	(-)
ε	Turbulent kinetic energy dissipation rate	(m^2/s^3)
C	Concentration	(-)
C^0	Average coefficient of concentration	(-)
C^{1x}	x-directional slope coefficient of concentration	(-)
C^{1y}	y-directional slope coefficient of concentration	(-)
c_μ	Empirical constant in the RANS k-ε model	(-)
C_h	DG2 approximation of concentration	(-)
c_r	Courant number	(-)
d	Cylinder diameter	(m)
D_t	Turbulent diffusivity	(m^2/s)
D_x	Reach-scale longitudinal dispersion coefficient	(m^2/s)
D_y	Reach-scale transverse dispersion coefficient	(m^2/s)
f_S	Shedding frequency	(s^{-1})
g	gravitational acceleration	(m/s^2)
h	Water depth	(m)
k	Turbulent kinetic energy or TKE	(m^2/s^2)
k_S	Scalar factor for Manning's formula	($m^{1/2}$ s^{-1})
L	Spatial operator	(-)
l_m	Mixing length	(m)
L^a	Spatial advective transport operator	(-)
L^d	Spatial diffusive transport operator	(-)
$L^{0,a}$	Average coefficient of spatial advective transport operator	(-)
$L^{0,d}$	Average coefficient of spatial diffusive transport operator	(-)

$L^{1x,a}$	x-directional slope coefficient of spatial advective transport operator	(-)
$L^{1y,a}$	y-directional slope coefficient of spatial advective transport operator	(-)
n	Normal direction to the cylinder boundary	(-)
n_M	Manning's roughness coefficient	($m^{1/6}$)
N_x	x-directional number of grids	(-)
N_y	y-directional number of grids	(-)
P_f	Positivity preserving factor	(-)
Q	Computational grid element	(-)
q_x	x-directional flow discharge per unit width	(m^2/s)
q_y	y-directional flow discharge per unit width	(m^2/s)
R_{ed}	cylinder Reynolds number	(-)
S_{ct}	Turbulent Schmidt number	(-)
S_t	Strauhal number	(-)
t	Time	(s)
t^*	Dimensionless time unit	(-)
u	x-directional/longitudinal velocity	(m/s)
u^0	Average coefficient of longitudinal velocity	(m/s)
$u^{1x'}$	Fluctuating x-directional slope coefficient of longitudinal velocity	(m/s)
u^{1x}	x-directional slope coefficient of longitudinal velocity	(m/s)
$u^{1y'}$	Fluctuating y-directional slope coefficient of longitudinal velocity	(m/s)
u^{1y}	y-directional slope coefficient of longitudinal velocity	(-)
U_∞	steady inflow velocity	(m/s)
v	y-directional/transverse velocity	(m/s)
$v^{1x'}$	Fluctuating x-directional slope coefficient of transverse velocity	(m/s)
v^{1x}	x-directional slope coefficient of transverse velocity	(m/s)
$v^{1y'}$	Fluctuating y-directional slope coefficient of transverse velocity	(m/s)
v^{1y}	y-directional slope coefficient of transverse velocity	(m/s)
ω	Vorticity	(s^{-1})

x	Coordinate along the horizontal axis of a plane/longitudinal distance in a domain	(m)
x_{gc}	*x*-directional coordinate of the gravity centre of the concentration field	(m)
y	Coordinate along the vertical axis of a plane/transverse distance in a domain	(m)
y_{gc}	*y*-directional coordinate of the gravity centre of the concentration field	(m)
y_w	The distance from the wall	(m)
z	Bed topography level	(m)
z^0	Average coefficient of bed topography	(m)
z^{1x}	*x*-directional slope coefficient of bed topography	(m)
z^{1y}	*y*-directional slope coefficient of bed topography	(m)
z_h	Approximation of the bed topography	(m)

Publication

The content in Chapter 3 (about hydrodynamic) of this thesis has been published in:

Sun, X., Kesserwani, G., Sharifian, M.K. and Stovin, V., 2023. Simulation of laminar to transitional wakes past cylinders with a discontinuous Galerkin inviscid shallow water model. *Journal of Hydraulic Research*, *61*(5), pp.631-650.

1 Introduction

1.1 Background

Emergent aquatic vegetation is of great importance for physical and biological processes in natural water bodies (Darby, 1999; O'Hare, 2015; Sonnenwald et al., 2017). The presence of aquatic vegetation alters the hydrodynamics, changing the directions and magnitudes of velocities, thus creating heterogeneities in the flow fields. These vegetation-flow interactions in turn affect the mixing process, namely the transport of solutes such as nutrients and pollutants. Understanding the flow fields within and around patches of vegetation is fundamental to the prediction and analysis of the advection and dispersion of solutes in slow, steady flows with quasi-periodic motion, such as vegetated ponds (Marjoribanks et al., 2017; Nepf, 1999; Sonnenwald et al., 2019a). Understanding the mixing process within vegetation is also crucial for helping environmental hydraulics practitioners effectively design vegetated water bodies to treat pollutants.

Experimental models and numerical simulators have been applied to investigate the hydrodynamics and solute transport in vegetated flows, typically using rigid circular cylinders to represent emergent vegetation (Hamidifar et al., 2015; Tanino and Nepf, 2009; White and Nepf, 2003). Experimental studies have been conducted to explore the structures and characteristics of flows within cylinder arrays under different configurations, providing detailed spatial velocity distributions (Corredor-Garcia et al., 2020; Ricardo et al., 2016a). There are also some laboratory measurements describing the mixing process and quantifying the reach-scale longitudinal and transverse dispersion coefficients (Sonnenwald et al., 2017; Tanino and Nepf, 2008a; White and Nepf, 2003). However, experimental explorations often face practical issues. For example, acquiring detailed and informative velocity and concentration data requires expensive equipment, and building laboratory setup and installing the cylinder arrays are time-consuming and laborious manual work. Therefore, numerical simulators have been used as a direct alternative to experimental explorations, or to complement the analysis of data from laboratory measurements.

When simulating flow past cylinders, a key difficulty is to accurately capture the wake flow patterns featuring vortical structures behind the cylinders in laminar to low-turbulence flow regimes representative of slow, quasi-steady flows in ponds and wetlands (Franke et al., 1990; King, 2006; Mittal, 2005). Such flows correspond to cylinder Reynolds numbers of $R_{ed} = U_\infty d/\nu_k \leq 450$, where U_∞ denotes the steady inflow velocity, d is the cylinder diameter, and ν_k is the kinematic viscosity. Within this context, the spatial distribution of the velocity field in the vertical direction is mostly uniform and two-dimensional (2D) viscous turbulence models can produce reliable flow fields while avoiding the heavy computational costs of three-dimensional (3D) simulators (Kim et al., 2018; Li et al., 2012; Ricardo et al., 2016a; Tanino, 2008; Zong and Nepf, 2012). These 2D turbulence models are typically

numerically solved by the second-order finite volume (FV2) methods (Ginting, 2019; Qu et al., 2013; Rajani et al., 2009; Stovin et al., 2022). However, the FV2 methods suffer from the fast growth of numerical error dissipation, which may prohibit the formation of vortices and lead to unrealistically flat and symmetrical flow patterns behind the cylinder (Braza et al., 1986; Franke et al., 1990; Mittal, 2005). To cope with these adverse effects, simulations using the FV2 methods require fine grid resolutions, which inevitably increase computational runtime and memory costs (Ginting, 2019).

The second-order discontinuous Galerkin (DG2) method (Reed and Hill, 1973) is an alternative to FV2 methods that is more complex numerically and more resistant to the growth of numerical error dissipation. This is because a DG2 method uses two directionally independent local slope coefficients in addition to the local averages of velocity variables to model smooth piecewise-planar flow fields, whereas an FV2 method uses one coefficient of a piecewise-averaged flow data (Kesserwani et al., 2018; Kesserwani and Wang, 2014). The DG2 solver to the inviscid hydrodynamic model of the depth-averaged Shallow Water Equations (SWE) (herein referred to as the DG2-SWE solver) induces a *certain* amount of numerical error dissipation (or called numerical diffusion), which, when applied to the momentum (advection) quantities, is termed numerical viscosity (Ramshaw, 1994). The effects of numerical viscosity may, to a *certain* extent, imitate the true turbulence effects of kinematic and eddy viscosity from viscous turbulence models. In contrast to the DG2-SWE solver, the FV2 solver to the SWE (herein referred to as the FV2-SWE solver) introduces a larger amount of the numerical viscosity which may mask the turbulence effects. Given its numerical complexity, the DG2-SWE solver has shown great ability to capture advective fluxes and can reproduce the small-scale eddies around the obstacles well, even without incorporating extra kinematic and turbulent/eddy viscosity terms (Alvarez-Vázquez et al., 2008; Kesserwani et al., 2023; Kubatko et al., 2006). Moreover, unlike some 2D turbulence models that represent cylinders as voids by applying wall boundary treatment to their edges, the 2D depth-averaged SWE solvers explicitly represent the cylinders in the bed slope terms (abrupt vertices), causing the formation of local discontinuities that enable the flow separation and vorticity generation to be captured (Rizzi, 1982; Schär and Smith, 1993). Also, Manning's formula in the SWE solver comes in evaluating bed stress effects, which are omitted in some 2D models (Bonetti et al., 2017; Gioia and Bombardelli, 2001; Stovin et al., 2022). However, the potential suitability of the DG2-SWE solvers for the computation of the wake flow patterns with vortical structures in the context of laminar to low-turbulence flows past cylinders has not been explored so far.

To simulate the solute transport past explicitly modelled cylinder arrays, numerical models are commonly applied to solve the advection diffusion equation (ADE), requiring the time-averaged flow fields and turbulent diffusivity, D_t, as the inputs (Mignot et al., 2023). Generally, the flow fields are obtained from the viscous turbulence models and the D_t fields are implicitly calculated from the associated built-in turbulence closures (Golzar et al., 2018, 2017; Okamoto and Nezu, 2010; Stovin et

al., 2022). Unsurprisingly, only a few studies have focused on this topic, subject to the heavy computational costs for large scale applications.

The potential benefits of the DG2-SWE solver to produce reliable flow fields around cylinders provide the motivation to develop an ADE solver linked to the DG2-SWE solver. This might allow simulating solute transport within a domain containing a large number of cylinders at affordable computational costs. Given the good capability of the DG2 method in treating the advective fluxes, it may be an attractive candidate method to solve the ADE to form the DG2-ADE solver, especially as the advection transport typically dominates the mixing process. However, the development of this DG2-ADE solver raises two important concerns. The first concern is the specific treatments to robustly incorporate the presence of the cylinders and to preserve the positivity of the concentration fields. This is because the discretisation of the advective fluxes, although requires high-order solver, might lead to unphysical negative concentration due to knock-on effects from the numerical solver's slope limiter that appears to be inevitable for applications including the cylinders (Tsai et al., 2002). The second concern is to generate valid D_t fields explicitly from the DG2-SWE simulated flow fields, as this procedure is different from the implicit calculations of D_t in the conventional viscous turbulence models incorporated with built-in turbulence closures (Mignot et al., 2023). The potential suitability of applying this DG2-ADE solver to reproduce the solute transport within cylinder arrays and yield reliable dispersion coefficients has not yet been identified and explored. This is the scope of this contribution.

1.2 Research aim and objectives

This PhD research aims to produce an efficient and accurate numerical tool that provides detailed flow field information around cylinders to effectively simulate solute transport within a cylinder array for environmental hydraulics practitioners to estimate the dispersion coefficients. This numerical tool should link the 2D DG2-SWE solver to a newly developed 2D DG2-ADE solver, and both solvers are parallelised on graphics processing unit (GPU) for conducting fast simulations. The research aim can be divided into the following objectives:

1. To assess the suitability of the DG2-SWE solver in the context of laminar to low-turbulence flow past cylinders, and validate it relative to the FV2-SWE solver with reference to the FV2-based 2D turbulence model (e.g. FV2-based 2D Reynolds-Averaged Navier-Stokes (RANS) simulators), and experimental measurements.
2. To develop a GPU-parallelised DG2-ADE solver for simulating the solute transport past cylinders and validate it against the standard FV2-ADE solver based on the theoretical test with the analytical solution, and qualitatively compared with the commercial modelling tool (2D scalar transport available in ANSYS Fluent) based on the case involving cylinders.
3. To generate the valid flow fields and D_t fields from the DG2-SWE solver that meet physically acceptable ranges, and then to apply the DG2-ADE solver to reproduce laboratory-scale

experiments of solute transport within cylinder arrays and validate it with the measured data under laminar, transitional, and low-turbulence regimes.

1.3 Thesis structure

After this current chapter introduces the research background and objectives, **Chapter 2** presents a review of relevant published literature. The basic concepts and theories related to hydrodynamics around cylinders and the mixing process within the cylinder array are introduced and defined based on the literature review. Numerical studies focused on simulating flow past cylinders are then reviewed, including some discussions on different viscous turbulence models. This chapter also introduces the inviscid SWE model and the DG2 numerical method, demonstrating the superiority of the DG SWE solver in other hydraulic applications, including flood inundation, coastal embayment and estuary structure modelling. The final section in this chapter overviews the previous numerical studies on mixing within a cylinder array and highlights the research gaps.

Chapter 3 is dedicated to addressing **Objective 1**, whilst overviewing the DG2- and FV2-SWE solvers with a focus on highlighting their differences in numerical complexity. The convergence ability and predictive accuracy of the DG2-SWE solver are investigated across two representative test cases. The first test case is the classical benchmark of flow past one cylinder at three different R_{ed} representing laminar to transitional flow regimes, and compares the DG2-SWE solver against the FV2-SWE solver with reference to the FV2-based 2D RANS simulators. The second test case simulates experimental laminar and transitional flows past a large number of randomly distributed cylinders. The DG2-SWE solver's simulation results are assessed based on qualitative and quantitative comparisons with the experimental measurements.

After demonstrating the suitability of the DG2-SWE solver applied in **Chapter 3**, **Chapter 4** aims to address **Objective 2**, and is centred around developing a DG2-ADE solver linked to the DG2-SWE solver. Apart from describing the discretisation for ADE, the specific treatments to incorporate the presence of the cylinders and explicit generation of D_t using the simulation results of the DG2-SWE solver are also presented. Validation of implementing the DG2-ADE solver is then done via the advection dispersion test cases with and without cylinders.

Chapter 5 builds on the outcomes of **Chapter 3** and **Chapter 4** to address **Objective 3**. This chapter first introduces the experimental test case of solute transport and then describes the numerical setting for the DG2-SWE and DG2-ADE simulations. After obtaining the physically valid flow fields and D_t field, the DG2-ADE solver is applied to reproduce the laboratory-scale experiments of solute transport within cylinder arrays to assess its feasibility.

A summary of this research work, along with the key findings obtained in achieving the objectives, is presented in **Chapter 6**. The recommended future research directions are also raised at the end of this chapter.

2 Literature Review

2.1 Chapter overview

In this chapter, Sec. 2.2 reviews the hydrodynamics around one cylinder and within cylinder arrays, and Sec. 2.3 introduces the mixing process, to provide the basic concepts of this study. Numerical studies on simulating flow past cylinders are then overviewed in Sec. 2.4, demonstrating the shortcoming of the FV2-based complex turbulence simulators and introducing the potential benefits of the DG2-SWE solver. Finally, Sec. 2.5 overviews the numerical studies on mixing within cylinder arrays, discussing the few studies that have focused on this field.

2.2 Hydrodynamics around cylinders

This section starts with introducing the hydrodynamics around one circular cylinder since it is the most classic case study, from the perspective of fluid mechanics. Zdravkovich (1997) and Sumer (2006) provided the most comprehensive studies regarding flow past one cylinder and these two books are the main source of the following brief introduction. Immediately after, the basic hydrodynamics within cylinder arrays are explained by reviewing the experimental studies.

2.2.1 Flow past one cylinder

The cylinder alters flow velocities. According to the velocity variation, there are generally four regions used for defining the velocity distributions around the cylinder. As displayed in Fig 2.1, there is a very narrow region (see region (i) in Figure 2.1) in front of the cylinder, in which retarded flow exists, and region (ii) refers to the boundary layers attached to the cylinder surface. Two lateral sides of the cylinder form region (iii) where velocities are higher than upstream. Region (iv) is located downstream of the cylinder where velocities are lower than the inflow, termed the wake region.

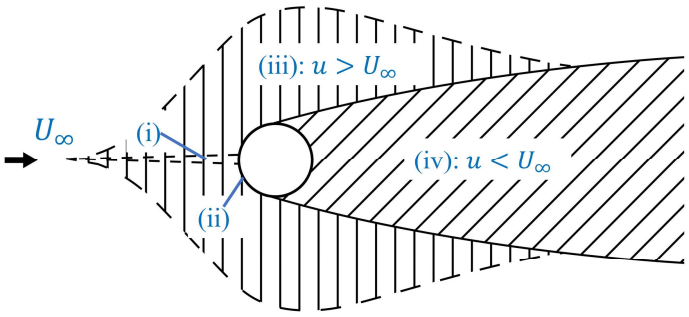

Figure 2.1. Four regions defining the velocity distribution around the cylinder. Source: Zdravkovich (1997).

The cylinder Reynolds number R_{ed} is a key parameter to determine the flow structures around the cylinder. It can be defined as $R_{ed} = U_\infty d/\nu_k$, where U_∞ denotes the steady inflow velocity, d is the cylinder diameter, and ν_k is the kinematic viscosity. As the flow rate, in turn R_{ed} increases, the flow develops into different stages. It can be classified as laminar ($0 < R_{ed} < 200$), transitional ($200 \leq R_{ed} < 400$) and turbulent ($R_{ed} \geq 400$) regimes (Sumer, 2006; Zdravkovich, 1997). For the laminar regime, it also contains three different stages defined as:

- Creeping flow regime ($0 < R_{ed} < 5$)
- Steady separation of the closed near-wake regime ($5 \leq R_{ed} < 47$)
- Periodic laminar regime ($47 \leq R_{ed} < 200$)

Creeping flow regime refers to the phenomenon that creeping flow attaches to the surface of the cylinder. Figure. 2.2a provides an example of creeping flow around a cylinder. When R_{ed} increases to the range of $5 \leq R_{ed} < 47$, namely, in the steady separation of the closed near-wake regime, a steady, symmetrical wake zone forms with a fixed pair of vortices behind the cylinder (see Figure. 2.2b). As R_{ed} further increases ($47 \leq R_{ed} < 200$), this wake zone becomes unstable and laminar eddies (vortices) are formed. These vortices are shed periodically and alternately at either side of the cylinder, as seen in Figure. 2.2c. This is the phenomenon of vortex shedding, also known as “Karman vortex street”. The formation of vortices is because, for values of R_{ed} greater than 47, sharp velocity gradients and adverse pressure gradients around the cylinder cause rotational instability (vorticity), prompting flow separation. This vorticity feeds into the cylinder downstream inducing the formation of vortices, which draws the opposing vortices on the other side of the cylinder, creating the recirculation zone behind the cylinder. The shedding frequency of vortices can be determined by extracting the time series of instantaneous velocity. With an increase in R_{ed} ($200 \leq R_{ed} < 400$), the flow is in the transitional regime, where the periodic vortices become unstable and are in transition to turbulence. For $R_{ed} \geq 400$, the flow regime is completely turbulent.

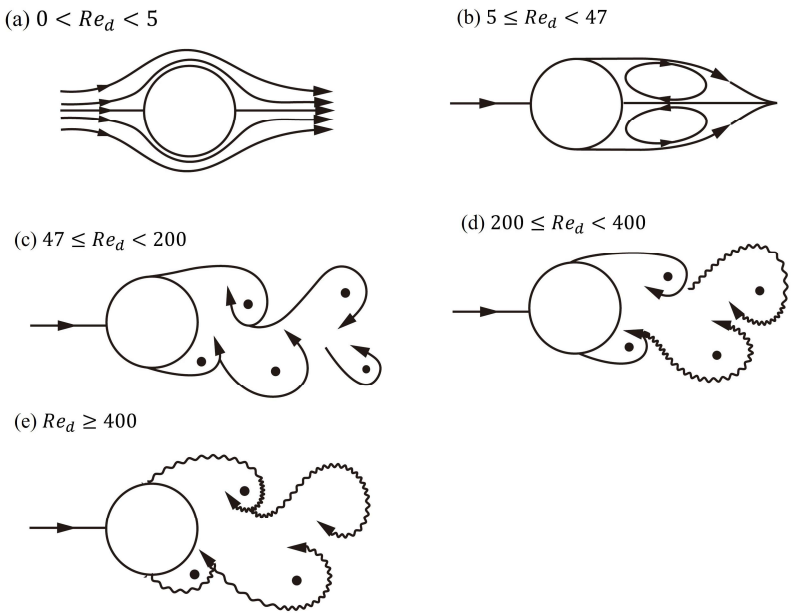

Figure 2.2. A collection of the demonstration for flow fields at different cylinder Reynolds numbers for different flow regimes. (a) Creeping flow regime ($0 < R_{ed} < 5$); (b) Steady separation of the closed near-wake regime ($5 \leq R_{ed} < 47$); (c) Periodic laminar regime ($47 \leq R_{ed} < 200$); (d) transitional flow regime ($200 \leq R_{ed} < 400$); (e) turbulent flow regime ($R_{ed} \geq 400$). Source: Sumer (2006).

The turbulence related information, like turbulent intensity (TI) and turbulent kinetic energy (TKE), behind the cylinder is also of interest. The turbulence related information is related to the fluctuating velocity components u', which is calculated as the difference between the instantaneous velocity components and time-averaged velocity components $u' = u - \bar{u}$. TI, which is defined as the ratio of the standard deviation of the fluctuating velocity components $\text{TI} = \frac{\sqrt{\overline{u'^2}}}{\bar{u}}$, is used to quantify the level of turbulence relative to the mean velocity (Raupach et al., 1991). Similar to TI, TKE represents the total kinetic energy associated with the turbulent fluctuations (Baldyga and Bourne, 1999). 2D TKE can be expressed as $\frac{1}{2}\left(\overline{u'^2} + \overline{v'^2}\right)$, omitting the vertical direction.

Paranthoën et al. (1999) concluded experimental measurements to characterize TI behind the cylinder at laminar R_{ed} between 47 and 73. At various R_{ed}, the time-averaged longitudinal velocity $\bar{u}$ in the cylinder wake were extracted. Figure 2.3a displays the distribution of the dimensionless TI (scaled with respect to their maximum values) along the cylinder centreline, showing the similar variation trend at different laminar R_{ed}. It also shows that, behind the cylinder, the turbulent intensity increases until reaching a peak value, and then decreases in the far cylinder wake area. Another experimental measurement (Uzun and Yousuff Hussaini, 2012) observed the similar variation trend in 2D TKE (red triangular markers in Figure 2.3b), even at very high turbulent R_{ed} of 1.6×10^6. Singh and Mittal (2004)

also demonstrates that the TKE structures are similar even over a broad range of R_{ed} between 10 and 10^7.

Recently, Lee et al. (2023) utilized particle image velocimetry (PIV) measurement technique to investigate the flow characteristics around one cylinder at turbulent R_{ed} of 1.4×10^{-5}. The time-averaged flow fields and turbulent-related quantities (Reynolds shear stress and TKE) behind one cylinder are included in Figure 2.4. Again, it clearly demonstrates that $\bar{u}$ initially decreases to negative values, then gradually increases with distance (Figure 2.4a). The distribution of time-averaged transverse velocity, $\bar{v}$, and Reynolds shear stress are symmetrical and with the opposite values along the centreline (Figure 2.4b-c). As for TKE, it increases and reaches peaks after some distances behind the cylinder, in line with the observation in Figure 2.3.

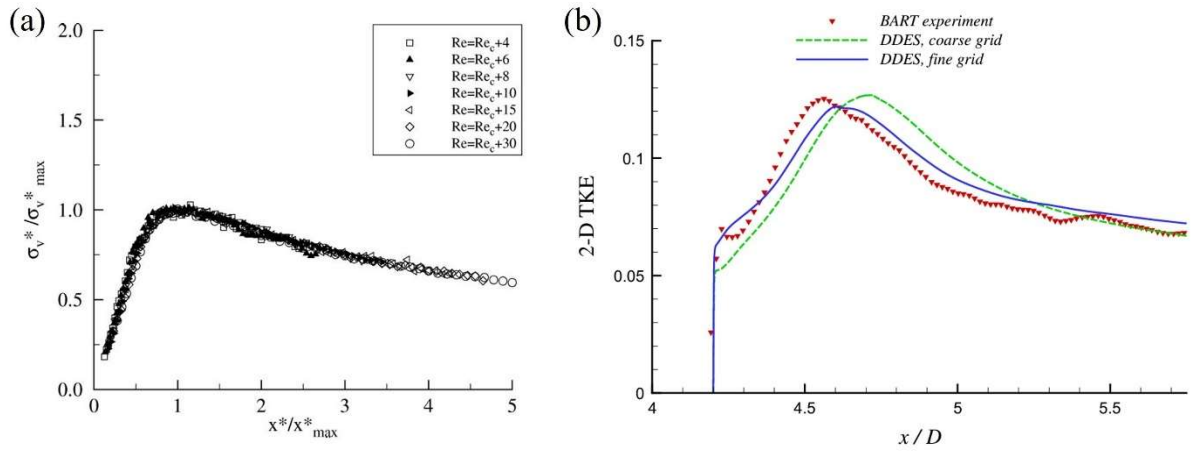

Figure 2.3. The distribution of the (a) dimensionless turbulent intensity at laminar R_{ed} and (b) 2D turbulent kinetic energy at turbulent R_{ed}, along the cylinder centreline. Source: Paranthoën et al. (1999); Uzun and Yousuff Hussaini (2012).

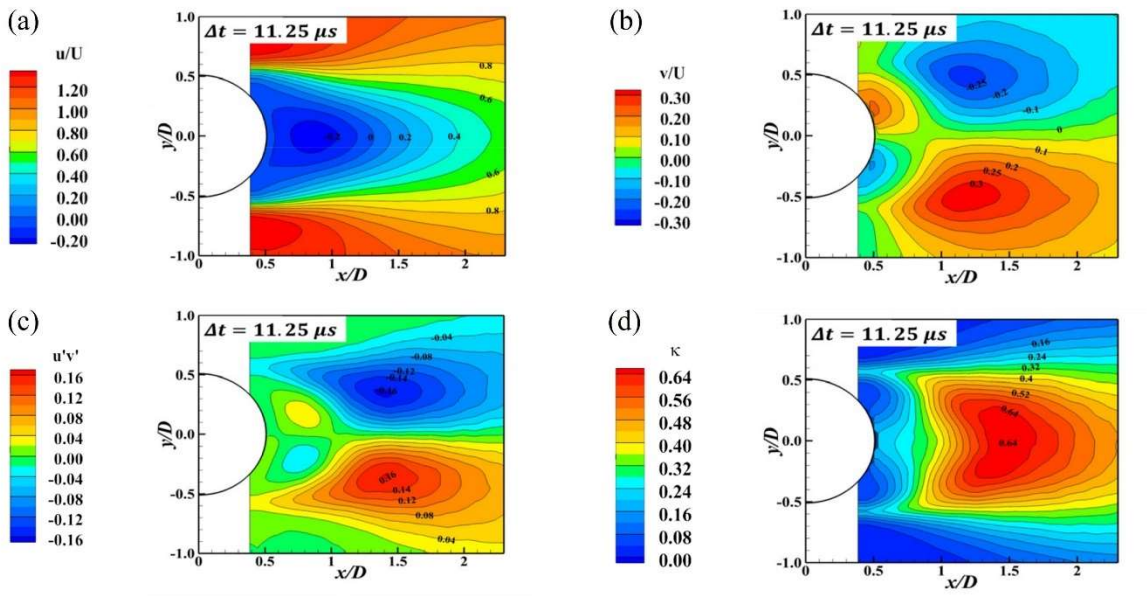

Figure 2.4. Time averaged (a) longitudinal velocity component, (b) transverse velocity component, (c) Reynolds shear stress, and (d) turbulent kinetic energy behind one cylinder, from PIV measurement at turbulent R_{ed}. Source: Lee et al. (2023).

2.2.2 Flow within cylinder arrays

When there are two or more closely located cylinders, their interactions with flows become more complex, leading to changes in flow patterns and vortex shedding frequency (Nepf, 1999; Ricardo et al., 2016b). This interaction mainly depends on the flow rates and the distribution of cylinders. The latter can be classified as regular or random cylinder arrangements. A regular distribution, for example, inline and staggered arrays often cause repeated, predictable flow patterns (Golzar et al., 2018).

To better mimic the real-world vegetated water bodies, a random distribution is of interest to environmental hydraulics practitioners and is also the focus of this study. Solid volume fraction (ϕ) is a widely used metric to describe the density of randomly distributed cylinder. It represents the fraction of the domain the cylinders occupy i.e. the density of the cylinder array, and can be calculated as $\phi = n_c \times \pi d^2/4$, where n_c denotes the number of cylinders per unit horizontal area.

ad, a dimensionless cylinder density metric is another used parameter (Chang and Constantinescu, 2015; White and Nepf, 2003), which represents the portion of the flow domain volume occupied by the cylinders. *ad* can be expressed as:

$$ad = \frac{d^2}{< s_n >_A{}^2} \tag{2.1}$$

where $< s_n >_A$ represents the average edge-to-edge spacing distance between the cylinder and its nearest neighbour.

Liu et al. (2008) conducted a comprehensive laboratory study to measure the longitudinal and vertical velocities together at multiple locations for flow past emergent and submerged rigid cylinders (represented by dowels in the experiment). This experimental study considered a single, fixed cylinder diameter d, and various cylinder conditions of roughness, solid volume fraction ϕ, staggered arrangements. As depicted in Figure 2.5a-b, for the flow within emergent cylinder arrays, the longitudinal and vertical velocity at different measurement locations almost remain constant in the vertical direction, except for the region near the bed. They also found that increasing the bed and/or dowel roughness does not result in notable alternations to the velocity profiles, still showing the similar distribution. The velocity profiles in the vertical direction within randomly distributed cylinder arrays under different ϕ were also investigated in Ricardo et al. (2016a). The laboratory measurement results again showed that the vertical spatial distribution of both longitudinal and vertical velocities is almost constant (see Figure 2.5c-d), affirming the findings made by Liu et al. (2008). Moreover, the distribution of the longitudinal and vertical turbulent intensity, TI, were also explored in both Liu et al. (2008) and Ricardo et al. (2016a). As shown in Figure 2.6, either under staggered or random distribution, both the longitudinal and vertical TI profiles are also approximately constant in the vertical direction. These observations have also been revealed by Tanino and Nepf (2008a).

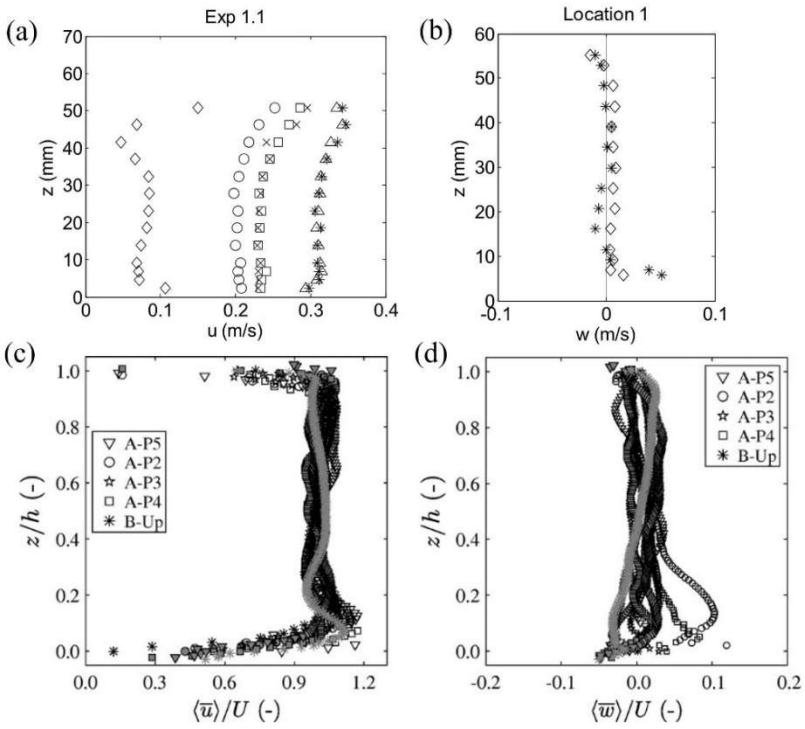

Figure 2.5. Velocity profiles in the vertical location: (a) and (b) are the longitudinal velocity at different locations and the vertical velocity distribution at one location (Source: Liu et al. (2008)) Liu et al. 2008), (c) and (d) are the normalised longitudinal vertical velocity (Source: Ricardo et al. (2016a)).

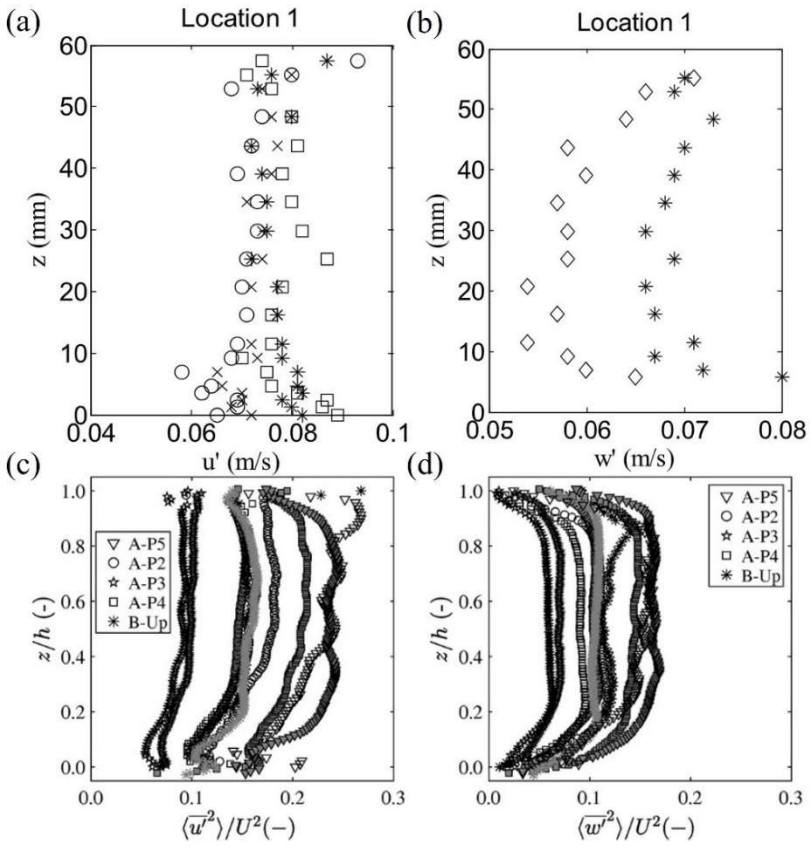

Figure 2.6. Turbulent intensity profiles in the vertical location: (a) and (b) are the longitudinal and vertical turbulent intensity at one location (Source: Liu et al. (2008)), (c) and (d) are the normalised longitudinal vertical turbulent intensity (Source: Ricardo et al. (2016a)).

Apart from investigating the flow and turbulent properties in the vertical direction, turbulent properties in the horizontal plane were also investigated. Horizontal TI was found to be almost 4-fold greater than the vertical (Tanino and Nepf, 2008a). This may be attributed to the heterogeneous nature of the wake generated by the cylinders, which primarily promotes turbulence in the horizontal plane rather than the vertical direction. The horizontal spatial heterogeneity of flow and TKE fields were also explored by (Ricardo et al., 2014). This laboratory study considered randomly distributed cylinders with a single fixed diameter and involved varying the density of cylinders longitudinally. Figure 2.7 provides an illustrative example of flow heterogeneities around the cylinders, clearing showing the high velocities patterns at two lateral sides of the cylinder and velocity-defect behind the cylinder. These patterns can be observed regardless of the density and distribution of the cylinders. They also noticed that most of the TKE production occurs due to the shedding of vortices from the individual cylinder. The rate of TKE production is greater in the wake region, while negative production of TKE was observed between closely spaced cylinders, linked to local accelerations in the flow field. Ricardo et al. (2016b) also focused on studying the influence of background turbulence caused by the randomly distributed neighbouring cylinders on vortex shedding, with results showing that the background turbulence can increase the shedding frequency.

Corredor-Garcia et al. (2020) utilized the measurement technique of Surface Particle Image Velocimetry (SPIV) to retrieve high-quality 2D instantaneous velocity maps around cylinders. Their dataset will be used for validation of the numerical model within this thesis.

More recently, Corredor-Garcia (2023) carried out a laboratory work to investigate the characteristic of flow and TKE fields within an array of cylinders with varying diameters at a range of R_{ed} between 50 and 1000. Figure 2.8 shows the 2D distribution of $\bar{u}$ and TKE. The flow field displays evident wake zones downstream of the cylinders, notable high-velocity paths between the cylinders, and indicates the complex wake interaction effects between adjacent cylinders. TKE is predominantly concentrated in the vicinity of cylinders. The TKE patterns behind cylinders of varying diameters exhibit similarities, which also resembles the one in Figure 2.4d. Moreover, the production of TKE is found to be proportional to the cylinder diameter, and the localized production of TKE is primarily attributed to vortex generation within the flow field.

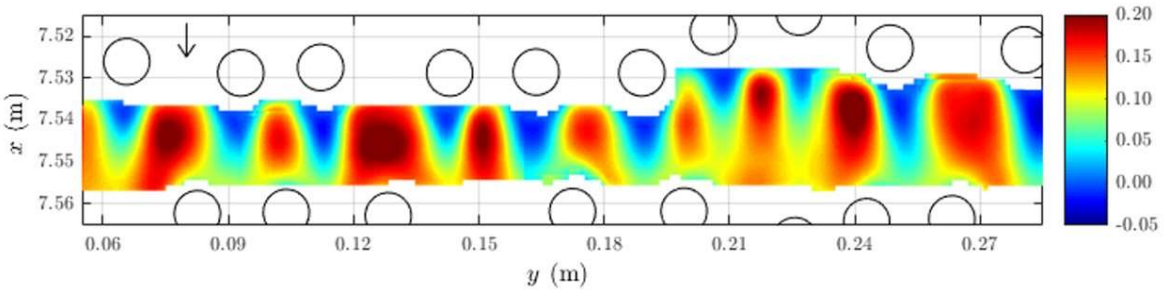

Figure 2.7. 2D distribution of time-averaged longitudinal velocity from the experimental measurement. Source: Ricardo et al. (2014).

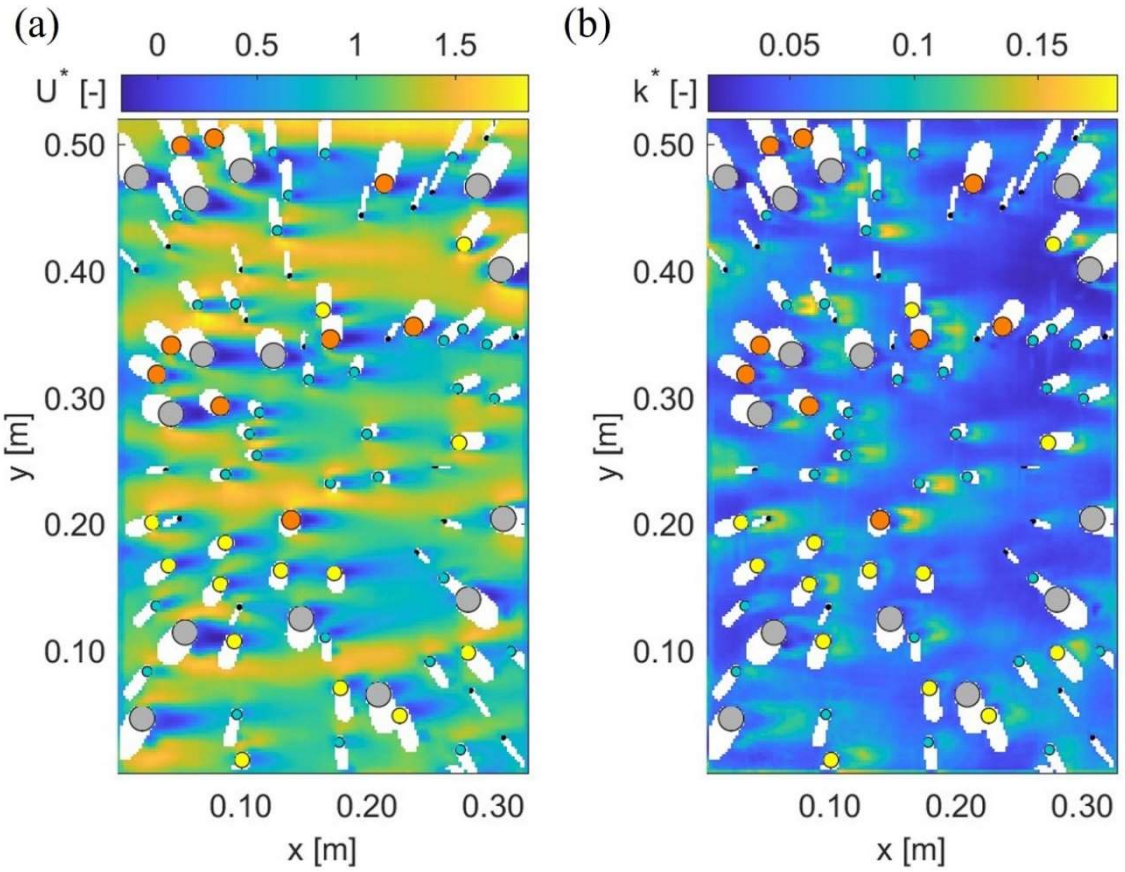

Figure 2.8. 2D map of the dimensionless longitudinal velocity and TKE within an array of cylinder with varying diameters at R_{ed} = 617 (flow is from left to right). Source: Corredor-Garcia (2023).

Apart from analysing the spatial distribution of TKE, Tanino and Nepf (2008a) quantify the spatially averaged TKE (denoted by *k* in the following equations) within the cylinder array, which could be described by the proposed function related to the drag coefficient (Nepf, 1999), given by

$$\frac{\sqrt{k}}{U_\infty} = \alpha_s (C_D a d)^{\frac{1}{3}} \tag{2.2}$$

where α_s is a scale factor around the value of 1, and C_D denotes drag coefficient. An expression of describing C_D is proposed in Tanino and Nepf (2008b) expressed as $C_D = 2\left(\frac{\alpha_0}{R_{ed}} + \alpha_1\right)$ where α_0 and α_1 are two respective coefficients related to viscous and inertial effects. The values of α_0 and α_1 depends on the configuration of cylinder arrays and these values were also further estimated based on the experimental measured C_D (Tinoco and Cowen, 2013). Under the same framework, Sonnenwald et al. (2019b) derived a new function used to estimate C_D given as $C_D = 2\left(\frac{6475d+32}{R_{ed}} + 17d + 3.2\phi + 0.5\right)$.

As for the spatial average TKE, a robust function is also provided in (Tanino and Nepf, 2008a):

$$\frac{\sqrt{k}}{U_\infty} = \begin{cases} 1.1\left[C_D \dfrac{\phi}{\frac{(1-\phi)\pi}{2}}\right]^{\frac{1}{3}}, & d/\langle s_n\rangle_A < 0.56 \\ 0.88\left[C_D \dfrac{\langle s_n\rangle_A}{d} \dfrac{\phi}{\frac{(1-\phi)\pi}{2}}\right]^{\frac{1}{3}}, & d/\langle s_n\rangle_A \geq 0.56 \end{cases} \tag{2.3}$$

where C_D can be expressed as an empirical function related to the cylinder density as $2[(0.46 \pm 0.11) + (3.8 \pm 0.5)\phi]$.

In the context of flow past rigid cylinders, the flow resistance has also been investigated and is found to be mainly affected by several factors, i.e., bed and walls' roughness, the diameter and the density of the cylinders. Manning's coefficient n_M can be expressed as the sum of these effects, and used for describing the flow resistance and also suitable for 2D depth-averaged numerical models (Chow, 1959; Wilson and Horritt, 2002). Typically, n_M ($m^{1/6}$) is obtained based on Manning's formula using the hydraulic parameters from measurement, given as:

$$n_M = k_S \frac{R_h^{\frac{2}{3}} S^{\frac{1}{2}}}{U_\infty} \tag{2.4}$$

where k_S ($m^{1/2}$ s^{-1}) is the scale factor with value of 1 to ensure the equation dimensionally correct, R_h represents the hydraulic radius (m), and S is the bed slope (m m^{-1}). Liu et al. (2008) also utilized the Manning's formula to estimate n_M for describing the flow resistance. In addition, n_M is also found to depend on the ratio of the water depth and emergent or submerged rigid cylinder height (Baptist et al., 2007; Katul et al., 2002; Shields et al., 2017). Following Luhar and Nepf (2013), n_M value can also be derived based on the density of cylinders and flow depth, which can be express as:

$$n_M = \frac{k_S h^{\frac{1}{6}}}{g^{\frac{1}{2}}} \left(\frac{C_f}{2}\right)^{\frac{1}{2}} (1 - B_x)^{-\frac{3}{2}} \tag{2.5}$$

where h denotes the water depth, g is the gravity acceleration, C_f is a dimensionless coefficient which is suggested to be around 0.13, and B_x represents the blockage factor. Since the bed slope (S in Eq. 2.4) is not available sometimes, this equation can be used instead to estimate n_M.

2.3 Mixing process within the cylinder array

Mixing processes can be classified as differential advection, turbulent diffusion and molecular diffusion (Fischer, 1979). The presence of cylinders primarily contributes to the first two effects. All these effects can be aggregated to a single reach-scale dispersion coefficient in each direction. This section introduces and explains these concepts about mixing, along with the relevant published literature.

2.3.1 Molecular diffusion

Molecular diffusion, D_m, is a mixing process which refers to the random movement of molecules, as the result of Brownian motion. This spreading process is extremely slow and can be described by Fick's first law. Namely, the mass flux is proportional to the concentration gradient and the proportionality factor is the molecular diffusion coefficient. The molecular diffusion coefficient is a fluid property, depending on the temperature, pressure and molecular intrinsic properties. Its typical values in water are around 0.5 - 2 × 10^{-9} m^2/s (Rutherford, 1994), which are negligible compared with other processes. This means that molecular diffusion can be ignored in vegetated flows and thus is not considered in the following of this study.

2.3.2 Turbulent diffusion

An increase in velocity, and in turn R_{ed}, contributes to the variation in the spatial distribution of velocity, leading to the formation and evolution of turbulent eddies. These turbulent eddies result in fluctuations of velocity with time. For the flow past one cylinder, the eddies are generated behind the cylinders, where velocities vary with time at a certain frequency, namely vortex shedding as mentioned earlier in Sec. 2.2. When the solute is injected into the flow at relatively high R_{ed}, turbulence eddies affect the velocity and in turn the solute to spread randomly over space and time. This process can be termed turbulent diffusion, and it is also a dominant process of solute mixing. In comparison to the spread that only occurs due to advection alone, turbulence has the effect of accelerating diffusion, leading to the solute spreading more rapidly. Turbulent diffusion coefficients, also called turbulent diffusivity, denoted by D_t, can be used to reflect the concentration variation due to turbulent diffusion. Turbulent diffusivity D_t is dependent on the flow velocities, turbulence and also the geometry, and it is typically of the order 10^{-3} to $10^{-1} m^2/s$ in the open channel flow (Rutherford, 1994).

Turbulence eddies transfer both the flow momentum and the solute mass. The transfer rate of momentum and the transfer rate of mass, due to the turbulent transport, were found to be less than or equal to 1 (Rutherford, 1994). Therefore, turbulent Schmidt number S_{ct} is a scaling parameter used to describe the ratio between these two transfer rates, and also connects a direct relationship between turbulent diffusivity D_t and eddy viscosity ν_t, given as $D_t = \nu_t / S_{ct}$. However, as S_{ct} represents distinct characteristics of turbulent flows, there is no commonly agreed-upon value for S_{ct}.

Gualtieri et al. (2017) firstly provided a review of past research on the choice of S_{ct} values, which range between 0.3 and 1, within environmental flows. In the context of flow and solute transport in open channels or a contact tank, the selected values of S_{ct} in experimental and numerical studies. Among these, values of 0.7 and 1 were the preferred options (Arnold et al., 1989; Djordjevic, 1993; Lin and Shiono, 1995; Rauen et al., 2012). Arnold et al (1989) conducted a systematic experimental evaluation of S_{ct} under the condition of flow within the compound channel and found that higher values of S_{ct} were observed with more significant flow interactions. Djordjevic (1993) examined solute

transport within rectangular and compound channels and discovered that the eddy viscosity approximately equals the transverse dispersion coefficient, therefore suggesting the value of S_{ct} was close to 1. A value of 0.7 was selected in the numerical model to investigate solute transport within the contact tank, and this choice can also produce reliable concentration fields (Angeloudis et al., 2015, 2014). The choice of S_{ct} is also influenced by the complexity of the numerical model. Specifically, a simpler numerical model tends to use in a lower value for S_{ct} compared to a mathematically more complex model (Duan, 2004; Ye and McCorquodale, 1997).

In vegetated flow scenarios, various values of S_{ct} have been chosen, and its range is between 0.47 and 1. Ghisalberti and Nepf (2005) experimentally determined S_{ct} around 0.47 in a vegetated shear zone, while Zhang et al. (2009) found S_{ct} to be around 1 in a non-shear zone. Sonnenwald et al. (2019a) adopted an S_{ct} of 0.7 to accurately simulate mixing within vegetation. Additionally, S_{ct} was assumed to be 1 in some past numerical studies to reproduce vegetated mixing (Lu and Dai, 2018, 2016; Okamoto and Nezu, 2010; Stovin et al., 2022).

Typically, D_t can be scaled with the turbulence kinetic energy and the characteristic length scale of turbulent mixing, l_t, that is, $D_t \propto \sqrt{k} l_t$. For the cylinder array, l_t is considered to be d when the cylinder spacing is smaller than the water depth, h, namely, D_t is proportional to $\sqrt{k} d$ (Nepf, 1999). A scale factor of 0.9 was obtained by fitting to the experimental measurement at turbulent regimes in a staggered cylinder array with ϕ = 0.0046 (Nepf, 1999), but this relationship of $D_t = 0.9\sqrt{k} d$ is not applicable for the cylinder arrays with high ϕ (Tanino and Nepf, 2008a). Like the turbulent intensity, D_t can alternatively be linked to the drag coefficient (see Eq. 2.2) as $D_t \propto (C_D a d)^{\frac{1}{3}} U d$ (Nepf, 1999).

2.3.3 Differential advection

Once injected into motion flow, the solute moves downstream driven by the flow velocity, and this movement characterised by uniform velocity is termed advection. The flux of a solute due to advection can be described by the product of the flow velocity and the solute concentration. When different particles of the solute move at different velocities, this process is named differential advection. Differential advection leads to a cloud of the solute being stretched. Also, longitudinal differential advection leads to a concentration gradient in the transverse direction, which acts to increase the transverse mixing.

As introduced in Sec. 2.2, cylinders cause the flow velocities to increase in the regions between stems (see region (iii) in Figure. 2.1) and produce velocity deficits downstream (see region (iv) in Figure. 2.2). White and Nepf (2003) theoretically and experimentally investigated the impact of velocity heterogeneity on solute transport in randomly distributed cylinder arrays. They found that in the cylinder wake (see region (iv) in Figure. 2.1), there are two main mechanisms contributing to the

longitudinal dispersion. The cylinder wake can be divided into two regions, named the primary wake and secondary wake, which are, respectively, green and blue regions in Figure. 2.3.

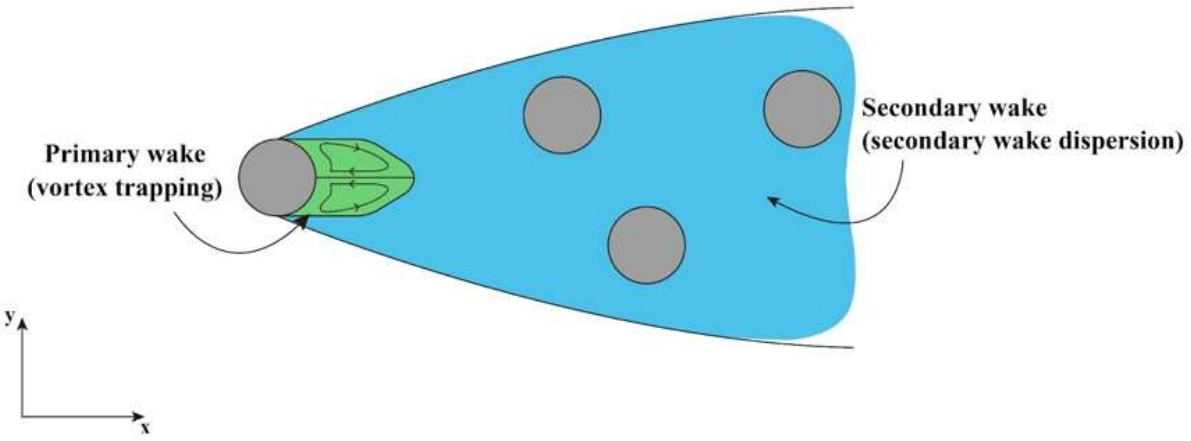

Figure 2.9. The primary wake (green region) and the secondary wake (blue region) behind the cylinder. Source: White and Nepf (2003).

The primary wake refers to the unsteady recirculation region, and the flow field in this region exhibits recirculation. The solutes fed into the primary wake are temporarily trapped and then released to move downstream. This mechanism is called vortex trapping. Following White and Nepf (2003), Murphy (2006) proposed a simplified expression to describe vortex trapping ($D_{x,VT}$) when cylinder density (ad) exceeds 0.1, given as:

$$D_{x,VT} \cong 5adUd \tag{2.6}$$

The secondary wake is the velocity deficit region downstream of the cylinder (and also downstream of the primary wake). The superposition of the secondary wakes behind the neighbouring cylinders creates the random flow field, whose heterogeneity enhances the effect of differential advection and thus contributes to the longitudinal dispersion. Secondary wake dispersion is used to term this mechanism by White and Nepf (2003). For cylinder arrays at low densities ($ad < 0.1$), in comparison with vortex trapping, secondary wake dispersion has a more significant impact on longitudinal dispersion. White and Nepf (2003) also provided an expression used to determine the second wake dispersion ($D_{x,SW}$):

$$D_{x,SW} = 2\sigma_u^{*2} s^* \sqrt{\frac{S_{ct}}{S_{ct}+1}} Ud \tag{2.7}$$

where σ_u^{*2} is the non-dimensional variance of u with respect to $\bar{u}$, and $s^* = (s+d)/d$. Lightbody and Nepf (2006) provide another expression to approximate the secondary wake dispersion at low densities ($ad < 0.1$):

$$D_{x,SW} = \frac{1}{2} C_D^{\frac{3}{2}} Ud \tag{2.8}$$

Apart from these two main mechanisms, White and Nepf (2003) also introduced another process contributing to the longitudinal dispersion. This process is induced by the velocity acceleration within the gaps between the cylinders, $D_{x,G}$, and can be expressed as:

$$D_{x,G} = \frac{C_D ad}{4(1-ad)} Ud \tag{2.9}$$

Due to the minimal velocity variations in the gaps between transversely neighbouring cylinder, White and Nepf (2003) assumed that this process $D_{x,g}$ can therefore be considered negligible.

2.3.4 Dispersion

Dispersion is not a physical property but is an approximation to account for the combined effect of differential advection and turbulent diffusion. The majority of mixing processes are dominated by longitudinal and transverse processes which can be described by the reach-scale longitudinal dispersion coefficient, D_x and the reach-scale transverse dispersion coefficient, D_y, respectively.

2.3.4.1 Longitudinal dispersion

Longitudinal dispersion is the mixing processes that affect the injected solute as it moves downstream. It can be seen from Figure. 2.10 that as a line source injected solute is carried downstream, the peak concentration magnitude decreases with the distance/time and the concentration profile begins to follow an approximate Gaussian distribution after a certain distance.

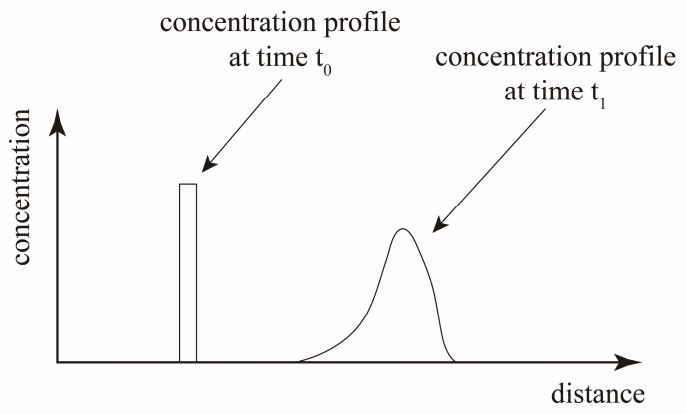

Figure 2.10. The longitudinal movement of the line source injected concentration profile. Source: Rutherford (1994).

Following Rutherford (1994), the movement of solutes is mainly affected by the flow velocity near the injection points, where the advective transport dominates over the diffusive transport. This region is called the "*advective zone*". After a certain time and distance, an equilibrium between velocity shear and diffusion in the transverse direction becomes established at a point. Beyond this point, the

solute enters the "*equilibrium zone*", and its mixing characteristics, including the variance and skewness, accordingly change. As depicted in Figure. 2.11, the variance begins to increase linearly with time/distance, and the skewness starts to decay, approaching zero. The distribution of the concentration profile eventually becomes a Gaussian, bell-shaped curve. Shucksmith et al. (2007) highlighted the importance that the solute should be within the equilibrium zone when analysing D_x.

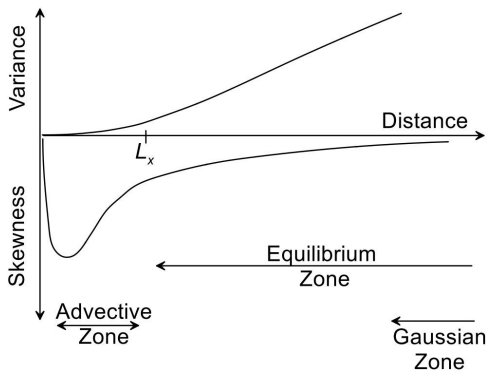

Figure 2.11. The variation trend in variance and skewness of the concentration profiles from the Fickian model. Source: Rutherford (1994).

In the context of longitudinal dispersion within emergent vegetation, White and Nepf (2003) conducted the experiment of solute transport within a randomly distributed cylinder array to investigate the longitudinal dispersion at R_{ed} between 10 and 1000. A conceptual expression used for the prediction of D_x within the cylinder array was presented. As introduced above, turbulent diffusion D_t, vortex trapping $D_{x,VT}$, and secondary wake dispersion $D_{x,SW}$ mainly contributed the longitudinal dispersion D_x, while the molecular diffusion D_m and dispersion due to gaps $D_{x,G}$ are negligible. Consequently, D_x can be expressed as the sum of these processes, namely $D_x = D_t + D_{x,VT} + D_{x,SW}$.

The longitudinal mixing in the real natural vegetation was considered by (Shucksmith et al., 2010) covering the impacts of vegetation growth and age on flow and turbulent quantities along with D_x. For the production of turbulence, it tends to increase in the transverse direction and decrease along vertical direction due to the turbulence primarily being generated at the wake of the vegetation stem. D_x is primarily related to the water depth but is also influenced by the age of vegetation and D_x exhibited an inverse relationship with the age.

Sonnenwald et al. (2017) also focused on studying the longitudinal (and transverse) dispersion within the real vegetation for slow at R_{ed} between 27 and 524, and simultaneously quantify D_x and D_y for the first time. D_x is observed to be greater than D_y by approximately an order of magnitude. In contrast to the artificial vegetation (cylinder array), the dispersion within the real vegetation is more complex. Results show that there are some differences in dispersion within two different species of real vegetation across two seasons. This study also suggests that non-dimensionalisation of dispersion

coefficients cannot fully reply on the mean diameter of vegetation stems and recommends the further model should incorporate the probabilistic descriptions for both diameter and spacing of vegetation stem/cylinder.

Sonnenwald et al. (2019c) carried out the laboratory work of dye tracing to investigate the longitudinal dispersion within the cylinder arrays with different cylinder diameters under different cylinder densities. The experimental study proposed, for the first time, instead of the cylinder diameter, using median cylinder spacing (s_{50}) as the characteristic length scale is a better option for non-dimensionalising D_x. A new simple non-dimensional model was also proposed to predict D_x:

$$D_x = 0.6Us_{50} \tag{2.10}$$

This model can provide a robust estimation of D_x, which is the right order-of-magnitude when R_{ed} is greater than 100, demonstrating its suitability in the engineering application.

2.3.4.2 Transverse dispersion

As for the traverse dispersion within the cylinder array, Nepf et al. (1997) and Nepf (1999) stated that the transverse dispersion could be described as the linear sum of the turbulent diffusion and mechanical dispersion. The mechanical dispersion refers to the flow affected by the tortuosity resulting from the obstacle (i.e., cylinders). These two independent processes can be described by their proposed models

$$\frac{D_y}{Ud} = \alpha(C_D ad)^{\frac{1}{3}} + \left(\frac{\beta^2}{2}\right) ad \tag{2.11}$$

where α and β are the scaling coefficient, whose best fit values are 0.81 ± 0.09 and 1, respectively (Nepf, 1999). The first term on the right hand side represents the turbulent diffusion, and the second term on the right denotes the mechanical dispersion.

According to this equation (Eq. 2.11), Serra et al. (2004) unitized the squared ratio of cylinder diameter and mean cylinder spacing to replace the cylinder density (*ad*) to predict D_y, given as

$$\frac{D_y}{Ud} = \alpha\left(C_D\left(\frac{d}{s}\right)^2\right)^{\frac{1}{3}} + \left(\frac{\beta^2}{2}\right)\left(\frac{d}{s}\right)^2 \tag{2.12}$$

Tanino and Nepf (2008a) conducted a systematic experimental measurement to introduce a new model to quantify the transverse dispersion within the emergent, randomly distributed cylinders featured with ϕ between 0.01 and 0.35. The transverse dispersion is still expressed as the linear sum of the turbulent diffusion and mechanical dispersion, which two independent processes can be described by as:

$$\frac{D_{y,T}}{Ud} = 4.0\frac{4}{\pi}\phi\left\langle\frac{\sqrt{k}}{U}\right\rangle P_{s_{nc}>r^*}\frac{\langle s_n^2\rangle_{s_{nc}>r^*}}{d^2} \tag{2.13}$$

where r^* represents the smallest distance between two neighbouring cylinders required to permit the occurrence of turbulent diffusion, and is consider to be equal to 2*d*.

$$\frac{D_{y,M}}{Ud} = 0.34 P_{s_{nc}<5d} \frac{\pi}{4096} \left(\frac{d^2}{k_\perp}\right)^{\frac{3}{2}} \frac{1-\phi}{\phi^2} \tag{2.14}$$

where s_{nc} is the centre-to-centre distance between the cylinders, $P_{s_{nc}<5d}$ is the probability the nearest cylinder is located within $5d$, and $k_\perp$ is the permeability in the direction of flow.

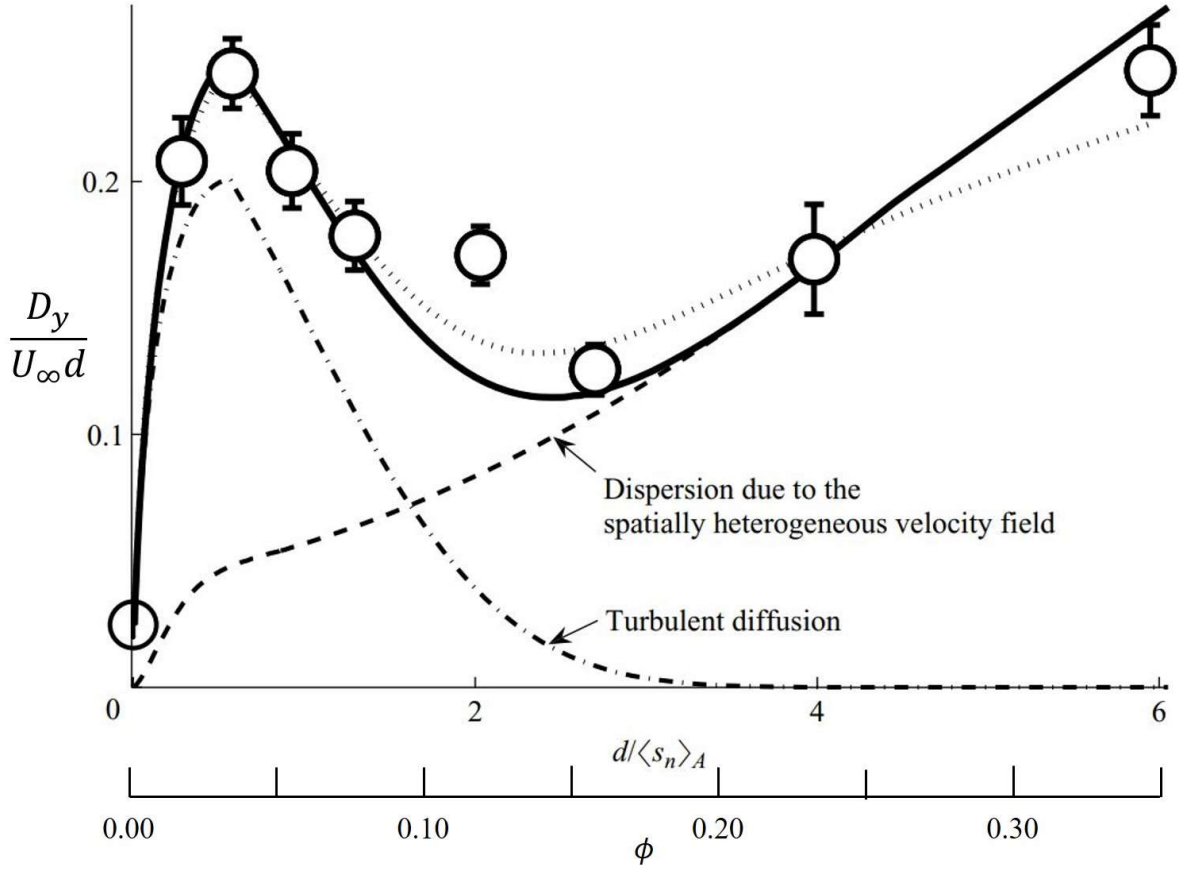

Figure 2.12. Contribution to non-dimensional transverse dispersion coefficients ($D_y/U_\infty d$), as a function of the solid volume fraction. Source: Tanino and Nepf (2008a).

As shown in Figure 2.12, an *N*-shaped relationship between the non-dimensional transverse dispersion coefficients (D_y/Ud) and the cylinder density ($d\ /\ \langle s_n \rangle_A$ or ϕ) can be observed. D_y/Ud, first increases almost linearly for ϕ lower than 0.031 (equivalent to $d\ /\ \langle s_n \rangle_A$ = 0.58), and then decreases for ϕ between 0.031 and 0.2 (equivalent to $d\ /\ \langle s_n \rangle_A$ = 0.58 and 2.7), and finally increases gradually ranging from 0.2 to 0.35 (equivalent to $d\ /\ \langle s_n \rangle_A$ = 2.7 and 6). It is worth noting that turbulent diffusion appears to be zero at high cylinder density ($d\ /\ \langle s_n \rangle_A$> 3 or ϕ > 0.25). However, this arises some concerns since either experimentally measurement or numerical simulation result shows that TKE still exist at such cylinder density (Tanino and Nepf, 2008a). An alternative option about the contribution of turbulent diffusion to transverse dispersion will be presented later in Sec. 2.5.1.

A simplified model used to estimate D_y was suggested in (Nepf, 2012). This model links the non-dimensional transverse dispersion coefficient D_y/Ud to the cylinder density (ϕ). For $\phi < 0.1$ where the turbulent diffusion dominates the transverse mixing, D_y is around $0.2Ud$, while for $\phi > 0.1$ where the mechanical dispersion is the primary contribution, D_y is related to cylinder density: $D_y = adUd$.

2.3.4.3 Calculation of dispersion coefficients

To characterise the longitudinal dispersion, concentration data at different sampling points are transversely averaged along the transverse cross-sections or spatially-averaged within small sampling windows. Their time series $C(x,t)$ are then used to calculate their temporal moments to reveal its mixing characteristics and to derive D_x. Regarding the transverse dispersion, concentration data along difference transverse cross-sections are temporally averaged, and the variance of $C(x,y)$ are used to obtain D_y.

Once the concentration data is available, two methods are typically used to derive D_x and D_y, which are the method of moments and (optimisation) routing solution. If the solute follows Fickian behaviour, the method of moment could be considered. Since the concentration is typically recorded in the form of time series at some specified locations, it is therefore convenient to calculate the moment of the temporal concentration profiles to derive D_x. The temporal moment of the concentration profiles can be expressed as (Rutherford, 1994):

$$M_0(x) = \int_{-\infty}^{\infty} C(x,t)dt \tag{2.15}$$

$$M_1(x) = \int_{-\infty}^{\infty} C(x,t)tdt \tag{2.16}$$

$$M_2(x) = \int_{-\infty}^{\infty} C(x,t)t^2dt \tag{2.17}$$

where M_0, M_1 and M_2 refer to the zeroth, first and second moment, respectively, and $C(x,t)$ is the concentration at location x and time t. From these moments, the variance of the concentration profiles can be obtained as:

$$\sigma_t^2(x) = \frac{M_2}{M_0} - \overline{t_c}^2 \tag{2.18}$$

where $\sigma_t^2(x)$ is the variance at location x, and $\overline{t_c}$ represents the centroid of the concentration profile defined as $\overline{t_c} = M_1/M_0$. the longitudinal dispersion can be derived from the variance (Rutherford, 1994):

$$D_x = \frac{1}{2}\left(\frac{x_2 - x_1}{\overline{t_c}(x = x_2) - \overline{t_c}(x = x_1)}\right)^2 \frac{\sigma_t^2(x = x_2) - \sigma_t^2(x = x_1)}{\overline{t_c}(x = x_2) - \overline{t_c}(x = x_1)} \tag{2.19}$$

where x_1 and x_2 denote the upstream and downstream locations.

However, the concentration data in the experiment may be non-Gaussian distributed (Rutherford, 1994). The (optimized) routing solution can be employed to derive the D_x and D_y, which has been shown to provide a better estimation of these coefficients from the experimental measured data (Corredor-García, 2023; Rutherford, 1994). Under the "frozen cloud approximation", i.e., assuming that no dispersion takes place during the movement of the solute cloud past a location, the (optimized) routing solution can predict the downstream concentration data according to the available upstream concentration profile, travel time/velocity (i.e, $(x_2 - x_1)/U$) and the dispersion coefficient. The latter two values can be obtained via the aforementioned method of moment.

Taking these values from the method of moment as the initial input, the routed downstream concentration profiles for the longitudinal and transverse dispersion are given as:

$$C(x_2,t) = \int_{\tau=-\infty}^{\infty} \frac{C(x_1,t)U}{\sqrt{4\pi D_x(x_2-x_1)/U}} \exp\left(-\frac{U^2((x_2-x_1)/U - t + \tau)^2}{4D_x(x_2-x_1)/U}\right) d\tau \tag{2.20}$$

$$C(x_2,y) = \int_{0}^{y} \frac{C(x_1,y)\Delta x}{\sqrt{4\pi D_y(x_2-x_1)/U}} \exp\left(\frac{-(\lambda - y - V(x_2-x_1)/U)^2}{4D_y(x_2-x_1)/U}\right) d\lambda \tag{2.21}$$

where τ and λ are the respective dummy time and width variable for integration. The travel time and dispersion coefficient can then be optimised to best fit the known (measured or simulated) downstream concentration profile. Namely, the difference between the routed concentration profile and the known profile is minimised by using the MATLAB `lsqcurvefit` function to produce the optimised dispersion coefficients. By doing so, the optimised D_x and D_y are derived separately through the 1D routing solution (Fischer, 1979).

Given the accessible 2D concentration data, Baek et al. (2006) introduced a 2D routing solution, allowing for simultaneous derivation of both D_x and D_y, that can be expressed as:

$$C(x_2,y,t) = \int_{-\infty}^{\infty}\int_{-\infty}^{\infty} \frac{C(x_1,\lambda,\tau)U}{4\pi\tau\sqrt{D_xD_y}} \exp\left(-\frac{U^2(\bar{t}-t+\tau)^2}{4D_x\bar{t}} - \frac{(y+\lambda)^2}{4D_y\bar{t}}\right) \tag{2.22}$$

However, Sonnenwald et al. (2017) demonstrated the utilization of separate 1D routing solutions does not impact the precision of the optimised D_x and D_y in comparison to the 2D version. Moreover, to evaluate the similarity between two concentration profiles (C and $\hat{C}$), goodness of fit, R_t^2, has been considered as a robust criteria (Sonnenwald et al., 2013) and can be quantified as follows (Young et al., 1980):

$$R_t^2\left(C,\hat{C}\right)=1-\frac{\int_{-\infty}^{\infty}\int_{-\infty}^{\infty}\left(C(x_2,\lambda,\tau)-\hat{C}(x_2,\lambda,\tau)\right)^2\,d\lambda d\tau}{\int_{-\infty}^{\infty}\int_{-\infty}^{\infty}C(x_2,\lambda,\tau)^2\,d\lambda d\tau} \tag{2.23}$$

2.4 Numerical studies on flow around cylinders

2.4.1 Review of numerical models

The fluid motion can be described through numerically solving a set of partial differential equations in different dimensions, which serve as mathematical expressions of the conservation laws of physics (for example, mass, momentum, and energy). Numerical models can be accordingly classified into different categories, such as the spatial dimensionality, governing equations, and discretisation methods used to solver the equations, etc. This subsection provides a review of numerical models across these three main categories.

2.4.1.1 3D and 2D models

Starting with the dimensions, both three-dimensional (3D) and two-dimensional (2D) numerical models have been considered to predict and analyse the spatial heterogeneous flow structures. 3D numerical models, although accurately delivering complex turbulence flow patterns, are too expensive for most practical applications. To circumvent these high computational burdens, 2D numerical models have been obtained by solving the 2D equations depth-averaged from the original 3D equations.

In the field of 2D modelling, there are two commonly used approaches for flow field approximation and representation of the obstacles (take the cylinder as an example), as shown in Figure 2.13. One is a 2D (planar) model that focuses on simulating flow behaviour within a 2D horizontal plan under the assumption of infinite water depth and without considering the bed resistance effects. In this approach, the cylinders are explicitly represented as voids (see Figure 2.13a) by applying wall boundary treatments to their edges (Golzar, 2018; Qu et al., 2013; Rajani et al., 2009; Stovin et al., 2022). The other approach is the 2D depth-averaged model, which accounts for the depth-averaged flow variables and bed resistance by assuming flow is integrated over the vertical dimension. The topography term (also named bed slope term) of the depth-averaged models can be used to explicitly represent the cylinders (Ginting, 2019; Ginting and Ginting, 2019). As illustrated in Figure 2.13b, the bed elevation is set higher than the water depth, creating vertical emergent cylinders that penetrate the water surface.

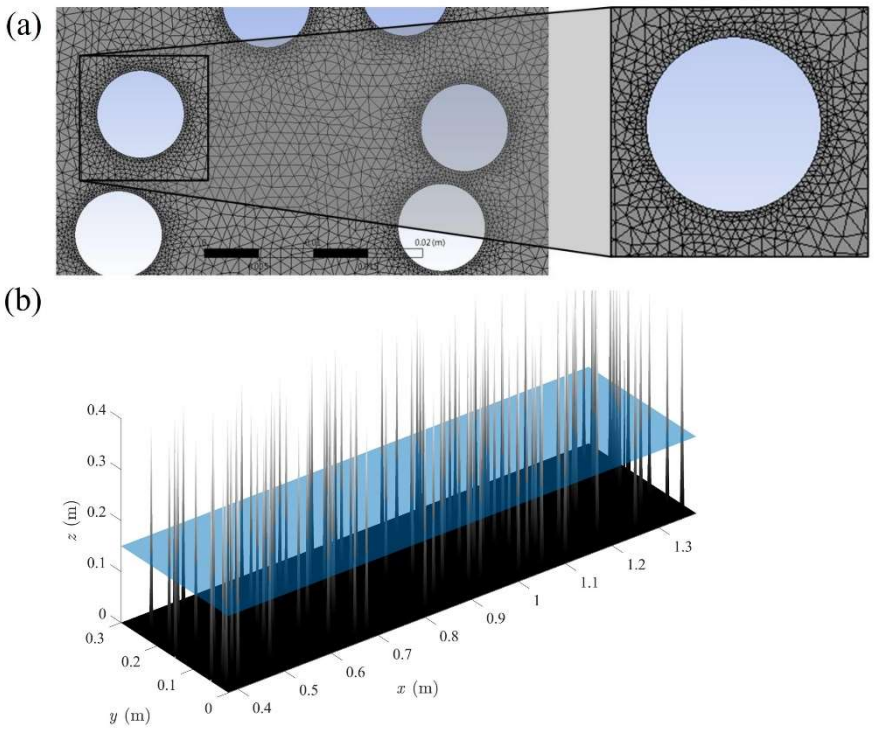

Figure 2.13. Representation of cylinders from 2D models: (a) 2D (planar) model represents cylinders as voids and apply wall boundary treatment along cylinders' edges (Source: Golzar (2018)); (b) 2D depth-averaged model represents cylinders by bed slope terms.

2.4.1.2 Viscous turbulence models and the inviscid model

From the perspective of the governing equation, numerical models can be mainly classified as Direct Numerical Simulations (DNS), Large Eddy Simulation (LES), Reynolds-Averaged Navier-Stokes (RANS) and Shallow Water Equation (SWE) models. As depicted in Figure. 2.14, these models are sorted in descending order of mathematical complexity, and more mathematical complexity correlates with higher computational costs, including computational memory and runtime. Among them, DNS, LES and RANS models are regarded as the viscous turbulent models, whereas the SWE model is considered an inviscid model which neglects the effect of viscosity.

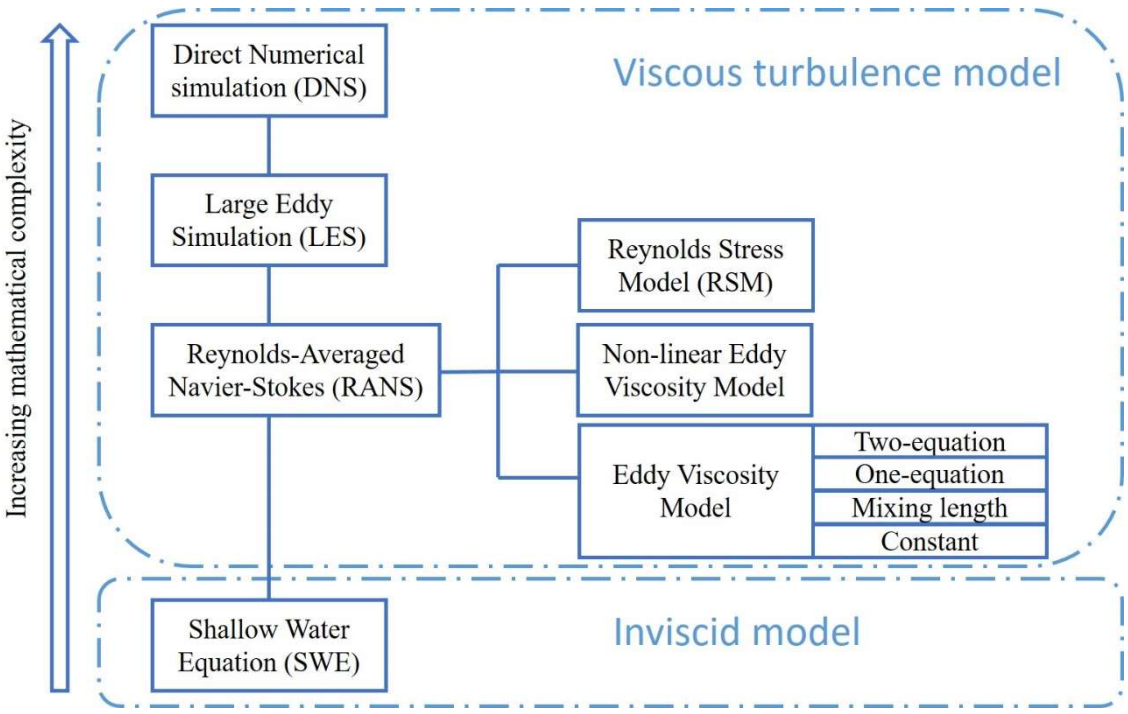

Figure 2.14. A sketch that includes different viscous turbulence models and the inviscid model, which are sorted in descending order of mathematical complexity.

DNS models, which are applied to directly solve the original Navier-Stokes equations, directly resolve all turbulent motions of all scales, requiring very fine grid resolution and providing the closest approximations to the realistic physical hydrodynamics. The advantage of using DNS models is to acquire the velocity information at all turbulent scales without any assumptions of modelling, thereby suitable for conducting fundamental research to understand turbulence. However, owing to the extremely fine resolution required, the DNS methods face the extremely high computational cost and are limited to flow at low R_{ed} within the small computational domain with simple geometries.

In the LES models, a spatial filter is applied to the Navier-Stokes equations with a filter width equal to the size of the computational grid. Turbulent eddies whose scales are larger than the scale of the grid size are resolved by directly solving the Navier-Stokes equations, while the eddies whose scales are smaller than the grid size are simulated by a subgrid-scale model. The LES models are more computational efficient than the DNS models and capable of simulating flow for a broad range of R_{ed} within a computational domain featuring complex geometries. However, the LES models are still computational expensive and not practical for large scale simulations.

The idea behind the RANS models is that the Navier-Stokes equations are time-averaged and decomposed into the mean and fluctuating parts. The equations governing the mean part are called the RANS equations (Rodi, 2017). As for the fluctuating part, it acts as stresses (generally referred to as the Reynolds stress) on the fluid and its appearance also leads to the need for additional turbulence modelling to close the RANS equations. Boussinesq (1877) proposed an approximation to introduce an

artificially isotropic eddy viscosity, in addition to the kinematic viscosity, to model the Reynolds stress. This eddy viscosity is not a real fluid property but depends on the local turbulence state. Under such assumption, different eddy viscosity models have been developed to account for the fluxes of eddy viscosity and they can be categorized into four types as follows (see Figure 2.14):

- The simplest turbulence closure is to use a constant value to represent the eddy viscosity, which is selected based on the empirical equations or case-dependent calibration. This constant eddy viscosity model has often been used for the real-world coastal application (Brière et al., 2007; Hervouet, 1999).
- The mixing length model proposed by (Prandtl, 1925) is another classical turbulence model, which assumes that the turbulent length scale is related to the water depth. The mixing length eddy viscosity model is simple and robust; however, obtaining a suitable choice of the mixing length scale is difficult.
- One-equation model is another type of turbulence model, which solves one transport equation for the turbulent quantity (turbulent kinetic energy or eddy viscosity). This one equation is more popular in aerospace, rather than in hydraulic applications (Spalart and Allmaras, 1992).
- Unlike the three eddy viscosity models mentioned above, two-equation models do not rely on empirical assumptions for determining the length scale or any other turbulent quantity. Instead, it involves two additional transport equations to represent turbulence characteristics (Rodi, 1993). k-ε is one of the most common types in the class of the two-equation models. For k- ε, one equation is for the transport of turbulent kinetic energy (k), and another one is for the dissipation rate, ε, of turbulent kinetic energy.

To address the weakness of assuming an isotropic eddy viscosity to compute Reynolds Stress, the non-linear eddy viscosity model and Reynolds stress model (RSM), also known as the second moment closure model, have been developed to account for the anisotropy of turbulence, thus better representing the realistic turbulent effects (Rodi, 1976) and providing more accurate prediction. The non-linear eddy viscosity model is more rigorous than the eddy viscosity model or can be considered as a simplified RSM. It employs the algebraic non-linear extension of eddy viscosity model to solve Reynolds stress (Ginting, 2019). On the other hand, RSM, as the most complex turbulence closure in the RANS model, solves one transport equation for each Reynolds stress (three in 2D model and six in 3D model) alongside two additional equations to model the turbulence kinetic energy and its dissipation rate. In other words, 2D RSM turbulence closure is mathematically most complex model in the RANS framework as it need solve five equations.

In terms of these turbulence models, owing to the simpler mathematical complexity, the RANS models' computational expense is less than the DNS and LES models, which make it more broadly applicable in environmental hydraulic modelling (Rodi, 2017). Moreover, when using the viscous

turbulence model, it is also necessary to implement the wall treatment around the boundary edges (Ginting, 2019).

Apart from the aforementioned turbulent viscous models, Shallow Water Equations (SWE) models can also be used to reproduce the flow fields with eddies. In the scope of the SWE model, only the advective fluxes and the hydrostatic pressure term with bed slope source terms are used to evolve the conserved momentum quantities, while bed resistance effects are incorporated in the friction source terms involving Manning's friction formula (Toro and Garcia-Navarro, 2007). Manning's formula comes in as an implicit model of the vertical turbulence structure, which is good for evaluating bed stress effects, but excludes horizontal eddy viscosity (Bonetti et al., 2017; Gioia and Bombardelli, 2001). Moreover, numerical SWE solvers explicitly represent the cylinders in the bed slope terms (abrupt vertices), causing the formation of local discontinuities that enable the flow separation and vorticity generation to be captured (Rizzi, 1982; Schär and Smith, 1993). However, the wall treatment is not incorporated within SWE.

To better understand the difference between the inviscid SWE model and viscous turbulent models, Table 2.1 lists the mathematical equation of the 2D depth averaged SWE and the widely used depth averaged RANS model with k-ε turbulence closure without considering the bed slope and friction terms. The first equation (second row in Table 2.1) is mass conservation equations, which are same for both models. The second and third equations are the momentum conservation equations in x- and y-directions, and both models sharing the same left-hand sides (advective fluxes) in these two equations. The right-hand sides of these two equations in RANS denote the kinematic and eddy viscosity terms used to account for the turbulence effects, which are absent in SWE. In contrast to SWE, the fourth and fifth equations in RANS are two additional transport equations of turbulent kinetic energy (k) and its dissipation rate (ε) used to predict the turbulence characteristics, which helps to determine the eddy viscosity. In other words, compared to RANS, SWE does not incorporate any viscosity terms beyond Manning's formula to account for turbulence effects.

Inviscid SWE numerical solvers may fall short in their capability to predict vortical structures. Nonetheless, there is an ongoing debate that such SWE solvers can, to a *certain* extent, imitate the viscosity effects of the turbulent models. This arises from the fact that the numerical approximation of the governing equations through different discretization methods induces a *certain* amount of numerical error dissipation, which can also be called numerical diffusion. When such numerical diffusion applies to the momentum quantities of the governing equations (advective fluxes in SWE), it is referred to as numerical viscosity (Ramshaw, 1994). Such numerical viscosity may mimic the actual physical kinematic and eddy viscosity present in turbulence models, which is absent in the SWE (Kesserwani et al., 2023). The amount of numerical viscosity is dependent on the grid resolution and the numerical

discretisation methods. The finer grid resolution and/or the numerically more complex discretisation methods, the less numerical viscosity.

With respect to viscous turbulence models, refining the grid resolution and/or using more complex discretization methods is necessary to reduce the amount of numerical viscosity, hence leading to more accurate simulated flow fields that are closer to the actual measurements. Otherwise, when choosing the coarse grid resolution, the increased numerical viscosity can affect the true physical viscosity effects captured by the turbulence model, manifesting as deviations in the simulated eddy sizes and velocity recovery rates. Choosing a practical resolution is crucial for viscous turbulence models, not only to avoid impractical computational costs but also to prevent numerical viscosity from affecting the physical viscosity (Dairay et al., 2017; Landmann et al., 2008). Ideally, such resolution should be close to the problem-specific turbulence length scale, and much less than the characteristic length.

Unlike viscous turbulence models, the SWE solver uses an unusually coarse resolution that is much larger than the turbulence length scale but still smaller than the characteristic length, in order to induce numerical viscosity that mimics physical viscosity absent in SWE (Kesserwani et al., 2023). Grid resolution refinement, although alleviating numerical viscosity, leads to the SWE simulated flow fields diverging from those obtained using the viscous turbulence model. In contrast, the DG2-SWE simulations offer the most reliable predictions even at coarse resolution (discussed next in Sec. 2.4.3.2). Investigating the utility of the SWE simulator at coarse resolution to model the cylinder wake is the scope of this study.

Table 2.1. Difference in the mathematical complexity (governing equations) between 2D depth-averaged SWE and RANS model.

Eq. No.	2D Depth-averaged SWE	2D Depth-averaged RANS with k-ϵ turbulence closure
1	$$\frac{\partial h}{\partial t}+\frac{\partial (hu)}{\partial x}+\frac{\partial (hv)}{\partial y}=0$$	$$\frac{\partial h}{\partial t}+\frac{\partial (hu)}{\partial x}+\frac{\partial (hv)}{\partial y}=0$$
2	$$\frac{\partial (hu)}{\partial t}+\frac{\partial (hu^2+\frac{1}{2}gh^2)}{\partial x}+\frac{\partial (huv)}{\partial y}=0$$	$$\frac{\partial (hu)}{\partial t}+\frac{\partial (hu^2+\frac{1}{2}gh^2)}{\partial x}+\frac{\partial (huv)}{\partial y}=\frac{\partial \left(2h(\nu_k+\nu_t)\frac{\partial u}{\partial x}-\frac{2}{3}hk\right)}{\partial x}+\frac{\partial \left(h(\nu_k+\nu_t)\left(\frac{\partial u}{\partial y}+\frac{\partial v}{\partial x}\right)\right)}{\partial y}$$
3	$$\frac{\partial (hv)}{\partial t}+\frac{\partial (huv)}{\partial x}+\frac{\partial (hv^2+\frac{1}{2}gh^2)}{\partial y}=0$$	$$\frac{\partial (hv)}{\partial t}+\frac{\partial (huv)}{\partial x}+\frac{\partial (hv^2+\frac{1}{2}gh^2)}{\partial y}=\frac{\partial \left(h(\nu_k+\nu_t)\left(\frac{\partial u}{\partial y}+\frac{\partial v}{\partial x}\right)\right)}{\partial x}+\frac{\partial \left(2h(\nu_k+\nu_t)-\frac{2}{3}hk\right)}{\partial y}$$
4		$$\frac{\partial (hk)}{\partial t}+\frac{\partial (hku)}{\partial x}+\frac{\partial (hkv)}{\partial y}=\frac{\partial \left(h(\nu_k+\nu_t)\frac{\partial k}{\partial x}\right)}{\partial x}+\frac{\partial \left(h(\nu_k+\nu_t)\frac{\partial k}{\partial y}\right)}{\partial y}+hP_k-h\varepsilon$$
5		$$\frac{\partial (h\varepsilon)}{\partial t}+\frac{\partial (h\varepsilon u)}{\partial x}+\frac{\partial (h\varepsilon v)}{\partial y}=\frac{\partial \left(h(\nu_k+\nu_t)\frac{\partial \varepsilon}{\partial x}\right)}{\partial x}+\frac{\partial \left(h(\nu_k+\nu_t)\frac{\partial \varepsilon}{\partial y}\right)}{\partial y}+hc_{\varepsilon 1}\frac{\varepsilon}{k}P_k-hc_{\varepsilon 2}\frac{\varepsilon^2}{k}$$

where v_k is kinematic viscosity, $v_t = c_\mu \frac{k^2}{\varepsilon}$ represents the eddy viscosity, P_k denotes the turbulent kinetic energy production from the velocity gradients, and c_μ, $c_{\varepsilon 1}$, and $c_{\varepsilon 2}$ denotes the empirical constant coefficients.

2.4.1.3 Numerical methods

Based on the spatial discretisation methods, numerical models are often classified into the following three major groups, which are the finite difference (FD) (Huang et al., 2022; Lei et al., 2000; Rizzetta et al., 2008), finite volume (FV) (Hou et al., 2015; Toro, 2001; Wang et al., 2011) and finite element (FE) (Horritt and Bates, 2001; Zhang et al., 2016) methods employed with different orders-of-accuracy.

Among these three methods, the FD method stands out as the most straightforward to implement, and its practical applicability has been widely recognized. The FD method approximates the unknown variables (for example, mass, momentum, and energy) by replacing their derivatives in the governing equations at discrete grid points (Smith, 1985). Although the FD method is generally reliable, it is limited to geometric flexibility and tends to produce spurious numerical oscillations near the abrupt changes in the solution (e.g. flash flooding simulations) (Kvočka et al., 2015; Liang et al., 2007).

In the FE method, a solution space is discretized into a finite number of elements, within which the weak form of the governing equations can be solved by multiplying a test function (also known as a basis function), yielding approximate solutions to the variables (Reddy, 1993). Compared to the FD method, the numerical foundation of the FE method is more rigorous. Such numerical complexity of the FE method entails expensive computational costs and also pose challenges in grid generation when suitable tools are not available. Despite these shortcomings, the FE method could achieve higher prediction accuracy and benefits from geometric flexibility to handle more complex and irregular computation boundaries (Fringer et al., 2019; Legrand et al., 2006).

The FV method is preferred over FD or FE methods for numerical simulations due to its stability and robustness, making it a reliable choice in various computational applications (Teng et al., 2017). The FV method works by integrating the governing equations over non-overlapping finite volumes discretized from the solution space (Godunov, 1959; Toro, 2001). Using the FV method also offers other advantages including conservation properties, geometric flexibility, and numerical simplicity to implement (Hou et al., 2015, 2014). However, the FV method tends to suffer from the fast growth of numerical dissipation error, meaning that the FV method relies on the fine grid resolution to alleviate such adverse effects (Cea et al., 2007; Navas-Montilla et al., 2019)s.

The discontinuous Galerkin (DG) method (Reed and Hill, 1973) has emerged as an alternative discretisation way and has been applied in recent decades to improve the aforementioned conventional methods (Ayog et al., 2021; Kesserwani and Wang, 2014). A detailed introduction to the DG method along with comparison to the FV method will follow in the next section (Section 2.4.3).

Furthermore, for these spatial discretisation methods, the computational domain is typically discretised on either structured (quadrilateral/square) (Ayog et al., 2021; Neal et al., 2012; Shaw et al., 2021), unstructured (triangular) (Sridharan et al., 2021; Wang et al., 2023), or the recently developed flexible grids (Fernández-Pato et al., 2018; Kesserwani and Sharifian, 2023). When comparing the utilization of square and triangular grids, the advantages of square grids lie in their accuracy and computational efficiency, whereas triangular grids are better suited for handling complex geometry (Wirasaet et al., 2014).

2.4.2 Previous numerical studies on flows around cylinders

This section reviews numerical models used to simulate flow fields around one cylinder or within an array of cylinders. The models presented below are mostly solved by the second-order finite volume (FV2) methods.

2.4.2.1 Flow past one cylinder

3D DNS models, as the most accurate models, are often applied to predict and comprehend the understanding of the flow interaction with cylinder. A series of 3D DNS simulations were performed in Wissink and Rodi (2008) to investigate the wake zone behind one cylinder. The high-quality detailed flow information were provided, including the time-averaged longitudinal and transverse velocity profiles along different cross-sections and together with turbulence statistics. Jiang et al. (2016) utilized the 3D DNS model to present the high-resolution vortical flow structures behind one cylinder to study the transition process of the cylinder wake. In the work of Jiang and Cheng (2017), the 3D DNS model is applied to numerically investigate the relationship between vortex shedding frequency and the cylinder Reynolds number, for flow past one cylinder.

3D LES models have also been proposed to obtain the flow fields around one cylinder (Hinterberger et al., 2007; Jiang and Cheng, 2021). 3D RANS models, as more economical alternatives to 3D DNS and LES models, were also widely carried out to investigate flow structure around cylinders (Ayyappan and Vengadesan, 2008; Gao et al., 2019; Li et al., 2016; Nishino et al., 2008; Rajani et al., 2009). One of the findings in these 3D numerical studies is that, for laminar and transitional regimes, the distribution of velocity and turbulent intensity in the vertical direction remains almost uniform. This finding corroborates with the aforementioned laboratory measurement in Tanino(2008) and Ricardo et al. (2014), confirming the fact that the 2D models can be used to simulate flow past cylinders to avoid overwhelming high computational burdens.

Hinterberger et al.(2007) examined the performance of the 2D LES model in terms of flow past one cylinder, by comparing it with the 3D LES model. The comparison results revealed that the flow structures obtained from the 2D LES model, although less realistic than the 3D LES model, are sufficiently accurate for practical application, such as for predicting flow pattern around bridge pier and/or cylindrical hydraulic structures. Rajani et al. (2009) applied the 2D RANS k-ε model to concentrate on the cylinder wake at laminar to transitional flow regimes, with results showing that the physical flow features were well captured at R_{ed} between 100 and 400. It contains the analysis of vortex shedding frequency, and vortical flow structures, like vorticity. An example of the simulated vorticity contours at R_{ed} = 250 are presented in Figure 2.15, which is used as the reference in the latter performance evaluation. Qu et al. (2013) used the 2D RANS k-ω model to reproduce laminar flow structures around one cylinder, which are in good agreement with the published numerical and experimental results. This numerical study also focuses on investigating the impact of R_{ed} on flow fields. At R_{ed} between 50 and 200, the frequency of vortex shedding increases with the increase in R_{ed} and the recirculation length (distance between the cylinder edge to the point where $\bar{u}$ changes from negative to zero) of the wake zone decreases. Flow structures behind the cylinder were also explored in terms of comparing the distribution of instantaneous vorticity. An illustrative example of vorticity contours is presented in Figure 2.15. Since the flow regimes considered in Rajani et al. (2009) and Qu et al. (2013) are in the same scope as this PhD study, their flow information will be used as the reference to assess the performance of the numerical model of flow past one cylinder.

Ginting (2019) applied RANS model with algebraic stress turbulence closure model to perform simulations at very find grid resolution to explore the cylinder wake at turbulent R_{ed} of 5900. Instantaneous velocity components were used to visualise the vortex street pattern, via the streamline over one shedding cycle (see Figure 2.16). The streamline for the flow past one cylinder at laminar R_{ed} = 100 (Hajihassanpour and Hejranfar, 2020) is also included in Figure 2.16. Generally speaking, the numerical studies on flow past one cylinder often extract instantaneous velocity component to explore the evolution of vortices, via the streamline and vorticity, and utilize time-averaged velocity components to investigate its distribution along the centreline. Moreover, using a sufficiently fine grid resolution has proved necessary with FV solvers to counterbalance their tendency to develop numerical error dissipation (Ginting 2019). In other words, computational runtime and memory costs inevitably increase for FV solvers to capture the wake evolution and interactions past a large number of cylinders.

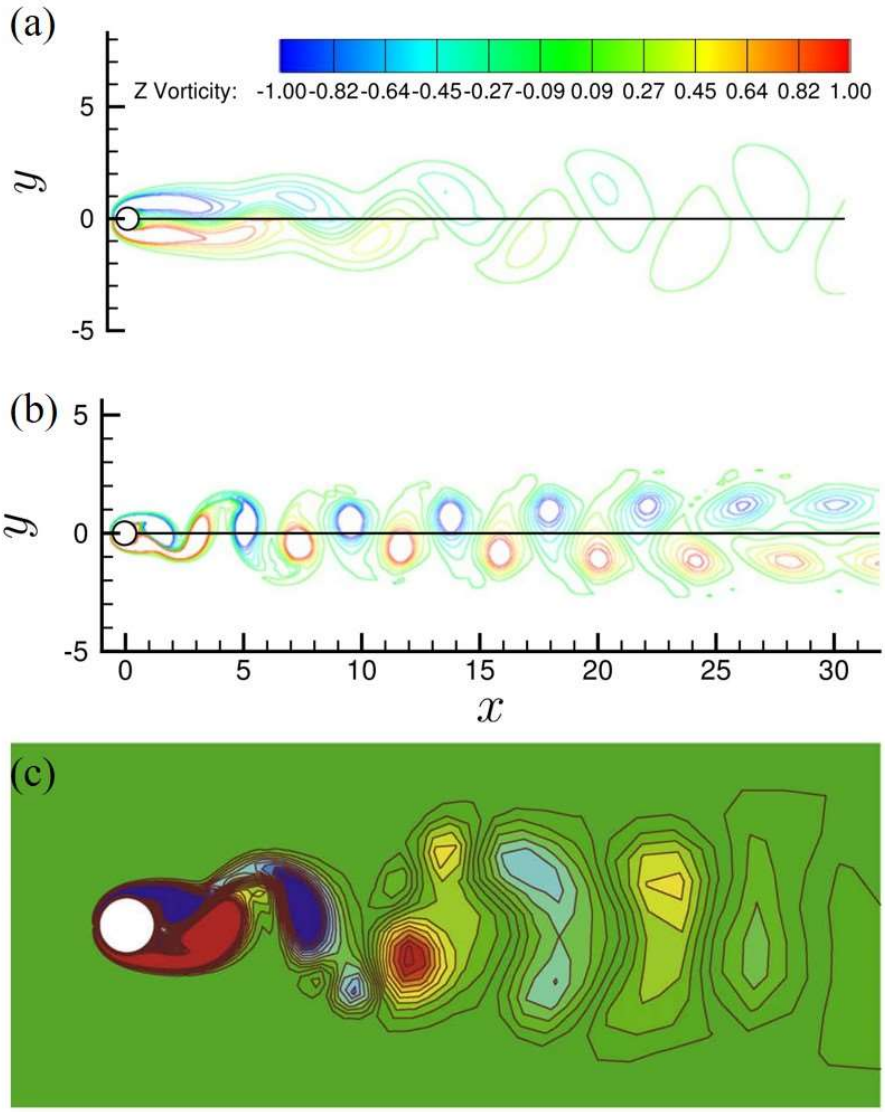

Figure 2.15. Numerical simulated instantaneous vorticity contours behind one cylinder at R_{ed} = (a) 50, (b) 200 and (c) 250. Source: first two rows are from Qu et al. (2013) and the last row is from Rajani et al. (2009).

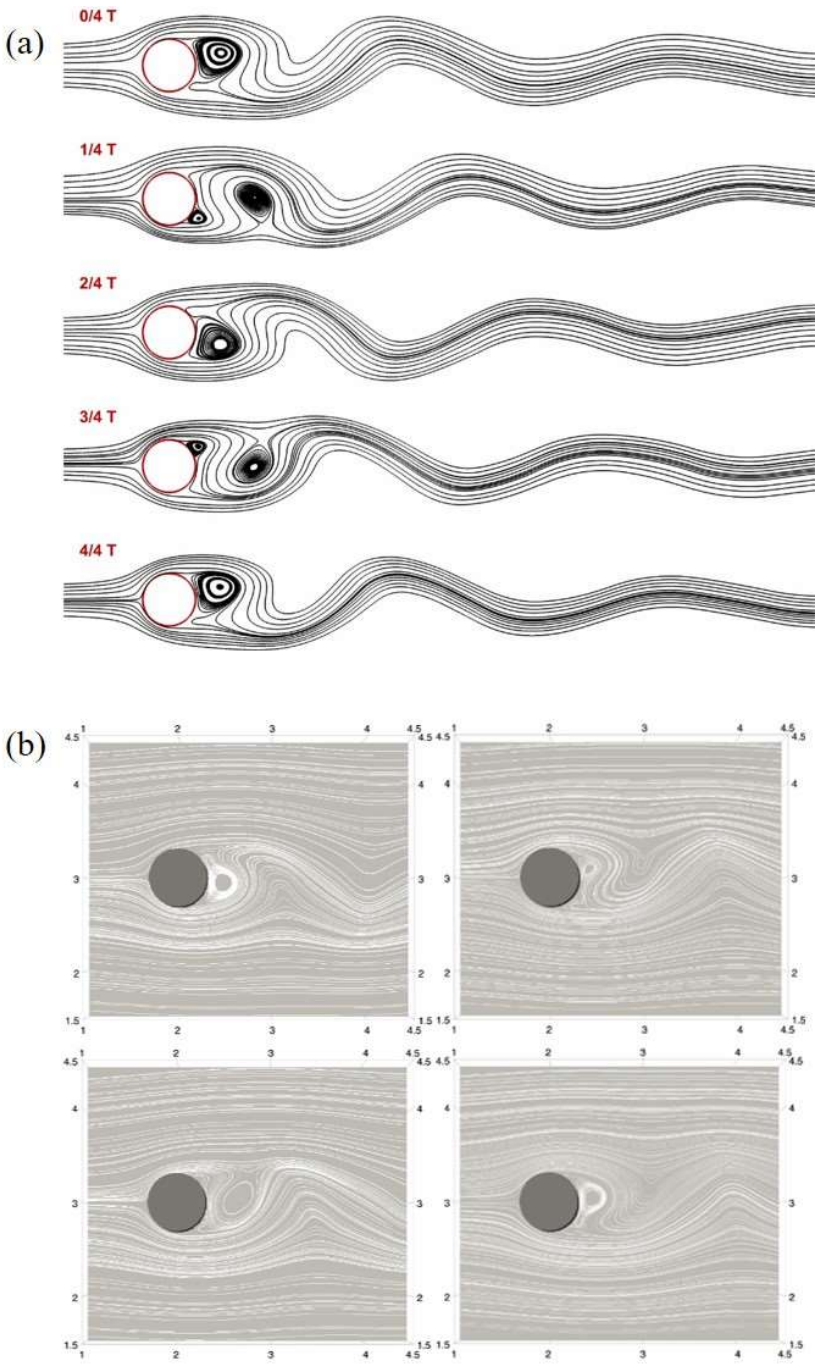

Figure 2.16. Numerical simulated instantaneous streamline over one shedding cylinder behind a single cylinder at (a) laminar (Source: Ginting (2019)) and (b) turbulent R_{ed} (Source: Hajihassanpour and Hejranfar (2020).

2.4.2.2 Flow past a group of cylinders

In the field of numerically investigating the flow within cylinder arrays, currently, there are two strategies which have been used to take the cylinder arrays into consideration. One is a bulk-scale approach to treat the cylinder array as a porous media (Tsavdaris et al., 2015), and the other approach is to explicitly model each cylinder in the computational domain. The former approach requires choosing suitable bulk-scale drag coefficients to represent vegetation effects, which are case-dependent and are not straightforward to obtain. The main benefit of this approach is computational efficiency; it is feasible to implement bulk-scale coefficients to represent the effects of multiple cylinders within one very coarse computational grid, thereby modelling ponds or river reaches at full scale. In contrast, the latter approach is computationally expensive, and is only practically applicable at small scales, such as the representation of an individual patch of vegetation. The explicit modelling approach only needs the cylinder locations and can better reproduce the interactions between flows and cylinders, as well as the mixing process; Fundamental hydraulic relationships are used to identify the flow field and the resulting solute mixing processes. This study only focuses on the approach of modelling cylinders explicitly.

Tong (2014) and Tong et al. (2014, 2015) focused on analysing the complex flow interactions with two to four cylinders under the different spatial arrangements, through the 3D DNS models. The results revealed that (i) multiple cylinders distributed sparsely (there are no interactions between eddies introduced by cylinders) share similar flow patterns to that behind a single cylinder, (ii) vortex shedding frequencies depend on the spatial distance between two adjacent cylinders, and (iii) the laminar and transitional flows ($R_{ed} < 400$) are predominantly two dimensional, which is in line with the experimental observation.

In Stoesser et al. (2010), a 3D Large-Eddy Simulation (LES) model was employed to simulate the flow past three groups of staggered cylinders with varying cylinder densities at turbulent R_{ed} of 500 and 1340. Either instantaneous or time-averaged flow and turbulence structures from the 3D LES simulation are in close agreement with the experimental measurements from Liu et al. (2008), demonstrating the capability of 3D LES in investigating the detailed and informative flow and turbulence mechanics. They also found that the density of cylinders has a greater influence on flow properties than R_{ed}. At low cylinder density, the wake flow and turbulent structures closely resemble those observed in the case of flow past one cylinder, while at high cylinder density, the structures behave quite differently due to the complex flow interactions with densely distributed cylinders.

Etminan et al., (2017) also applied 3D LES models to investigate the impact of cylinder density on flow structures around the cylinder. This study considers a staggered array of cylinders with six densities at R_{ed} between 200 and 1340. They found that, as the cylinder density increases, the flow path between the cylinders becomes increasingly tortuous. In terms of the cylinder wakes, there is an inverse relationship between wake length and width with changes in cylinder densities. Furthermore, the

difference between the maximum and minimum time-averaged (and vertical averaged) velocities is found to increase with the cylinder density. The spatial variance of time-averaged velocities also appears to increase, as discussed in White and Nepf (2003). The shedding frequency is also affected by the width of cylinder wake: the narrower width leads to the higher shedding frequency. Although these 3D numerical simulators lead to unrivalled flow field predictions, they often entail overwhelmingly high computational costs as the physical scale of the application becomes large (horizontal area exceeding 1 m^2).

Golzar et al. (2018) employed the 2D RANS with Reynolds Stress Model turbulence closure to compare the effects of cylinder arrays due to regular or random distribution on the simulated flow fields. The simulated flow field within the regular cylinder array exhibits a periodic, repetitive pattern. Under the same cylinder diameter and density, the random distribution results in a higher maximum velocity compared to that observed with a regular distribution. Also, a relatively higher velocity shear can be seen in the random cylinder array.

Stovin et al. (2022) also employed the same 2D RANS model with RSM turbulence closure to simulate turbulent flow (with R_{ed} around 500) past cylinder arrays. The simulations covered a broad range of cylinder densities and included uniform/non-uniform cylinder diameter distributions. In the simulated flow fields, regardless of the distribution of cylinders, there are clear wake zones behind the cylinders and high-velocity flow in the open areas.

To the author's best knowledge, the 2D depth-averaged SWE models have never been applied to simulate laminar to low-turbulent ($R_{ed} \leq 450$) flows past one or a group of circular cylinders, however, these models have been applied to investigate the flow structures around the vortical structures at high turbulent flows. These studies will be discussed in the next section.

2.4.3 DG2-SWE solver

2.4.3.1 DG method

DG method was first introduced and implemented to solve steady linear hyperbolic equations in the work of Reed and Hill (1973). Later, the DG method with a focus on high order discretisation in space and time was developed to solve time-dependent non-linear hyperbolic equations (Cockburn et al., 2000; Cockburn and Shu, 2009). The DG method integrates the local conservation principle of the FV method with the weak formulation of the FE method to approximate solutions over grid elements. In essence, it evolves a local Legendre polynomial solution over each grid element, utilizing both the local information and adjacent neighbour's information for numerical flux calculation.

Compared to the FV (or FE) method which only evolves one average coefficient to model the piecewise-average approximation of the variables, the DG method uses one average coefficient and additional local slope coefficients to model the piecewise-planar approximation. In the DG method, the

required number of coefficients varies based on the order-of-accuracy and the dimensionality of the governing equations (Caviedes-Voullième and Kesserwani, 2015). This means that the numerical complexity of the DG formulation is proportion to the order of accuracy. Increasing the order of accuracy entails greater computation costs, thereby impacting computational efficiency, often rendering it unsuitable for practical applications. Kesserwani and Liang (2011) and Kesserwani and Wang (2014) have suggested the use of second-order DG (DG2) method as a trade-off between the computational accuracy and efficiency.

Kesserwani et al. (2018) developed a simplified DG2 formulation called slope-decoupled formulation, which uses a simplified calculation stencil (see Figure 2.17a) to replace the standard calculation stencil (see Figure 2.17b). The calculation stencil refers to the arrangement of points surrounding a central point (e.g., (x_c, y_c)) within a computational grid element, determining which points are involved in calculation operations. Compared to the standard DG2 method, which requires 32 calculation operations within a grid element, the simplified DG2 method reduces this to only 12 calculation operations, therefore gaining a 2.6-fold speed up. As for the accuracy, this simplified DG2 method can still preserve second-order accuracy and yield prediction results very close to those of the standard DG2 method. This demonstrates its appeal for application in solving different numerical models/governing equations. A graphics processing unit (GPU)-parallelised version of this simplified DG2 solver to the 2D depth-averaged SWE was released in Shaw et al. (2021) and integrated into LISFLOOD-FP for reducing computational runtime costs.

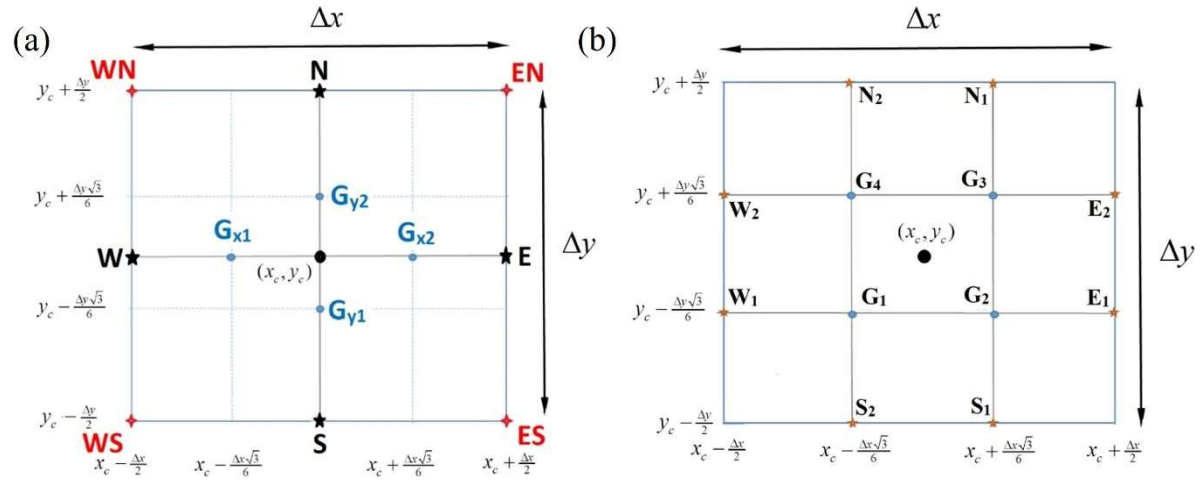

Figure 2.17. Calculation stencil of a grid element at (x_c, y_c) for the (a) simplified ('slope-decoupled') formulation and (b) standard formulation of the DG2 method. Source: Kesserwani et al. (2018).

2.4.3.2 Comparison between DG2-SWE solvers and FV2-SWE solvers

Second-order discontinuous Galerkin (DG2) solvers of the SWE (i.e., herein referred to as DG2-SWE solvers) are numerically more complex than FV2-SWE solvers. To better understand the

difference in numerical complexity, Table 2.2 compares how the DG2-SWE and FV2-SWE solvers represent the flow variables (i.e., the conserved mass quantity, or the water depth h and the conserved momentum quantities, or the unit-width discharges q_x/q_y) and topography, z, over a computational grid. Figure 2.18 also provides the sketch illustrating the shape of flow variables and topography from both solvers. In a Godunov-type framework, both solvers update flow data elementwise based on the inter-elemental advective flux exchange provided by the Riemann problem solutions (Toro and Garcia-Navarro, 2007). In contrast to an FV2-SWE solver, which generates and updates one coefficient of piecewise-averaged flow data (Figure 2.18b), a DG2-SWE solver involves three coefficients, of an average and two directionally independent slopes, to generate and update piecewise-planar flow data (Figure 2.18a). The update step in the DG2-SWE solver extends the Godunov-type interpretation to further evolve the slope coefficients from the inter-elemental advective flux exchange while using piecewise-planar representations of the bed elevation (Figure 2.18c). A description of the DG2-SWE solver alongside the FV2-SWE solver is provided in Appendix A.

Generally, the extra numerical complexity of DG-based solvers makes them superior to equally accurate FV-based solvers in capturing advective fluxes over and past sharp obstacles (Kesserwani, 2013), and in delivering faster mesh-convergence rates at smaller errors (Kesserwani, 2013; Zhang and Shu, 2005; Zhou et al., 2001) – thus more accurate predictions at coarser grid resolutions. For flood inundation modelling, although the DG2- and the FV2-SWE solvers can both deliver second-order convergence rates (Kesserwani and Wang, 2014), the former excels in maintaining a significantly lower and slowly evolving amount of numerical error dissipation despite grid resolution coarsening (Ayog et al. 2021). Practically, the properties of the DG2-SWE solver lead to more accurate and conservative velocity predictions at 4 to 10 times coarser grid resolutions, as shown in alternative studies focused on transient flood modelling (Kesserwani and Wang, 2014; Shaw et al., 2021; Vater et al., 2017).

Table 2.2. Difference in the numerical complexity (spatial discretisation) between DG2-SWE and FV2-SWE solvers.

	DG2-SWE	FV2-SWE
Flow variables	$\boldsymbol{U_h}(x, y, t) = \mathbf{U_c} \cdot \boldsymbol{P} = \begin{bmatrix} h_c^0 & h_c^{1x} & h_c^{1y} \\ q_{x_c}^{\ 0} & q_{x_c}^{\ 1x} & q_{x_c}^{\ 1y} \\ q_{y_c}^{\ 1x} & q_{y_c}^{\ 1x} & q_{y_c}^{\ 1y} \end{bmatrix} \cdot \begin{bmatrix} 1 \\ 2\sqrt{3}(x - x_c)/\Delta x \\ 2\sqrt{3}(y - y_c)/\Delta y \end{bmatrix}$	$\boldsymbol{U_h}(x, y, t) = \boldsymbol{U_c^0} \cdot P = \begin{bmatrix} h_c^0 \\ q_{x_c}^{\ 0} \\ q_{y_c}^{\ 0} \end{bmatrix} \cdot 1 = \begin{bmatrix} h_c^0 \\ q_{x_c}^{\ 0} \\ q_{y_c}^{\ 0} \end{bmatrix}$
topography	$z_{\boldsymbol{h}}(x, y) = \boldsymbol{z_c} \cdot \boldsymbol{P} = \begin{bmatrix} z_c^0 & z_c^{1x} & z_c^{1y} \end{bmatrix} \cdot \begin{bmatrix} 1 \\ \dfrac{2\sqrt{3}(x - x_c)}{\Delta x} \\ \dfrac{2\sqrt{3}(y - y_c)}{\Delta y} \end{bmatrix}$	$z_{\boldsymbol{h}}(x, y) = \boldsymbol{z_c} \cdot P = z_c^0 \cdot 1 = z_c^0$

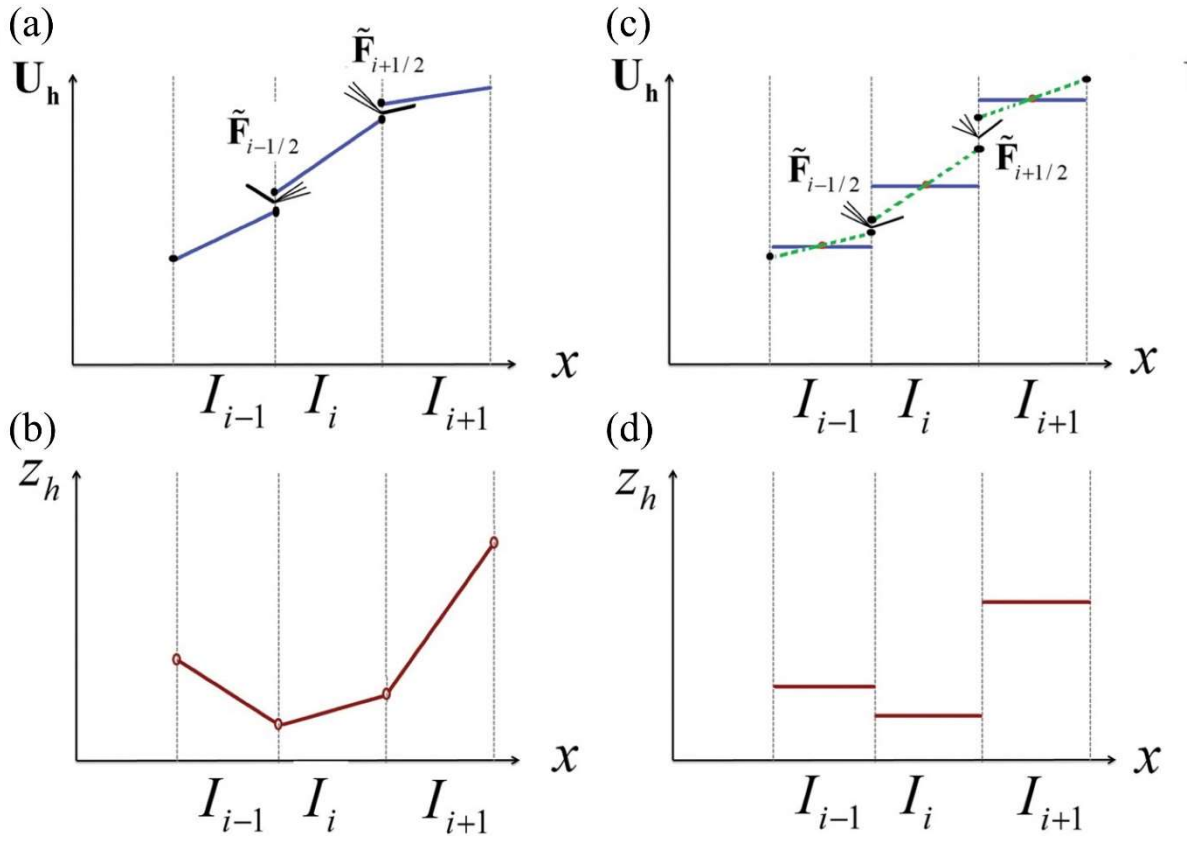

Figure 2.18. 1D Local spatial discretisation of the flow variables (upper panel) and topography (lower panel) in *x*-direction: (a) and (b) are from the DG2-SWE solver, while (c) and (d) are from the FV2-SWE solver.

For coastal and estuary modelling applications, the extra numerical complexity of the DG2-SWE solver makes it able to capture the eddies within its 2D flow field predictions, as hinted in a few

published papers. Kubatko et al. (2006) examined the capabilities of the DG2-SWE solver as well as the higher-order DG SWE solvers in producing well-resolved flow fields around the coastal tidal inlet. It was shown that the DG2-SWE solver excels in capturing eddies around the inlet and delivers the flow field as accurately as other higher-order DG solvers' solutions. Alvarez-Vázquez et al. (2008) utilised the DG2-SWE solver to investigate the flow interactions with the hydraulic structure of river fishways, demonstrating its suitability for capturing recirculation eddies induced by obstacles. The performance of the DG2-SWE solver in predicting the vortical flow structures around hydraulic engineering structures was also explored in the work of Kesserwani et al. (2023).

Kesserwani et al. (2023) applied both DG2-SWE and FV2-SWE solvers to simulate the flow diversion within a T-junction shaped domain where there is a square obstacle in the main branch (see Figure 2.19a). As shown in Figure 2.19b and c, there is a big discrepancy between their simulated time-averaged flow fields within the separation area (vertical area). In this area, the DG2-SWE solver even at 4-fold coarser grid resolution is able to capture the recirculating eddies, whereas the FV2-SWE prediction appears to spuriously elongate the eddies. This unrealistically flattened vortical flow structure in the FV2-SWE prediction can be attributed to the fact that FV2-SWE solver suffers from the fast growth of numerical error dissipation that manifests in a large amount of numerical viscosity which, in turn, masks the turbulence effects. Such adverse effects of the FV2-SWE solver, as also observed in earlier findings by (Cea et al., 2007) and Navas-Montilla et al. (2019) can be mitigated by incorporating eddy viscosity terms within the solver, as suggested by Syme (2008).

DG2-SWE solver is also applied to simulate the formation of vortices behind a conical island at high turbulent flow condition, and its simulated velocity vectors are compared with the ones from the third order finite volume (FV3) SWE solver (Figure 2.20a vs. b). The higher-order FV3-SWE solver delivers the spurious asymmetry of eddies in the region far away from the cylinder (Figure 2.20b), whereas the DG2-SWE solver yields reasonable 'vortex street'. The DG2-SWE simulated velocity vectors behind the conical island at the fine (Figure 2.20d), medium (Figure 2.20e) and coarse grid resolution (Figure 2.20f) are compared with the measurement within three subregions (Figure 2.20c). Compared to the measured vectors, at coarse grid resolution, the DG2-SWE solver provides the best directional alignment, whereas distorted simulated eddies can be observed in simulated vectors at fine resolution. This implies that, for the DG2-SWE solver, using fine resolution leads simulated flow fields converged to a state with increasingly less numerical viscosity, which would then diverge from the actual flow state with turbulent effects. This can be alleviated by incorporating the turbulence closure models. However, resolution coarsening retains a certain amount of numerical error dissipation (numerical diffusion) which can approximate the true kinematic and eddy viscosity effects, therefore providing better results than those from fine resolution.

Quantitative and qualitative analyses demonstrated the DG2-SWE solver is a competitive choice for acquiring reliable 2D flow field predictions. Despite these merits, the DG2-SWE solver is not applied for modelling the laminar to low-turbulence flows past the cylinders. The influence of the advective fluxes on the computation of wake flow patterns with vortical structure behind cylindrical obstacles is yet to be examined with reference to the DG2- and FV2-SWE solvers. This is the novel objective and scope of this contribution.

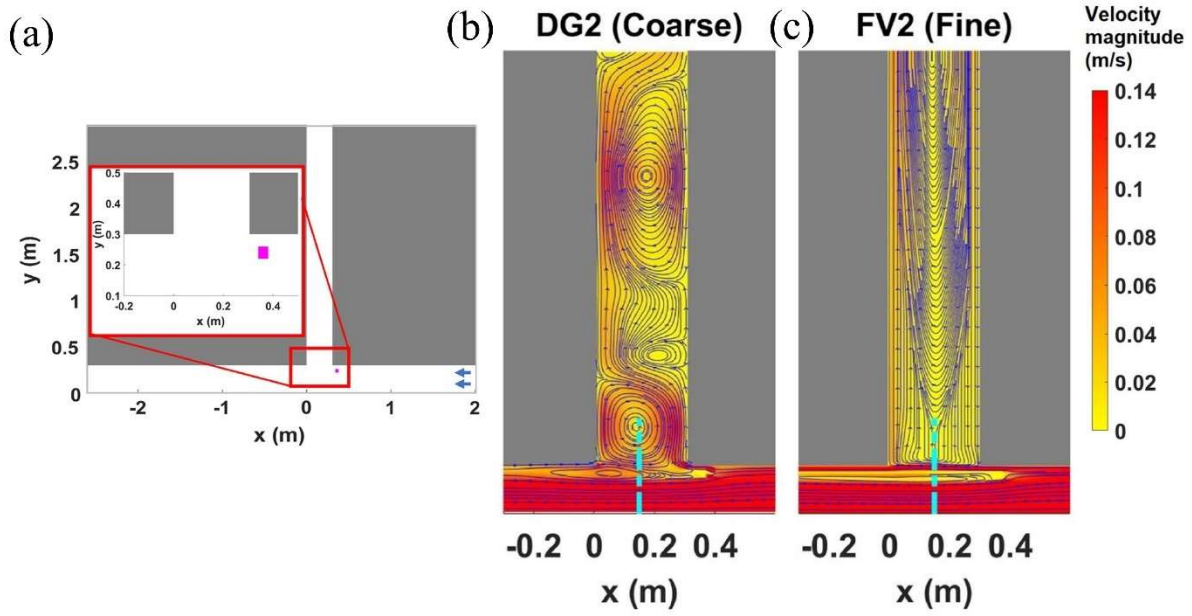

Figure 2.19. Flow (from right to left) past a square obstacle at a T-junction: (a) a sketch of T-junction involving a square obstacle, and the streamlines of simulated time-averaged flow fields from (b) the DG2-SWE solver at coarse grid resolution and (c) the FV2-SWE solver at fine grid resolution. Source: Kesserwani et al. (2023).

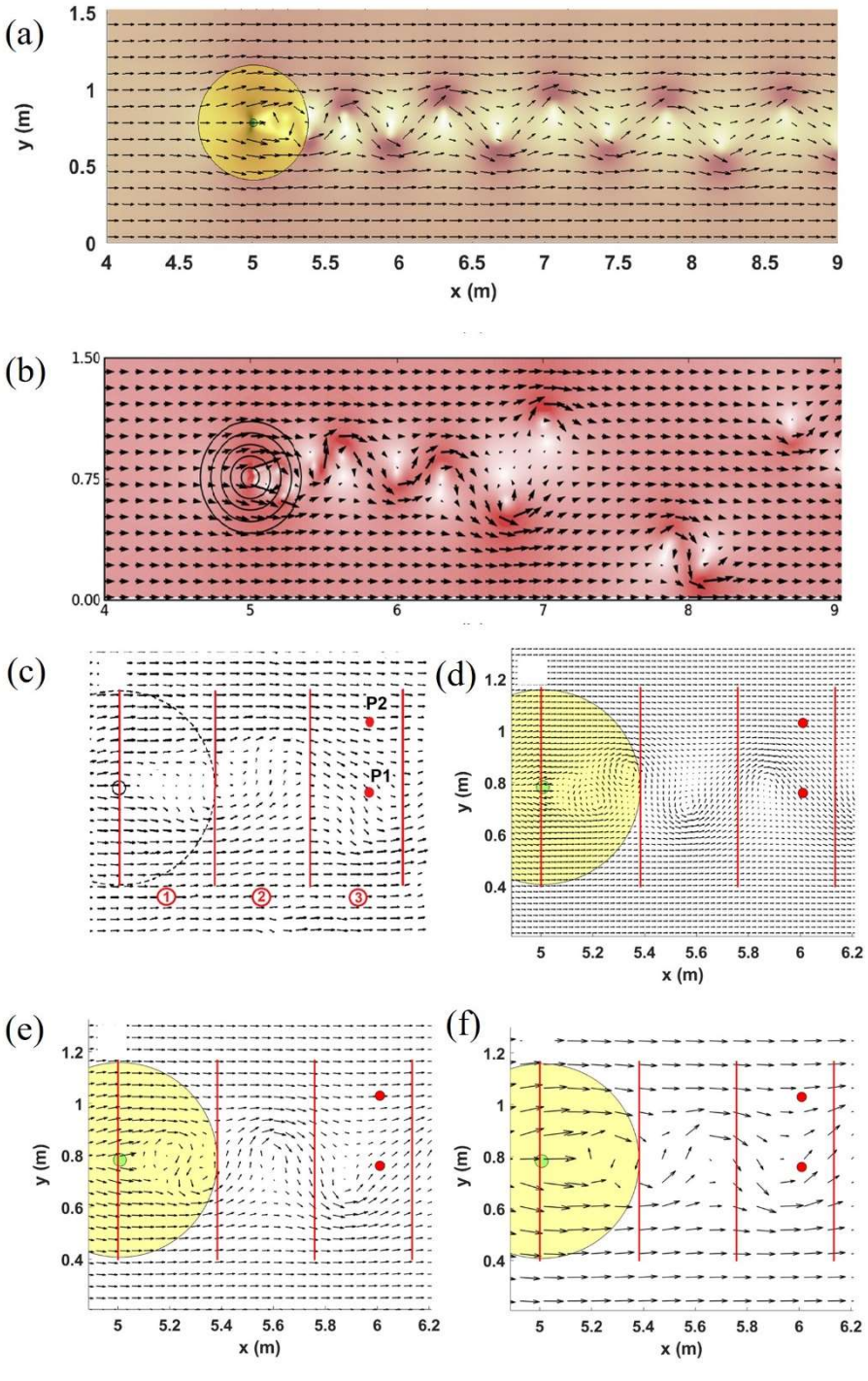

Figure 2.20. Flow past one conical island: velocity vectors from (a) the DG2-SWE solver (coarse grid resolution), (b) the FV3-SWE solver, and velocity vectors behind the conical island (zoom-in view) from (c) experimental measurement, and the DG2-SWE solver at (d) fine resolution, (e) medium resolution, and (f) coarse resolution. Source: Kesserwani et al. (2023)

2.5 Numerical studies on mixing within cylinder array

2.5.1 Previous numerical studies on mixing within cylinder array

Numerical solute transport models, which typically solve the advection diffusion equation (ADE), are often used to simulate solute transport, and require the flow fields and turbulent diffusivity (D_t) as inputs. The computation of flow fields was introduced in the previous section. It is often hindered by the impractical memory and runtime costs associated with the use of viscous turbulent flow simulators, due to the need to deploy a grid resolution close to the turbulence-length (Alfonsi, 2009; Qu et al., 2013).

As for D_t, its determination for practical applications in real-world also poses a notable challenge (Mignot et al. 2023). Typically, there are three ways to estimate D_t. The first way is to directly specify a constant coefficient. However, this constant coefficient was set to be zero or arbitrarily (not justified) selected (Lee and Kim, 2012; Murillo et al., 2006; Pathirana et al., 2011). The second way is to determine D_t based on the local friction velocity, also known as the Elder approach, namely $D_t \propto hu^*$ where h is the water depth and u^* represents the friction velocity (Duan, 2004; Elder, 1959; Fischer, 1979; Hu et al., 2017). In previous research (Fang et al., 2022; Liang et al., 2010; Park et al., 2016), the value of D_t has been sourced either from existing literature or calibrated based on experimental data. The third way relies on the turbulent Schmidt number S_{ct} and eddy viscosity obtained from various turbulent closure models. Different turbulent closures (recall Sec. 2.4.2 or Figure 2.14) give rise to four commonly used approaches for estimating D_t.

The first and simplest approach (corresponding to the constant eddy viscosity model) is to select a constant eddy viscosity. The second approach is related to the mixing length model and uses the mixing length (l_m) and velocity gradient (longitudinal velocity with respect to the transverse direction) to estimate D_t (Stansby, 2006), given as:

$$\nu_t = \left|\frac{\partial u}{\partial y}\right| l_m^2 \tag{2.24}$$

l_m can be calculated (Stansby, 2006) as:

$$l_m = \begin{cases} \kappa_c y_w, & y_w/\delta < \lambda_c/\kappa_c \\ \lambda_c \delta, & \lambda_c/\kappa_c \le y_w/\delta < 1 \end{cases} \tag{2.25}$$

where κ_c denotes the von Karman constant coefficient, typically valued at 0.41, y_w is the distance from the wall, δ represents the thickness of the boundary layer and λ_c is a constant value, which is typically set as 0.09.

The third, and the most widely used approach (corresponding to two-equation model) is to calculate D_t based on the turbulent kinetic energy (k) and its dissipation rate (ε) (Ye and McCorquodale, 1997), expressed as:

$$\nu_t = \frac{c_\mu k^2}{\varepsilon} \tag{2.26}$$

where c_μ is an empirical constant and was set to 0.09 (Wu et al., 2000; Wu, 2004). The last approach is using Smagorinsky formulation to determine D_t , which relies on the subgrid model of LES (Hinterberger et al., 2007; Okamoto and Nezu, 2010).

$$\nu_t = (C_s\Delta)^2\sqrt{2\overline{S_{ij}}\,\overline{S_{ij}}} \tag{2.27}$$

where C_s is the Smagorinsky constant taken to be 0.12 for flow around obstacle (Tominaga and Stathopoulos, 2012), Δ denotes grid resolution and S_{ij} is the resolved strain rate.

Like the numerical simulations of flows within cylinder arrays, the simulations of solute transport within cylinder arrays also treat cylinders in two ways: either by using a bulk scale approach to represent cylinders (Sonnenwald et al., 2019a, 2018; Yan et al., 2017), or by explicitly modelling each cylinder. The latter approach has the advantage of including the mixing process specifically due to the cylinders, such as secondary wake dispersion, vortex trapping, turbulent diffusion and mechanical dispersion. In contrast, the bulk-scale-based approach should additionally involve these processes (Sonnenwald et al., 2019a).

However, it is worth noting that, to date, limited studies focused on simulating the solute transport within explicitly modelled cylinder arrays, implying the necessity of developing a numerical tool in this context. Okamoto and Nezu (2010) implemented a 3D LES model to yield 3D flow fields together with D_t which are taken as the inputs of 3D ADE solute transport model for predicting the movement of the solute. D_t is derived from the Smagorinsky model, depending on the grid size and velocity gradient. Although the concentration fields were provided, the reach-scale dispersion coefficients were not discussed, perhaps due to the limited size of the computational domain. Note that this work uses thin plates to represent vegetation, instead of cylinders. In contrast with the 3D ADE model, the 2D ADE models are more commonly used to avoid high computational expenses.

Golzar et al. (2017) applied a 2D scalar transport model available in Fluent to simulate solute advection and dispersion for investigating transverse dispersion of the solutes within random cylinder arrays under different configurations. This 2D scalar transport model takes the flow fields produced from the second order Fluent RANS RSM turbulence simulator and the associated D_t via the ν_t and S_{ct} as the required inputs. The latter is isotropic and is determined from the simulated Reynolds stresses in the RSM turbulence model using a similar way to other k-ε turbulent models (Versteeg, 2007). The results reveal that the numerically generated reach-scale transverse dispersion coefficients D_y are in the

correct order-of-magnitude with the previously published laboratory data sets in Tanino and Nepf (2008a), demonstrating the validity of this numerical tool to help understanding solute mixing.

In Golzar et al. (2018), this validated numerical tool was chosen to characterise mixing within two kinds of arrays featuring regularly and randomly distributed cylinders. For the cylinder arrays considering the same cylinder diameter and solid volume fraction ϕ, the random distribution leads to greater longitudinal and transverse dispersion than the regular distribution due to the high velocity shear induced by randomly distributed cylinders. This also implies that the cylinder diameter might not be the most appropriate characteristic length to non-dimensionalise the dispersion coefficients.

Stovin et al. (2022) extended the research of Golzar et al. (2018) to employ the same numerical tool to further study the longitudinal and transverse dispersion within the randomly distributed cylinders under different configurations at turbulent R_{ed} around 500. This study further validated the 2D scalar transport model by comparing with the experimental measured concentration profiles presented in Sonnenwald et al. (2019c). Goodness of fit between the simulated concentration profiles and the measured ones was quantified, via the coefficient of R_t^2 (Young et al., 1980). R_t^2 values exceeding 0.97 again demonstrated the feasibility of combining the Fluent RANS model with scalar transport model to predict dispersion coefficients. Fluent RANS simulated flow field and concentration profiles as well as the experimental measured concentration data will be considered as the reference for the numerical models' validation within this thesis.

Furthermore, unlike the previous numerical studies considering the single fixed cylinder diameter, Stovin et al. (2022) included the non-uniform cylinder diameter distribution for mimicking the heterogeneous distribution of real vegetation, as suggested by Sonnenwald et al. (2017). The simulation results reveal that the variation in cylinder diameters does not affect the dispersion processes. This study also focuses on identifying a characteristic length associated with the dispersion coefficients. In addition to considering the cylinder diameter, *d*, as the characteristic length, this study also takes into account the cylinder spacing. A systematic analysis shows that the cylinder spacing appears to be a more suitable characteristic length. There exists a linear relationship between the non-dimensional dispersion coefficients (normalised with cylinder spacing) and the cylinder densities (*d*/*s*), in line with the experimental observation (Sonnenwald et al., 2019c). This suggested relationship can also be converted into D_x/Ud = 1.04 and D_y/Ud = 0.111. However, a '*N*'-shaped distribution of the non-dimensional transverse dispersion coefficients D_y/Ud with respect to cylinder density was not retrieved since turbulent diffusion still contributes to the dispersion (corresponding D_t is non-zero throughout the range of the cylinder density d / $\langle s_n \rangle_A$ or ϕ).

In addition, this study also investigates the contribution of different processes to the dispersion processes, as shown in Figure 2.21. They found that at very low cylinder density, the value of D_t (black circle markers) is close to the D_y (red circle markers). This indicates that transverse dispersion is almost

totally composed of the effects of turbulent diffusion because few cylinders cause the solute to move transversely. As for the longitudinal dispersion, D_x (blue circle markers) is found to be almost one order-of-magnitude higher than D_y (and D_t at low very cylinder density). This means that, compared with the effects of turbulent diffusion, the differential advection mainly contributes to the longitudinal dispersion. Such 10-fold ratio is a common value in many vegetated flows and in line with earlier findings in Sonnenwald et al. (2017).

However, there are differing options regarding the contribution of turbulent diffusion to transverse dispersion at high cylinder densities. Tanino and Nepf (2008a) stated that when d/s (or ϕ) exceeds 3 (or 0.25), only mechanical dispersion contributes to the transverse dispersion, while turbulent diffusion decreases to zero (recall Figure 2.12). Instead, the opinion of Stovin et al. (2022) is that, although D_t decreases with increasing cylinder density, D_t is always higher than zero, meaning that it still contributes to transverse dispersion at different cylinder densities under different configuration, as shown in Figure 2.21.

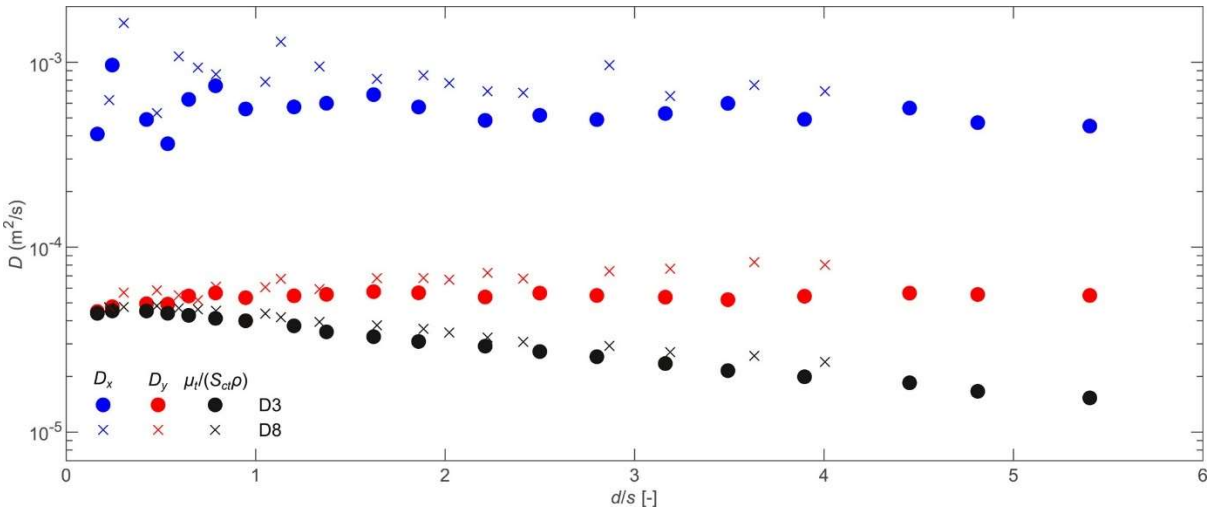

Figure 2.21. The contribution of turbulent diffusion (black circle) to the longitudinal (blue circle) and transverse dispersion (red circle) over two different cylinder configurations.

Overall, these studies' inputs of D_t and reliable flow fields were obtained from the built-in turbulence closure terms of the viscous turbulence models. There is an interesting question of whether applying the DG2-SWE solver's simulated flow fields and the associated explicitly generated D_t into an ADE model can effectively reproduce the solute transport and yield reliable the reach-scale dispersion coefficients in both directions.

2.5.2 DG2-ADE solver

The second-order finite difference (FD2) methods and the FV2 method are broadly implemented to deal with the spatial discretisation of 2D ADE (Badrot-Nico et al., 2007; Man and Tsai, 2008; Tsai et al., 2001), as for example is in industrial ADE modules in popular software packages [TUFLOW AD

(Waltham et al., 2014), MT3DMS (Russell et al., 2003), Mike (Nguyen et al., 2018; Zhang, 2011) and MOUSE (Bouteligier et al., 2005)]. Since the diffusion process is typically slow, the FD2 method is an effective way to solve the diffusion equation of the ADE to reproduce the diffusive transport of the solute, especially on fine grid resolution. However, major issues with the FD2 and FV2 methods are associated with the simulation of advective transport, namely solving the advection equation of the ADE (Liang et al., 2010). They are excessive numerical dissipation errors, spurious oscillations around sharp concentration fronts and the production of unrealistic, negative concentration values (Tsai et al., 2002).

As depicted in Figure 2.22, a series of numerical models including the conventional FE, FV and FD methods have been applied to simulate the pure advection (Tsai et al., 2002). However, all of these models predict the negative concentration values varying between -0.001 and -2, which contradicts physical reality. Moreover, the spurious oscillation is also observable in the region of $45 < x < 60$. This demonstrates most of the conventional solute transport model suffers from generation of unphysical negative concentration and oscillation. Furthermore, these adverse effects will be amplified in the solute transport model during simulations that include obstacles, such as cylinders. The treatment employed to ensure that simulated concentration fields remain non-negative are referred to as positivity-preserving procedure (Cockburn and Shu, 1998; Zhang and Shu, 2011). Slope limiter (Ayog et al., 2021; Kesserwani and Liang, 2012) is another treatment to avoid spurious oscillations around sharp discontinuities.

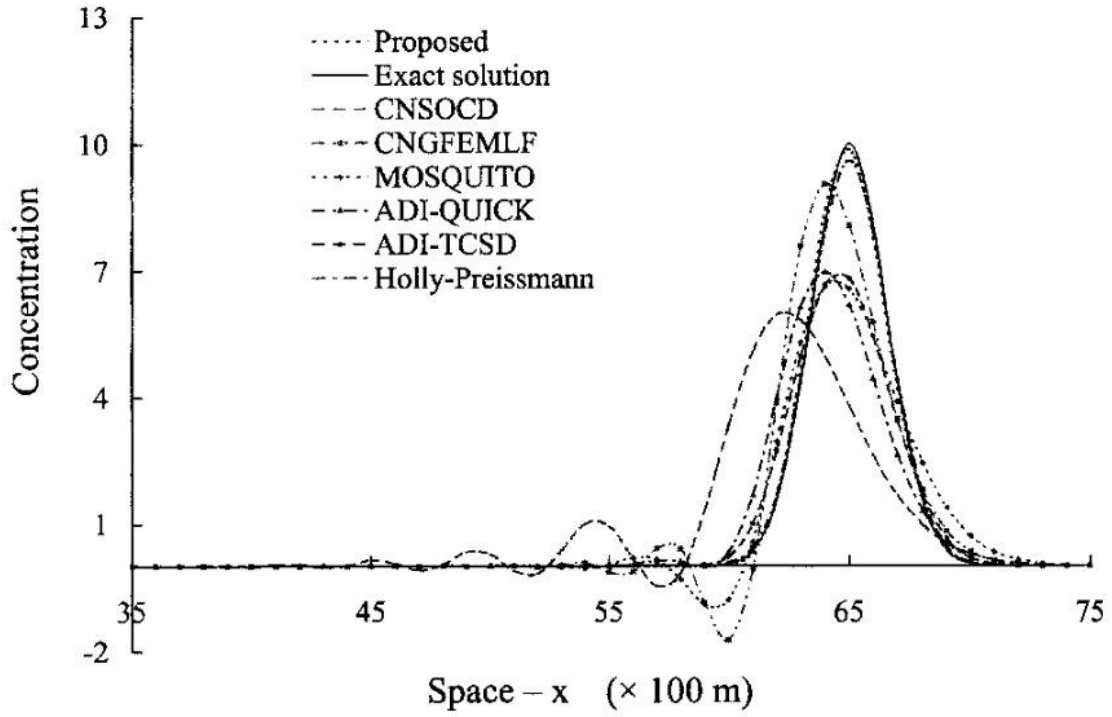

Figure 2.22. The simulated concentration profiles along the line of $y = x$ from the various numerical models. Source: (Tsai et al., 2002).

To improve the capabilities of the FD2- and FV2-ADE solvers, the DG2 solvers to the ADE have emerged as an attractive alternative given their aforementioned superiority in treating the advective fluxes (Zhang and Shu, 2011). However, these DG2-ADE solvers are mainly designed for theoretical modelling of solute movement and spread in a uniform flow without obstacle, rather than for practical applications of solute transport past obstacles under non-uniform flow and D_t fields. To date, there seems to be no DG2-ADE solver linked with the DG2-SWE solver, specifically tailored for simulating solute transport past explicitly represented cylinders. This capability is crucial for addressing practical hydraulic engineering needs, including the prediction of reach-scale dispersion coefficients, as explored in this study.

When applied to simulate solute transport within a cylinder array, two challenges are posed to the DG2-ADE solver. One is the appropriate treatment for the presence of cylinders to guarantee the mass-balance of the solute and the positivity of the solute value, while preserving second-order accuracy. The other challenge is how to explicitly generate the reliable D_t used for the simulation of solute transport within a large number of cylinders. As an inviscid model, the DG2-SWE solver does not incorporate any turbulence closure model, therefore this study will also focus on how to generate the initial conditions/inputs from the DG2-SWE simulated flow fields around cylinders. One of the contributions of this study is the development of the DG2-ADE solver to address these two problems.

Overall, the newly developed DG2-ADE solver is formulated based on the simplified "slope-decoupled" stencil (recall Figure 2.17a) as suggested by Kesserwani et al. (2018) and parallelised on GPU to conduct fast simulation. The utility of such a DG2-ADE solver linked to the DG2-SWE solver will also be investigated in the context of solute transport within a cylinder array, as another contribution of this research.

2.6 Concluding remarks

In this chapter, the basic concept of flow hydrodynamics around cylinders and the mixing processes were first explained by reviewing the published textbook and experimental studies. After briefly introducing the numerical models, the detailed review of the numerical studies on flow past cylinders were then provided, clarifying that the advanced turbulence models can provide high-quality flow but their computational costs are very high. Additionally, these advanced turbulence models are often solved by the FV2 method. However, the FV2 method suffers from the fast growth of numerical dissipation errors and may fail to capture vortical flow structures around the cylinders. This adverse effect can only be alleviated by using very fine resolution but inevitably increases the computational costs. The DG2 method was then introduced, which is numerically more complex than the FV2 method, demonstrating the benefits of the DG2 methods in producing the informative flow fields. Even without incorporating the turbulent viscosity terms, the DG2 solver to the inviscid hydrodynamic model, that is the DG2-SWE solver, can capture small-scale eddies around the hydraulic engineering structures. However, the DG2-SWE solver has not yet been explored for laminar or transitional flow past cylinders.

The review on numerical studies on mixing within cylinder arrays showed that very few studies have focused on simulating solute transport past explicitly modelled cylinders, meaning that this research area requires further investigations. The inputs of theses solute transport models, namely the ADE solver, require the flow fields from the advanced turbulence models, and the associated turbulent diffusivity from the built-in turbulence closure. At present, there is no specific ADE solver taking the output from the inviscid hydrodynamic numerical solver, like the DG2-SWE solver. Given its superior capability in treating advective fluxes, the DG2 solver to ADE was also an attractive candidate to improve the prediction accuracy of the advection transport. Overall, this chapter of literature review demonstrates the necessity of developing an efficient and accurate numerical tool combining the hydrodynamic model and the solute transport model to model flow and mixing within cylinder array.

3 Evaluation of the DG2-SWE solver simulated flow fields around cylinders

Content used to prepare for this chapter has been published in the following publication:

Sun, X., Kesserwani, G., Sharifian, M.K. and Stovin, V., 2023. Simulation of laminar to transitional wakes past cylinders with a discontinuous Galerkin inviscid shallow water model. *Journal of Hydraulic Research*, *61*(5), pp.631-650. https://doi.org/10.1080/00221686.2023.2239750

3.1 Chapter overview

This chapter seeks to address the first objective of assessing the suitability of the DG2-SWE solver in computing laminar to turbulent wake flow patterns featuring vortical structure behind the cylinders. This chapter is organised as follows. Sec. 3.2 overviews the DG2-SWE and FV2-SWE solvers, with a focus on the differences in their numerical complexity and how elementwise flow data have been used to generate vorticity fields. In Sec. 3.3.1, the capability of the existing DG2-SWE solver to reproduce laminar and transitional wake patterns is investigated for classical steady flows past a single cylinder at $R_{ed} \leq 250$, against the patterns predicted by the FV2-SWE solver and the reference predictions. Sec. 3.3.2 reports a new application for the DG2-SWE solver for reproducing experimental flow fields featuring wake formations and interactions from laminar and transitional flows past a large number of cylinders. Sec. 3.3.3 reproduced the flow fields of flow past an array of cylinders at a turbulent flow with available results simulated with Fluent RANS. Sec. 3.4 draws the conclusions from the comparative analyses.

3.2 DG2-SWE and FV2-SWE solvers

The DG2-SWE and FV2-SWE solvers are based on the 2D depth-averaged SWE with topography and friction source terms written in the following conservative vector form:

$$\partial_t U + \partial_x F(U) + \partial_y G(U) = S_b(U) + S_f(U) \tag{3.1}$$

where ∂ represents a partial derivative operator and $U(x, y, t) = [h, q_x, q_y]^T$ is the vector of flow variables at time t and location (x, y), which includes water depth h and the discharge per unit width, $q_x = hu$ and $q_y = hv$, involving the depth-averaged longitudinal and transverse velocities u and v, respectively. The operator symbol, T, represents the transpose of a vector of matrix. $F = [q_x, q_x^2/h + gh^2/2, q_x q_y/h]^T$ and $G = [q_y, q_x q_y/h, q_y^2/h + gh^2/2]^T$ are vectors representing the components of physical advective flux field, and g is the gravity acceleration. $S_b = [0, -gh\partial_x z, -gh\partial_y z]^T$ is the source term vector representing topography gradients while $S_f = [0, -C_f u\sqrt{u^2 + v^2}, -C_f v\sqrt{u^2 + v^2}]^T$ is the vector representing the friction effects expressed as a function of the roughness coefficient $C_f = gn_M^2/h^{1/3}$ in which n_M is the Manning's resistance parameter.

Both solvers assume a 2D domain discretised into N non-overlapping and uniform square grids Q_c ($c = 1, \ldots, N$), centred at (x_c, y_c) with horizontal dimensions ($\Delta x = \Delta y$), over which the discrete flow vector $U_h(x, y, t)$ and topography $z_h(x, y)$ will be approximated. The DG2-SWE solver is formulated upon the "slope-decoupled" simplified stencil (see the explanation of stencil in Sec. 2.4.31 and Figure 2.17a), that is made similar to the stencil of the FV2-SWE solver (Ayog et al., 2021; Kesserwani et al., 2018). The DG2-SWE solver stores piecewise-planar flow vectors $U_h(x, y, t)$ from which the inter-elemental advective fluxes, linking the flow discontinuities, are used to perform elementwise update after applying local limiting to the natural slope coefficients from which vorticity fields can be directly calculated. In contrast, the FV2-SWE solver adopts the Monotonic Upstream-centred Scheme for Conservation Laws (MUSCL) after global slope limiting to extrinsically differentiated slopes to update piecewise averaged flow vectors (Ayog et al., 2021) that need to be again differentiated to estimate vorticity fields. For the targeted simulations, flow discontinuities occur either around the vortices or steep topographies representing the cylinders that are integrated as part of the digital elevation model. The advective fluxes are computed using the Harten, Lax and van Leer (HLL) approximate Riemann solver, which is an appropriate choice compared to other Riemann solvers (Kesserwani et al., 2008). The full technical descriptions of the DG2-SWE and FV2-SWE solvers are detailed in Ayog et al. (2021). The codes of these solvers, parallelised on Graphical Processing Units (GPU), are openly accessible from the University of Sheffield local repository of the LISFLOOD-FP 8.0 (The University of Sheffield, 2021; Shaw et al., 2021). In this work, these codes were run on a personal desktop computer with an Nvidia GeForce RTX 3090 GPU card. Table 3.1 summaries the differences in the flow vector's structure and numerical complexity between the DG2-SWE and FV2-SWE solvers.

Table 3.1. Differences in the level of numerical complexity between the DG2-SWE and FV2-SWE solvers.

Flow solver	DG2-SWE (Shaw et al., 2021)	FV2-SWE (Ayog et al., 2021)
Dimension	2D depth-averaged	
Governing equations	SWE with Manning's formula	
Grid type	Non-overlapping uniform square grid	
Shape of U_h over Q_c	Planar variation that is spanned by an average coefficient, $\boldsymbol{U_c^0}$, and two slope coefficients, $\boldsymbol{U_c^{1x}}$ and $\boldsymbol{U_c^{1y}}$. $\boldsymbol{U_h}(x,y,t) = \boldsymbol{U_c^0}(t)+\frac{2\sqrt{3}(x-x_c)}{\Delta x}\boldsymbol{U_c^{1x}}(t) +\frac{2\sqrt{3}(y-y_c)}{\Delta y}\boldsymbol{U_c^{1y}}(t)$	Constant variation spanned by one average coefficient $\boldsymbol{U_c^0}$
Slope limiting	Locally applied to limit the slope coefficient variations. These coefficients are used to the get limits of the piecewise-planar solutions for estimating spatial fluxes.	Globally applied in the MUSCL reconstruction to estimate the piecewise-linear solution limits for estimating spatial fluxes.
Fluxes calculation	HLL Riemann solver called six times in three spatial operators	HLL Riemann solver called two times in one spatial operator
Representation of the cylinder	Piecewise planar topography $\boldsymbol{z_h}$ with wet-dry treatments, expressed as: $\boldsymbol{z_h}(x,y) = z_c^0+\frac{2\sqrt{3}(x-x_c)}{\Delta x}z_c^{1x} +\frac{2\sqrt{3}(y-y_c)}{\Delta y}z_c^{1y}$	Piecewise constant topography z_h with wet-dry treatments, expressed as: $z_h=z_c^0$
Time integration	Second-order Runge-Kutta (Courant number = 0.3)	Second-order Runge-Kutta (Courant number = 0.5)
Vorticity over Q_c	$\omega_c = \frac{q_{y\,c}^{1x}}{h_c^0} - \frac{q_{x\,c}^{1x}}{h_c^0}$	$\omega_c = \frac{\left(\frac{q^0_{y_{nei_E}}}{h^0_{nei_E}} - \frac{q^0_{y_{nei_W}}}{h^0_{nei_W}}\right)}{2\Delta x} - \frac{\left(\frac{q^0_{x_{nei_N}}}{h^0_{nei_N}} - \frac{q^0_{x_{nei_S}}}{h^0_{nei_S}}\right)}{2\Delta y}$*
Grid resolution	$0.25d$	$0.025d$

* where '*nei*' is the index of the direct neighbour; *E*, *W*, *N* and *S* are east, west, north, and south sides

3.3 Results: laminar to transitional wakes past cylinders

Considering slow quasi-steady flows at $R_{ed} \leq 450$, the influence of the advective part of the inviscid SWE numerical models is examined with the DG2-SWE and FV2-SWE solvers with respect to the computation of wake flow patterns with vortical structure behind cylindrical obstacles. First, classical flows past one cylinder are investigated to analyse the potential of the DG2-SWE solver to produce more accurate and faster-converging flow fields compared with the FV2-SWE solver, on a grid with one order-of-magnitude coarser resolution (Sec. 3.3.1). Then, the DG2-SWE solver is further evaluated when applied to reproduce laboratory-scale flow experiments in a flume with randomly distributed cylinders, by comparing its velocity predictions to measured Surface Particle Image Velocimetry (SPIV) data (Sec. 3.3.2). The DG2-SWE simulation result is finally compared with the second order RANS model available in ANSYS Fluent.

In these test cases, the initial flow conditions consist of a uniform water depth and a steady unit-width discharge. The mainstream flow is driven by fixing the steady unit-width discharge at the inflow and the uniform depth at the outflow. The left and right boundary conditions are treated as solid walls. The parameters of physical lengths are scaled with respect to the cylinder diameter d, velocities are scaled with the imposed steady inflow velocities U_∞, and the dimensionless time unit is defined as $t^* = tU_\infty/d$. The Strouhal number S_t is used to quantify the period of vortex shedding for analysing the characteristics of the simulated wake flow patterns. The S_t number is determined as $S_t = f_s d/U_\infty$, where f_s is the shedding frequency detected from the time-series of the transverse velocity, v, recorded at a distance of $2.5d$ from the cylinder's centre, which distance was suggested by Gerrard (1978). Further analysis of the simulated flow fields is carried out based on post-processing the longitudinal, u, and transverse, v, components of velocity according to test-specific validation criteria.

3.3.1 Flow past one cylinder

This classical test case has been used to validate 2D RANS models in reproducing wake flow characteristics occurring in quasi-periodic, steady, slow flows (Qu et al., 2013; Rajani et al., 2009). It is here used to assess the capability of the DG2-SWE solver to treat the advective fluxes in relation to reproducing the wake evolution, and comparatively unravel the performance of the FV2-SWE solver. The comparisons are performed with the reference predictions in Qu et al. (2013) and/or Rajani et al. (2009) from 2D RANS models, whose grid resolutions closest to the cylinder are very fine, namely $0.0054d$ and $0.0001d$, respectively.

The test case involves a cylinder of diameter $d = 4$ mm in the $30.5d \times 32d$ computational area shown in Figure. 3.1. The area dimensions are selected to avoid any impact from the boundaries on near-cylinder flow structures (Behr et al., 1991; Seo and Song, 2012; Tezduyar and Shih, 1991). The area is assumed to have a flat surface with a Manning's coefficient of 0.01 $m^{1/6}$ (Ginting, 2019). Steady flow cases are explored for $R_{ed} = 47$, 200 and 250, whose corresponding inflow velocities are set to be

0.01175 m s^{-1}, 0.05 s m^{-1} and 0.0625 s m^{-1}. As the flow passes the cylinder, it generates vortices that shed periodically and alternately from the cylinder for $R_{ed} \geq 47$ (Zdravkovich, 1997). The higher the R_{ed}, the more inertial forces dominate over the viscous forces as the vortices develop behind the cylinder (Balachandar et al., 1997). A grid resolution analysis was conducted to identify the coarsest resolution at which the DG2-SWE and FV2-SWE solvers were able to excite vortex shedding (see Appendix B). This was achieved at a resolution of 0.25*d* and 0.025*d* for the DG2-SWE and FV2-SWE solvers at R_{ed} = 250 (equivalent to 1 mm and 0.1 mm), respectively.

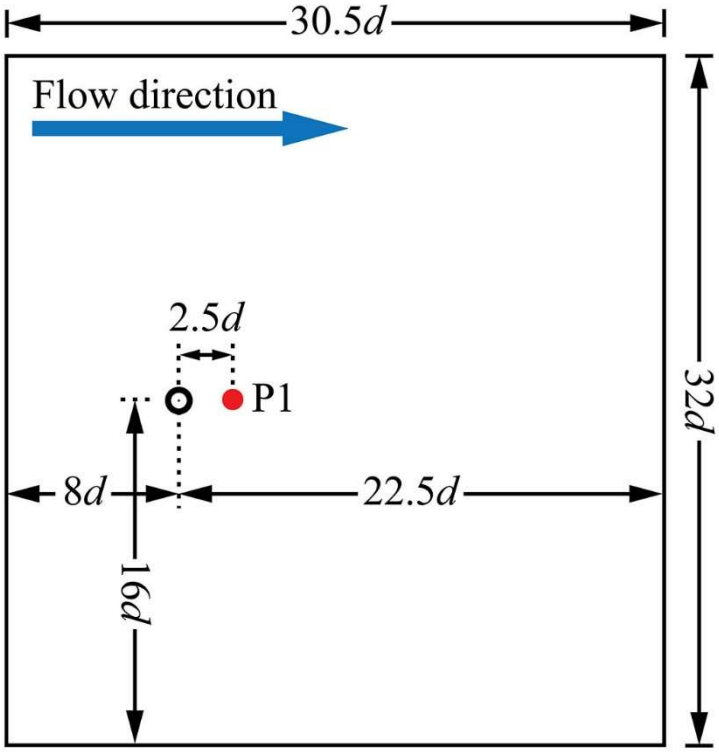

Figure 3.1. Computational domain for steady flows past one cylinder. The cylinder has a diameter *d* of 4 mm, and point P1 is located 2.5*d* behind the cylinder centre along the cylinder centreline.

The v time series recorded at P1, shown in Figure. 3.2, is first extracted to analyse the characteristics of the flow state. Informed by this analysis, instantaneous flow fields, at selected time instants, are then compared in terms of streamlines and vorticity contours extracted from u and v. Finally, time-averaged velocity profiles, $\bar{u}$, are analysed along the x-directional centreline.

3.3.1.1 Quasi-steady state convergence

The convergence of the DG2-SWE and FV2-SWE simulations to the periodic quasi-steady state is analysed. As this aspect becomes more challenging for a numerical solver with lower R_{ed} (Franke et al., 1990; Laroussi et al., 2014), it is first analysed for the highest R_{ed} = 250. Figure. 3.2 shows the scaled v

time-series recorded during the DG2-SWE and FV2-SWE simulations for the flow case at R_{ed} = 250. The captions D1-D3 and F1-F3 in Figure. 3.2 refer to the time when the DG2-SWE and FV2-SWE solvers experience different flow states, respectively. Both series exhibit periodic oscillatory patterns that reflect the presence of vortex shedding cycles, with the series of DG2-SWE being quasi-periodic. DG2-SWE predicts a start in the sinusoidal fluctuations, at time D1, which is around $100t^*$ earlier than the FV2-SWE predictions, at time F1. The appearance of these fluctuations means that both solvers can capture the presence of vortex shedding. After 9 shedding cycles, the first vortex generated advects downstream and exits at the outlet, meaning that both solvers converge to fully developed quasi-steady state with almost the same flow patterns repeating every period, at times D2 and F2, respectively. At these times, the instantaneous spatial flow patterns simulated by the DG2-SWE and FV2-SWE solvers are then analysed. The simulations were terminated after the next 50 vortex shedding cycles, at times D3 and F3, respectively. Rajani et al. (2009) has suggested that a period of 50 cycles is typically sufficient. Hence, time-averaged velocities were extracted from the instantaneous flow fields between the 10th and 60th cycles. This applies to both cases of flow past a single cylinder and the cylinder array.

The convergence properties of the DG2-SWE and FV2-SWE solvers are assessed by looking at t^* required to reach quasi-steady state, the GPU runtime cost, and shedding frequency predicted. From Figure. 3.2, it can be seen that DG2-SWE requires $95.5t^*$ (D1, Figure. 3.2), whereas FV2-SWE takes $190t^*$ (F1, Figure. 3.2) to excite the vortex shedding. In this sense, DG2-SWE is about twice as fast as FV2-SWE to converge to a fully developed quasi-periodic steady state. Their GPU runtimes are recorded at the time when the vortex shedding was first triggered (D1 and F1, Figure. 3.2), when it fully developed in the quasi-steady state profile (D2 and F2, Figure. 3.2), and at the end of the simulation after 50 cycles (D3 and F3, Figure. 3.2), respectively. These runtimes for DG2-SWE at a grid resolution of $0.25d$ are 3 minutes, 5 minutes and 11 minutes, whereas the runtimes for FV2-SWE at a 10 times finer resolution of $0.025d$ are 84, 70 and 90 times slower, respectively. See Appendix B for a detailed analysis of GPU runtime costs comparing the DG2-SWE and FV2-SWE solvers.

Table 3.2. Flow past one cylinder: S_t values predicted by the DG2-SWE and FV2-SWE solvers for flow cases at R_{ed} = 47, 200 and 250. These values are compared with those reported in Qu et al. (2013) and Rajani et al. (2009) from 2D RANS models whose grid resolutions around the cylinders are very fine, of 0.0054*d* and 0.0001*d*, respectively.

R_{ed} (-)	S_t (-)		
	Reference	DG2-SWE	FV2-SWE
47	0.124 (Qu et al., 2013)	0.142	-
200	0.196 (Qu et al., 2013; Rajani et al., 2009)	0.152	-
250	0.205 (Rajani et al., 2009)	0.155	0.105

'-' indicates no such data was obtained.

The predicted S_t values are obtained after detecting the shedding frequency f_s from the v time-series using Fast Fourier Transforms. Table 3.2 includes the S_t values predicted by the DG2-SWE and FV2-SWE solvers and the value from the reference prediction for R_{ed} = 250 (Rajani et al., 2009). It can be seen that the S_t values predicted by DG2-SWE and FV2-SWE are both lower than reference S_t value. This is expected with inviscid SWE numerical solvers lacking kinematic and eddy viscosity (Y. Li et al., 2009), and indicates that both DG2-SWE and FV2-SWE solvers cannot precisely reproduce the wake evolution. However, the S_t value from the FV2-SWE solver is much further from the reference value, suggesting that its predictions of the flow fields are more severely affected than the DG2-SWE predictions.

At R_{ed} = 200, no S_t value is extracted for FV2-SWE as it did not trigger any vortex shedding (instead it predicted a constant v time series that is not shown). Refinement of the grid is expected to reduce the numerical viscosity with the FV2-SWE solver to make it potentially able to trigger vortex shedding; but at a computational cost that cannot be justified practically. In contrast the DG2-SWE solver, even at a 10 times coarser grid resolution, preserves its ability to predict vortex shedding cycles as R_{ed} reduces. This can be confirmed by considering its predicted S_t value of 0.152 (Table 3.2), which, although lower than the reference S_t, is in agreement with values from the reference prediction for R_{ed} = 200 (Qu et al., 2013; Rajani et al., 2009). The same is observed for the flow at the lowest R_{ed} = 47, where excitation of vortex shedding is even more difficult for the solvers in the near-cylinder flow region where viscosity effects are higher (Balachandar et al., 1997; Braza et al., 1986). As expected, in this case, FV2-SWE also fails to predict the formation of any vortex and DG2-SWE predicts a S_t value, of 0.142, which is slightly higher than the S_t value of 0.124, seen with the reference prediction for a similar flow at R_{ed} = 47 (Qu et al., 2013).

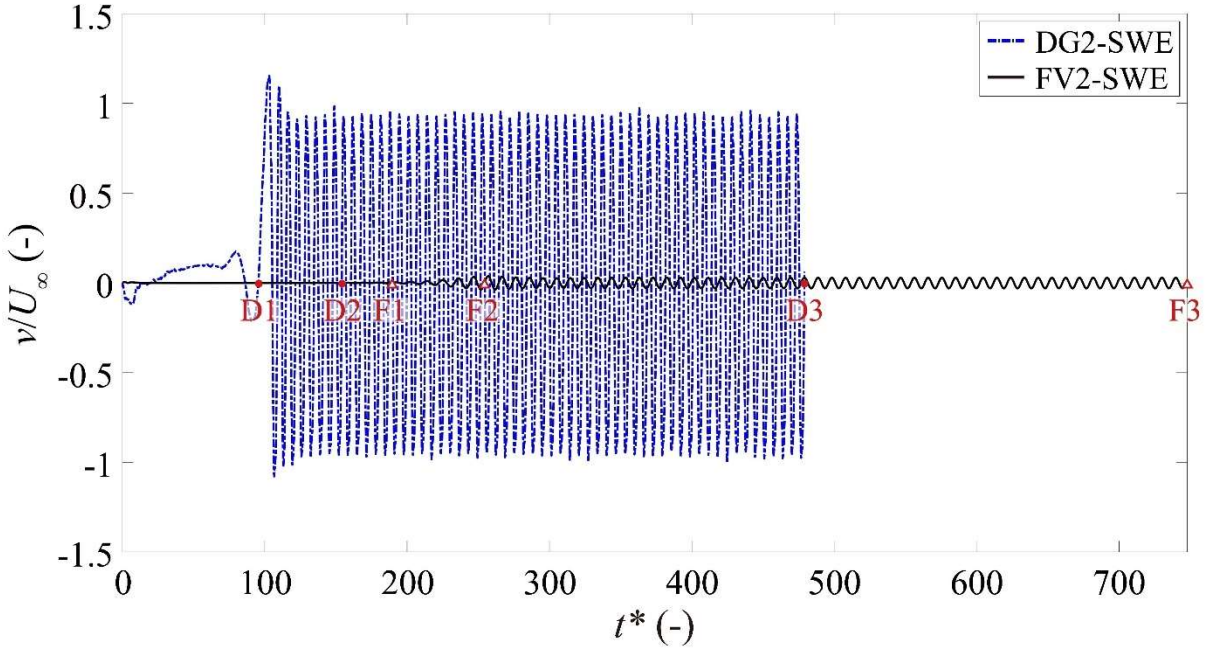

Figure 3.2. Flow past one cylinder: Time ($t^* = tU_\infty/d$) series of the scaled transverse velocities (v/U_∞) simulated by the DG2-SWE and FV2-SWE solvers at R_{ed} = 250; D1&F1: the time when vortex shedding is triggered for the DG2/FV2-SWE solver; D2&F2: the time when fully developed periodic quasi-steady state is established for the DG2/FV2-SWE solver; D3&F3: the time of simulation termination for the DG2/FV2-SWE solver.

3.3.1.2 Instantaneous streamlines and vorticity contours

Figure. 3.3 compares the instantaneous streamlines generated from the flow fields simulated by the DG2-SWE and FV2-SWE solvers after 9 shedding cycles, for the flow cases at R_{ed} = 47, 200 and 250. At R_{ed} = 250, both DG2-SWE and FV2-SWE solvers simulate the closed vortex occurring downstream of the cylinder (Figure. 3.3e vs. Figure. 3.3f). Compared with the FV2-SWE simulation, DG2-SWE simulates the vortex closer to the cylinder, which suggests that it produces a flow pattern that is in a better agreement with the expected flow (Hajihassanpour and Hejranfar, 2020; Zdravkovich, 1997). Far downstream of the cylinder, DG2-SWE simulates streamline fluctuations that are more pronounced than those simulated by FV2-SWE, which indicates that DG2-SWE also performs better in capturing the details of the flow fields in the far wake (see reference streamline figure of Figure. 2.16). For the lower R_{ed} of 200 and 47, (Figure. 3.3c vs. Figure. 3.3d, and Figure. 3.3a vs. Figure. 3.3b), the better performance of DG2-SWE is even more noticeable. DG2-SWE captures the swirling vortex shedding from the cylinder and the associated streamline fluctuations, which were not present within the FV2-SWE simulations. Instead, FV2-SWE seems to simulate elongated recirculation zones without any sign of vortex formation or waviness in the simulated streamlines.

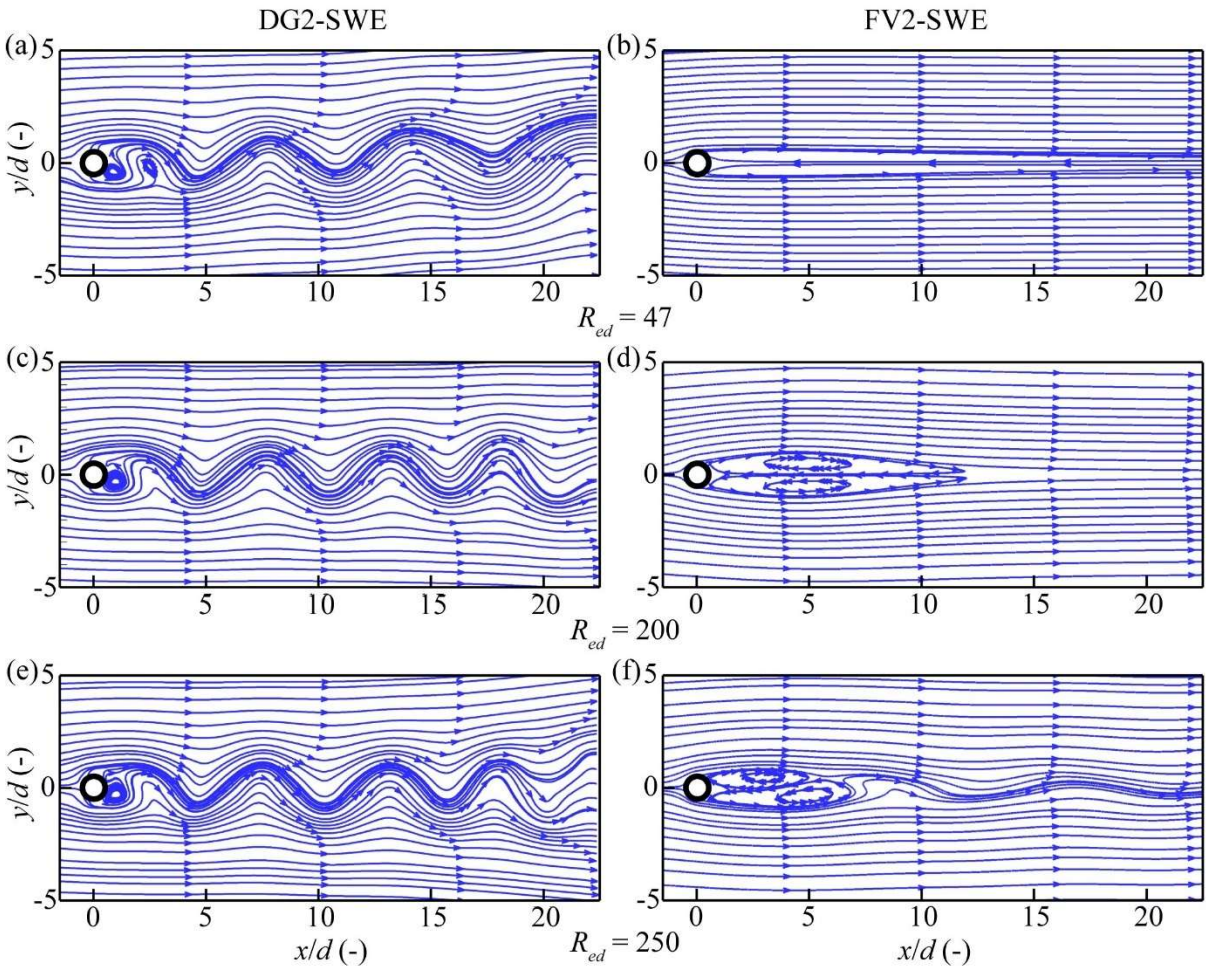

Figure 3.3. Flow past one cylinder: Instantaneous streamlines at the start of the fully developed quasi-steady state; The left panel contains the DG2-SWE simulated results (at time D2 in Figure. 3.2, while the right panel contains the FV2-SWE simulated results (at time F2 in Figure. 3.2). From top to bottom, the flow cases are at R_{ed} = 47, 200 and 250, respectively.

The scaled vorticity ω contours processed from the DG2-SWE and FV2-SWE flow fields are shown in Figure. 3.4. It can be seen that the DG2-SWE solver can reproduce the evolution of the shedding vortices featured with a decay of the peak vorticity within the core of each vortex, producing classical vorticity patterns such as those reported in Ponta (2010). These vorticity patterns exhibit the S-shaped detachment from the cylinder's surface, agreeing with the reference predictions (compare with Figure. 3.13 in Qu et al. (2013) and Figure. 3.8 in Rajani et al. (2009) (see reference vorticity figure of Figure. 2.15). This suggests that the DG2-SWE solver has an advantage in treating the advective fluxes, as it represents the cylinders as piecewise-planar bed slope terms and reduces the amount of numerical viscosity. This makes it a better alternative to predict local flow discontinuities and thereby a more accurate prediction of vortical structure. Nonetheless, compared with the reference cases (see reference vorticity figure of Figure. 2.15), the DG2-SWE vorticity distributions are sparser for R_{ed} = 200 and 250, and exhibit a higher frequency for R_{ed} = 47, which is consistent with the aforementioned deviations

between the S_t value predicted by DG2-SWE and the reference values. In contrast, FV2-SWE fails to reproduce the typical vorticity patterns for R_{ed} = 47, 200 and 250 (Figure. 3.4, right), leading to an almost symmetrical and elongated wake flow.

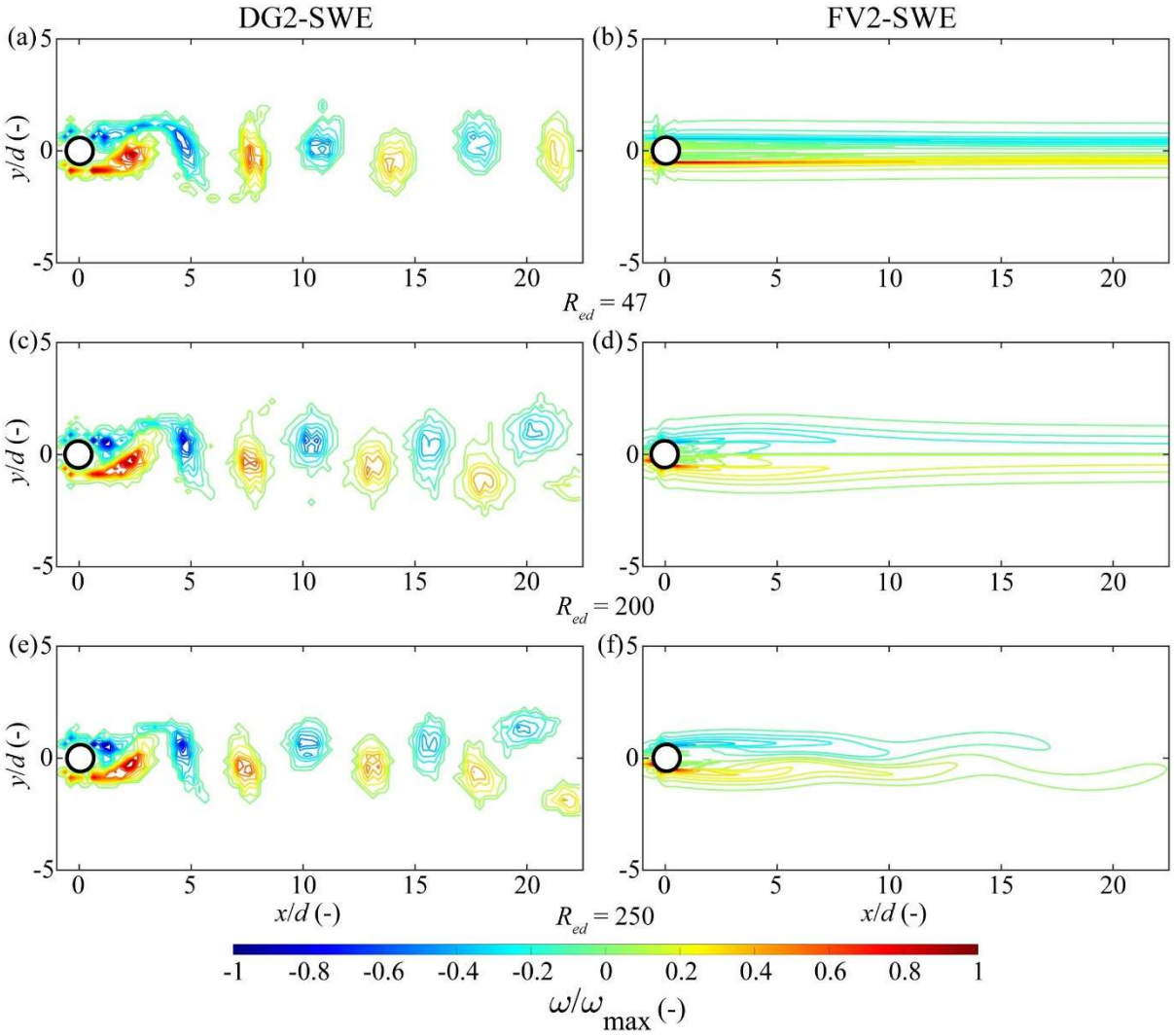

Figure 3.4. Flow past one cylinder: Instantaneous scaled vorticity contours at the start of the fully developed quasi-steady state; The left panel provides the results processed from the DG2-SWE simulated flow fields (at time D2 in Figure. 3.2) and the right panel provides the results processed from the FV2-SWE simulated flow fields (at time F2 in Figure. 3.2). From top to bottom, each row refers to the flow cases at R_{ed} = 47, 200 and 250, respectively.

3.3.1.3 Time-averaged longitudinal velocity

Figure. 3.5 compares the scaled time-averaged longitudinal velocity $\bar{u}$ profile along the wake centreline $y/d = 0$ simulated by the DG2-SWE and FV2-SWE solvers with the reference numerical predictions from 2D RANS model reported in Qu et al. (2013) alongside the experimental measurement reported in Paranthoën et al. (1999). In the figure, $x/d = 0$ is the location of the cylinder, $0 \leq x \leq 0.5d$ represents the cylinder radius shown as the light grey shading, $0.5d < x \leq 4d$ covers the near-cylinder region, and

the area spanning $x > 4d$ represents the far-wake region. The recirculation length along the cylinder centreline is the distance starting from the cylinder edge to the point where $\bar{u}$ changes its sign to positive. The velocity recovery rate can be analysed by examining the gradient of the slope in the $\bar{u}$ profile. It should be noted that the profile generated for $R_{ed} = 250$ is excluded from the analysis as no reference data are found for quasi-steady flow case at this R_{ed}, and only the measured $\bar{u}$ profile at $R_{ed} = 47$ is available.

At $R_{ed} = 200$, the $\bar{u}$ profile simulated by DG2-SWE (blue dashed line) is in a reasonable agreement with the reference $\bar{u}$ profile (red dashed line). In the near-cylinder region, the $\bar{u}$ profile simulated by DG2-SWE is below but nearly parallel to the reference profile and lags behind it by $0.8d$ before reaching the same peak of 0.75. This suggests that DG2-SWE can reproduce an almost consistent velocity recovery rate but yields an elongated recirculation length. In the far-wake region, DG2-SWE slightly overpredicts the reference profile but maintains a similar (decreasing) trend with minor fluctuations. In contrast, the FV2-SWE simulated $\bar{u}$ profile (black dashed line) is negative until $x > 18d$ and shows a much longer recirculation length and a much slower velocity recovery rate than the reference profile. In particular, at $x = 5d$, FV2-SWE reaches the lowest value of -0.55, whereas the associated reference value is around 0.7, reinforcing that FV2-SWE tends to yield simulation results that deviate significantly from expected simulated behaviour.

At $R_{ed} = 47$, as the viscosity effect becomes more dominant, the $\bar{u}$ profile simulated by DG2-SWE (blue solid line) shows less agreement with two closely aligned reference profiles from the 2D RANS model (red solid line) and the measurement (green circle). Compared to the reference profiles, in the near-cylinder region, DG2-SWE overpredicts the $\bar{u}$ profile and exhibits a much steeper slope, showing that a DG2-SWE prediction would lead to faster velocity recovery rate and shorter recirculation length. In the far-wake region, the $\bar{u}$ profile simulated by DG2-SWE tends to become closer to the reference profiles with increased distance, $x > 15d$. Again, FV2-SWE (black solid line) fails to capture the velocity recovery behind the cylinder and the negative $\bar{u}$ along the centreline indicates persistent velocity deficit downstream. This is in noticeable disagreement with the reference numerical simulated and experimental measured results.

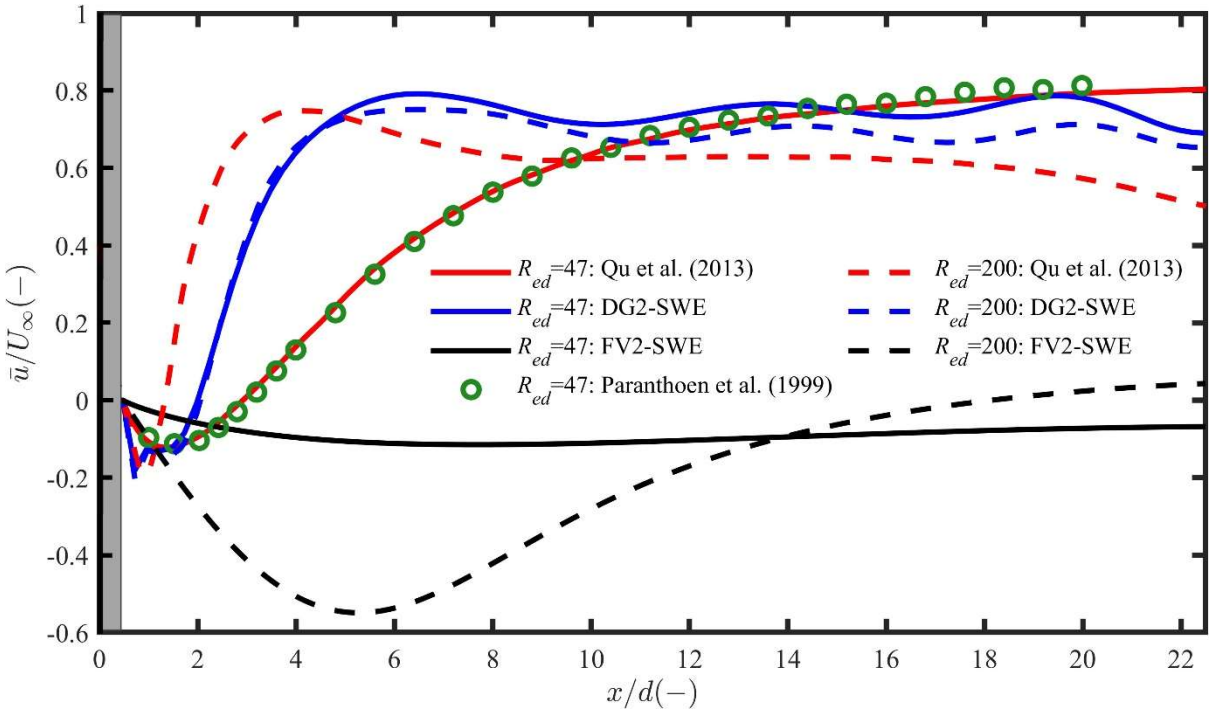

Figure 3.5. Flow past one cylinder: Profiles of the time-averaged longitudinal velocity simulated by the DG2-SWE (blue lines) and FV2-SWE (black lines) solvers extracted along centreline y/d = 0 relative to the reference simulated profiles (red lines) at R_{ed} = 47 (solid lines) and 200 (dotted lines) and the reference measured profiles (green circle) at R_{ed} = 47. The light grey shade indicates the cylinder.

Hence, it could be inferred from the results that, when applied to simulate flow past a cylinder, the DG2-SWE solver is a much better choice than the conventional FV2-SWE solver, to at least produce reliable results in the far-wake region regardless of R_{ed}. Near the cylinder, with a fairly high R_{ed}, around 200 and higher, the DG2-SWE simulated profiles are closer to the reference profiles than with very low R_{ed}, around 47. Still, given the absence of kinematic and eddy viscosity in the present DG2-SWE solver, it is expected to yield profiles with an elongated recirculation length for transitional R_{ed} and with underestimated recirculation length with laminar R_{ed}. Moreover, the absence of viscosity terms introduces another limitation: the DG2-SWE solver provides similar scaled velocity predictions even at different R_{ed}, which is not as good as the RANS model at producing R_{ed}-dependent results.

The analyses of Sec. 3.3.1 suggest that a DG2-SWE solver's run at a resolution of 0.25d is much faster to trigger vortex shedding than an FV2-SWE solver's run at a 10 times finer resolution of 0.025d, making it 90 times faster to complete a converged simulation. Therefore, compared to the FV2-SWE solver, the DG2-SWE solver is a more accurate and efficient alternative to simulate flow within cylinder arrays to at least capture the flow characteristics in the far-wake region. This will be investigated next with respect to a new laboratory-scale application.

3.3.2 Laminar and transitional flows within an array of cylinders: comparison with measurement

The DG2-SWE solver is further explored through the simulation of experimental flow fields within randomly distributed cylinders of diameter d = 4 mm in a 3750d × 75d (equivalent to 15 m × 0.3 m) flume. The experiment was conducted at the University of Warwick, and involved SPIV measurements of instantaneous u and v data, comprising 250 data sets within 10 seconds (Corredor-Garcia et al., 2020; Sonnenwald et al., 2019c). Within the flume, a random distribution of cylinders with a cylinder density ϕ of 0.005 was generated for a 625d × 75d (equivalent to 2.5 m × 0.3 m) baseplate, and duplicates of this baseplate were used to cover a total length of 1875d (equivalent to 7.5 m) (Figure. 3.6a). SPIV data (Corredor-Garcia et al., 2020) was collected for an area 137.5d × 75d (equivalent to 0.55 m × 0.3 m), located 1332.5d (equivalent to 5.33 m) from the start of the cylinder section (Figure. 3.6b), i.e. in a downstream section where the flow was believed to be fully developed. The computational domain covered the full 1875d channel length, again to ensure that the flow field was fully developed. Four cases with different R_{ed} are reported (Corredor-Garcia, 2021), but for consistency with Sec. 3.3.1, only the flows with the lowest and highest R_{ed} of 53 and 220, representing the laminar and transitional flow regimes, are investigated here. Table 3.3 shows the hydraulic and experimental parameters used to run the DG2-SWE simulations for each of the selected R_{ed}. It should be noted that the projection bias from the SPIV measurement has not been corrected, and this therefore shifts the measured cylinder positions. The cylinders project above the surface of the flow, which leads to missing hydrodynamic information (data shadows) where visualisation of the flow surface is blocked by the projected cylinders. Finally, it should also be noted that, whereas the laboratory cylinders were truly cylindrical, the numerical cylinders are approximated by rectilinear shapes on the 1 mm square computational grid.

Table 3.3. Flow within an array of cylinders: The hydraulic and experimental parameters for flow cases at R_{ed} = 53, 220 and 450.

R_{ed} (-)	U_∞ (m s^{-1})	d (m)	h (m)	q_x (m^2 s^{-1})	S_0 (m m^{-1})	n_M (m$^{1/6}$)
53	0.0147	0.004	0.15	0.002205	0.0	0.045
220	0.06			0.009	4.6×10^{-4}	
450	0.0556	0.008		0.00834	9×10^{-4}	0.054

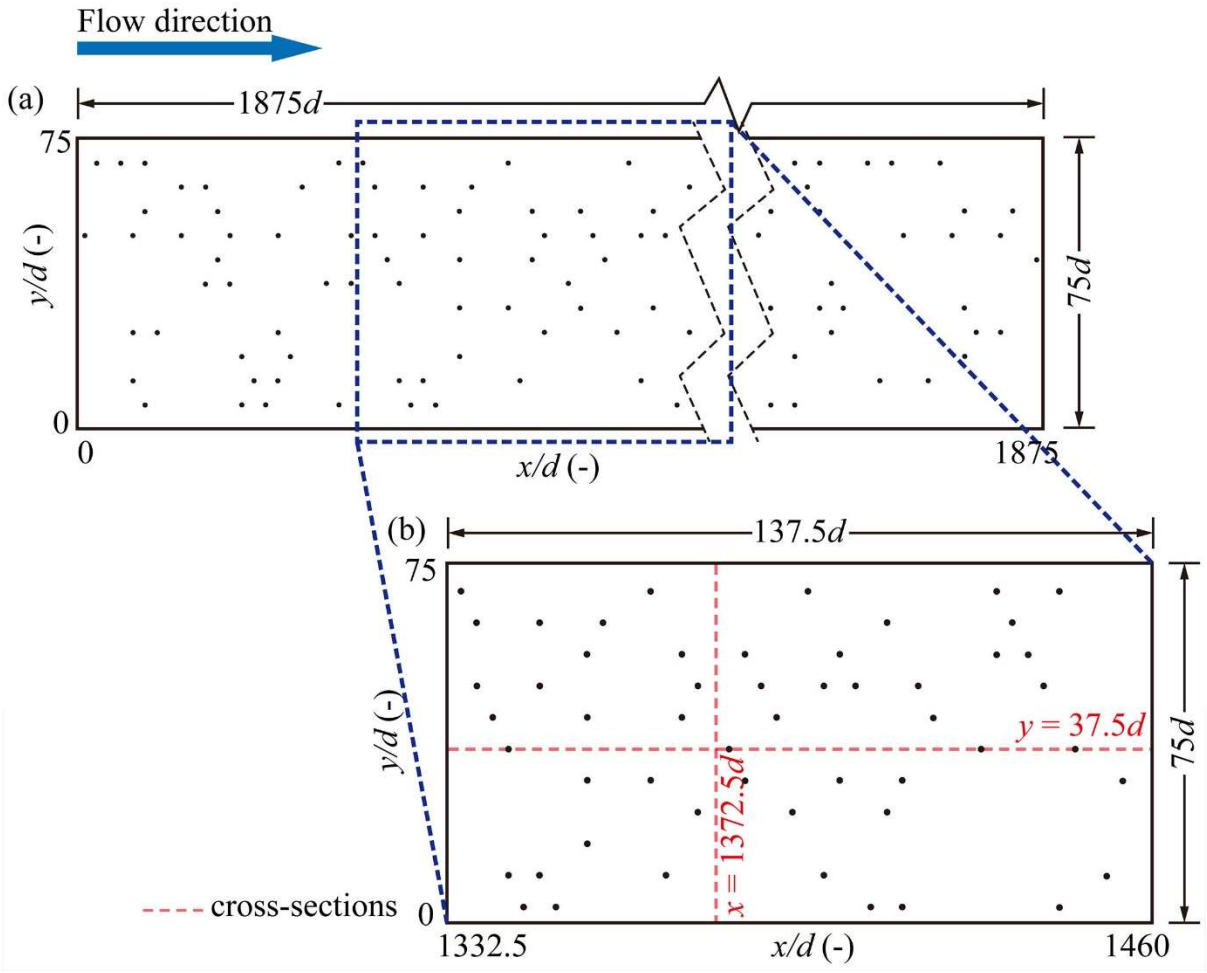

Figure 3.6. Flow within an array of cylinders: (a) Schematic plan view of the randomly distributed cylinders in the flume; (b) cylinders' spatial distribution in the SPIV measurement section (Corredor-Garcia et al., 2020; Sonnenwald et al., 2019c).

The DG2-SWE simulations are run on a grid with the same resolution of 0.25d identified in Sec. 3.3.1 (i.e., 1 mm), which also matches the 1 mm pixel resolution of the SPIV datasets. The DG2-SWE simulated instantaneous u and v components of velocity are recorded at the same time interval as the SPIV measuring frequency of 25 frames per second to allow for consistent comparisons. The shedding frequencies are first analysed to study quasi-steady state convergence, and further investigations are done using time-averaged 2D velocity maps and 1D profiles along the longitudinal and transverse cross sections y = 37.5d and x = 1372.5d, respectively. The average deviation errors between the simulated and reference data are quantified using the L^1-norm error (Ayog et al., 2021; Kesserwani et al., 2023) that is expressed as:

$$L^1\text{-norm error} = \frac{1}{N}\left(\sum_{k=1}^{N}\left|z_k^{Num} - z_k^{Ref}\right|\right) \tag{3.2}$$

where N denotes the number of grid elements, and z_k^{Num} and z_k^{Ref} are the respective numerically simulated and reference $\bar{u}$ or $\bar{v}$ values. R^2 coefficient is also considered to quantify the correlation between the DG2-SWE simulation and reference solution (Ayog et al., 2021; Kesserwani et al., 2023), given as:

$$R^2 = \frac{\sum_{k=1}^{N}\left(z_k^{Num} - \overline{z_k^{Num}}\right)\left(z_k^{ref} - \overline{z_k^{ref}}\right)}{\sqrt{\sum_{k=1}^{N}\left(z_k^{Num} - \overline{z_k^{Num}}\right)^2 \sum_{k=1}^{N}\left(z_k^{Ref} - \overline{z_k^{Ref}}\right)^2}} \tag{3.3}$$

To quantify the extent of directional alignment between the simulated and reference flow fields, the Relevance Index (R_I) (Liu and Haworth, 2011; Willman et al., 2020) is used, defined as:

$$R_I = \frac{1}{N}\left(\sum_{k=1}^{N} \frac{< V_k^{Num}, V_k^{Ref} >}{\left\| V_k^{Num} \right\| \left\| V_k^{Ref} \right\|}\right) \tag{3.4}$$

where V is the time-averaged velocity vector consisting of components $\bar{u}$ and $\bar{v}$, < > denotes the inner product operator, and || || indicates the magnitude of $V = \sqrt{\bar{u}^2 + \bar{v}^2}$. The R_I takes values between -1 and 1, with 1 indicating a perfect alignment of the simulated and reference velocity vectors.

Table 3.4. Flow within an array of cylinders: DG2-SWE simulated and SPIV measured shedding frequencies and S_t ranges for the cylinder array within the SPIV measurement section for each flow condition after 50 shedding cycles.

R_{ed} (-)	f_s (s^{-1})		S_t (-)	
	SPIV	DG2-SWE	SPIV	DG2-SWE
53	0.56 ± 0.2	0.4 ± 0.21	0.15 ± 0.054	0.11 ± 0.057
220	2.9 ± 0.8	1.6 ± 0.85	0.2 ± 0.055	0.11 ± 0.057

3.3.2.1 Quasi-steady state convergence

For each flow case, the simulation is set to terminate after 50 cycles when a fully developed quasi-periodic steady state is reached, as suggested by Rajani et al. (2009) and also justified in Appendix C. Steady state convergence is analysed in terms of vortex shedding frequency f_s and Strouhal number S_t. Since the flow is influenced by the background turbulence imposed by the adjacent cylinders (Nepf, 1999; Ricardo, Sanches, et al., 2016), f_s values sampled behind all the cylinders should have a range of variations. Table 3.4 also includes the mean and standard deviation values for simulated and measured f_s and S_t. These values have been derived from the time histories of v for all the cylinders located within the portion of SPIV data measurements, at a distance of 2.5d behind each cylinder's centre using Fast Fourier Transforms. For both flow cases at R_{ed} = 53 and 220, the mean values for f_s and S_t simulated by the DG2-SWE solver are lower than the estimates from the SPIV data. Such discrepancy may be due to

the overpredicted velocities near the sidewalls (as shown later in Figure. 3.7), which may exert an influence on the wake flow evolution and thereby distort the shedding frequency. Still, for both cases, the DG2-SWE predicted ranges for standard deviation of f_s and S_t are close to the ranges estimated from the SPIV data, showing a satisfactory level of agreement. The associated time-averaged velocities extracted over the 50 cycles are then analysed.

3.3.2.2 Time-averaged scaled flow fields

Figure. 3.7 compares the scaled $\bar{u}$ contour maps obtained from the DG2-SWE solver's simulations to the measured ones at R_{ed} = 53 and 220, showing generally good agreement. This is confirmed by the small magnitude of the L^1-norm errors (≤ 0.2). R^2 coefficient for both flow cases are higher than 0.65. This might be lower than expected, being affected by the aforementioned projection bias in the SPIV data. At R_{ed} = 53 (Figure. 3.7b vs. Figure. 3.7a), DG2-SWE simulates elongated wake flow areas behind all the cylinders as compared with the measured data. The observed over-expansion of the wake flow patterns is expected to occur due to the mismatch between numerical viscosity and true kinematic and eddy viscosity. At the higher R_{ed} = 220 (Figure. 3.7d vs. Figure. 3.7c), the simulated $\bar{u}$ map better matches the measured $\bar{u}$ map, as both L^1-norm error and R^2 coefficient is smaller. This indicates a better performance for the DG2-SWE solver at R_{ed} = 220 where there is more dominance from the advective fluxes over the viscosity effects. This also implies that the DG2-SWE solver introduces an amount of numerical viscosity for the flow at the higher R_{ed} that helps imitate the effects of the true kinematic and eddy viscosity. The most noticeable differences between the measured and simulated flow fields are in the right hand one third of the channel ($0 < y/d < 30$) where a high velocity preferential flow path forms between widely-spaced cylinders; this is far less evident in the simulation compared with the measured data. Also, for both flow cases, the simulated $\bar{u}$ near the sidewalls are overpredicted, and this may be caused by the lack of an explicit wall treatment function within the DG2-SWE solver (Ginting, 2019).

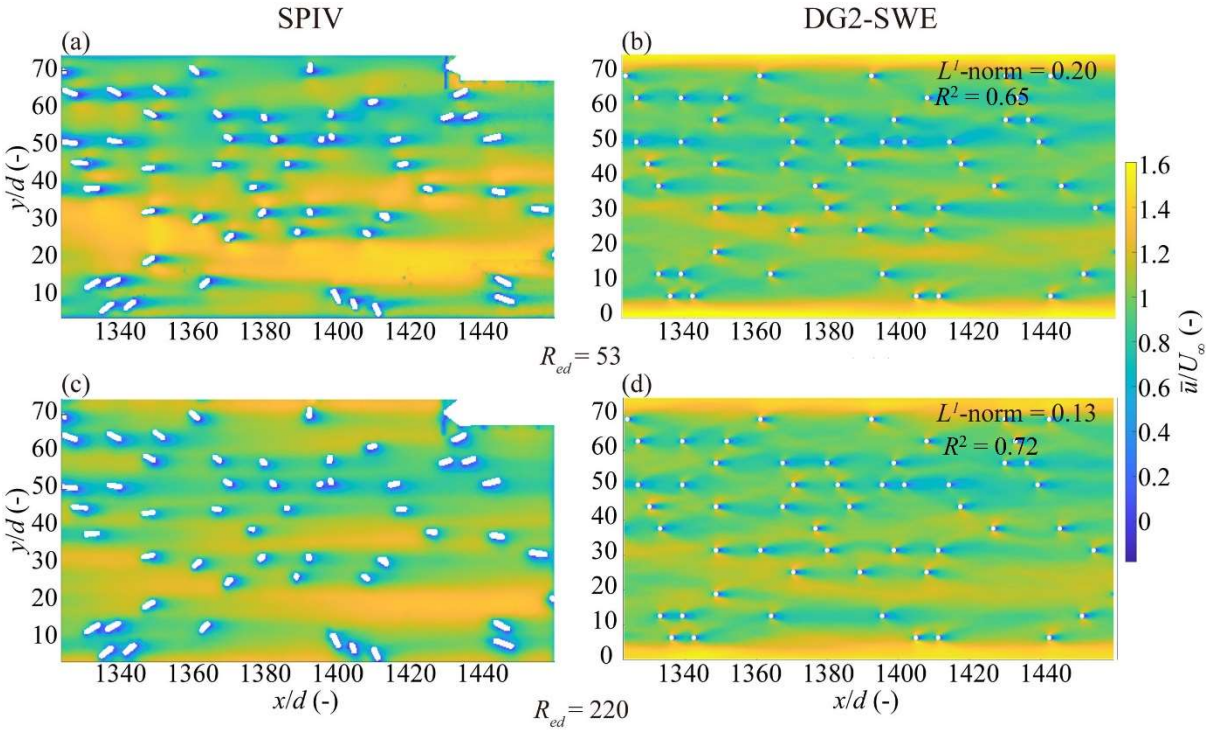

Figure 3.7. Flow within an array of cylinders: Contours of the scaled time-averaged longitudinal velocity and the L^1-norm errors. The upper panel contains the results for the flow case at R_{ed} = 53: (a) SPIV measurement and (b) DG2-SWE simulation, while the lower panel contains those for the flow case at R_{ed} = 220: (c) SPIV measurement and (d) DG2-SWE simulation.

In Figure. 3.8, the scaled $\bar{v}$ contour maps acquired from the DG2-SWE simulations are compared with the measured $\bar{v}$ maps at R_{ed} = 53 and 220. Generally, the simulated $\bar{v}$ maps are in close agreement with measured maps and the L^1-norm errors are not greater than 0.05. R^2 coefficient for both cases are still around 0.60, probably due to the aforementioned projection bias. The DG2-SWE solver is seen to reproduce the alternating and symmetrical patterns along each cylinder's wake centreline, which are observed in the measured $\bar{v}$ maps. At R_{ed} = 53 (Figure. 3.8b vs. Figure. 3.8a), the measured $\bar{v}$ patterns along the cylinders are bigger in magnitude than the simulated patterns. This underestimation of transverse velocities implies that the simulation tends to underestimate the extent to which the streamlines curve around the cylinders. Reduced streamline curvature is also evident in the velocity vector maps (as shown later in Figure. 3.11). This may arise as a result of the rectilinear representation of the cylinder geometry, and the mismatch between numerical viscosity and true kinematic and eddy viscosity. At R_{ed} = 220, the simulated patterns agree better with the measured patterns for $\bar{v}$ (Figure. 3.8d vs. Figure. 3.8c), which is in line with the better agreement observed between the simulated and measured $\bar{u}$ at R_{ed} = 220 (recall Figure. 3.7).

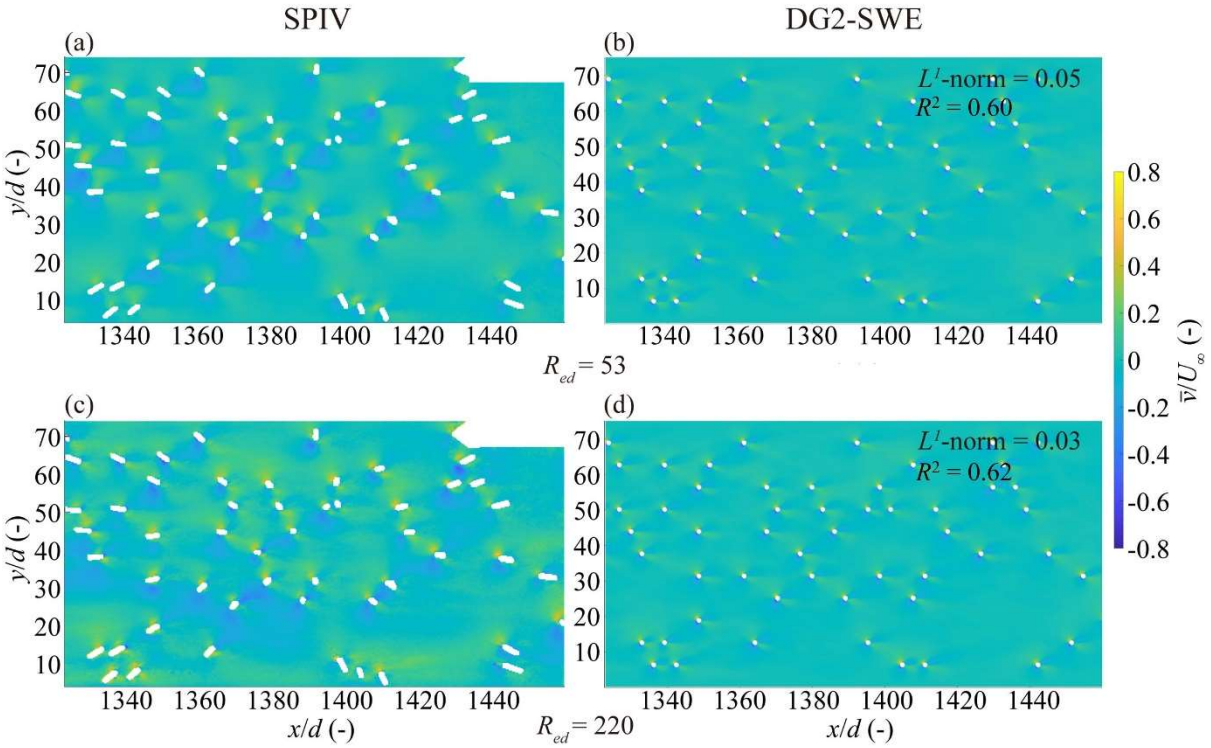

Figure 3.8. Flow within an array of cylinders: Contours of the scaled time-averaged transverse velocity and the L[1]-norm errors. The upper panel contains the results for the flow case at R_{ed} = 53: (a) SPIV measurement and (b) DG2-SWE simulation, while the lower panel contains those for the flow case at R_{ed} = 220: (c) SPIV measurement and (d) DG2-SWE simulation.

To closely analyse the simulated wake flow features, Figure. 3.9 compares the simulated and measured $\bar{u}$ profiles along $y = 37.5d$ and $x = 1372.5d$, for $R_{ed} = 53$ (left) and 220 (right). Along $y = 37.5d$ (Figures. 3.9a and 3.9b), the $\bar{u}$ profiles are only analysed up to the second cylinder (the predictions around the last two cylinders may be subject to position shift from the projection bias). At $R_{ed} = 53$, in the near-cylinder regions, the simulated profile (blue dashed line) is above the measured one (red solid line) with a steeper slope, showing that DG2-SWE overpredicts the measured $\bar{u}$ magnitude as observed in the findings of Sec. 3.3.1. In the far-wake regions, the simulated profile is below but almost parallel to the measured profile, confirming that DG2-SWE produces a similar velocity recovery rate to the measured one but underestimates the $\bar{u}$ magnitudes. Such underestimation of the $\bar{u}$ magnitudes also reflects the difference between the simulated and measured $\bar{u}$ contours in the far-wake regions, as discussed previously for Figures 3.7a and 7b. At $R_{ed} = 220$, the simulated $\bar{u}$ profile achieves a closer agreement with the measured profile than that at $R_{ed} = 53$, which again reinforces that the DG2-SWE solver predicts closer results at higher R_{ed}. Along $x = 1372.5d$, at $R_{ed} = 53$ (Figure. 3.9c), the simulated $\bar{u}$ profile agrees well with the measured one, albeit with slight deviations assumed due to the projection bias. At $R_{ed} = 220$ (Figure. 3.9d), the DG2-SWE solver produces a generally good agreement with the measured profile but yields sharper peaks near the two cylinders spanning $20d < y < 30d$ and $45d < y < 55d$.

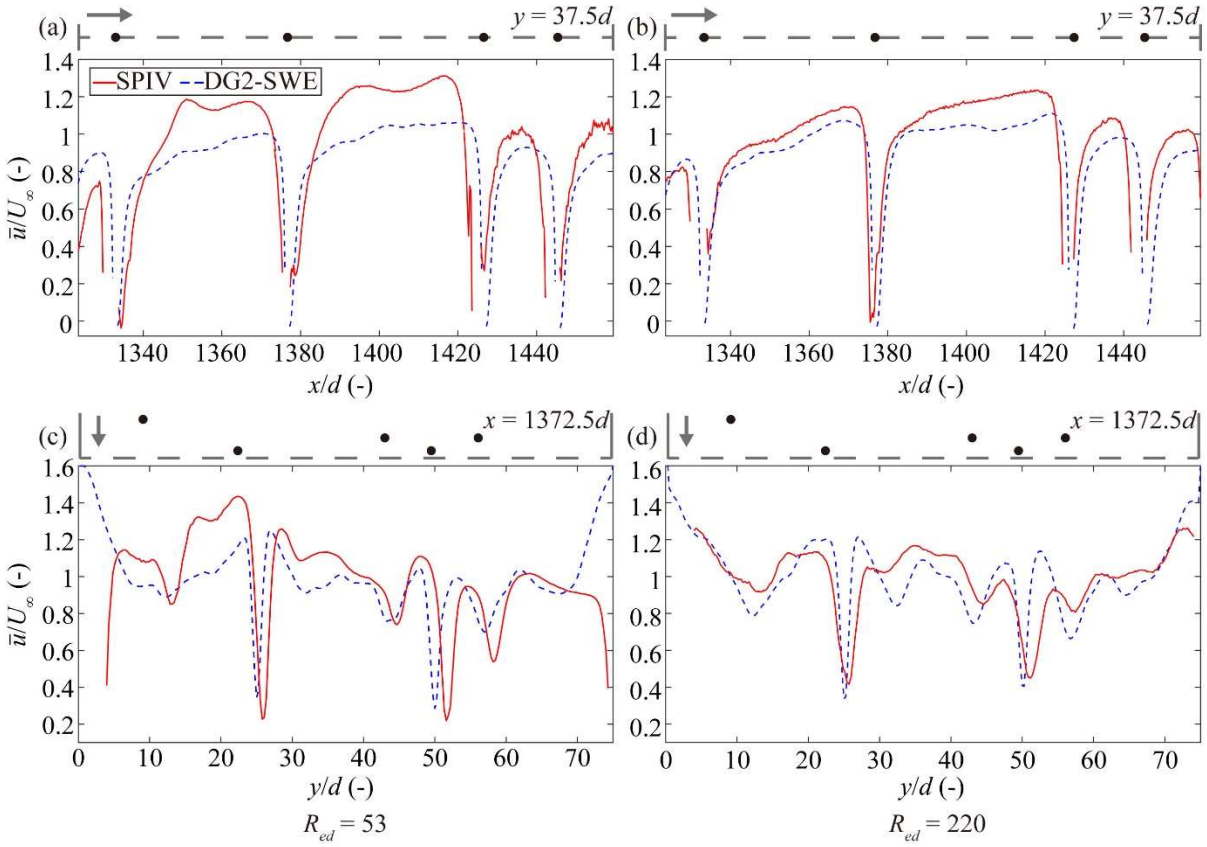

Figure 3.9. Flow within an array of cylinders: Time-averaged longitudinal velocity profiles measured by SPIV (red solid lines) and simulated by DG2-SWE (blue dashed lines), at R_{ed} = 53 (left) and 220 (right). (a) and (b) show the profiles along $y = 37.5d$. (c) and (d) show the profiles along $x = 1372.5d$. The upper part of each sub-plot shows the positions of cylinders (black dots) and the flow direction (grey arrows).

From Figure. 3.10, a similar analysis can be conducted for the simulated and measured $\bar{v}$ profiles. Along $y = 37.5d$, at $R_{ed} = 53$ (Figure. 3.10a), the simulated profile (blue dashed line) deviates from the measured profile (red solid line), which is expected, as the overall variation in measured $\bar{v}$ is more pronounced compared with the simulation (recall Figures. 3.8a vs. 3.8b). However, at $R_{ed} = 220$ (Figure. 3.10b), the simulated $\bar{v}$ profile is very close to the measured profile. Along $x = 1372.5d$, at $R_{ed} = 53$ (Figure. 3.10c), the DG2-SWE solver produces smoother variations in the simulated $\bar{v}$ compared with the measured $\bar{v}$ that have lower magnitudes. At $R_{ed} = 220$ (Figure. 3.10d), the simulated profile resembles the measured profile, but DG2-SWE yields sharper $\bar{v}$ peaks within zones $20d < y < 30d$ and $45d < y < 55d$. Such overestimation is expected due to the rectilinear representation of the cylinders, as discussed previously for Figure. 3.8.

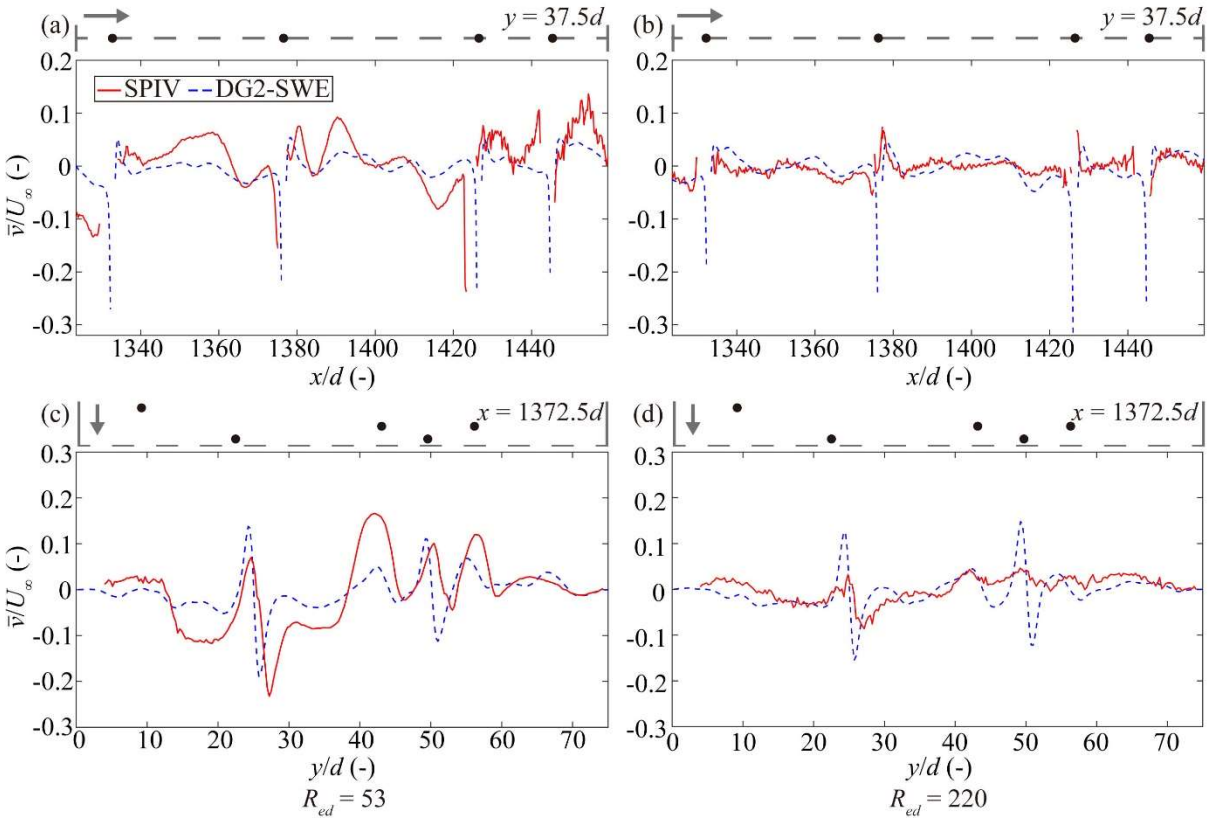

Figure 3.10. Flow within an array of cylinders: Time-averaged transverse velocity profiles measured by SPIV (red solid lines) and simulated by DG2-SWE (blue dashed lines), at R_{ed} = 53 (left) and 220 (right). (a) and (b) show the profiles along y = 37.5d. (c) and (d) show the profiles along x = 1372.5d. The upper part of each sub-plot shows the positions of cylinders (black dots) and the flow direction (grey arrows).

Figure. 3.11 displays the Relevance Index (R_I) fields [a score used to describe the velocity directional alignment, see Eq. (3.4)] calculated from the simulated and measured velocity vectors for flow cases at R_{ed} = 53 (top panel) and 220 (bottom panel), to further assess the agreement in directionalities of flow fields. Figures. 3.11a and 3.11c show the R_I fields within the whole measurement section. Figures. 3.11b and 3.11d illustrate the zoomed-in view of the simulated and measured time-averaged velocity vectors superimposed onto the R_I fields, which are around the cylinder located at (1370.3d, 25d). This cylinder was selected due to the overlap between the position of the simulated cylinder and the measured one. Within data shadows, the green circle indicates the actual cylinder position, the area with black outline represents the simulated cylinder, and the light grey shading shows the blocked hydrodynamic information around the measured cylinder.

At R_{ed} = 53, Figure. 3.11a shows a fairly strong alignment between the simulated and measured flow directions in the majority of the R_I field. This can be confirmed by the whole mean R_I value which is close to 1. However, misalignment of the flow direction can be seen in the areas around the cylinders, owing to the difference between the simulated and measured cylinder positions and data shadows. Figure. 3.11b clearly identifies this relatively poor alignment, and the mean R_I value in this zoomed-in portion, of 0.84 is lower than the whole mean R_I value of 0.99. There are small included angles between

some of the simulated and measured velocity vectors. The greater curvature visible in the measured vectors is consistent with the fact that the magnitude of measured $\bar{v}$ around the cylinder is higher than the simulated one (recall Figures. 3.8a and 3.8b). At R_{ed} = 220 (Figure. 3.11c), the simulated flow direction almost perfectly matches the measured one as the whole mean R_I value is very close to 1. Figure. 3.11d shows that the DG2-SWE solver can closely reproduce the measured velocity vectors around the cylinder. The mean R_I value in the zoomed-in portion of 0.95 indicates a better directional alignment at higher R_{ed}.

The analysis in Sec. 3.3.2 shows that at the laminar to transitional regimes, the DG2-SWE solver can reproduce the complex wake evolution patterns and closely reproduce the flow directions around cylinders, and the reliability of its predictions would be enhanced with the increase in R_{ed}.

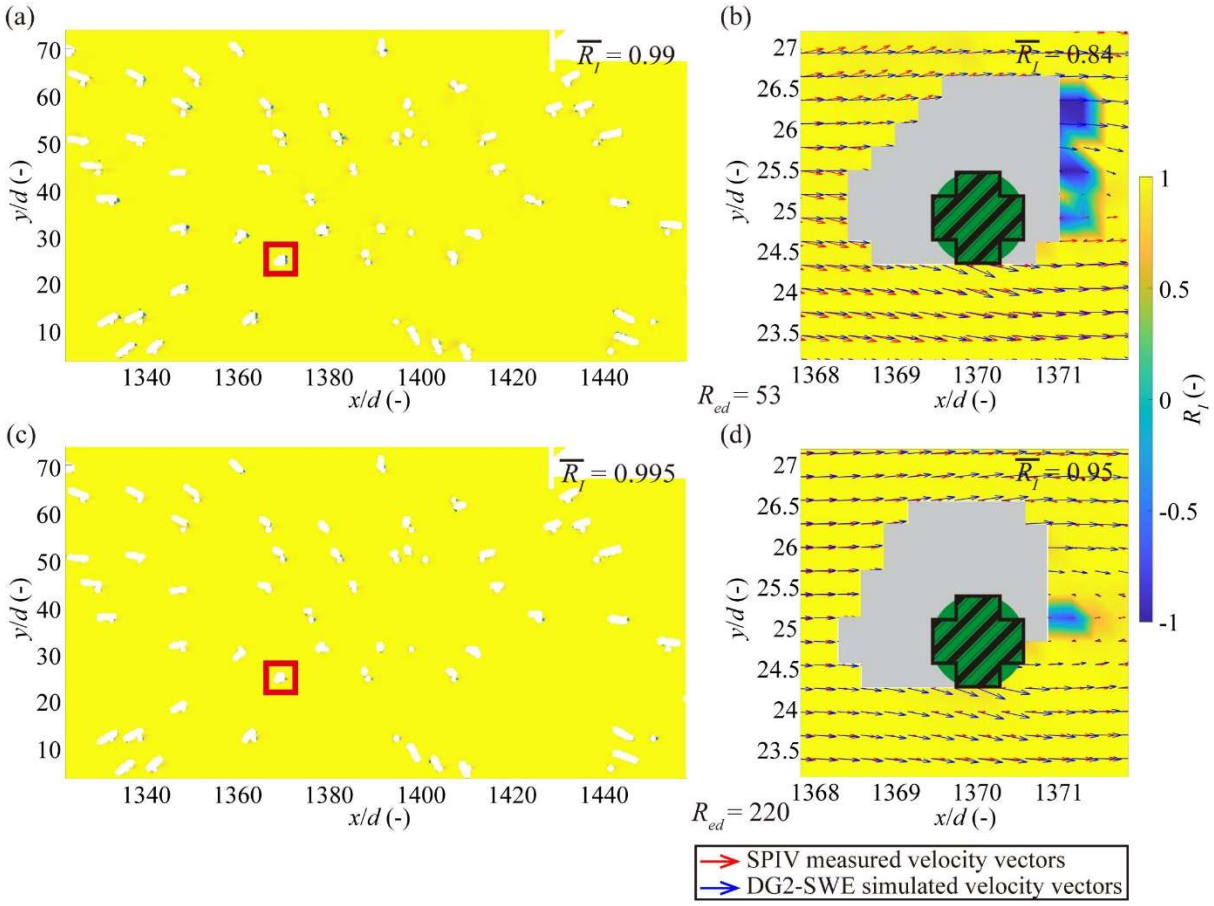

Figure 3.11. Flow within an array of cylinders: Relevance Index fields (left panel) and zoomed-in view of spatial velocity vectors of DG2-SWE (blue arrows) and SPIV (red arrows) superimposed onto Relevance Index fields and around one cylinder *x*, *y* = 1370.3*d*, 25*d* (right panel); The upper panel (a and b) is for the flow case at R_{ed} = 53, whereas the lower panel (c and d) is for the flow case at R_{ed} = 220. The Relevance Index coefficients are provided in each panel.

3.3.3 Turbulent flow within an array of cylinders: comparison with numerical simulation

After being validated against experimental results for laminar to transitional flow conditions, the DG2-SWE solver is here compared with the Fluent RANS model to further validate its performance under turbulent flow condition. Similar to the previous section (Sec. 3.3.2), the DG2-SWE solver is again applied to simulate flow past the random cylinder array in the same aforementioned flume at the University of Warwick (Corredor-Garcia et al., 2020; Sonnenwald et al., 2019c). Low-turbulence flow cases at R_{ed} = 450 are explored, whose corresponding inflow velocity is set to be 0.0556 s m^{-1}. Apart from R_{ed}, there is a main difference from the previous section (Sec. 3.3.2). The difference lies in the configuration: this time, cylinders with a diameter d = 8 mm were randomly inserted into a shorter baseplate of 125d × 37.5d (equivalent to 1 m × 0.3 m) featuring a denser cylinder density of ϕ = 0.027 (Figure 3.12), and 8 replicas of this baseplate cover a total length of 1125d (equivalent to 9 m). Hydraulic and experimental parameters can be found in Table 3.3. Note that, since no value for the bed slope in longitudinal direction, S_{0x}, was reported, n_M was estimated as 0.054 m$^{1/6}$ using another empirical formula based on ϕ (Luhar and Nepf, 2013). S_{0x} is accordingly set as 9 × 10^{-4} (m/m) to numerically preserve the uniform water depth of 0.15 m.

Due to the absence of available experimental measured velocity data under such configuration, the performance of the DG2-SWE solver is only evaluated with respect to the Fluent RANS model. This utilized Fluent RANS model is a 2D model incorporating the Reynolds Stress Model for turbulence closure, under second-order accuracy in both spatial and temporal discretisation. Triangular computational grids were applied with a fine resolution of 0.025d (equivalent to 0.2 mm) close to cylinder edges and sidewalls and a coarse resolution of 0.125d (equivalent to 1 mm) away from the cylinder. This Fluent RANS model and related setting were justified in Golzar (2018) and Stovin et al. (2022). The more detailed setup of this Fluent RANS model can be found in Golzar (2018) and Stovin et al. (2022).

The DG2-SWE simulation is run on a grid with the same resolution of 0.25d (equivalent to 2 mm) in a computational domain covering a total length of 1125d, which can ensure the flow field was fully developed. Termination criteria, recording frequency and validation criteria (except for S_t unavailable in Fluent RANS) of the DG2-SWE simulation are same as the setting in Sec. 3.3.2. The DG2-SWE simulated velocity are extracted within an area of (x, y) ∈ [750d, 875d] × [0, 37.5d] where the flow was believed to be fully developed. Comparisons are conducted using the time-averaged longitudinal velocity $\bar{u}$ field and 1D profiles along the longitudinal and transverse cross-sections y = 18.75d and x = 812.5d. Directional alignment of velocity direction is then investigated.

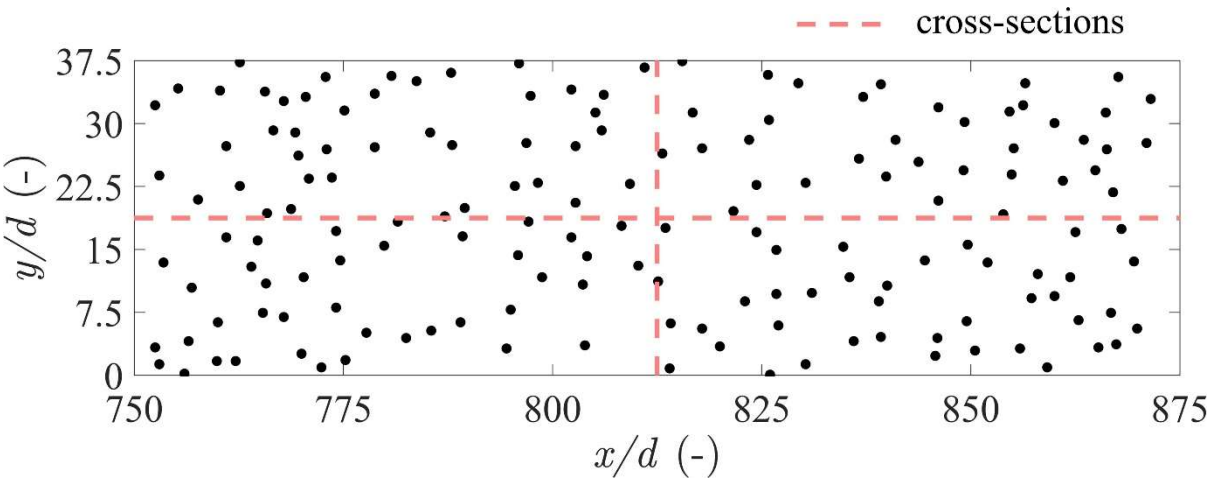

Figure 3.12. Spatial distribution of randomly distributed cylinders (Sonnenwald et al., 2019c).

Figure 3.13 compares the time-averaged longitudinal velocity $\bar{u}$ maps simulated by Fluent RANS and DG2-SWE, showing that the DG2-SWE simulated $\bar{u}$ map resembles the one from the Fluent RANS. High velocities at the lateral sides of the cylinders and wake zones behind the cylinders are reasonably captured by the two models. The L^1-norm error and R^2 coefficient between the DG2-SWE and Fluent RANS for this simulated time-averaged flow fields are 0.18 and 0.84 respectively, which may again indicate the good agreement between the simulated results of the two models. However, a big difference in simulated $\bar{u}$ maps can be observed near the sidewalls. As discussed above (recall Figure 3.7), this might be attributed to the absence of wall treatment within the DG2-SWE solver (Ginting, 2019). Also, for some regions where the cylinders are further away from each other (e.g. between x/d = 800 and 825), the DG2-SWE solver appears to overestimate velocities than the Fluent RANS.

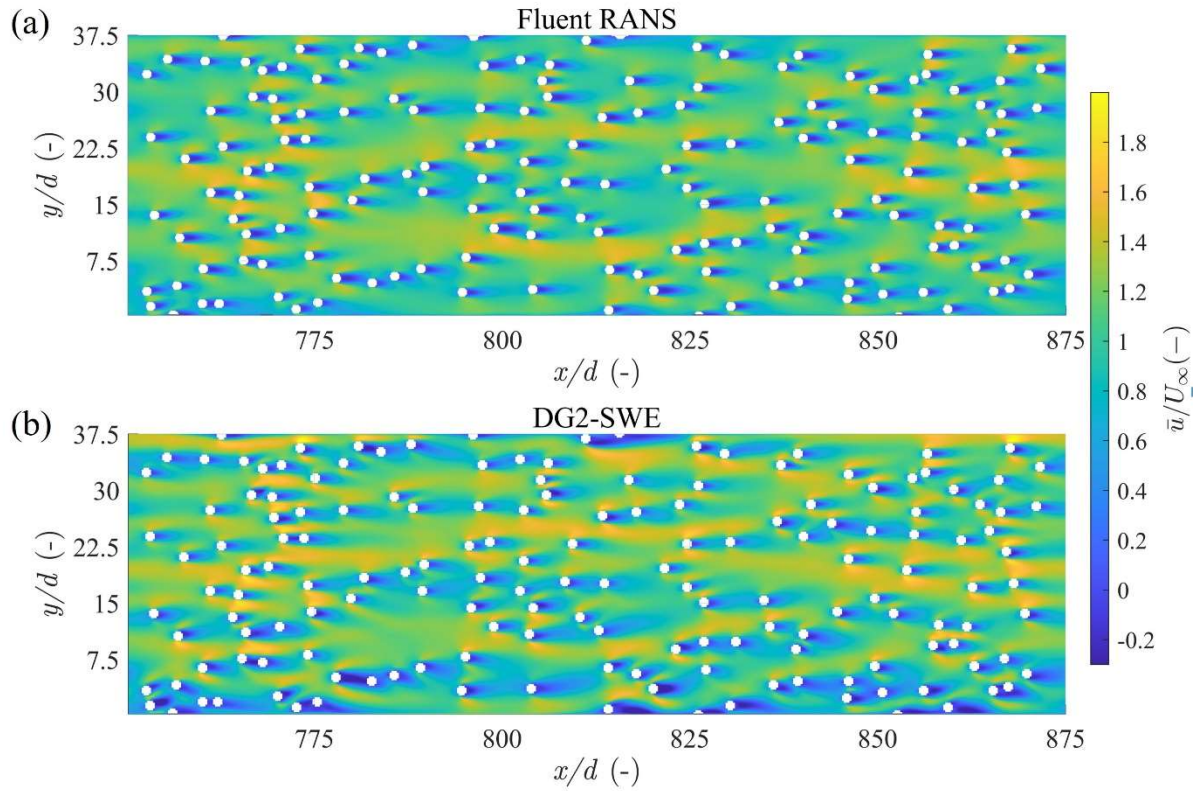

Figure 3.13. Flow within an array of cylinders: Contours of the scaled time-averaged longitudinal velocity at turbulent R_{ed} = 450. (a) The upper panel contains the simulation results from Fluent RANS, and (b) the lower panel contains the simulated results from the DG2-SWE solver.

Further comparison between the DG2-SWE and Fluent RANS model was investigated by comparing the time-averaged longitudinal velocity along the longitudinal cross-section/centreline of $y = 18.75d$ (Figure 3.14a) and transverse cross-section of $x = 812.5d$ (Figure 3.14b). Along the longitudinal centreline, time-averaged longitudinal velocity profile simulated by the DG2-SWE solver (blue dashed line) is quite consistent with the one simulated by Fluent RANS (red solid line), despite there being a minor difference at no-cylinder regions (i.e. $825 < x/d < 850$) and just behind the cylinders ($x/d = 850$) where DG2-SWE simulates higher velocities than Fluent RANS. Along the transverse cross-section, the difference between the simulation results of the two numerical models can be found near the side walls (e.g. $0 < y/d < 5$ and $30 < y/d < 37.5$), as observed in Figure 3.13. In the rest of the regions, the simulated profiles from DG2-SWE and Fluent RANS can match with each other.

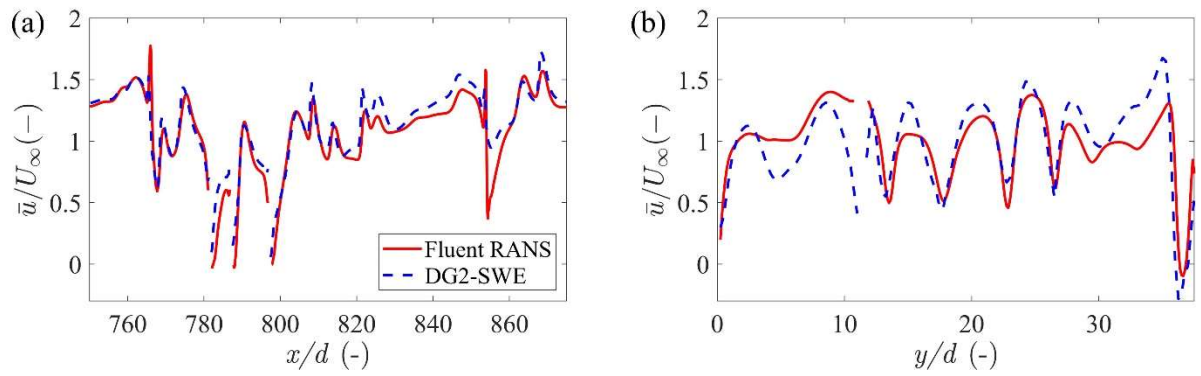

Figure 3.14. Flow within an array of cylinders: Time-averaged longitudinal velocity profiles along y = 37.5d and (b) x = 1625d simulated by Fluent RANS (red solid lines) and DG2-SWE (blue dashed lines) at turbulent R_{ed} = 450.

The direction alignment of the simulated velocities (vectors) is then considered by assessing the R_I fields, as shown in Figure 3.15. Generally, the DG2-SWE simulated vectors are well aligned with the Fluent RANS results and mean R_I value is around 0.93. The discrepancy in the velocity direction is mainly near the side walls and also behind the cylinders. However, the overall results from DG2-SWE are comparable with Fluent RANS.

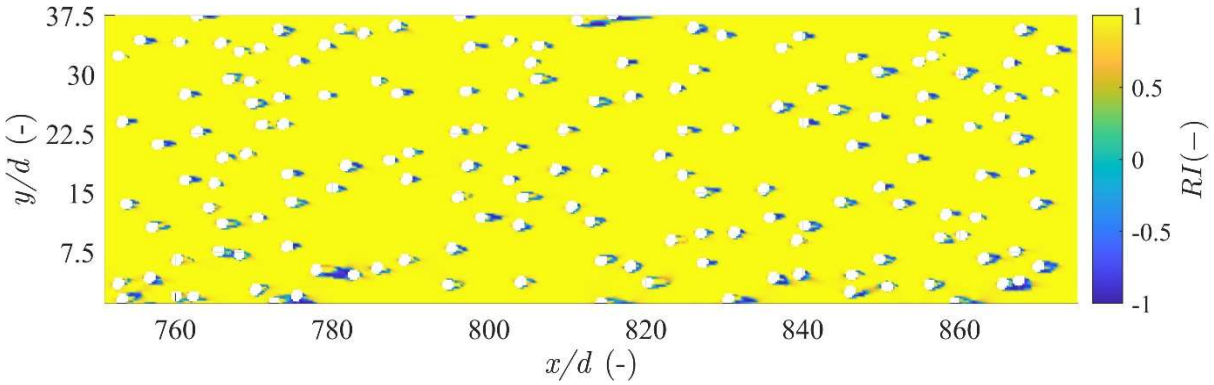

Figure 3.15. Flow within an array of cylinders: Relevance Index fields between the Fluent RANS and DG2-SWE velocity simulations.

The results analysis in this section shows that at the low-turbulence regime, the DG2-SWE solver on a coarse grid resolution (10-fold coarser near the cylinder twice coarser away from the cylinder) can still efficiently simulate accurate wake formations that resemble those produced by mathematically more complex turbulence model. This suggests that the DG2-SWE solver can be a practical modelling tool for environmental hydraulic applications involving a quasi-steady, slow flow past large-scale cylinder arrays.

3.4 Concluding remarks

Inviscid numerical solvers of the two-dimensional (2D) depth-averaged SWE integrate the advective fluxes and bed slope terms and use Manning's formula as an implicit model of the vertical turbulence

structure. Although these solvers exclude the viscous and turbulent eddy viscosity terms, they introduce an amount of numerical viscosity that may imitate kinematic and eddy viscosity of viscous turbulent models. When simulating laminar to transitional wakes past cylinder(s) in slow quasi-steady flows (R_{ed} $\leq$ 250), an FV2-SWE solver fails to detect the wake formation at practically affordable grid resolution. It is affected by fast growth of numerical error dissipation that manifests as large numerical viscosity. The extra numerical complexity in a DG2-SWE solver provides a more accurate treatment of the advective fluxes and bed slope terms, generally resulting in better predictions at coarser grid resolutions and much lower numerical viscosity.

The advantage of the DG2-SWE solver over the FV2-SWE solver was first diagnostically evaluated in simulating wake evolution for classical flows past a single cylinder. The comparative analysis included convergence speed to complete 50 vortex shedding cycles, ability to excite and capture periods of vortex shedding, and to capture vortical structures and longitudinal velocity profiles. The analysis confirms that the DG2-SWE solver is more suited to efficiently model the wake formation, despite the limitation of solving the inviscid SWE. Therefore, its reliability to predict the wake formation improves with a R_{ed} > 200 compared to a R_{ed} around 50 where viscosity effects are more significant. This capability for the DG2-SWE solver was then verified by applying it to reproduce laboratory-scale flows past an array of randomly distributed cylinders with validation against measured velocity fields. The laboratory-scale tests reinforce that the DG2-SWE solver is a useful tool to efficiently simulate sufficiently accurate wake formations that would resemble the measurements and those produced by more complex models. Being far less dissipative than the FV2-SWE solver, the findings suggest that the DG2-SWE solver is a promising alternative to also improve the predictive capability of depth-averaged RANS models using the SWE with the equations integrating the viscous and/or the turbulent fluxes.

4 Development of the DG2-ADE solver for simulating solute transport past cylinders

4.1 Chapter overview

This chapter is related to Objective 2, elucidating the development of the second order discontinuous Galerkin (DG2) solver based on the two-dimensional (2D) advection diffusion equation (ADE) used for simulating solute transport past cylinders. Sec. 4.2 presents the development of the DG2-ADE solver with a focus on how it links to the DG2-SWE solver. Sec. 4.2.1 introduces how to post-process the DG2-SWE simulated output to generate the initial conditions/inputs of the DG2-ADE simulations. Sec. 4.2.2 presents the discretization of the ADE along with the specific treatments to preserve the simulated concentration positive and to handle the presence of the cylinder. The DG2-ADE solver is then validated in Sec. 4.3. In Sec. 4.3.1, the advection diffusion test cases without the cylinder are tailored to evaluate the performance of the DG2-ADE solver relative to the conventional equally accurate ADE solver. The advection diffusion test cases with cylinder(s) are included in Sec. 4.3.2 to verify the mass-balance and positivity-preserving properties of the DG2-ADE solver and to further assess its capability in capturing the solute spread around the cylinder(s) by comparing with the commercial software model.

4.2 The DG2-ADE solver on LISFLOOD-FP

The DG2-ADE solver adapts the simplified, slope-decoupled DG2 formulation (Kesserwani et al., 2018; Shaw et al., 2021) to solve ADE (Eq. 4.1) for predicting solute transport concentration C (x, y, t) at time t (s) and spatial position (x, y) in Cartesian coordinates (m).

$$\frac{\partial C}{\partial t} + \bar{u}\frac{\partial C}{\partial x} + \bar{v}\frac{\partial C}{\partial y} = \frac{\partial}{\partial x}\left(D_t \frac{\partial C}{\partial x}\right) + \frac{\partial}{\partial y}\left(D_t \frac{\partial C}{\partial y}\right) \tag{4.1}$$

In Eq. (4.1), ∂ is the partial derivative operator, $\bar{u}$ and $\bar{v}$ (m/s) are time-averaged fields of the longitudinal and transverse components of the velocity, and D_t (m^2/s) is the 2D turbulent diffusivity field (assumed isotropic). Running a DG2-ADE simulation requires a priori generation of initial conditions for the $\bar{u}$, $\bar{v}$ and D_t fields (Section 4.2.1) and ensuring a positivity-preserving formulation to predict reliable solute concentration predictions around emergent cylinders (Section 4.2.2). In the following, the generation of initial conditions and the proposed DG2-ADE solver's formulation are described, for a raster-formatted grid made of square elements, $Q_{i,j}$, of equal dimensions ($\Delta x = \Delta y$), centred at the point $(x_{i,j}, y_{i,j})$.

4.2.1 Generation of the initial conditions

From a DG2-SWE simulation, the generation of 2D maps for $\bar{u}$,$\bar{v}$ and D_t can be extracted from the simulated maps of the flow vector $\mathbf{U} = [h\ hu\ hv]^T$, where h (x, y, t) is the water depth variable, and hu (x, y, t) and hv (x, y, t) are unit-width discharges variables incorporating the u (x, y, t) and v (x, y, t)

components of the velocity field. Over a discrete element $Q_{i,j}$, the simulated DG2-SWE outputs take the shape of piecewise-planar solution, packed in a vector $\mathbf{U_h}(x,y,t)|_{Q_{i,j}} = \left\{\mathbf{U}_{i,j}^{K}(t)\right\}_{K=0,1x,1y}$, in which $\mathbf{U}_{i,j}^{0}$ is a coefficient of an average, and $\mathbf{U}_{i,j}^{1x}$ and $\mathbf{U}_{i,j}^{1y}$, are x- and y-directional slope coefficients:

$$\mathbf{U_h}(x,y,t)|_{Q_{i,j}} = \mathbf{U}_{i,j}^{0}(t) + \frac{2\sqrt{3}(x-x_{i,j})}{\Delta x}\mathbf{U}_{i,j}^{1x}(t) + \frac{2\sqrt{3}(y-y_{i,j})}{\Delta y}\mathbf{U}_{i,j}^{1y}(t) \tag{4.2}$$

During the DG2-SWE simulation, the instantaneous coefficients $\left\{\mathbf{U}_{i,j}^{K}(t)\right\}_{K=0,1x,1y}$, defining the piecewise-planar solution $\mathbf{U_h}(x,y,t)|_{Q_{i,j}}$, have been recorded (such as, per 0.04 s in Chapter 3) to yield a time-series of size N_t. As shown in Figure. 4.1, from these time-series of instantaneous coefficients, those associated with the longitudinal and transverse velocity components, $u_h(x,y,t)|_{Q_{i,j}} = \left\{u_{i,j}^{K}(t)\right\}_K$ and $v_h(x,y,t)|_{Q_{i,j}} = \left\{v_{i,j}^{K}(t)\right\}_K$ are then produced: by dividing the unit-width discharge coefficients in $\left\{\mathbf{U}_{i,j}^{K}(t)\right\}_K$ by the average water depth coefficient $h_{i,j}^{0}$. The instantaneous time-series of $\left\{u_{i,j}^{K}(t)\right\}_K$ and $\left\{v_{i,j}^{K}(t)\right\}_K$ can further be decomposed into time-averaged parts, denoted by $\left\{\overline{u_{i,j}^{K}}\right\}_K$ and $\left\{\overline{v_{i,j}^{K}}\right\}_K$, and fluctuating parts, denoted by $\left\{u_{i,j}^{K\prime}(t)\right\}_K$ and $\left\{v_{i,j}^{K\prime}(t)\right\}_K$, as is standard in turbulent flow analysis (Pokrajac et al., 2008).

Using the elementwise approximate velocity component solutions, $u_h(x,y,t)|_{Q_{i,j}} = \left\{u_{i,j}^{K}(t)\right\}_K$ and $v_h(x,y,t)|_{Q_{i,j}} = \left\{v_{i,j}^{K}(t)\right\}_K$, the elementwise partial derivatives for the velocity components read:

$$\left.\frac{\partial u}{\partial x}\right|_{Q_{i,j}} = \frac{\partial}{\partial x}\left[u_h(x,y,t)|_{Q_{i,j}}\right] = \frac{2\sqrt{3}}{\Delta x}u_{i,j}^{1x}(t) \tag{4.3a}$$

$$\left.\frac{\partial u}{\partial y}\right|_{Q_{i,j}} = \frac{\partial}{\partial y}\left[u_h(x,y,t)|_{Q_{i,j}}\right] = \frac{2\sqrt{3}}{\Delta y}u_{i,j}^{1y}(t) \tag{4.3b}$$

$$\left.\frac{\partial v}{\partial x}\right|_{Q_{i,j}} = \frac{\partial}{\partial x}\left[v_h(x,y,t)|_{Q_{i,j}}\right] = \frac{2\sqrt{3}}{\Delta x}v_{i,j}^{1x}(t) \tag{4.3c}$$

$$\left.\frac{\partial v}{\partial y}\right|_{Q_{i,j}} = \frac{\partial}{\partial y}\left[v_h(x,y,t)|_{Q_{i,j}}\right] = \frac{2\sqrt{3}}{\Delta y}v_{i,j}^{1y}(t) \tag{4.3d}$$

Similarly, the elementwise approximate velocity components of the fluctuating parts, $u_h'(x,y,t)|_{Q_{i,j}} = \left\{u_{i,j}^{K\prime}(t)\right\}_K$ and $v_h'(x,y,t)|_{Q_{i,j}} = \left\{v_{i,j}^{K\prime}(t)\right\}_K$ can be use to produce their elementwise derivatives as:

$$\left.\frac{\partial u}{\partial x}\right|'_{Q_{i,j}} = \frac{\partial}{\partial x}\left[u_h'(x,y,t)|_{Q_{i,j}}\right] = \frac{2\sqrt{3}}{\Delta x}u_{i,j}^{1x\prime} \tag{4.4a}$$

$$\left.\frac{\partial u}{\partial y}\right|'_{Q_{i,j}} = \frac{\partial}{\partial y}\left[u_h'(x,y,t)|_{Q_{i,j}}\right] = \frac{2\sqrt{3}}{\Delta y}u_{i,j}^{1y\prime}(t) \tag{4.4b}$$

$$\left.\frac{\partial v}{\partial x}\right|'_{Q_{i,j}} = \frac{\partial}{\partial x}\left[v_h'(x,y,t)|_{Q_{i,j}}\right] = \frac{2\sqrt{3}}{\Delta x}v_{i,j}^{1x\prime}(t) \tag{4.4c}$$

$$\left.\frac{\partial v}{\partial y}\right|'_{Q_{i,j}} = \frac{\partial}{\partial y}\left[v_h'(x,y,t)|_{Q_{i,j}}\right] = \frac{2\sqrt{3}}{\Delta y}v_{i,j}^{1y\prime}(t) \tag{4.4d}$$

The 2D maps for $\bar{u}$ and $\bar{v}$ are directly taken to be the maps of average velocity coefficients from the time-averaged parts, which include $\{\overline{u_{i,j}^0}\}$ and $\{\overline{v_{i,j}^0}\}$. Whereas the generation of the D_t map requires elementwise evaluation of $D_t|_{Q_{i,j}}$:

$$D_t|_{Q_{i,j}} = \frac{\nu_t|_{Q_{i,j}}}{S_c} \tag{4.5}$$

which boils down to elementwise evaluation of the eddy-viscosity, $\nu_t|_{Q_{i,j}}$, as turbulent Schmidt number S_c = 1 (Lu and Dai 2016; Okamoto and Nezu 2010; Stovin et al. 2022; Wu et al. 2000). In turn, since ν_t depends on the turbulent kinetic energy (TKE) and dissipation rate, denoted by k and ε, respectively (Wang et al. 2021), to be evaluated as follows:

$$\nu_t|_{Q_{i,j}} = c_\mu \frac{\left(k|_{Q_{i,j}}\right)^2}{\varepsilon|_{Q_{i,j}}} \tag{4.6}$$

where, c_μ = 0.09 is an empirical constant (Wu 2004; Wu et al. 2000), and the terms $k|_{Q_{i,j}}$ and $\varepsilon|_{Q_{i,j}}$ denote the elementwise evaluation of k and ε over each a discrete element, $Q_{i,j}$, as follows:

$$k|_{Q_{i,j}} = \frac{1}{2\,N_t}\left[\sum_1^{N_t}\left(u_{i,j}^{0'}(t)\right)^2 + \sum_1^{N_t}\left(v_{i,j}^{0'}(t)\right)^2\right] \tag{4.7}$$

$$\varepsilon|_{Q_{i,j}} = \frac{2\,\nu_k}{N_t}\left\{\begin{array}{c}\displaystyle\sum_1^{N_t}\left(\frac{\partial u}{\partial x}\Big|'_{Q_{i,j}}\right)^2 + \sum_1^{N_t}\left(\frac{\partial v}{\partial y}\Big|'_{Q_{i,j}}\right)^2 + \frac{1}{2}\sum_1^{N_t}\left(\frac{\partial u}{\partial y}\Big|'_{Q_{i,j}}\right)^2 \\ \displaystyle+\frac{1}{2}\sum_1^{N_t}\left(\frac{\partial v}{\partial x}\Big|'_{Q_{i,j}}\right)^2 + \sum_1^{N_t}\left(\frac{\partial u}{\partial y}\Big|'_{Q_{i,j}}\frac{\partial v}{\partial x}\Big|'_{Q_{i,j}}\right)\end{array}\right\} \tag{4.8}$$

where, ν_k = 10^{-6} is the kinematic viscosity (m^2/s) (Wu 2004; Wu et al. 2000), and the $\frac{1}{N_t}\sum_1^{N_t}(\,)$ denotes the time-averaging operator of the fluctuating coefficients over a time-series of N_t coefficients. Plugging Eqs. (4.7-4.8) into Eq. (4.5) yields elementwise piecewise-average evaluation of $D_t|_{Q_{i,j}}$ that can be assembled over all grid elements to produce a non-uniformly distributed 2D map of the D_t field (see Figure. 4.1). This map will hereafter be referred to as "non-uniform D_t".

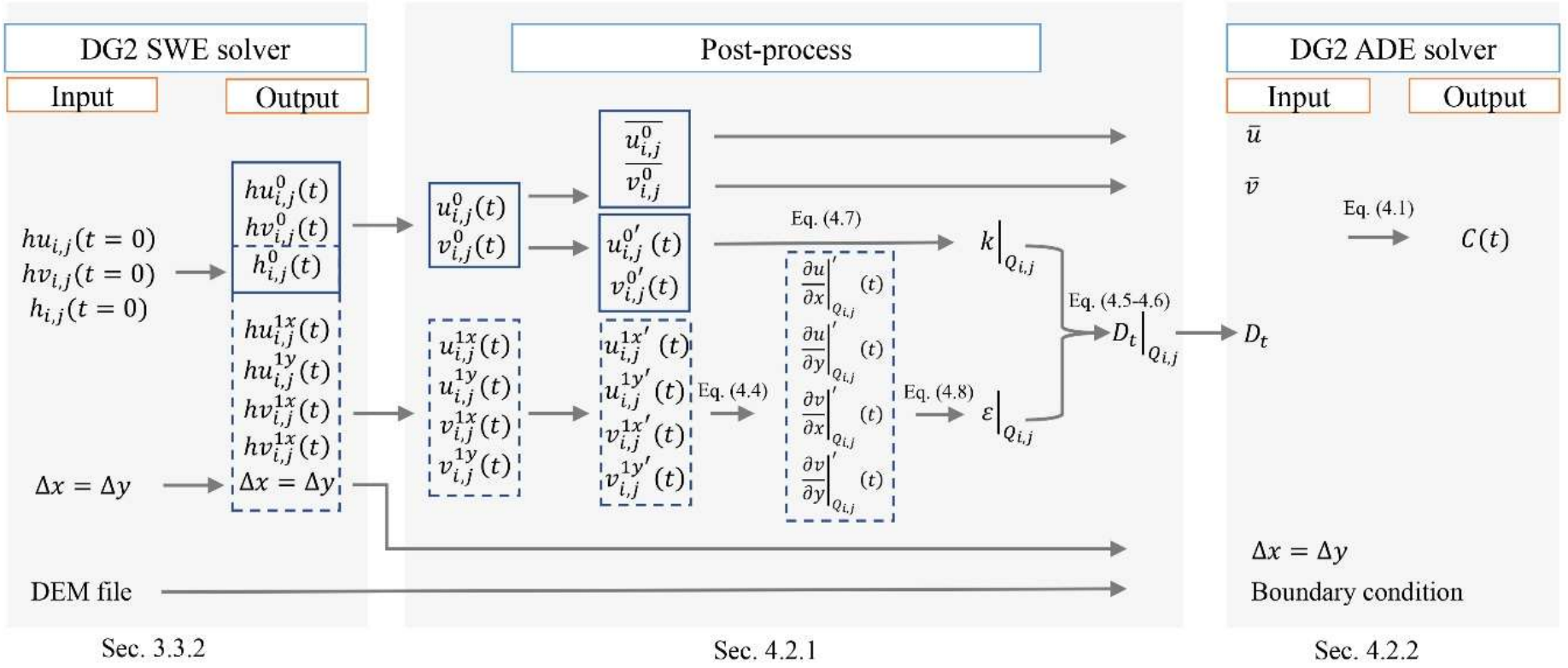

Figure 4.1. Procedures for using the DG2-SWE simulation outputs to generate the initial conditions (time-averaged flow fields and turbulent diffusivity field) of the DG2-ADE solver.

4.2.2 Positivity-preserving formulation

The DG2-ADE solver should be run on the same uniform square grid used by the DG2-SWE simulation and takes the 2D maps for $\bar{u}$,$\bar{v}$ and D_t as the inputs. This is necessary to identify those elements including emergent cylinders to then be flagged into either a "cylinder element", such that the bed elevation is higher than the initial water level (e.g., the shaded grid elements in Figure. 4.2), or otherwise a "non-cylinder element" (e.g., the blank grid elements in Figure. 4.2). Figure. 4.2 shows an example of an emergent cylinder discretisation involving cylinder elements surrounded by non-cylinder elements. Over any element $Q_{i,j}$, a piecewise-planar DG2 concentration solution is sought, $C_h(x,y,t)|_{Q_{i,j}} = \{C_{i,j}^K(t)\}_K$, which writes:

$$C_h(x,y,t)|_{Q_{i,j}} = C_{i,j}^0(t) + \frac{2\sqrt{3}(x-x_{i,j})}{\Delta x} C_{i,j}^{1x}(t) + \frac{2\sqrt{3}(y-y_{i,j})}{\Delta y} C_{i,j}^{1y}(t) \tag{4.9}$$

Coefficients $\{C_{i,j}^K(t)\}_K$ have to be evolved in time via a two-stage Runge-Kutta time stepping scheme, based the local element evaluation for the advective transport operator, $L^a = -(\bar{u}\,\partial C/\partial x + \bar{v}\partial C/\partial y)$, and the diffusive transport operator, $L^d = \frac{\partial}{\partial x}(D_t \partial C/\partial x) + \frac{\partial}{\partial y}(D_t \partial C/\partial y)$, identified from Eq. (4.1).

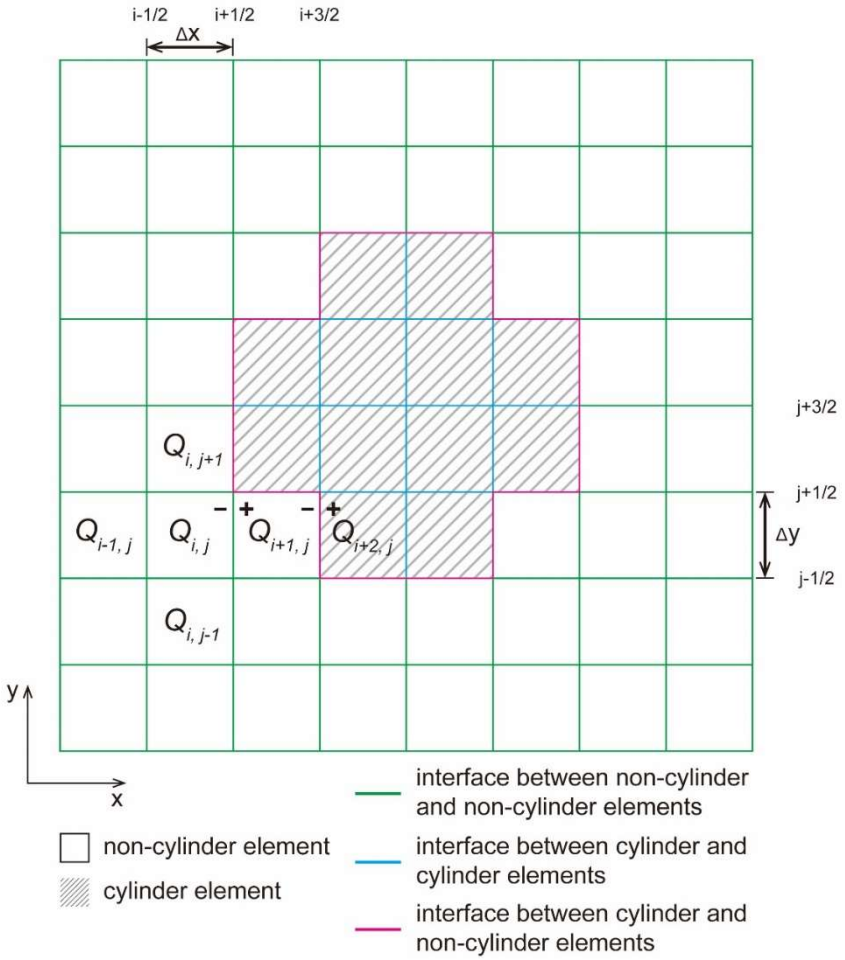

Figure 4.2. A sketch of the distribution of cylinder (blank grids) and non-cylinder (shaded grids) elements together with three different types of interfaces. Green lines represent the interfaces between non-cylinder and non-cylinder elements, blue lines denote the interfaces between cylinder and cylinder elements, and pink lines are the interfaces between cylinder and non-cylinder elements.

The elementwise evaluation, of L^a on element $Q_{i,j}$, denoted by $L^a_{i,j}$, must involve three spatial discrete DG2 operators, $\{L^{K,a}_{i,j}\}_K$ for updating each $\{C^K_{i,j}(t)\}_K$. Simplified expressions of the $\{L^{K,a}_{i,j}\}_K$ operators can be derived by replacing $C(x,y,t)$ by $C_h(x,y,t)|_{Q_{i,j}}$ in the standard finite element weak formulation (Kesserwani et al., 2018) and exploiting the orthonormality properties of the scaled, slope-decoupled Legendre basis functions (Kesserwani and Sharifian, 2020), to read:

$$L^{0,a}_{i,j} = -\left(\frac{f^{LLF}_{i+\frac{1}{2},j} - f^{LLF}_{i-\frac{1}{2},j}}{\Delta x} + \frac{g^{LLF}_{i,j+\frac{1}{2}} - g^{LLF}_{i,j-\frac{1}{2}}}{\Delta y}\right) \tag{4.10a}$$

$$L^{1x,a}_{i,j} = -\frac{\sqrt{3}}{\Delta x}\left(f^{LLF}_{i+\frac{1}{2},j} - f^{LLF}_{i-\frac{1}{2},j} - f\left(C^0_{i,j} - C^{1x}_{i,j}\right) - f\left(C^0_{i,j} + C^{1x}_{i,j}\right)\right) \tag{4.10b}$$

$$L_{i,j}^{1y,a} = -\frac{\sqrt{3}}{\Delta y}\left(g_{i,j+\frac{1}{2}}^{LLF} - g_{i,j-\frac{1}{2}}^{LLF} - g\left(C_{i,j}^{0} - C_{i,j}^{1y}\right) - g\left(C_{i,j}^{0} + C_{i,j}^{1y}\right)\right) \tag{4.10c}$$

In Eq. (4.10), $f_{i+1/2\,,j}^{LLF}$, $f_{i-1/2\,,j}^{LLF}$, $g_{i,j+1/2}^{LLF}$ and $g_{i,j-1/2}^{LLF}$ are inter-elemental advective fluxes at eastern, western, northern and southern face-centres that are evaluated by numerical flux functions, denoted by f^{LLF} and g^{LLF}, based on the Local Lax Friedrich (LLF) Riemann solver (Kesserwani et al., 2008) that generally has the better positivity-preserving properties than other Riemann solver (Zhang and Shu, 2011). However, these inter-elemental fluxes as well as the inner-elemental fluxes ($f(C) = \bar{u}\,C$ and $g(C) = \bar{v}\,C$) in Eqs. (10b-c) involve the slope coefficients $C_{i,j}^{1x}$ and $C_{i,j}^{1y}$ that may need to be limited, to avoid any spurious oscillations, and corrected to avoid any possibility to predict negative concentrations. Therefore, after applying local slope limiting to the slope coefficients $C_{i,j}^{1x}$ and $C_{i,j}^{1y}$ (Ayog et al., 2021), the positivity correction of Cockburn and Shu (1998) is also applied. This correction is achieved by potentially altering the magnitudes of the slope coefficients, that could occur when $C_{i,j}^{0}(t) - \left|C_{i,j}^{1x}(t)\right| - \left|C_{i,j}^{1y}(t)\right| < \frac{1}{2\sqrt{3}} C_{i,j}^{0}(t)$, by multiplying the slope coefficients $C_{i,j}^{1x}$ and $C_{i,j}^{1y}$ by the following positivity preserving factor, P_f:

$$P_f = \frac{1}{2\sqrt{3}} \frac{C_{i,j}^{0}(t)}{\left|C_{i,j}^{1x}(t)\right| + \left|C_{i,j}^{1y}(t)\right|} \tag{4.11}$$

Moreover, as shown in Figure. 4.2, face-centres between two adjacent elements are classified into three scenarios of: (1) a face-centre, separating non-cylinder elements (green lines); (2) a face-centres separating cylinder elements (blue lines); and (3) a face-centre shared by a cylinder element and a non-cylinder element (pink lines). The advective numerical fluxes $f_{i+1/2\,,j}^{LLF}$, $f_{i-1/2\,,j}^{LLF}$, $g_{i,j+1/2}^{LLF}$ and $g_{i,j-1/2}^{LLF}$ evaluation is scenario-specific and it suffices to describe it for $f_{i+1/2\,,j}^{LLF}$ at the face-centre $(x_{i+1/2}, y_j)$ located between elements $Q_{i,j}$ and $Q_{i+1,j}$, since $f_{i-1/2\,,j}^{LLF}$, $g_{i,j+1/2}^{LLF}$ and $g_{i,j-1/2}^{LLF}$ can be evaluated in a similar way.

In scenario (1), the advective numerical flux $f_{i+1/2\,,j}^{LLF}$ should be computed using both limits of the approximate concentration solution, $C_h(x,y,t)$, at either side of $(x_{i+1/2}, y_j)$, based on the local characteristics speeds, or velocity magnitudes, extracted from the $\bar{u}$ and $\bar{v}$ maps. That is, $f_{i+1/2\,,j}^{LLF} = f^{LLF}(f_{i+1/2,j}^{-}, f_{i+1/2,j}^{+})$, where $f_{i+1/2,j}^{-} = \bar{u}_{i,j}\, C_{i+1/2,j}^{-}$ with $C_{i+1/2,j}^{-} = C_{i,j}^{0} + \sqrt{3}C_{i,j}^{1x}$ denoting the limit of $C_h(x,y,t)$ at non-cylinder element $Q_{i,j}$, and $f_{i+1/2,j}^{+} = \bar{u}_{i+1,j}\, C_{i+1/2,j}^{+}$ with $C_{i+1/2,j}^{+} = C_{i+1,j}^{0} - \sqrt{3}C_{i-1,j}^{1x}$ denoting the limit of $C_h(x,y,t)$ at the neighbour non-cylinder element $Q_{i+1,j}$ (see Figure. 4.2). In scenario (2), zero fluxes should be ensured by setting zero concentration and velocity components at both cylinder elements. In scenario (3), no-slip internal boundary conditions are applied to extrapolate the local characteristic speeds and concentration limits from the non-cylinder element into the cylinder element; that is, for example, assuming $Q_{i+2,j}$ to be a cylinder element located next to

the non-cylinder element $Q_{i+1,j}$ (see Figure. 4.2), the non-slip boundary conditions is applied at face-centre across $Q_{i+1,j}$ and $Q_{i+2,j}$ to set $C^{+}_{i+3/2,j} = C^{-}_{i+3/2,j}$ and $\bar{u}_{i+2,j} = -\bar{u}_{i+1,j}$ in order to evaluate $f^{LLF}_{i+3/2\,,j}$.

After the evaluation of the three discrete advective operators $\{L^{K,a}_{i,j}\}_K$, the discrete diffusive operator, $L^{0,d}_{i,j}$, should be evaluated over $Q_{i,j}$. This can be achieved by, first, appearing the terms $\partial D_t/\partial x$ and $\partial D_t/\partial y$, via the chain partial differentiation rule, in L^d, and then approximate them by a second-order finite difference discretisation to produce $L^{0,d}_{i,j}$ from the average concentration coefficients and the coefficients of the eddy-viscosity, as follows:

$$L^{0,d}_{i,j} = D_t|_{Q_{i,j}} \left(\frac{C^0_{i+1,j}(t) - 2C^0_{i,j}(t) + C^0_{i-1,j}(t)}{\Delta x^2} + \frac{C^0_{i,j+1}(t) - 2C^0_{i,j}(t) + C^0_{i,j-1}(t)}{\Delta y^2} \right) + \frac{D_t|_{Q_{i,j}} - D_t|_{Q_{i-1,j}}}{\Delta x} \frac{C^0_{i,j}(t) - C^0_{i-1,j}(t)}{\Delta x} + \frac{D_t|_{Q_{i,j}} - D_t|_{Q_{i,j-1}}}{\Delta y} \frac{C^0_{i,j}(t) - C^0_{i,j-1}(t)}{\Delta y} \tag{4.12}$$

It is commonly accepted to numerically discretise Eq. (4.12) by such a second-order central finite difference discretisation without slope limiter (Badrot-Nico et al., 2007; West et al., 2021). However, this discretisation has been adapted to the specific boundary treatments in respect of the scenarios (1) to (3).

For scenario (1), $L^{0,d}_{i,j}$ is directly evaluated, using Eq. (4.12), but must be set zeroed for scenario (2) and subjected to non-slip boundary conditions for scenario (3). That is, in the latter scenario, recalling the example shown in Figure. 4.2, $C^0_{i+2,j}$ and $D_t|_{Q_{i+2,j}}$ should be equated to $C^0_{i+1,j}$ and $D_t|_{Q_{i+1,j}}$, respectively. Once $L^{0,d}_{i,j}$ is evaluated, the total spatial operator $L^0_{i,j} = L^{0,a}_{i,j} + L^{0,d}_{i,j}$ should be used to update the average coefficient $C^0_{i,j}(t)$.

Now, the operators $\{L^K_{i,j}\}_K$ can be applied to update $\{C^K_{i,j}(t)\}_K$ by half of a time step $\Delta t/2$ in a first-order explicit Euler time-stage. The updated coefficients $\{C^K_{i,j}(t + \Delta t/2)\}_K$ are then employed to produce updated operators $\{L^K_{i,j}\}_K$, by reapplying Eqs. (4.10-12), for use to complete the second-stage of the Runge-Kutta scheme, thereby producing updated coefficients, $\{C^K_{i,j}(t + \Delta t)\}_K$.

After each calculation, the time step Δt must be selected as the minimum to satisfy the Courant-Friedrichs-Lewy condition with a Courant number c_r of 0.33 to ensure stability for the advective terms (Cockburn and Shu, 2001) as well as the Neumann analysis to ensure stability for the diffusion terms (Badrot-Nico et al., 2007; Noye and Tan, 1989). Therefore, the selection of the time-step follows:

$$\Delta t = \min\left(\frac{1}{2} \frac{\Delta x^2 \Delta y^2}{D_t|_{Q_{i,j}}(\Delta x^2 + \Delta y^2)}\,, c_r \frac{\Delta x}{|\bar{u}_{i,j}|}, c_r \frac{\Delta y}{|\bar{v}_{i,j}|} \right) \tag{4.13}$$

4.2.3 Code accessibility

Like the DG2-SWE solver, the DG2-ADE solver is also parallelised on graphics processing unit (GPU) to conduct fast simulation and has been integrated into the open source LISFLOOD-FP 8.0 hydraulic modelling framework. Appendix D provides the user guide of how to setup and run the DG2-ADE solver to reproduce solute transport within cylinder arrays on LISFLOOD-FP 8.0.

4.3 Validation of the DG2-ADE solver

This section covers the advection diffusion test cases without and without cylinders. In Section 4.3.1, the second-order accuracy of the DG2-ADE solver is verified for two theoretical test cases without a cylinder, and alongside alternative predictions by a second-order finite volume ADE solver, referred to as the FV2-ADE solver (Badrot-Nico et al., 2007). In Section 4.3.2, a diagnostic test case with a cylinder is designed to verify mass-conservation and positivity-preserving property of the DG2-ADE solver for the uniform D_t fields under different orders of magnitudes. The DG2-ADE simulated concentration fields are also qualitatively compared with the ones from a commercial software tool. Next, a test case involving an array of cylinders is considered to further validate the performance of the DG2-ADE solver. It is worth nothing that, except for the clear statement, the simulated concentration, C, is scaled with respect to the peak concentration value, C_{max}, becoming dimensionless relative concentration.

4.3.1 Advection diffusion test cases without cylinder

4.3.1.1 Order-of-accuracy

This is a well-known analytical test case of advection and diffusion of a solute (Noye and Tan, 1989). It considers a small rectangular domain 0 m $\leq x \leq$ 2 m and 0 m $\leq y \leq$ 2 m, here discretised with grids made of $N_x \times N_y$ =10 × 10, 20 × 20, 40 × 40 and 80 × 80 elements, respectively, to explore second-order convergence. The initial solute follows Gaussian-shaped field centred at (x_{gc}, y_{gc}) = (0.5 m, 0.5 m) with a height of 1, defined as:

$$C(x, y, t = 0) = \exp\left[-\frac{\left(x - x_{gc}\right)^2}{D_t} - \frac{\left(y - y_{gc}\right)^2}{D_t}\right] \tag{4.14}$$

where x_{gc} and y_{gc} denote the coordinates of the centroid of the concentration field. The solute spreads at the velocity of $\bar{u}$ = $\bar{v}$ = 0.8 m/s under a uniform D_t field of 0.01 m^2/s (Noye and Tan 1989). The simulation terminates at t = 1.25 s and the analytical solution is given as:

$$C(x, y, t) = \frac{1}{4t + 1}\exp\left[-\frac{\left(x - \bar{u} - x_{gc}\right)^2}{D_t} - \frac{\left(y - \bar{v} - y_{gc}\right)^2}{D_t}\right] \tag{4.15}$$

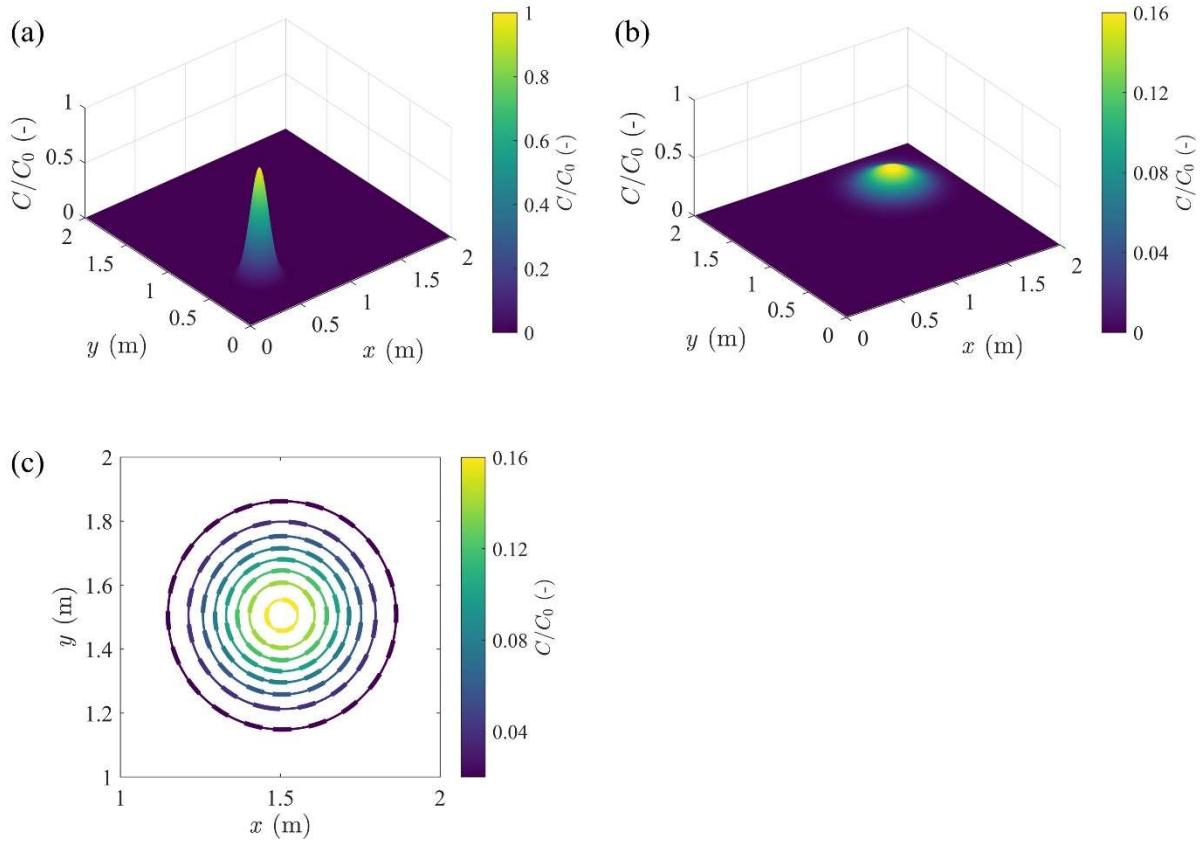

Figure 4.3. The DG2 solver simulated concentration fields on the grid enclosing 80 × 80 elements: (a) Three-dimensional perspective view of instantaneous concentration fields at t = 0 s; (b) Three-dimensional perspective view of instantaneous concentration t = 1.25 s; (c) The contour plots of the concentration fields from the DG2-ADE solver (solid line) and analytical solution (dashed line) at t = 1.25 s.

Figure. 4.3a and b shows the initial concentration field in the region (x, y) = (0 m, 1 m) × (0 m, 1 m) and the instantaneous simulated concentration field at t = 1.25 s in the region (x, y) = (1 m, 2 m) × (1 m, 2 m), on the grids enclosing 80 × 80 elements. To closely analyse the simulated concentration fields, Figure 4.3c compares the simulated concentration contour (solid line) with the analytical one (dashed line) at t = 1.25 s, showing that these two contours match perfectly (hard to see difference from two contours). This demonstrates that the DG2-ADE solver can properly reproduce the advection and diffusion of the solute over time.

Following Cockburn and Shu (2001), Duran and Marche (2014), and Kesserwani et al. (2018), the analysis of numerical order-of-accuracy is then performed based on the L^1-error, L^2-error and L^∞-error between the analytical and simulated concentrations, which are defined as below:

$$L^1 - error = \frac{1}{N_x \times N_y}\left(\sum_{i=1,j=1}^{N_x \times N_y} \left|C_{i,j}^{Num} - C_{i,j}^{Ana}\right|\right) \tag{4.16}$$

$$L^2 - error = \sqrt{\frac{\sum_{i=1,j=1}^{N_x \times N_y} \left(C_{i,j}^{Num} - C_{i,j}^{Ana}\right)^2}{N_x \times N_y}} \tag{4.17}$$

$$L^{\infty} - error = \left|C_{i,j}^{Num} - C_{i,j}^{Ana}\right| \tag{4.18}$$

where the superscript *Num* and *Ana* refer to the numerical solution and analytical solution, respectively. The rate of convergence is accordingly calculated as follows:

$$L^{1,2,\infty} - order = \frac{log\left(\frac{e_{finer}}{e_{current}}\right)}{log\left(\frac{M_{Q_{finer}}}{M_{Q_{current}}}\right)} \tag{4.19}$$

where e and M_Q denote the $L^{1,2,\infty}$-error values and the grid resolution; the subscript of *current* and *finer* represent the current grid and the immediate finer grid. The L^1-error, L^2-error and L^{∞}-error, along with the corresponding convergence rate produced by the DG2-ADE simulations for the different resolutions are listed in Table 4.1. The L^1-error, L^2-error and L^{∞}-error, as expected, decrease as the resolution increases and their orders are around 2, except for the L^1-order that shows an insignificant drop to 1.8 at the coarsest resolution of 10×10. This indicates the DG2-ADE solver delivers second-order accurate grid convergence in the prediction of concentration fields.

Table 4.1. L^1-error, L^2-error and L^∞-error and their corresponding order-of-accuracy predicted by the DG2-ADE solver for 2D advection diffusion test case of Noye and Tan (1989).

Grid. No	L^1-error	L^1-order	L^2-error	L^2-order	L^∞-error	L^∞-order
10 × 10	4.86×10^{-3}	-	1.54×10^{-2}	-	1.14×10^{-1}	-
20 × 20	1.39×10^{-3}	1.8014	3.76×10^{-3}	2.0339	2.36×10^{-2}	2.265
40 × 40	3.42×10^{-4}	2.0275	8.70×10^{-4}	2.1139	4.87×10^{-3}	2.278
80 × 80	8.14×10^{-5}	2.0701	1.99×10^{-4}	2.125	1.07×10^{-3}	2.191

4.3.1.2 Comparison with the FV2-ADE solver

Another analytical test case is considered (Badrot-Nico et al., 2007) to compare the performance of the DG2-ADE solver with respect to the numerical solution of an equally accurate FV2-ADE solver. The FV2-ADE solver has been formulated upon a similar computational stencil as the DG2-ADE solver, using the Monotonic Upstream-centred Scheme for Conservation Laws (MUSCL) discretisation of the advective transport, and the same finite difference method to integrate the diffusive transport operator. Compared to the test case in the previous section, a larger computational domain is considered in this section to evaluate the performance of the DG2-ADE and FV2-ADE solvers over a longer time simulation. The 2D computational domain is 0 m ≤ x ≤ 200 m and 0 m ≤ y ≤ 200 m, and the concentration field is advected at a constant velocity of $\bar{u}$ = 0.5 m/s and $\bar{v}$ = 0.3 m/s with a uniform D_t field of 0.01 m^2/s. The initial concentration is also featured by a Gaussian distribution, defined as:

$$C(x, y, t = 0) = \frac{1}{\sqrt{4\pi l_c^2}} \exp\left[-\frac{\left(x - x_{gc}\right)^2 + \left(y - y_{gc}\right)^2}{4l_c^2}\right] \tag{4.20}$$

where l_c =$\sqrt{10}$ (m) is the characteristic width of the concentration field and (x_{gc}, y_{gc}) = (75 m, 75 m) are the coordinates of the gravity centre at t = 0 s. Both DG2 and FV2-ADE solvers are run on the same grid resolution of Δx = Δy = 1 m for t = 200 s and the analytical solution at this output time follows:

$$C(x, y, t) = \frac{1}{\sqrt{4\pi(D_t t + l_c^2)}} \exp\left[-\frac{\left(x - \bar{u} - x_{gc}\right)^2 + \left(y - \bar{v} - y_{gc}\right)^2}{4(D_t t + l_c^2)}\right] \tag{4.21}$$

In Figure. 4.4, the contours of the instantaneous simulated concentration fields from DG2 (dashed line) and FV2 (dash-dotted line). The predictions by both ADE solvers are compared to the analytical solution (solid line) at t = 200 s. It can be observed that concentration fields simulated by both solvers can preserve an overall circular shape of the Gaussian curve, in good agreement with analytical solution. However, there is a difference in the vicinity of the gravity centre (x_{gc}, y_{gc}) = (175 m, 135 m), where the DG2-ADE solver predicts concentration contour that are closer to the analytical solution, compared to the predictions by the FV2-ADE solver. Also, the DG2-ADE solver predicts a higher peak concentration, of 0.0725, than that, of 0.0663, predicted by the FV2-ADE solver, which is

closer to the analytical peak value, of 0.081. This means that the DG2-ADE solver is more accurate than the FV2-ADE solver to produce second-order accurate solute transport predictions at coarser grid resolutions.

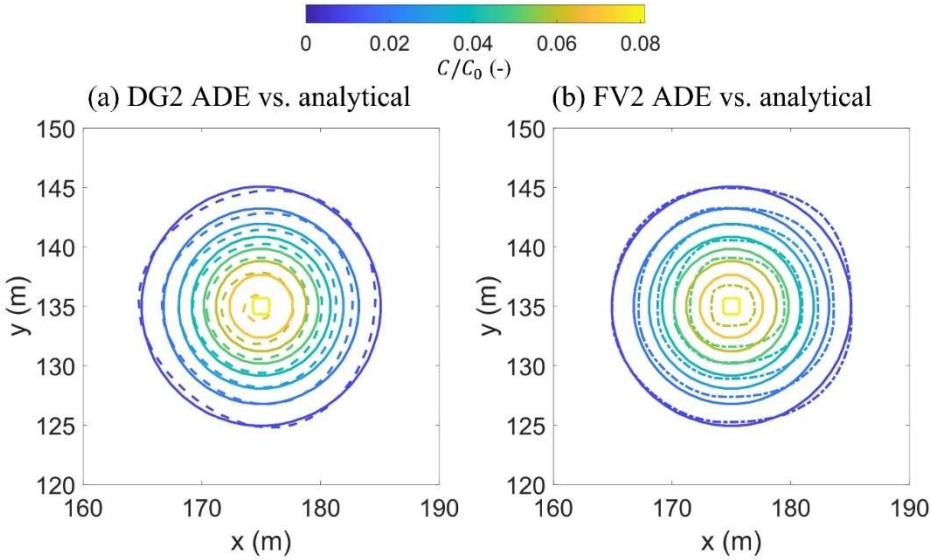

Figure 4.4. The contours of instantaneous 2D Gaussian concentration fields for a uniform D_t field of 0.01 m^2/s at t = 200 s. (a) the DG2-ADE solution (dashed line) *vs*. analytical solution (solid line); (b) the FV2-ADE solution (dash-dotted line) *vs*. analytical solution.

4.3.2 Advection diffusion test cases with cylinder(s)

After qualitative and quantitative assessments of the DG2-ADE solver for the theoretical test cases without the cylinder, this section considered the test case with cylinder(s). Since no experimental data are found for solute transport past one cylinder at low velocities, the DG2-ADE solver will be compared against the commercial software model, whose simulated $\bar{u}$ field and instantaneous concentration results were presented in Golzar (2018) and Stovin et al. (2022). Note that all D_t fields used in this section are not from the DG2-SWE simulations results, and DG2-SWE explicitly generated D_t fields will be present in next Chapter.

To conduct a side-by-side comparison, the DG2-ADE solver will utilize the same simulated fields of $\bar{u}$, $\bar{v}$ and D_t from the commercial modelling tool as inputs. The simulated $\bar{u}$ and $\bar{v}$ fields are obtained from the commercial software tool of ANSYS Fluent using 2D, second-order RANS model (i.e., herein referred to as Fluent RANS model) with Reynolds Stress Model (RSM) turbulence closure. An isotropic D_t field is implicitly calculated based on the built-in turbulence closure. The advection and diffusion of the solute is simulated by 2D second-order transient scalar transport in ANSYS Fluent (i.e., herein referred to as Fluent scalar transport model). In both flow and scalar transport simulations, the triangular mesh has a resolution of 0.2 mm near the cylinder, while it is 1 mm away from the cylinder. In the following Fluent simulations, all settings are in consistent with Golzar (2018) and Stovin et al.

(2022). It's worth noting that, since the DG2-ADE solver applies the uniform square grids, these Fluent simulated fields on triangular meshes will be interpolated to the square grid of 0.25d, in line with the choice in Section 3.3, based on the MATLAB `griddata` function (The MathWorkds Inc. 2023).

4.3.2.1 Solute transport past one cylinder

This test case considered the solute transport past one cylinder for uniform D_t fields under different order of magnitude. It has been designed with a threefold purpose: (a) to verify the mass-balance and positivity-preserving properties of the DG2-ADE solver; (b) to validate the DG2-ADE solver with respect to the commercial modelling tool; and (c) to investigate different temporal concentration profiles at different locations, such as within and outside wake zone (or referred to as recirculation zone).

This test case extends the classical steady flow past one cylinder of transitional R_{ed} = 250 explored in Section 3.3.1. The computational domain is 0.122 m × 0.128 m. A 2D Gaussian-shaped initial concentration field is introduced in front of the cylinder, located at (x, y) = (0.032 m, 0.064m), as depicted in Figure. 4.5, and its centroid is along the centreline:

$$C(x, y, t = 0) = \exp\left[-\frac{\left(x - x_{gc}\right)^2 + \left(y - y_{gc}\right)^2}{0.000001}\right] \tag{4.22}$$

where (x_{gc}, y_{gc}) = (0.02 m, 0.064m). As mentioned above, the flow fields, $\bar{u}$ and $\bar{v}$, fed into the DG2-ADE solver are from the Fluent RANS model. The streamline extracted from $\bar{u}$ and $\bar{v}$ are illustrated in Figure 4.5. A pair of symmetrical, recirculating vortices can be clearly seen in the wake zone. The flow drives the solute advecting from left to right towards the cylinder and further downstream of it. The presence of the cylinder produces velocity deficit downstream, and forms wake zone behind it, causing splitting of the solute and slowing down its movement. The diffusion of the solute depends on the uniform D_t field, and different values for uniform D_t are explored, of 10^{-6}, 10^{-5} and 10^{-4} m^2/s, which are the typical order-of-magnitude at low Re_d (Nepf, 1999; Nepf et al., 1997b).

The concentration profiles are recorded at three specified points (P1-P3) (see Figure 4.5) to investigate the impact of D_t on their time series within and outside the wake zone. Three specified point are located behind the cylinder and along the centreline. The coordinate of P1, located within the wake zone, is (x, y) = (0.038 m, 0.064 m), where $\bar{u}$ is at its minimum and negative. P2 is a point located at the edge of the wake zone where $\bar{u}$ equals zero, and its coordinate is (x, y) = (0.045 m, 0.064 m). As for P3, it's outside the wake zone at the coordinate of (x, y) = (0.054 m, 0.064 m). Simulations are run up to t = 8 s to allow the solute to move out of the computational domain for all D_t.

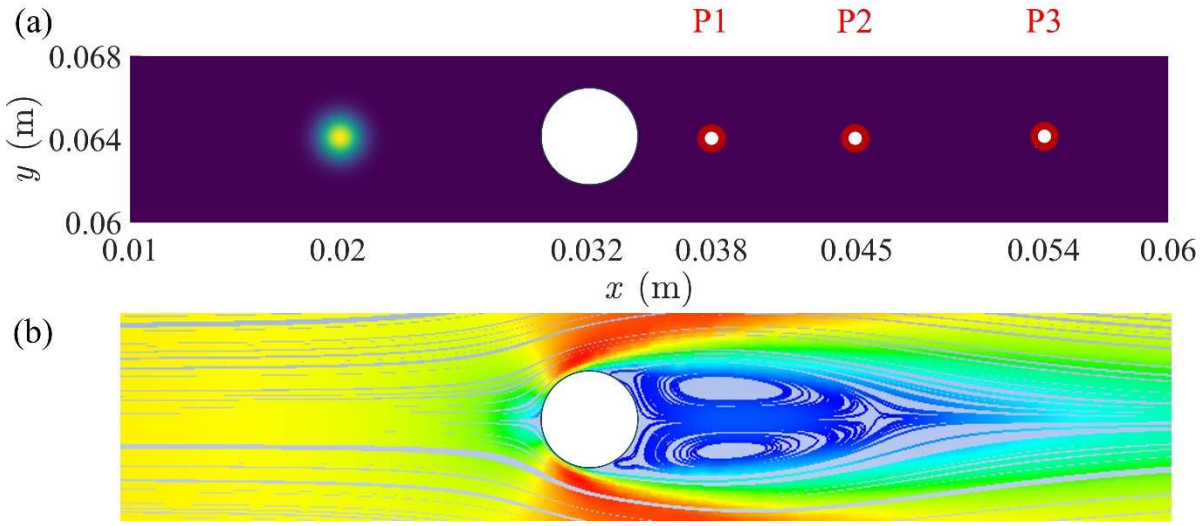

Figure 4.5. Solute transport past one cylinder: (a) Initial concentration field and three specified points along the centreline (P1: (x, y) = (0.038 m, 0.064 m); P2: (x, y) = (0.045 m, 0.064 m); P3: (x, y) = (0.054 m, 0.064 m)) used to record the time series of the simulated concentration; (b) the streamline of the simulated flow fields from Fluent RANS model.

The mass-balance property of the DG2-ADE solver is examined: the total mass of concentration fields at each time step are first extracted and the errors of the total mass between each two subsequent time steps are then calculated during $t \in [0\text{ s}, 1\text{ s}]$ when most of the solute does not exit from the outlet. The time series of total mass and mass errors between two subsequent time steps for different uniform D_t fields are plotted in Figure 4.6. The total mass does not change for $D_t = 10^{-6}$ and 10^{-5} m^2/s but the total mass decrease after 0.85 s for $D_t = 10^{-4}$ m^2/s as a part of solute starts to exit from the outlet. When the solute stays within the computational domain, the variation in mass error remains very small, around 10^{-13}. This indicates that the mass-balance is numerically preserved irrespective of the choice for D_t. Moreover, all minimum concentration values from the DG2-ADE simulations are non-negative despite the presence of the cylinder. This implies that the proposed DG2-ADE solver implementation is mass-conservative and preserves the positivity in solute concentration predictions past emergent cylinders.

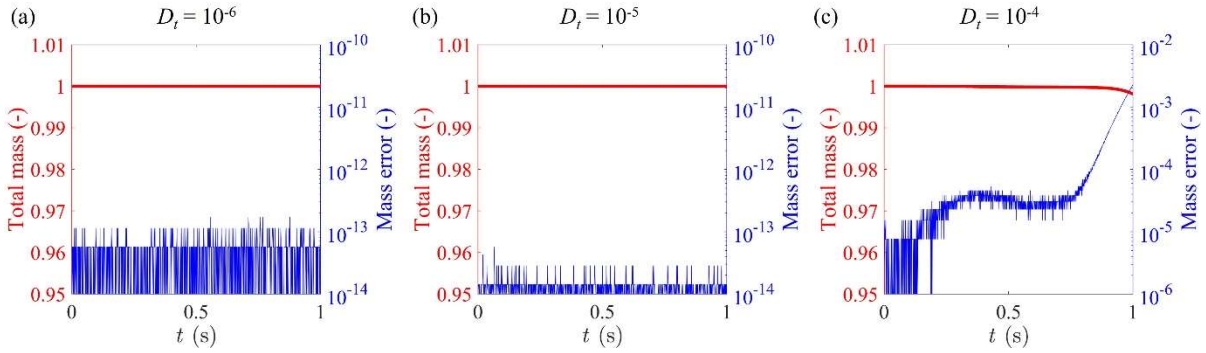

Figure 4.6. Solute transport past one cylinder: Time series of total mass (red lines) and mass errors between two adjacent time steps (blue lines) for different uniform D_t fields of (a) 10^{-6}, (b) 10^{-5}, and (c) 10^{-4} m^2/s during $t \in$ [0 s, 1 s].

Figure 4.7a-b compares the simulated instantaneous concentration fields obtained from Fluent scalar transport model and the DG2-ADE solver at t = 1 s for a uniform D_t field of 10^{-6} m^2/s. t = 1 s was selected as this is the time when most of the solute has passed the cylinder and stays within the computational domain. Both simulations show that the solute on the two lateral sides of the cylinder moves relatively rapidly than that behind the cylinder, due to the heterogeneity of the flow field. The distribution of the concentration is symmetric along the cylinder centreline. Further comparisons are made for the derived longitudinal sum and transverse sum of the concentration fields (Figures 4.7c and d) for this D_t. With all the lines setting upon each other, a good consistence between the DG2-ADE solver and Fluent model in the transverse and longitudinal spread of the solute is achieved. The above results confirms that the DG2-ADE solver can be used to model the variation of the solute concentration with flow past one single cylinder at this D_t.

A similar analysis is conducted for uniform D_t fields of 10^{-5} and 10^{-4} m^2/s. A good agreement has also been achieved between the DG2-ADE and Fluent scalar transport simulated concentration data for these two D_t values. In contrast to the uniform D_t field of 10^{-6} m^2/s (Figure 4.8-9 vs 4.7), the increase in D_t leads to a more pronounced spread. The solute exhibits the "Y" shaped distribution for D_t of 10^{-5} m^2/s, and 'heart' shape distribution for D_t of 10^{-4} m^2/s. Unsurprisingly, the spread effect in the transverse direction increases with the increase of D_t. This demonstrates that the DG2-ADE solver effectively reproduces the solute spread past the cylinder and provides a sensible response to D_t under different order-of-magnitude, as Fluent scalar transport model does.

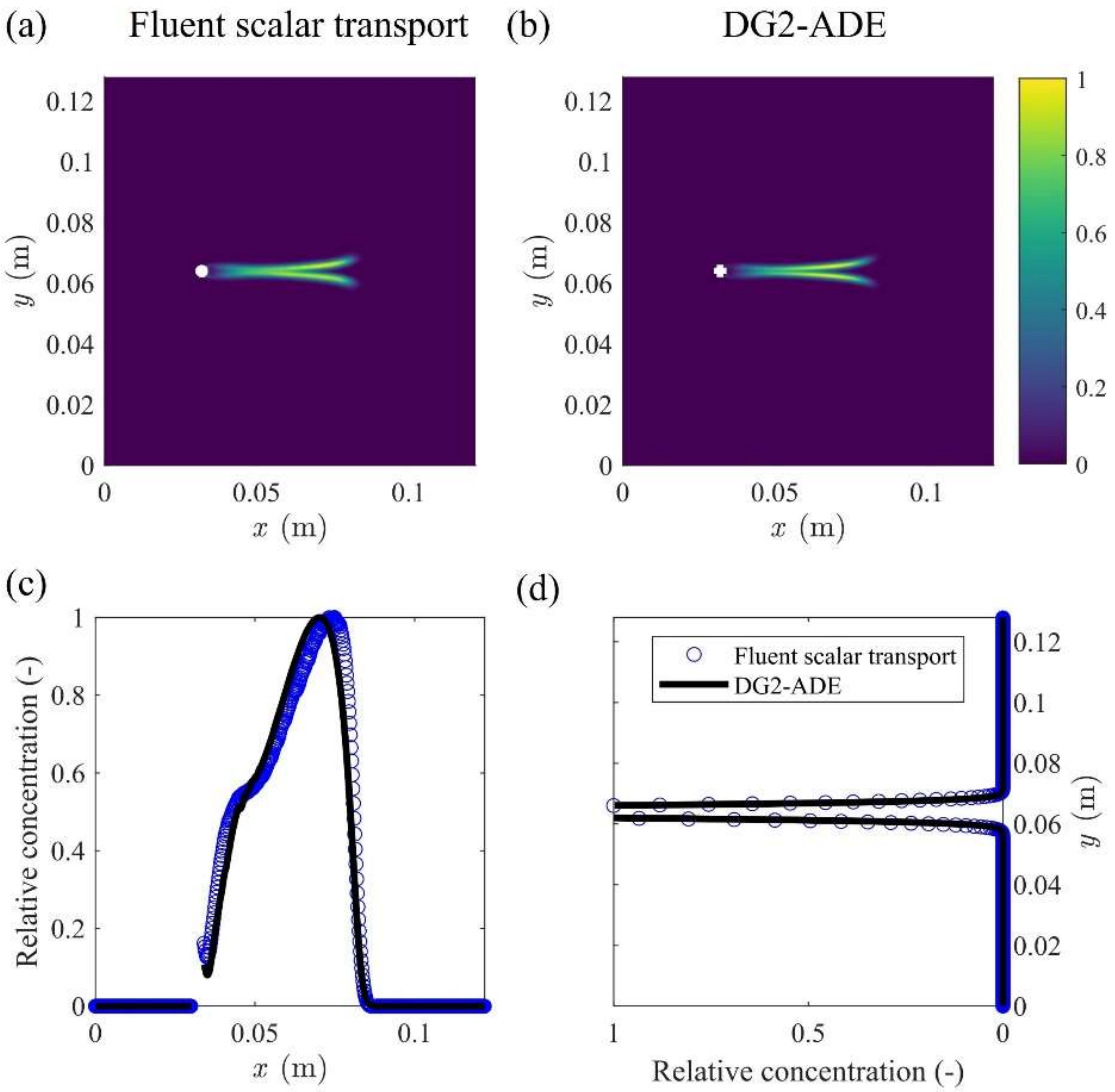

Figure 4.7. Solute transport past one cylinder at t = 1 s for D_t = 10^{-6} m^2/s: the simulated instantaneous concentration field from the Fluent scalar transport model and (b) the DG2-ADE solver; and (c) 1D longitudinal sum and (d) 1D transverse sum of the simulated instantaneous concentration fields from the Fluent scalar transport model (blue circle markers) and the DG2-ADE solver (black solid lines).

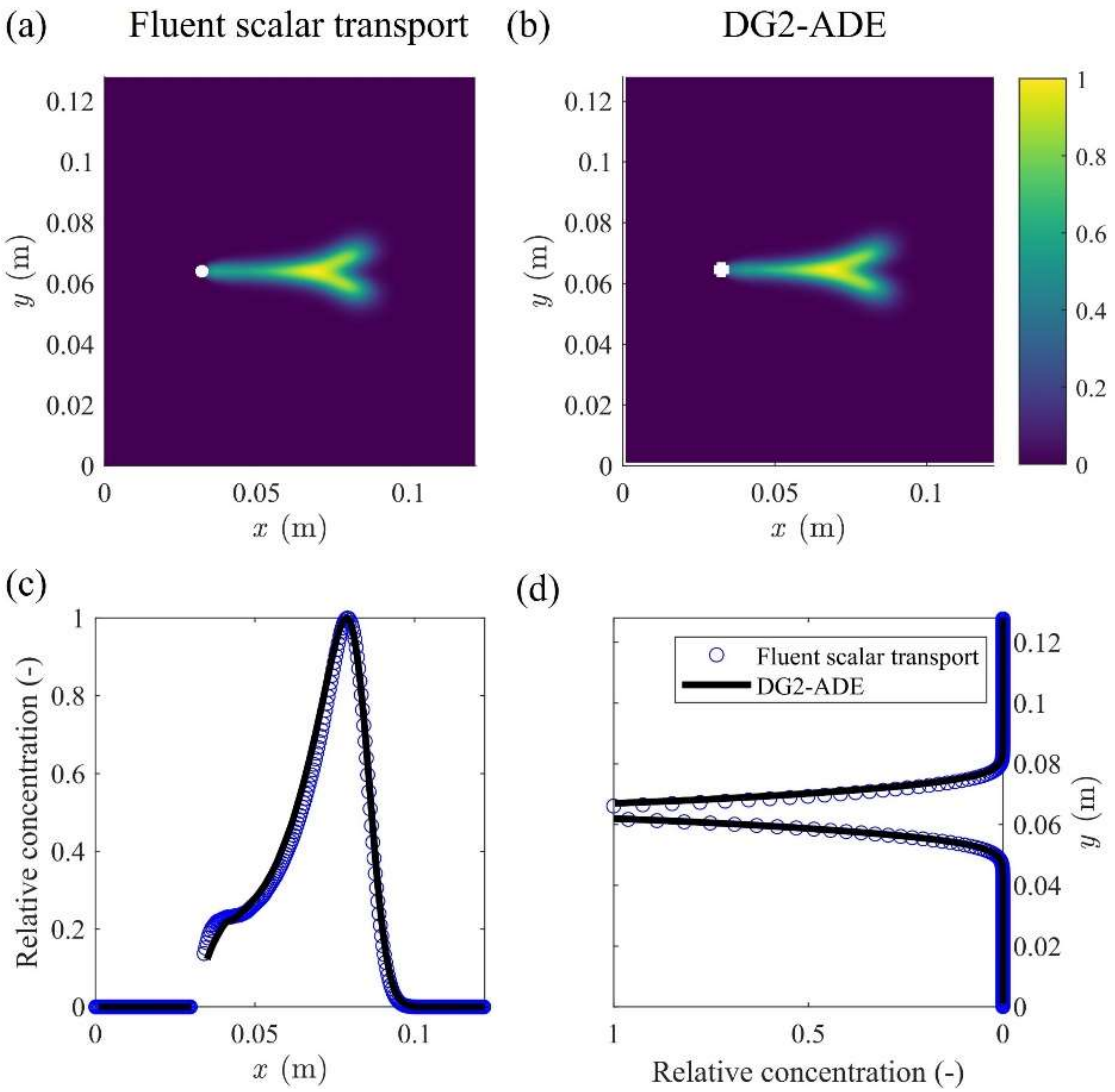

Figure 4.8. Solute transport past one cylinder at t = 1 s for D_t = 10^{-5} m^2/s: the simulated instantaneous concentration field from the Fluent scalar transport model and (b) the DG2-ADE solver; and (c) 1D longitudinal sum and (d) 1D transverse sum of the simulated instantaneous concentration fields from the Fluent scalar transport model (blue circle markers) and the DG2-ADE solver (black solid lines).

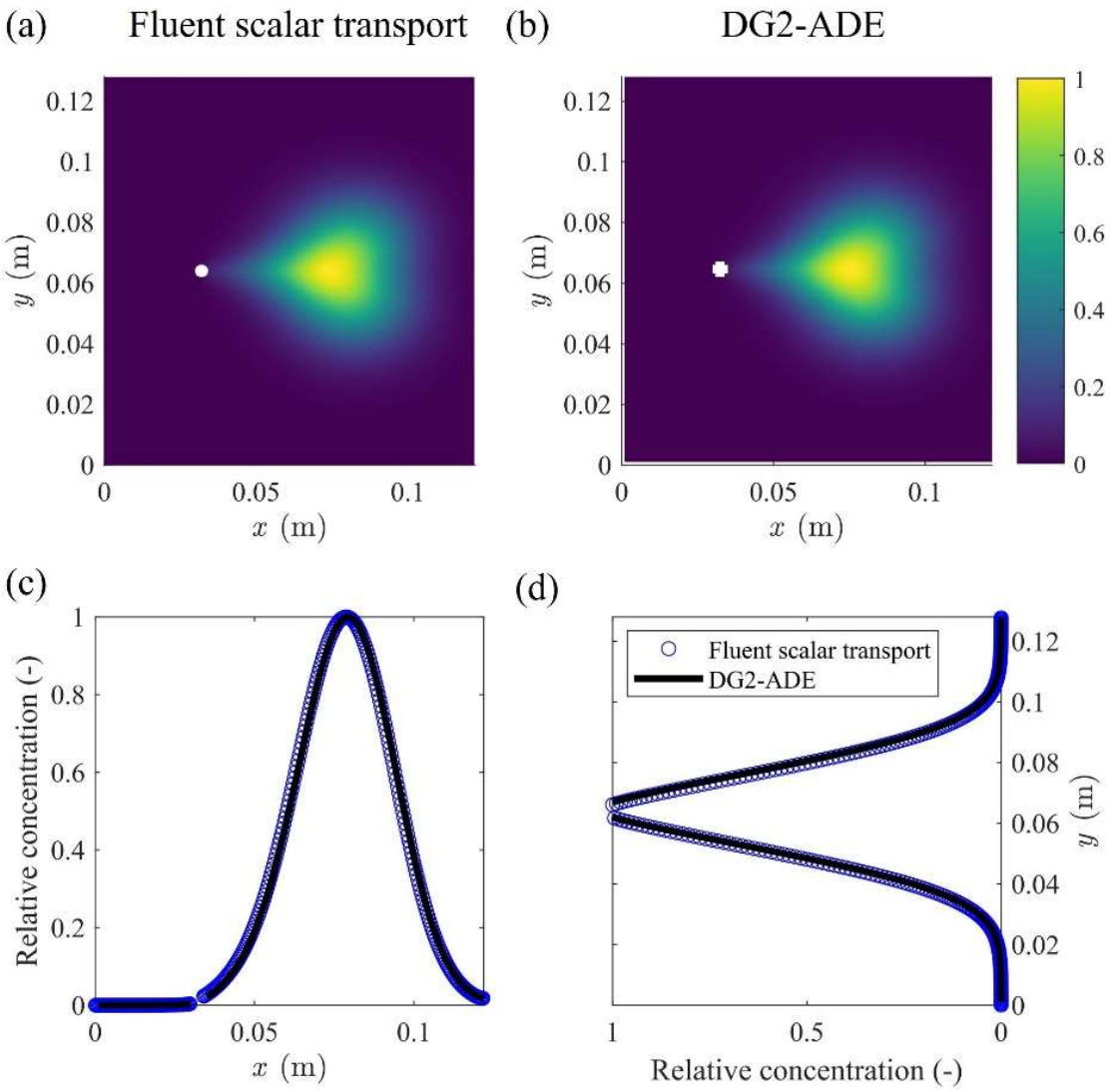

Figure 4.9. Solute transport past one cylinder at t = 1 s for D_t = 10^{-4} m^2/s: the simulated instantaneous concentration field from the Fluent scalar transport model and (b) the DG2-ADE solver; and (c) 1D longitudinal sum and (d) 1D transverse sum of the simulated instantaneous concentration fields from the Fluent scalar transport model (blue circle markers) and the DG2-ADE solver (black solid lines).

To analyse the impact of uniform D_t fields under different order-of-magnitudes on the solute spread, the time series of the simulated concentration profiles from the DG2-ADE solver and Fluent scalar transport model at three specified points (see Figure 4.5a) are extracted, as shown in Figure 4.10. It's worth noting that, to investigate the variation in concentration magnitude with time, in Figure 4.10a-c, the relative concentration is obtained by normalising all simulated temporal concentration profiles with the peak value of the initial (t = 0 s) concentration field. Still, the DG2-ADE simulated temporal concentration profiles are observed to closely follow the profiles from the Fluent scalar transport model, showing the same trend in the temporal concentration profiles.

In Figure 4.10a-c, for all three D_t values, the highest one of 10^{-4} (black markers and lines) enables the solute to reach all three specified points first, whereas the lowest D_t of 10^{-6} (red markers and lines) causes the solute to take more time to arrive at all three specified points last. It's also interesting to find that, under the same flow field, the centroids of the temporal concentration profiles at all three specified points change with the uniform D_t fields under different order-of-magnitude. In addition, Figure 4.10a shows that, the higher the D_t, the shorter the time required for the solute to decrease to zero. This means that, once trapped within the wake zone (P1), the solute becomes increasingly difficult to escape from as D_t decreases.

The mass of the solute at the specified points can also be analysed by integrating their temporal concentration profiles (i.e., the area below the profiles). It can be seen that, for the highest D_t of 10^{-4}, the mass of the solute concentration decrease as the solute moves farther away from the cylinder (from P1 to P3). This may be because under the same flow field, compared to the lower D_t, the higher D_t has more tendency to lead the solute spread in both longitudinal and transverse directions (recall Figure 4.9). This means that, a larger area is occupied by the solute leading to a lower concentration at a specified single point in the area. As D_t decrease to the lowest value of 10^{-6}, the solute movement is less affected by D_t, resulting in less solute spread and hence accumulating along the centreline (recall streamline in Figure 4.5b). Therefore, for this D_t, the mass is relatively higher at points farther away from the cylinder.

Overall, the qualitative comparison shows that the DG2-ADE simulation results are in good agreement with those from Fluent scalar transport model. This means that the DG2-ADE solver can provide reasonable mixing process behind the cylinder.

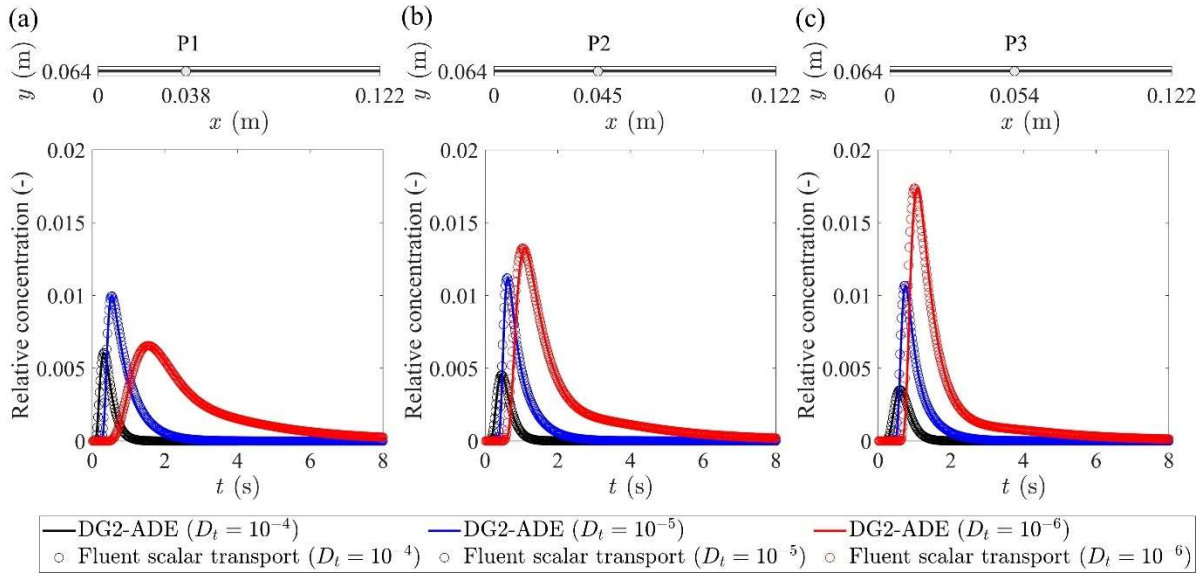

Figure 4.10. Time series of the simulated temporal concentration profiles from the Fluent scalar transport model (circle markers) and the DG2-ADE solver (solid lines) at three specified points of (a) P1: (x, y) = (0.038 m, 0.064 m); (b) P2: (x, y) = (0.045 m, 0.064 m); and (c) P3: (x, y) = (0.054 m, 0.064 m) for uniform D_t fields under different order of magnitude of 10^{-4} (black), 10^{-5} m^2/s (blue) and 10^{-6} (red) m^2/s. The upper part of each sub-plot shows the positions of three specified points (grey dots) and the flow is from left to right.

4.3.2.2 Solute transport within an array of cylinders

In this subsection, the DG2-ADE solver is further validated based on a test case of solute transport within the cylinder array, where the distribution of D_t field is non-uniform. This case considered the solute moves along the centreline (from left to right as shown in Figure 4.11) and past a large number of randomly distributed cylinders with d = 8 mm in a 1 m × 1 m computational domain at turbulent R_{ed} of 500. The DG2-ADE solver utilized the simulated fields of $\bar{u}$,$\bar{v}$ and D_t from Fluent RANS model as the inputs.

Figure 4.11 compares the DG2-ADE simulated instantaneous concentration fields at t = 4 s (first column), 8 s (second column) and 12 s (third column) with the ones from Fluent scalar transport model. The DG2-ADE solver is seen to the capture the movement and spread of the solute and the impact of cylinders on splitting the solute as it travels through the computational domain. Qualitatively, the DG2-ADE simulated instantaneous concentration fields are still close to Fluent scalar transport simulations at various time instants.

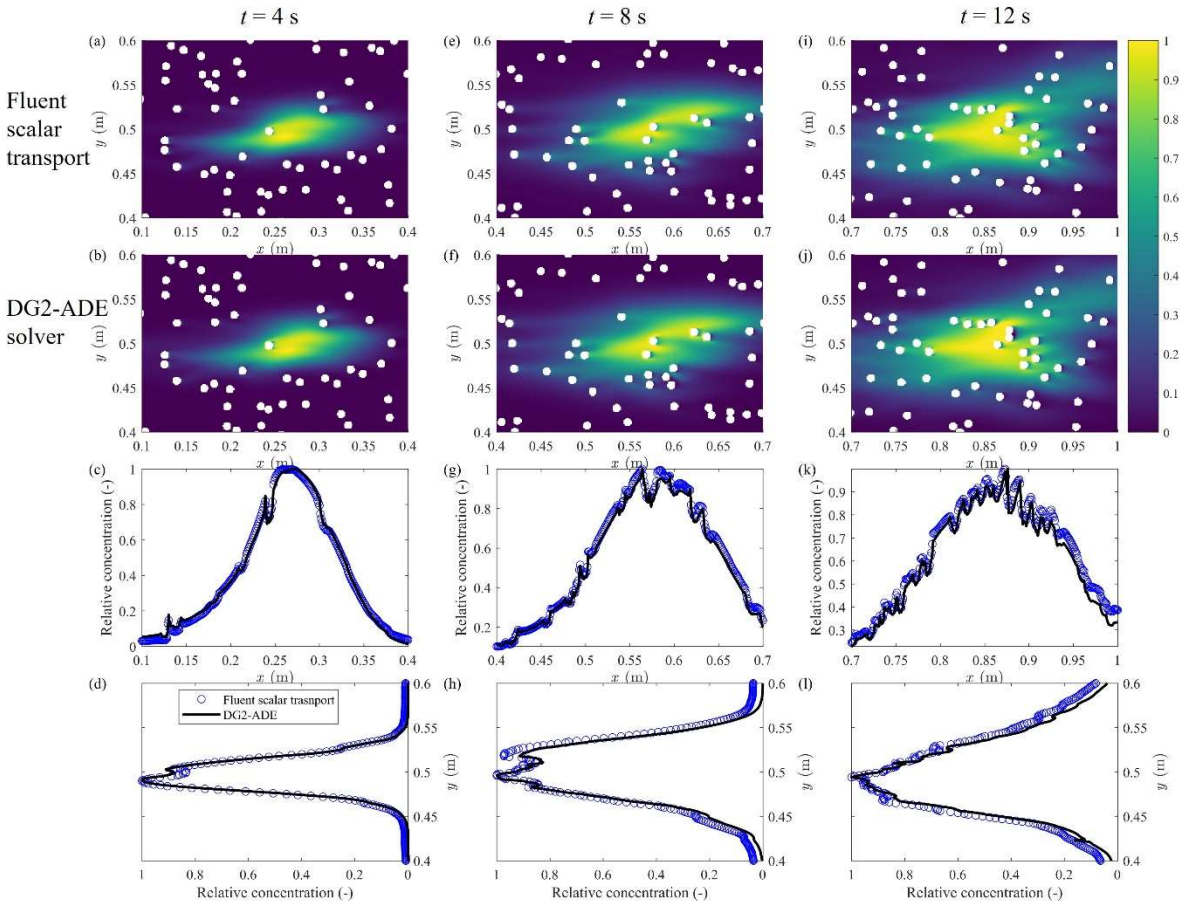

Figure 4.11. Zoom in view of 2D simulated instantaneous concentration maps from Fluent scalar transport model (first row) and from the DG2-ADE solver (second row), and 1D longitudinal sum (third row) and 1D transverse sum (fourth row) of the simulated instantaneous concentration fields from the Fluent scalar transport model (blue circle markers) and the DG2-ADE solver (black solid lines) at t = 4 s (first column), 8 s (second column) and 12 s (third column).

To closely analyse the performance of the DG2-ADE solver, the longitudinal sum and transverse sum of the concentration fields are compared with those from Fluent, showing good agreement (see the third and fourth rows in Figure 4.11). The discontinuities observed in these concentration profiles from both simulations arise from the presence of cylinders. This further demonstrates the capability of the DG2-ADE solver to accurately reproduce solute transport past one cylinder or an array of cylinders, using uniform D_t fields under different orders of magnitude or a non-uniform D_t field.

The analysis in Section 4.3.2 confirms that the DG2-ADE solver can effectively predict the solute movement past cylinders, supported by robust integration of cylinders with suitable treatment to conserve the mass and the positivity in the predictions. This also suggests the potential of combining this DG2-ADE solver with the DG2-SWE simulations for laboratory-scale applications involving cylinders featuring different configurations under different flow regimes.

4.4 Concluding remarks

This chapter developed a two-dimensional (2D), GPU-parallelised, second-order discontinuous Galerkin (DG2) solver of the advection diffusion equation (ADE) designed for simulating solute transport within cylinder arrays. This DG2-ADE solver is linked to the 2D, GPU-parallelised DG2 solver of Shallow Water Equations (SWE), taking this DG2-SWE solver's simulation results as initial conditions which are the time-averaged flow fields and turbulent diffusivity, D_t, field. The development of the DG2-ADE solver was presented with a focus on the explicit generation of D_t from the DG2-SWE solver's average and slope coefficients based on the concept of eddy viscosity. The discretization of the ADE was then introduced alongside the treatment to handle the presence of the cylinder and to preserve the simulated concentration fields positive.

After the development, the theoretical test cases of advection diffusion without the cylinder was used to validate the DG2-ADE solver's second-order accuracy and to demonstrate its superiority to the equally-accurate conventional FV2-ADE solver. The performance of the DG2-ADE solver was further evaluated based on the advection diffusion test cases with one cylinder and within an array of cylinders. Also, the DG2-ADE simulated concentration fields were qualitatively compared with the ones from the commercial modelling tool. The results show that the DG2-ADE solver is able to preserve the mass-balance and positivity of the simulated concentration, even with the presence of the cylinders. It can also reproduce the close temporal and spatial distribution of the solute around cylinder(s) as the commercial modelling tool when taking the same inputs. It can therefore be concluded that, combining with the DG2-SWE solver, the DG2-ADE solver has the potential to be applied to the simulate laboratory-scale solute transport within cylinder arrays.

5 Application of the DG2-ADE solver to reproduce laboratory-scale experiments

5.1 Chapter overview

This chapter, which seeks to address Objective 3, extends the validation of the newly developed DG2-ADE solver in Chapter 4. The DG2-ADE solver is applied to reproduce the laboratory-scale experiments with a focus on identifying its potential for simulating solute transport within arrays of emergent, randomly distributed cylinders. The experiments are briefly described in Section 5.2, and Section 5.3 introduces the numerical settings of the DG2-SWE and DG2-ADE solvers, including the choice of the grid resolution and the area for analysis, as well as the simulation termination criteria. In Section 5.4, the DG2-SWE simulations are calibrated to obtain the physically accepted $\bar{u}$, $\bar{v}$, and D_t fields for use to make the subsequent DG2-ADE simulations. The DG2-ADE solver is then validated by comparing the simulated concentration profiles with reference to the experimental measurement (Section 5.5), and by reproducing the contribution of D_t to both longitudinal and transverse dispersion processes in Section 5.6. The associated GPU-runtime costs are also presented in Section 5.7 to uncover the computational efficiency. Discussion and concluding remarks are made at the end of this chapter.

5.2 Overview of the experiments

The experiments of solute transport were conducted at the University of Warwick in a 15 m long and 0.3 m wide flume, fitted with emergent cylinders that were randomly distributed (Corredor-Garcia, 2023; Sonnenwald et al., 2019c). For each experiment, uniform flow conditions were ensured at a water depth of 0.15 m, by adjusting the longitudinal bed-slope, S_{0x}, and the tailgate of the flume. Three experiments were considered, for different quasi-steady flow cases, covering laminar, transitional and turbulent regimes.

The array of the emergent cylinders considered two different configurations for the cylinders' diameters, d, and their solid volume fraction (cylinder density), Φ. The first configuration used d = 4 mm and Φ = 0.005 inserted into a 2.5 m × 0.3 m baseplate, which was then duplicated to cover a length of 7.5 m (see Figure 5.1a) over which the laminar and transitional flow cases were generated. These flow cases had inflow velocities, U_∞, of 0.0145 and 0.0682 m s^{-1}, with cylinder Reynolds numbers, R_{ed}, of 53 and 250, respectively. The Manning's roughness coefficient, n_M, was estimated to 0.045 m$^{1/6}$ from known hydraulic and experimental parameters, using the Manning's friction formula with the longitudinal bed slope S_{0x} = 0 m m^{-1} for the laminar flow case and $S_{0x} \simeq 4.6 \times 10^{-4}$ m m^{-1} for the transitional flow case. The second

configuration used d = 8 mm and Φ = 0.027, inserted into a shorter baseplate, of 1 m × 0.3 m, with 8 replicas to cover a length of 9 m (see Figure 5.1b), along which the turbulent flow case was generated. This flow case had an inflow of U_∞ = 0.0556 m s^{-1}, with R_{ed} = 450. Due to the missing data on $S_{0x,}$ the $n_M \simeq$ 0.054 was estimated using alternative empirical formula involving the effects of emergent cylinders (Luhar and Nepf, 2013; Shields et al., 2017).

The experimental solute transport was generated by manually injecting a pulse of dye into the upstream of the flume (red dot in Figure 5.1), 4 m from which four equidistant fluorometers were installed. The fluorometers were located in the middle of the flume's width and at mid-depth below the water surface. Also, the area between the dye injection and the first fluorometer included emergent cylinders to ensure that the experimental flows were fully developed and the dye got well mixed before reaching the first fluorometer. From the four fluorometers, point measurements of the dye were conducted to record temporal concentration profiles at a frequency of 1 Hz. Using optimised routing of two consecutive concentration profiles, reach-scale longitudinal dispersion coefficients, D_x, were derived for three identical reaches, where a reach is here the distance between two subsequent fluorometers (Sonnenwald et al., 2019c). For each flow case, the experiment was repeated thrice and nine experimental D_x values were thus obtained that will be reported in terms of mean and standard deviation.

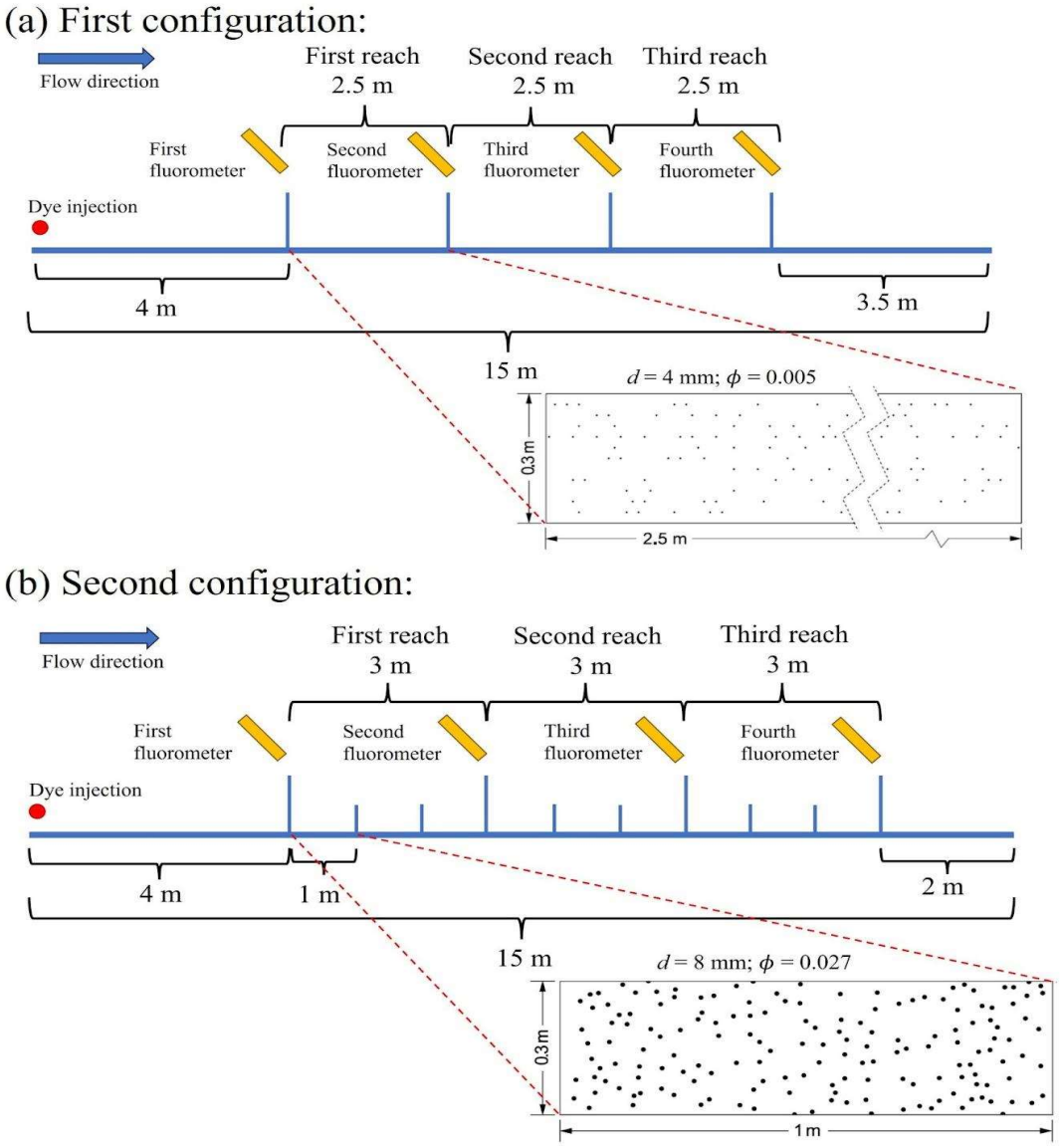

Figure 5.1. A schematic plan view of the experimental setup for solute transport within a 15 m long flume: (a) the first configuration involves randomly distributed d = 4 mm cylinders with Φ = 0.005, and (b) the second configuration involves randomly distributed d = 8 mm cylinders with Φ = 0.027. The location of fluorometers used to measure the temporal concentration profiles and the spatial distribution of cylinders for two configurations are also provided (Sonnenwald et al., 2019c).

5.3 Numerical simulation considerations

The grid resolution is commonly scaled to the characteristics length, d (Jiang and Cheng, 2017; Rajani et al., 2009; Uzun and Hussaini, 2012). When using complex turbulent flow simulators, such as Large Eddy

Simulation (LES) and Reynolds-Averaged Navier-Stokes (RANS) models, a fine grid resolution below 0.005d, is considered to capture the turbulence effects within the flow field predictions (Alfonsi, 2009; Qu et al., 2013). However, such effects can be approximated more efficiently, at up to 50-fold coarser resolution, by the inviscid DG2-SWE solver to simulate laminar to low-turbulence wakes past cylinders (Kesserwani et al., 2023; Sun et al., 2023). At such a coarse resolution, of 0.25d, it was shown that the numerical error dissipation introduced by the inviscid DG2-SWE solver can fairly approximate low-turbulence effects (Kesserwani et al., 2023) and can render the simulations of the laminar and transitional flow cases in less than a day [on an Nvidia GeForce RTX 3090 GPU card (Sun at al., 2023)]. Therefore, within the scope of this application, the 0.25d grid resolution will be retained to make the DG2-SWE and DG2-ADE simulations.

To minimise the runtime cost for the DG2-SWE simulations, the DG2-SWE solver was set-up and run to simulate the flow fields inside the three identical reaches. Figures 5.2 and 5.3 are illustrative examples of the DG2-SWE simulated time-averaged longitudinal velocity field and turbulent kinetic energy field (TKE) along the three reaches at $R_{ed} = 53$ with $n_M = 0.045$. The property of self-similarity in the DG2-SWE predicted flow fields and TKE fields was analysed across the three reaches, as a metric to identify that the numerically predicted flow is also fully-developed (Zampiron et al., 2023). Since this property could only be ensured across the second and third reaches (maximum error difference below 10^{-4}), the DG2-SWE simulation outputs in the first reach were excluded. As a result, the DG2-ADE simulations were conducted along the second and third reaches. In this computational domain, the left and right boundaries were treated as wall, or non-slip, boundary conditions (i.e. as for the cylinder treatments, see Section 4.2) and the outlet was given a slip downstream boundary condition.

For all three flow cases, the DG2-SWE simulations were set to terminate when extra 50 vortex shedding cycles were completed after reaching a converged, quasi-steady state (Rajani et al., 2009). On the other hand, the DG2-ADE solver simulations were set to stop when the solute exited the outlet.

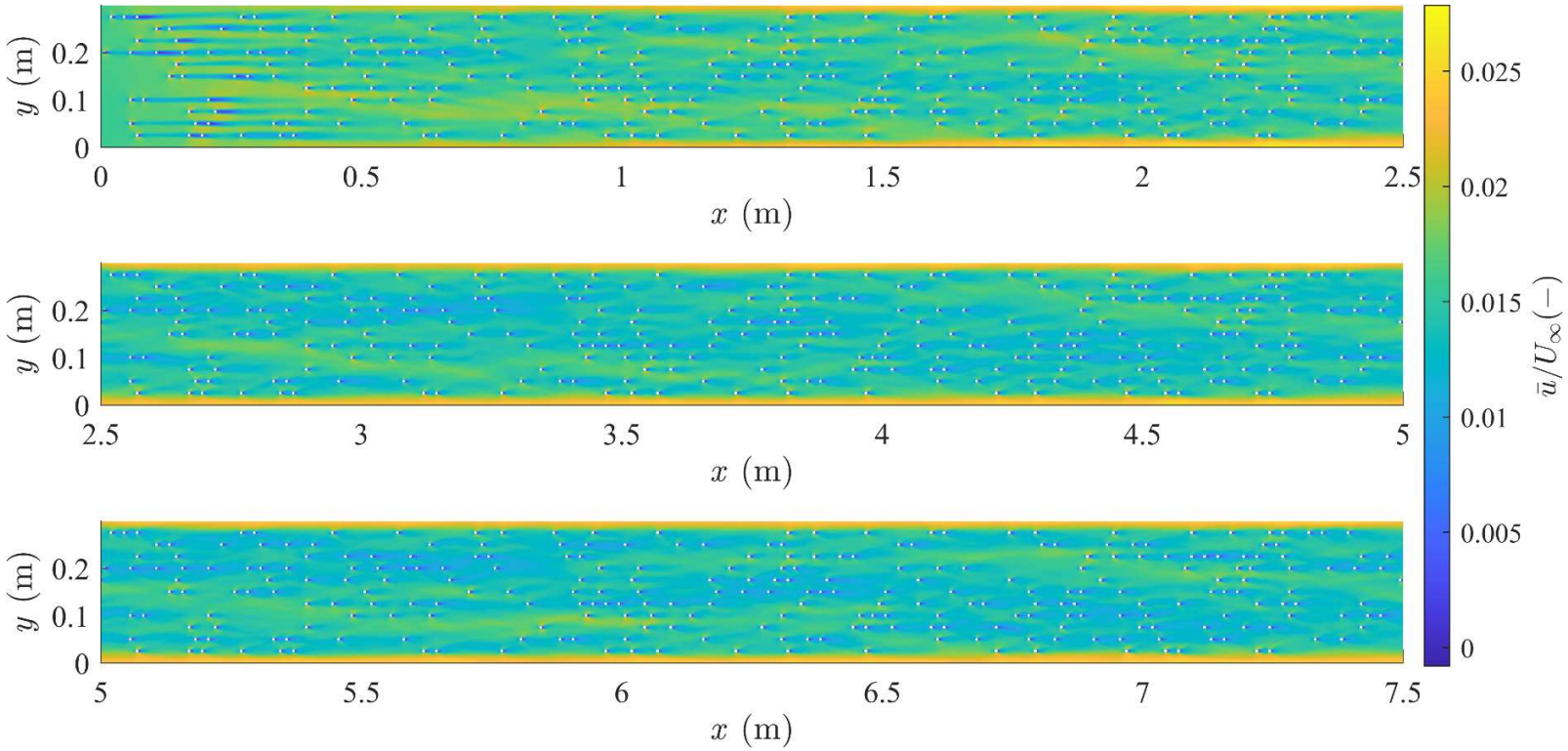

Figure 5.2. An illustrative example of the time-averaged longitudinal velocity field from the DG2-SWE simulation at R_{ed} = 53 with n_M = 0.045 m$^{1/6}$.

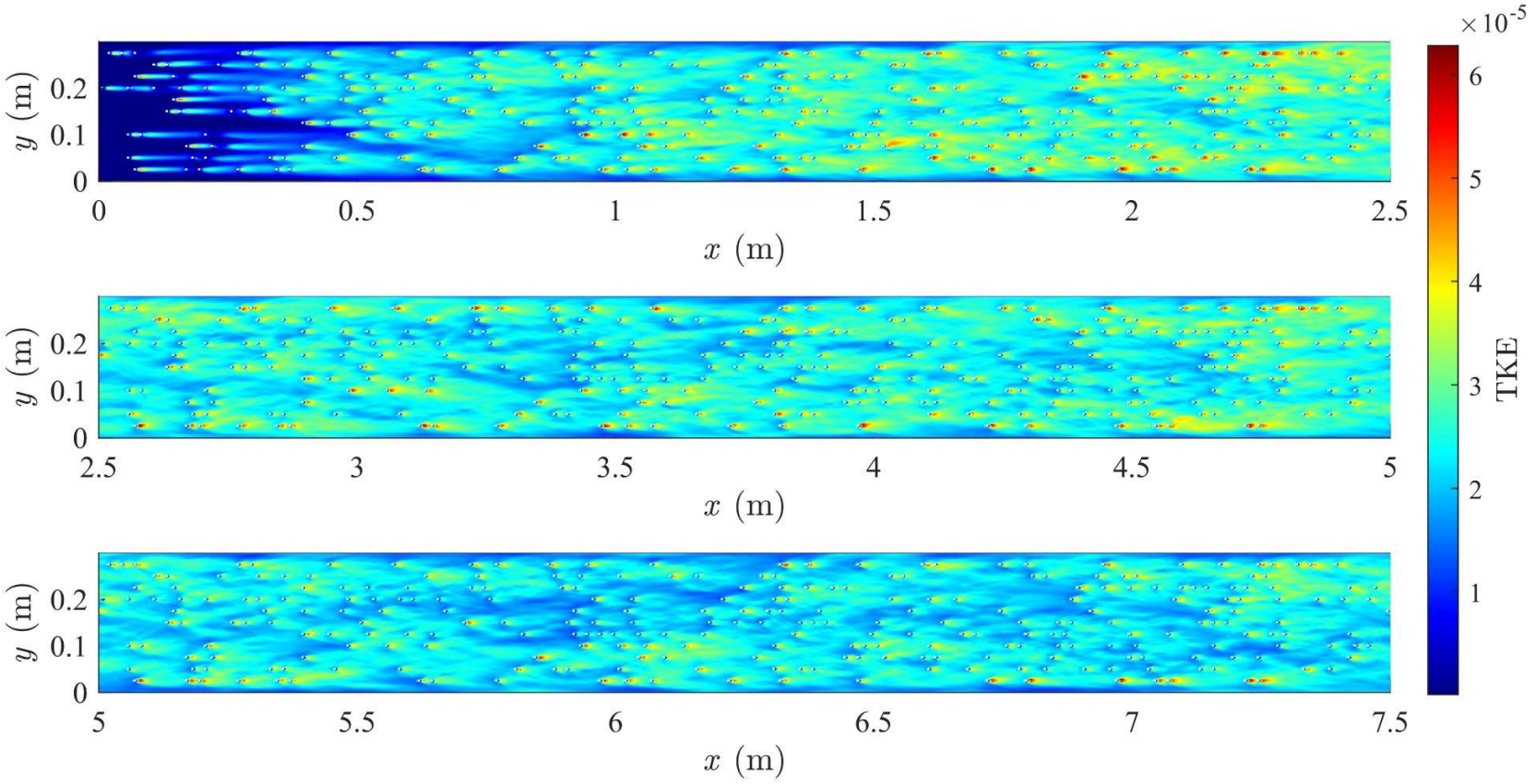

Figure 5.3. An illustrative example of turbulent kinetic energy field from the DG2-SWE simulation at R_{ed} = 53 with n_M = 0.045 m$^{1/6}$.

5.4 Calibrated DG2-SWE simulations

Since $\bar{u}$ and $\bar{v}$ maps can be approximated from the time-averaged parts of longitudinal and transverse velocity components, they can be reliably approximated by the DG2-SWE simulations (Section 3.3). However, the TKE and D_t maps, which are obtained from the fluctuating parts of longitudinal and transverse velocity components (Section 4.2.1), can be overly estimated. This can be seen in Figure 5.4, that shows, as highlight in yellow, when the DG2-SWE simulations used the experimentally estimated n_M (Section 5.2), TKE and D_t maps for all three flow cases are overly estimated than the physically acceptable ranges reported in the published literature. These overestimations may be expected to occur with the DG2-SWE simulations excluding any kinematic and eddy viscosity effects. This can be alleviated by using calibrated DG2-SWE simulations with artificially increased n_M to bring the average magnitudes of the predicted TKE and D_t maps down to the physically acceptable ranges. This is because the increased n_M reduces the amplitude of the fluctuating parts of longitudinal and transverse velocity components, thereby bringing down the TKE and D_t. However, since the increased n_M leads to increase in the water depth and the decrease in velocity, minor adjustments to longitudinal bed slope S_{0x} are made by incorporating the artificially increased n_M into Manning's formula (Eq. 2.4) to numerically preserve the uniform flow condition as illustrated in Figure 5.5. This ensures that the predictions of the flow fields remain unaffected.

Figure 5.4 presents the relationship between the average predicted TKE fields (Figure 5.4a), the average predicted D_t fields (Figure 5.4b), and the associated n_M values for all three flow cases. The data for the flow with R_{ed} = 53 is plotted using pink square markers and for the flow with R_{ed} = 250 is plotted using blue circle markers, whereas that for the flow with R_{ed} = 450 is plotted using green triangular markers. Shaded zones represent the physically acceptable ranges and order-of-magnitude for the averages of TKE and D_t fields. The range of TKE is estimated based on an empirical equation (Eq. 2.3) characterised by flow velocity, cylinder diameter, and density of cylinder arrays (Tanino and Nepf, 2008a). The order of magnitude of D_t is estimated based on the experimental measurements and numerical simulation (for R_{ed} = 450) reported in previous studies (Nepf, 1999; Nepf et al., 1997b; Stovin et al., 2022; Tanino and Nepf, 2008a).

The calibrated DG2-SWE simulations considered increasing the n_M values starting from those initially estimated from the experiments, up to identifying $n_M \in \{0.14, 0.15, 0.16\}$ as suitable values for the laminar and transitional flow cases, and $n_M \in \{0.15, 0.16, 0.17\}$ for the turbulent flow case. As shown in Figure 5.4a, first, the suitability of these values was identified upon retrieving the ranges of average predicted TKE field reported in Tanino and Nepf (2008a), between: 4.49×10^{-6} and 6.18×10^{-6} m^2 s^{-2} for the laminar flow case, 9.93×10^{-5} and 1.37×10^{-4} m^2 s^{-2} for the transitional flow case, and 2.33×10^{-4} and

3.13×10^{-4} m^2 s^{-2} for the turbulent flow case. Then, as can be seen in Figure 5.4b, the suitability of these values was also verified in retrieving the ranges of orders of magnitudes for the average predicted D_t fields reported in Tanino and Nepf (2008a) and White and Nepf (2003), between: 10^{-6} and 10^{-5} m^2 s^{-1} for the laminar flow case, and 10^{-5} and 10^{-4} m^2 s^{-1} for the transitional and turbulent flow cases.

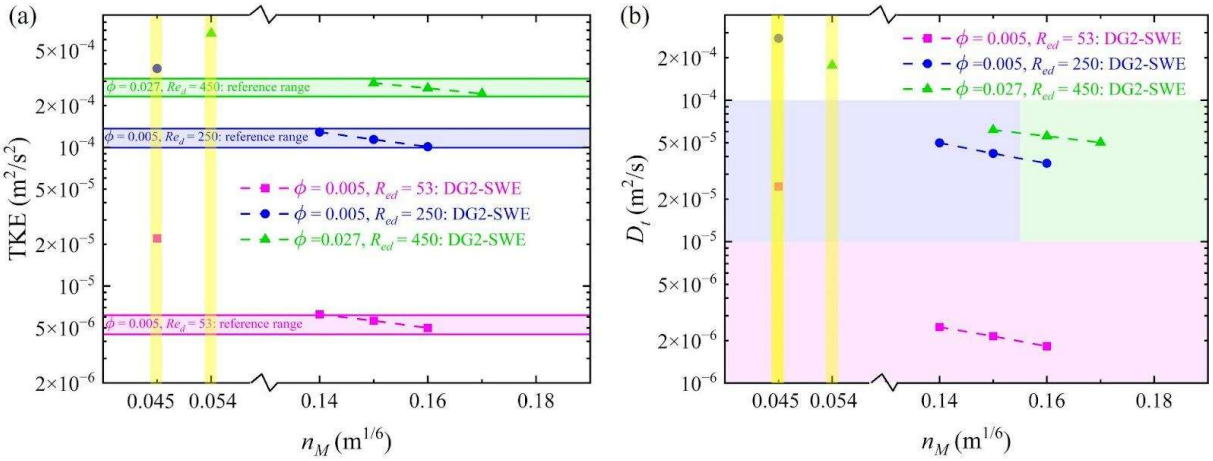

Figure 5.4. The variation trend of the average magnitudes of (a) turbulence kinetic energy (TKE) and (b) turbulent diffusivity D_t from the DG2-SWE simulations under different n_M values at Φ = 0.005, R_{ed} = 53 (pink square markers), Φ = 0.005, R_{ed} = 250 (blue circle markers), and Φ = 0.027, R_{ed} = 450 (green triangular markers) with respect to the reference ranges (shaded zones).

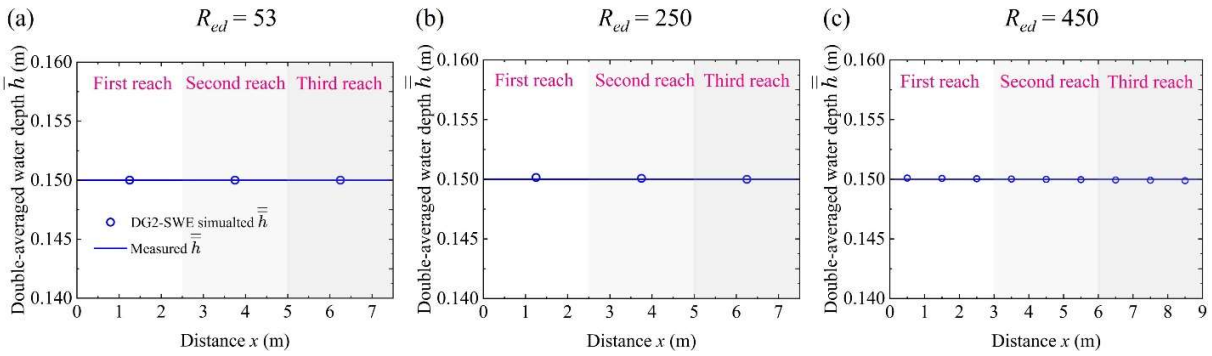

Figure 5.5. Double (time and space) averaged water depth from the measurement (solid lines) and the DG2-SWE simulations (circle markers) along three reaches at (a) Φ = 0.005, R_{ed} = 53, (b) Φ = 0.005, R_{ed} = 250, and (c) Φ = 0.027, R_{ed} = 450.

The simulated $\bar{u}$ and $\bar{v}$ fields remain unaffected by the use of identified n_M values, preserving as close (L^1-norm error), correlated (R^2 coefficient) and directionally aligned [relevance index (R_I)] fields with respect to the reference flow fields (Sun et al. 2023). That is, for the laminar, transitional and the turbulent

flow cases: L^1-norm error changes from 0.2 to 0.185, from 0.13 to 0.14, from 0.18 to 0.16; R^2 changes from 0.65 to 0.64, from 0.72 to 0.69, and from 0.84 to 0.86; and, R_I remains unchanged around 0.99, 0.99 and 0.93, respectively. This is also in line with the earlier findings in Cea et al. (2007). Moreover, using n_M of 0.15 $m^{1/6}$ is appropriate for all three flow cases. The advantage of using single n_M of 0.15 $m^{1/6}$ is it is desirable for a wider engineering application to the cases where the configuration is similar to the current study and the experimental data is not available for systematic calibration.

The suitability of using the same n_M = 0.15 $m^{1/6}$ for all three flow cases can further be qualitatively confirmed by comparing localised patterns of predicted scaled TKE fields to measured TKE fields, within two localities in the last two reaches: one behind an isolated cylinder (Figure 5.6a-d) and another featured by two consecutively aligned cylinders (Figure 5.6e-h). Figure 6a-d compares the simulated scaled TKE patterns behind one isolated cylinder for all three flow cases to the one from measurement (Lee et al., 2023). A remarkable similarity can be observed among the three simulated scaled TKE patterns, which is expected to occur as the scaled TKE patterns resemble at various R_{ed} (Singh and Mittal, 2004). The simulated scaled TKE patterns also match the measurement, although their peaks are located farther from the cylinder centre. In Figure 5.6e-h, the simulated scaled TKE patterns between two consecutive cylinders are compared with the measurement presented by Uzun and Yousuff Hussaini (2012), showing generally good agreement. However, the elliptical areas with a relatively large magnitude of TKE in the simulated patterns appear to be over-expanded. This discrepancy may be due to the fact that the DG2-SWE solver tends to produce elongated wake areas. From these calibrated DG2-SWE simulations with n_M of 0.15 $m^{1/6}$, their associated $\bar{u}$, $\bar{v}$ and D_t fields were produced and used to achieve the DG2-ADE simulations to simulate the concentration profiles at the third and fourth fluorometers, located in the second and third reaches (Section 5.5 and 5.6).

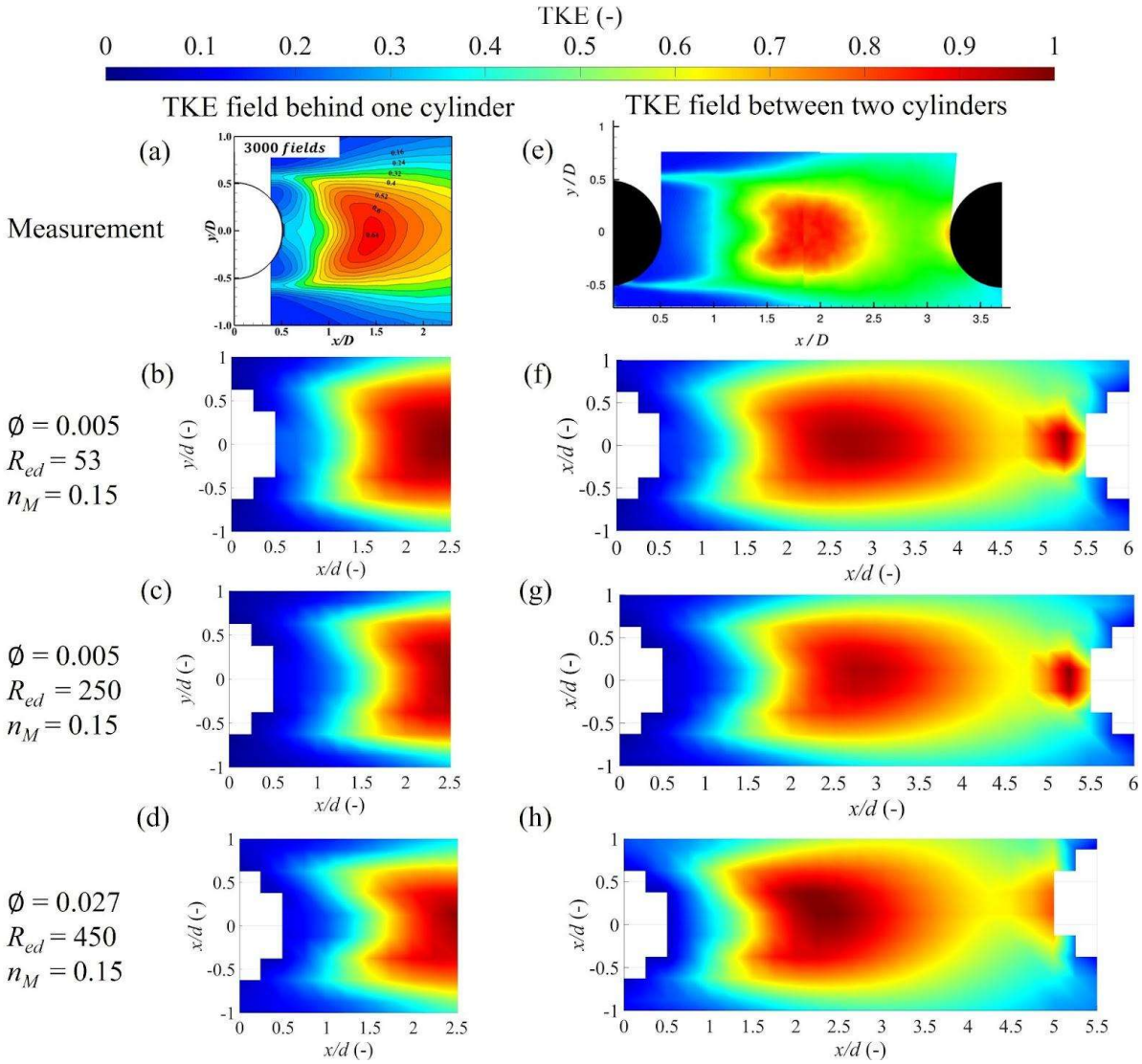

Figure 5.6. Illustrative example of the scaled turbulent kinetic energy (TKE) map behind one isolated cylinder (left panel) and between two consequent cylinders (right panel): the upper panel displays the experimentally measured TKE maps (Lee et al., 2023; Uzun and Yousuff Hussaini, 2012). The remaining panels show the TKE from the calibrated DG2-SWE simulations with n_M = 0.15 m$^{1/6}$.

5.5 DG2-ADE simulation results: comparing with experimental measurements

The performance of the DG2-ADE solver applied to reproduce experimental solute transport within cylinder arrays is first evaluated by comparing its prediction with the measurement. Its inlet boundary condition is set as the measured line source concentration profiles at the second fluorometer (i.e., at x = 2.5 m and 3 m for the first and second configuration, respectively). Like the point measurement conducted

in the experiment, the DG2-ADE simulated temporal concentration profiles at the third and fourth fluorometers (i.e., at x = 5 m and 7.5 m for the first configuration and x = 6 m and 9 m for the second configuration) were obtained by spatial averaging within a 3 × 3 grid sampling window. The centre grid of the sampling window is in the middle of the width of the last two reaches. From these simulated temporal concentration profiles, the simulated D_x can also be derived in the same manner as the measurement.

Figure 5.7 compares the DG2-ADE simulated concentration profiles (red dashed lines) with the measured ones (black solid lines) for all three flow cases. Generally, the DG2-ADE solver yields a very good fit to the reference measurement, and this can be confirmed by the goodness-of-fit coefficient R_t^2 values, all of which are greater than 0.97. For the laminar flow case with R_{ed} = 53, Figure 5.7a shows that the DG2-ADE simulated concentration profiles are in close agreement with the measured profiles. The simulated D_x is inside the range of derivation of the measured D_x. As for the transitional flow case with R_{ed} = 250 (Figure 5.7b), the simulated concentration profile also resembles the measured ones. However, the peak values of the simulated profiles are higher than that of the measurement, meaning that the simulated spread effect is relatively less significant than the actual. This can also manifest in the simulated D_x, which is lower than the measured D_x but still remains within the same order-of-magnitude.

For the second configuration, in the turbulent flow case with R_{ed} = 450, Figure 5.7c presents two distinct DG2-ADE simulated concentration profiles generated using two different inputs. One input is from the calibrated DG2-SWE simulation with n_M of 0.15 $m^{1/6}$, which is the same as the laminar and transitional cases. The other one is the $\bar{u}$, $\bar{v}$, and D_t fields (extrapolated to the uniform square grids with same resolution as DG2-SWE, 0.25d) from the Fluent RANS Reynolds Stress Model simulation (Stovin et al., 2022). When using the inputs from the calibrated DG2-SWE simulations, R_t^2 between the simulated and measured slightly decreases to 0.97, lower than that for laminar and transitional cases. This implies that the DG2-SWE solver might exhibit relatively less predictive capability for the turbulent case involving complex interactions with densely distributed cylinders. Compared to the measured profiles, the DG2-ADE simulated profiles are nearly parallel but located in front of it, probably owing to the simulated double-averaged velocity being faster than the actual. Moreover, the peak concentration from the simulation is lower than that from the measurement, showing that using such inputs might lead to an overestimation of the spread effect. The simulated D_x, albeit higher than the average of the measured D_x, still falls within the acceptable range.

On the other hand, when using the inputs ($\bar{u}$, $\bar{v}$, and D_t fields) from the Fluent RANS simulations (blue dashed lines), the DG2-ADE simulated temporal concentration profiles are in a good agreement with the measured ones. Also, these DG2-ADE simulated profiles are close to the ones from Fluent scalar transport model (Figure 4 in Stovin et al. (2022)) even at the coarser grid resolution than Fluent model (10-

fold coarser near the cylinders and twice coarser away from the cylinders). Moreover, the corresponding DG2-ADE simulated D_x is closer to the average of the measured D_x, compared to the simulated D_x using the inputs from the calibrated DG2-SWE simulation. This demonstrates that the DG2-ADE solver can be an accurate and efficient alternative to simulate solute transport past cylinders, and taking the inputs from the advanced turbulent models could enhance prediction accuracy.

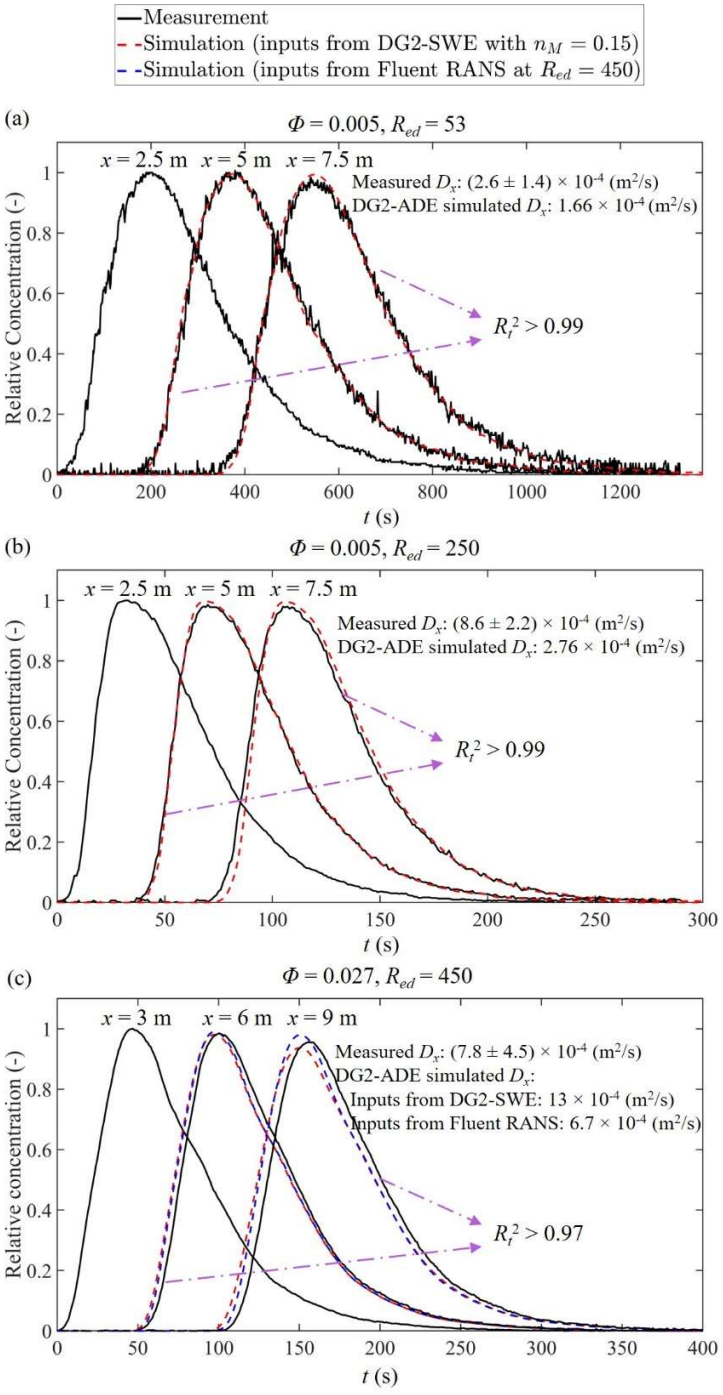

Figure 5.7. Time series extracted from the experimental measured and the DG2-ADE simulated concentration fields at (a) $\Phi = 0.005$, $R_{ed} = 53$, (b) $\Phi = 0.005$, $R_{ed} = 250$, and (c) $\Phi = 0.027$, $R_{ed} = 450$: black lines are the measured concentration profiles and among them, the profiles along $x = 2.5$ m for (a) and (b) and along $x = 3$ m for (c) are set as the inlet boundary conditions; red dashed lines represent the simulated profiles taking the inputs from the calibrated DG2-SWE simulations with $n_M = 0.15$ m$^{1/6}$, while the blue dashed lines in (c) denote the simulated profiles taking the inputs from the Fluent RANS model.

5.6 Application to further predict transverse dispersion coefficients

The capability of the DG2-ADE solver in characterising longitudinal and transverse mixing is further assessed by quantifying both D_x and the reach-scale transverse dispersion coefficient, D_y. To permit exploration of transverse dispersion, a Gaussian distributed concentration field was considered here as the initial condition (equivalent to the pulse point source injection) for all three flow cases. The initial concentration field was defined as $C(x, y, t = 0) = \exp[-((x - x_c)^2 + (y - y_c)^2)/10^{-5}]$, where x_c and y_c represent the coordinates of the centroid of the concentration fields in x- and y- directions. The centroid was set to be located in the middle of the flume's width and 0.03 m away from the second fluorometer (i.e., x_c = 2.53 m and y_c = 0.15 m for the first configuration, and x_c = 3.03 m and y_c = 0.15 m for the second configuration), to keep initial concentration away from the cylinders for all three flow cases.

The $\bar{u}$, $\bar{v}$, and D_t fields fed into the DG2-ADE solver were the same as the ones used in the previous subsection 5.5. The DG2-ADE simulation results taking inputs from the DG2-SWE solver were presented in the first three rows of Figure 5.8 for the three flow cases, while the DG2-ADE simulation results using the inputs from the Fluent RANS model for the turbulent case were shown in the last row of Figure 5.8.

Figure 5.8a-d presents the 2D instantaneous spatial distribution of the simulated solute when the solute moves around the second fluorometer (around 2.7 m for the first configuration and around 3.2 m for the second configuration). The impact of cylinders splitting the simulated solute can be clearly observed. Comparison between Figure 5.8a and 5.8b shows that under the same configuration, at higher R_{ed}, the transverse dispersion is expected to be more pronounced, due to the corresponding higher D_t. The different configurations of cylinder arrays also lead to a difference in the spatial distribution of the solute (see Figure 5.8a-b vs. 5.8c-d). Figure 5.8e-h displays the 2D instantaneous distribution of the solute when it moves around the third fluorometer (around 5.2 m for the first configuration and around 6.2 m for the second configuration). The simulated solute is, as expected, stretched more longitudinally and transversely as compared with the solute located around the second fluorometer (Figure 5.8e-h vs. 5.8a-d).

Figure 5.8i-l shows the time series of the concentration profiles transversely averaged along the cross-sections of x = 2.7 m and 5.2 m for the first configuration and of 3.2 m and 6.2 m for the second configuration. These temporal concentration profiles are used to derive D_x. It can be found that the simulated D_x is almost one order-of-magnitude greater than the simulated D_t, except for the transitional flow case (Figure 5.8j). However, the DG2-ADE solver also tends to underestimate D_x for this case, when taking the measured line source concentration profile as the inlet boundary condition (recall Figure 5.5b). Generally speaking, the DG2-ADE solver, either considering line source or equivalent point source injection, can

reproduce the expected contribution of D_t to the overall longitudinal dispersion process, that is, an approximate 10-fold ratio of D_x and D_t which was also well reported in Stovin et al. (2022).

Figure 5.8m-p displays the temporally averaged concentration profiles along the cross-sections of x = 2.7 m and 5.2 m for the first configuration and of 3.2 m and 6.2 m for the second configuration, which were used to obtain D_y. For all three flow cases, the simulated D_y is, as expected, close to D_t, meaning that transverse dispersion is almost totally composed of the effects of turbulent diffusion at the low cylinder density. In comparison to the first configuration (Figure 5.8m-n), more discontinuities are observed along the simulated concentration profiles for the second configuration (Figure 5.8o-p), attributed to the higher density of cylinders. Moreover, the simulated D_y for the second configuration is slightly higher than D_t. This is because, apart from D_t, the heterogeneity of flow fields induced by the cylinder also starts to contribute transverse dispersion as the cylinder density increases (Stovin et al., 2022; Tanino and Nepf, 2008a).

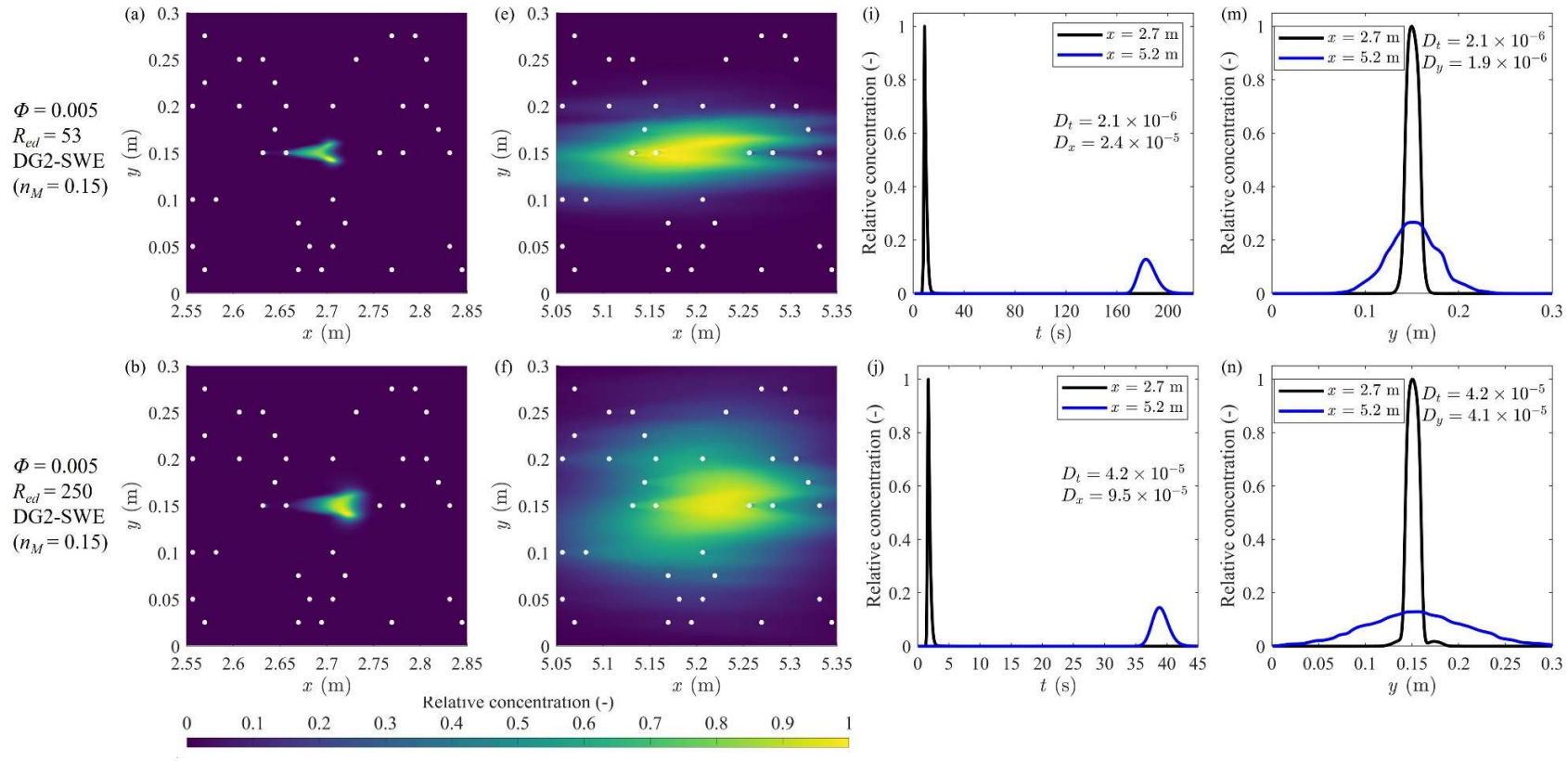

Figure 5.8. DG2-ADE simulated 2D instantaneous maps of solute concentration around the second fluorometers (first column, a-d) and third fluorometer (second column, e-h), and 1D temporal transversely averaged concentration profiles (third column, i-l) and spatial time-averaged concentration profiles (fourth column, m-p) extracted from the DG2-ADE simulations. The first three upper panels consider the inputs of flow and D_t fields from the calibrated DG2-SWE simulations with $n_M = 0.15$ m$^{1/6}$ at $\Phi = 0.005$, $R_{ed} = 53$ (first row), $\Phi = 0.005$, $R_{ed} = 250$ (second row), and $\Phi = 0.027$, $R_{ed} = 450$ (third row). The last lower panel considers the inputs from the Fluent RANS model (continued).

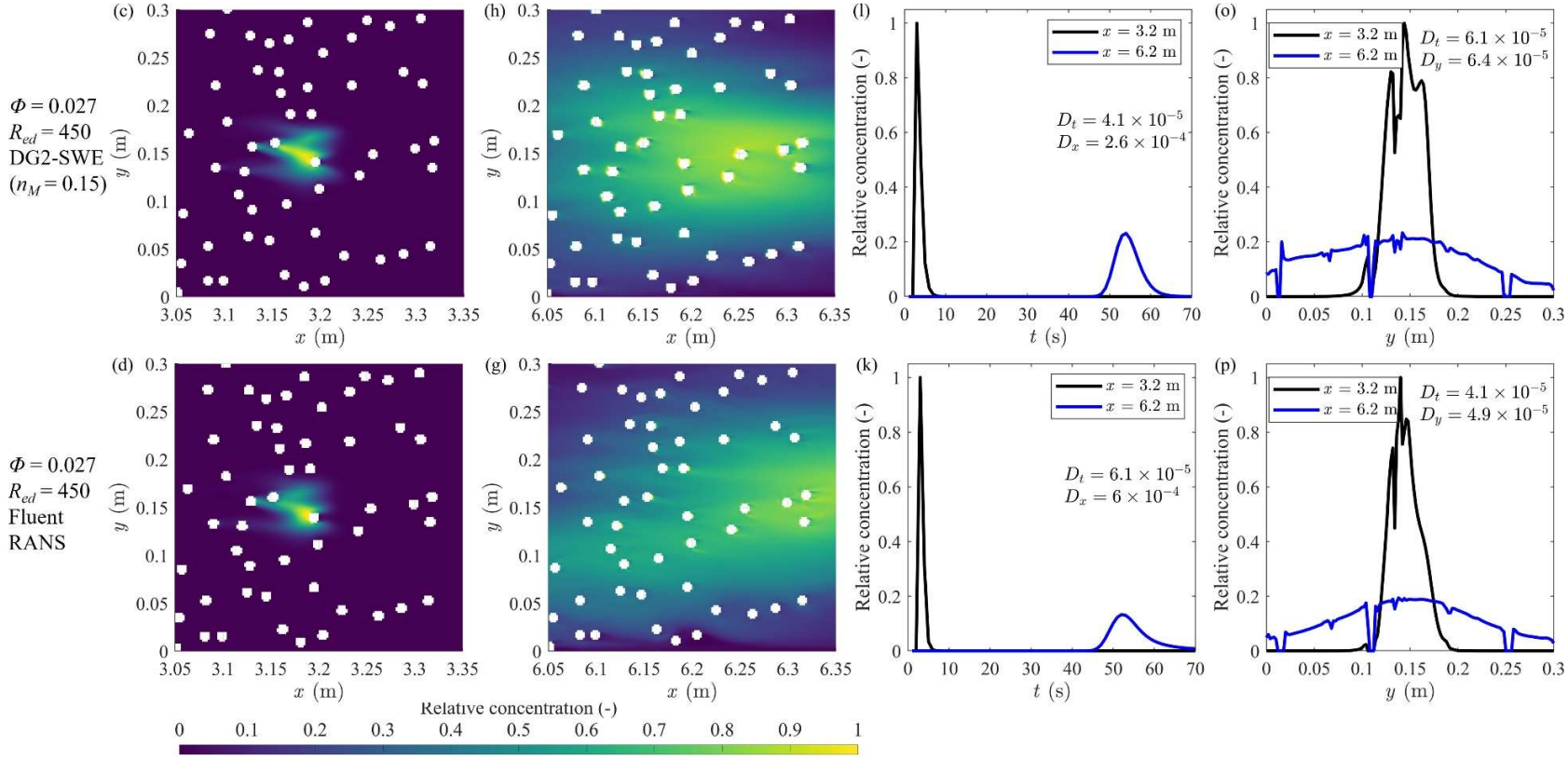

Figure 5.8. (continued) DG2-ADE simulated 2D instantaneous maps of solute concentration around the second fluorometers (first column, a-d) and third fluorometer (second column, e-h), and 1D temporal transversely averaged concentration profiles (third column, i-l) and spatial time-averaged concentration profiles (fourth column, m-p) extracted from the DG2-ADE simulations. The first three upper panels consider the inputs of flow and D_t fields from the calibrated DG2-SWE simulations with $n_M = 0.15$ m$^{1/6}$ at $\Phi = 0.005$, $R_{ed} = 53$ (first row), $\Phi = 0.005$, $R_{ed} = 250$ (second row), and $\Phi = 0.027$, $R_{ed} = 450$ (third row). The last lower panel considers the inputs from the Fluent RANS model.

Overall, the DG2-ADE simulated results are consistent with the findings in previously experimental and numerical studies (Sonnenwald et al., 2017; Stovin et al., 2022). This again confirms that the DG2-ADE solver can characterise the dispersion process - to reproduce the relative contribution of D_t to both D_x and D_y.

5.7 Computational costs: GPU-runtime

For all three flow cases in Section 5.3, 5.4 and 5.5, the GPU-runtimes were recorded in Table 1, using the same GPU card in Chapter 3. Note that these GPU-runtimes are not compared with the runtimes of the Fluent RANS and Fluent scalar transport simulations, as they were not reported.

For the DG2-SWE simulations, the laminar flow case undoubtedly requires the longest GPU-runtime since it takes the longest time (less than one day) to converge to quasi-steady state and completion of extra 50 shedding cycles. Significantly shorter computation times are needed, with GPU-runtimes not exceeding 3.7 hours for the transitional and turbulent flow cases. Moreover, there is no obvious difference in GPU-runtime when changing the values of n_M.

For the DG2-ADE simulations, the required GPU-runtimes considered both line source and equivalent point source injection, but the DG2-ADE simulations taking the inputs from FLUENT RANS were excluded. Unsurprisingly, line source injection consistent with the experiments required approximately 3.7-fold longer time for the solute to exit the outlet compared to the equivalent point source injection. All GPU-runtimes of the DG2-ADE solver are less than 13 hours, and the total GPU-runtimes are within 32.2 hours.

Overall, the DG2-SWE and DG2-ADE solvers can be favoured as a sufficiently efficient option to reproduce flow and mixing within cylinder arrays.

Table 5.1. GPU-runtime costs of the DG2-SWE simulations and DG2-ADE simulations considering the line source and equivalent point source injection for all three flow cases.

Flow cases	GPU-runtime (in hours)				
	DG2-SWE	DG2-ADE		Total (DG2-SWE + DG2-ADE)	
		(Line source injection)	(Equivalent point source injection)	(Line source injection)	(Equivalent point source injection)
Laminar (Φ = 0.005, Re_d = 53)	19.2	13	3.4	32.2	22.6
Transitional (Φ = 0.005, Re_d = 250)	3.7	2.5	0.65	6.2	4.35
Turbulent (Φ = 0.027, Re_d = 450)	1.3	3.5	0.95	4.8	2.25

5.8 Discussion

Computation of $\bar{u}$, $\bar{v}$ and D_t fields used as the inputs of the solute transport model are often hindered by the heavy costs of computational memory and runtime associated with the use of viscous turbulent models. This is due to the mathematical complexity of these turbulence models (recall Section 2.4.1) and the need to deploy a fine grid resolution. This challenge seems possible to be addressed by using the DG2-SWE solver with a coarse grid resolution of $0.25d$, which can provide acceptable $\bar{u}$ and $\bar{v}$ fields within most a day of runtime.

However, a major limitation of using the DG2-SWE simulated results as input for solute transport modelling is that the D_t fields for all three flow cases were overestimated when considering experimentally estimated n_M. Therefore, calibrated DG2-SWE simulations with artificially increased n_M were used to generate physically valid D_t fields required for the DG2-ADE simulations. In addition, for the turbulence case with complex flow interactions due to densely distributed cylinders, using calibrated DG2-SWE simulation results as the input leads to a slight decrease in the predictive accuracy of the DG2-ADE solver compared to the laminar and transitional cases. Furthermore, using inputs from

the viscous turbulence model results in the DG2-ADE simulated D_x is closer to the measured one than that obtained using inputs from the calibrated DG2-SWE.

In contrast to the conventional 2D RANS model (recall Figure 2.14), advantages of the 2D depth-averaged SWE solver are to (1) represent the cylinders and/or other topographies via the bed slope source term, thus better mimicking the real topographies, and (2) consider the bed roughness, that exists in the reality, via Manning's formula. For engineering purpose, one common n_M of 0.15 was selected to avoid the case-dependent calibration and found to be suitable for all three flow cases. This means that combining the DG2-SWE and DG2-ADE solvers has the potential to be a suitable numerical tool to simulate vegetated flow and mixing in natural water bodies such as ponds and wetlands featuring complex topography and roughness. Moreover, the high computational efficiency of the DG2-SWE and DG2-ADE solvers means that they might also be suitable for the real-time applications of solute transport, for example, predicting the movement of a pollution spill during a flood event.

5.9 Conclusions

In this chapter, the newly developed DG2-ADE solver was applied to simulate laboratory-scale solute transport within two configurations of cylinder arrays under laminar, transitional and low-turbulence regimes. The DG2-SWE simulated turbulent kinetic energy, TKE, fields and turbulent diffusivity fields, D_t, were evaluated and calibrated to meet the physically acceptable ranges by artificially increasing the Manning's coefficients, n_M which does not lead to a significant impact on the time-averaged flow fields, $\bar{u}$ and $\bar{v}$. One n_M of 0.15 $m^{1/6}$ is found to be suitable for all three flow cases. The calibrated DG2-SWE simulated results with n_M of 0.15 $m^{1/6}$ were fed into the DG2-ADE solver to examine its performance in predicting the spread of the solute for all three flow cases. For the turbulent case, the simulated $\bar{u}$, $\bar{v}$ and D_t fields from the viscous turbulence models such as the Fluent RANS model were also considered as the inputs to the DG2-ADE solver to conduct further analysis.

The results revealed that the DG2-ADE solver can deliver reliable concentration predictions in good agreement with the measurement. However, as the R_{ed} increases, the goodness-of-fit between the simulated and measured temporal concentration profiles appears to slightly decrease. Nevertheless, using the simulated fields from the Fluent RANS model showed a tendency to enhance the accuracy in prediction. The utility of the DG2-ADE solver was further assessed by retrieving the contribution of D_t to the reach-scale longitudinal and transverse dispersion coefficients, D_x and D_y, respectively. The findings showed that the DG2-ADE solver could provide a robust correct order-of-magnitude estimation of D_x and D_y. The high computational efficiency of the DG2-SWE and DG2-ADE solvers was also demonstrated by the GPU runtime costs. Overall, this suggests that the DG2-ADE solver combined with the output from the calibrated DG2-SWE simulation can be a useful tool to accurately

simulate solute transport and quantify the mixing process. It also has the potential to be applied for the vegetated flow and mixing in natural environments involving real topographies and bed roughness in large areas.

6 Conclusions

This chapter presents a summary of this PhD research work associated with the achieved objectives in Sec. 6.1, followed by the key findings and limitations in Sec. 6.2. The recommended future research directions that have arisen according to the research limitations are finally outlined in Sec. 6.3.

6.1 Summary of the thesis

The research background and motivation of this thesis were provided in Chapter 1, revealing the need for developing an efficient and accurate numerical tool to simulate flow and mixing within an array of cylinders and to provide reliable reach-scale longitudinal and transverse dispersion coefficient D_x and D_y. Before achieving this research aim, Chapter 2 presented a literature review to first introduce the basic concept of hydrodynamics around cylinders and the mixing processes within cylinder arrays. Numerical studies on simulating the flow past cylinders were then reviewed to demonstrate the shortcomings of the turbulence models (e.g. being extremely expensive and limited for large scale application) and the widely used second-order finite volume (FV2) solver (e.g. inducing the fast growth of numerical dispersion errors). The inviscid second-order discontinuous Galerkin (DG2) Shallow Water Equations (SWE) solver was then introduced along with the FV2-SWE solver, to demonstrate its potential benefit in simulating laminar to transitional flows past cylinders. This chapter ended with presenting the numerical models applied for mixing within cylinder arrays and showing there are only a few studies focused on this field, owing to the unaffordable computational expense. This again highlights the need for this research study.

The research aim is achieved through addressing the following three objectives. The first objective is to assess the suitability of the DG2-SWE solver in simulating laminar to transitional wakes behind cylinders, which has been addressed and studied in Chapter 3. The differences and similarities between the DG2-SWE solver and the standard FV2-SWE solver were discussed, especially listing the numerical complexity of the DG2-SWE solver in treating the advective fluxes. The capability of the DG2-SWE solver on the computation of wake flow patterns with vortical structures around cylinders was investigated across two representative test cases. The first test simulated the classical benchmark case of flow past one cylinder to compare the DG2-SWE solver's convergence ability and prediction accuracy against the FV2-SWE solver with reference to the FV2-based 2D Reynolds-Averaged Navier-Stokes (RANS) simulators. The second test case simulated experimental flow fields within a randomly distributed cylinder array and assessed the DG2-SWE simulation results based on qualitative and quantitative comparisons with the experimental measurements.

The second objective of this work was to develop a DG2 solver to the advection diffusion equation (ADE) for simulating the solute transport past cylinders, which has been addressed in Chapter 4. This DG2-ADE solver was linked to the DG2-SWE solver with a focus on the explicit generation of a non-uniform D_t field by using the eddy viscosity concept to process the DG2-SWE simulated flow fields. The DG2 discretisation for ADE was introduced, along with presenting the specific treatments to incorporate the presence of the cylinders and to preserve the positivity of the concentration. Validation was later done on the DG2-ADE solver considering test cases with and without cylinders. The order-of-accuracy of the DG2-ADE solver was identified based on the theoretical test case without the cylinder, followed by a comparative assessment between the DG2-ADE solver and a conventional FV2-ADE solver. Test cases with cylinder(s) were then considered to further validate the DG2-ADE solver by conducting a side-by-side comparison with the equally accurate, second-order commercial modelling tool (2D transient scalar transport available in ANSYS Fluent). Solute transport past one cylinder was selected to examine the mass-balance and positivity-preserving properties of the DG2-ADE solver, and to investigate the temporal concentration profiles within and outside wake zones for uniform D_t fields under different orders-of-magnitude. Finally, the performance of the DG2-ADE solver was again explored by reproducing solute transport within an array of randomly distributed cylinders where the distribution of the D_t field is non-uniform.

The newly developed DG2-ADE solver presented in Chapter 4 was implemented in Chapter 5 to address the third objective of effectively reproducing laboratory-scale experiments of solute transport past a large number of cylinders under laminar, transitional, and low-turbulent regimes. This chapter first introduced three experimental test cases considering two configurations of the randomly distributed cylinders, and described the related numerical setting of the DG2-SWE and DG2-ADE solvers. The DG2-SWE simulated fields of the turbulent kinetic energy, TKE, and the turbulent diffusivity, D_t, were then evaluated and calibrated to meet physically acceptable ranges. Subsequently, the DG2-ADE solver was validated against the experimental measurement data, by taking the measured temporal concentration profiles along the inlet as the boundary condition (equivalent to line source injection). Its capability of reproducing relative contribution of D_t to both longitudinal and transverse dispersion processes was further investigated by taking the Gaussian distributed concentration field as the initial condition (equivalent to point source injection). The associated runtime costs of the DG2-SWE and DG2-ADE simulations were also provided to reveal the computational efficiency.

The codes developed and implemented in this thesis are open source and can be accessed from https://www.seamlesswave.com.

6.2 Key findings and limitations

This section unfolds the key findings and limitations revealed in the completion of three objectives, as follows: The achievement of the first objective signifies that the inviscid DG2-SWE solver introduces an amount of "numerical error dissipation" whose effect may imitate kinematic and eddy viscosity of the turbulence effects, even excluding the viscous and turbulent eddy viscosity terms. Thanks to its extra numerical complexity, the DG2-SWE solver provides a superior treatment of the advective fluxes and bed slope terms, thus being able to trigger vortex shedding when applied to simulate laminar to transitional flows past one cylinder. In contrast, the FV2-SWE solver even on 10-folder finer grid resolution fails to capture the wake formations, owing to its relatively higher rate of numerical error dissipation. Furthermore, the DG2-SWE solver is shown to be approximately 90 times faster than the FV2-SWE solver in completing the simulations. Looking at the vortical flow structures, the DG2-SWE solver uses the piecewise-planar bed slope terms to explicitly represent the cylinders (abrupt vertices), contributing to causing the local discontinuity formations and in turn capturing the flow separation as well as vorticity generation. Also, the inherent linear slope coefficients of the DG2-SWE solver provide a straightforward way to evolve and obtain the velocity gradients and vorticities. The DG2-SWE simulated velocity components were compared to the reference simulated components from 2D RANS model with turbulence closure. Results show that the DG2-SWE solver tends to deliver more reliable velocity predictions in the far wake region than near the cylinder. In the laminar flow regime, the DG2-SWE solver yields a longitudinal velocity profile with a faster velocity recovery rate and shorter recirculation length than the reference profile, whereas its reliability to capture the wake formation improves as R_{ed} increases to the transitional regime. When applied to simulate flows within a laboratory-scale cylinder array, the DG2-SWE solver effectively reproduces the complex flow interactions with cylinders. These analyses suggest that the DG2-SWE solver can be a suitable numerical tool to yield competitively reliable fast-converged flow fields at affordable computational costs for simulating flow past a large number of cylinders.

The achievement of the second and the third objectives shows that the newly developed DG2-ADE solver is suitable for simulating solute transport within cylinder arrays. Given its extra numerical complexity in treating the advective fluxes, the DG2-ADE solver can achieve second-order accuracy and provide more accurate concentration fields than that from the standard FV2-ADE solver, as expected. Equipped with the specific treatment to the presence of the cylinders and the positivity-preserving correction procedure, the DG2-ADE solver can preserve mass-balance and non-negative concentration values in the context of the solute transport past cylinders. Moreover, the qualitative comparison shows that the DG2-ADE simulated instantaneous concentration fields around cylinders are in close agreement with the ones from the commercial model, revealing the suitability of this solver in reproducing the spread of the solute.

However, since the DG2-SWE solver does not incorporate any viscosity effects, it is necessary to calibrate the DG2-SWE simulations to ensure that the flow fields and D_t field required for the DG2-ADE simulations are physically valid. Artificially increasing Manning's coefficients, n_M, was found to be able to bring down the average magnitude of the TKE and D_t fields, while not significantly affecting the time-averaged flow fields. Using a single n_M of 0.15 $m^{1/6}$ appears to be suitable for all three flow cases (involving two configurations of cylinder arrays).

When taking the measured line source injection as the inlet boundary condition, the DG2-ADE simulated temporal concentration profiles are close to the measured ones, and the simulated reach-scale longitudinal dispersion coefficients, D_x, are also in the same order-of-magnitude as the measurement. These two observations demonstrate the robustness of the DG2-ADE solver using the inputs from the calibrated DG2-SWE simulations in reproducing the solute transport within cylinder arrays. Moreover, using the flow and D_t fields from a viscous turbulence simulator as the inputs, such as the Fluent FV2-RANS simulators, would enhance the accuracy of the simulated D_x. On the other hand, when considering the point source injection, the results show that the DG2-ADE solver could reproduce the expected mixing process: the simulated D_y is almost same as D_t, and the simulated D_x is approximately 10-fold greater than the simulated D_y and D_t. This again confirms that this new DG2-ADE solver can be a useful tool to accurately simulate solute transport within cylinder arrays and quantify the mixing processes in both x- and y- directions.

Throughout this research work, the primary limitation is the performance of the DG2-SWE solver, which incorporated only with the Manning's formula but lacks the kinematic and eddy viscosity terms. It is limited to use an unusual coarse grid resolution of $0.25d$, which is at least one order-of-magnitude coarser than the turbulence length scale but finer than the characteristic length, to keep a certain amount of numerical viscosity that would mimics the effects of true physical viscosity. In terms of the DG2-SWE simulated flow fields, its simulated wake flow patterns were over-expanded, and it also leads to an underestimation of the velocity of the preferential flow path. Moreover, under the same cylinder configuration, the DG2-SWE solver provided similar scaled velocity predictions even at different R_{ed}. On the other hand, in terms of the DG2-SWE simulated turbulence-related quantities such as TKE and D_t, their magnitudes were overestimated, exceeding the physically acceptable ranges when considering the experimentally estimated n_M. Therefore, the calibrated DG2-SWE simulations were used based on artificially increased n_M to bring down the magnitude of TKE and D_t to acceptable ranges before feeding into the DG2-ADE solver. Another limitation arises from the uniform grid discretization employed by both the DG2-SWE and DG2-ADE solvers, which maintain a fixed grid size/resolution throughout the computational domain. Therefore, this approach does not allow the use of fine grids around the cylinders and coarse grids elsewhere, potentially hindering efforts to maximize computational efficiency.

6.3 Recommendations for future research

According to the aforementioned research limitation, this section presents the recommended research directions to extend this research work in the future, including three perspectives. The first is to develop the DG2 solver to the viscous turbulent models (i.e., the conventional 2D depth-averaged RANS model). As the aforementioned limitation of the DG2-SWE solver, the absence of eddy viscosity terms results in delivering flow characteristics with less accuracy for the laminar flow regime and also leads to the overestimated magnitudes of the TKE (and in turn D_t) fields. This means that the DG2-RANS solver would bring out the potential to capture more accurate flow and TKE fields around the cylinders without calibration. A comparative study between the DG2-SWE solver and the DG2-RANS solver will be conducted to reveal how much the accuracy of the flow and TKE fields can be improved by adding the eddy viscosity terms. However, from a computational costing point of view, the mathematically more complex DG2-RANS solver contributes to much more expensive computational runtime and memory costs. A trade-off study between the computational costs and predictive accuracy will also be needed.

The second perspective is to further explore the behaviour of this numerical tool which links the DG2-SWE solver to the DG2-ADE solver in other test cases under different configurations. In addition to considering the cylinders with a single, fixed diameter, it is worth employing this numerical tool for applications involving non-uniform cylinder diameter distributions featured with a broad range of cylinder densities. Apart from the laboratory-scale simulations, it would also be interesting to apply this numerical tool to real-world cases, including reproducing the vegetated flow and mixing within the ponds or wetlands, or predicting the movement of a pollution spill during a flood event, and so on.

The third future research direction is to perform the simulations on adaptive non-uniform grids, instead of using uniform grids considered in this thesis, to reduce the computational costs. Recently, the adaptive grid refinement technique of MultiWavelets (MW) has emerged as an attractive way to be extended to the DG2 solver. The adaptive MWDG2 solver to SWE has been developed for flood inundation applications and has not been applied to explore its performance in simulating laminar to low-turbulent flows past cylinders so far. Compared to the DG2-SWE solver using the uniform grids, the MWDG2-SWE solver using the adaptive grids can preserve almost the same accuracy and achieve pronounced speed-up. The MWDG2-SWE solver automatically achieves fine grid resolution around steep velocity gradients and coarsen resolution in smooth regions, driven by a single user-prescribed parameter. This means that, with these advantages, the MWDG2-SWE solver potentially allows fine grid resolution around cylinders to produce the almost equally accurate flow fields as the DG2-SWE solver, and coarsens grid resolution to reduce the number of grids to improve the efficiency. More exploration can be made on the analysis of

vortex shedding frequency, generation of turbulent diffusivity and computational runtime costs. MW, although incorporated with the DG2-SWE solver, has not been adopted to extend the DG2-ADE solver to formulate the MWDG2-ADE solver. This also brings great potential for the MWDG2-ADE solver to boost the efficiency of the DG2-ADE solver, while accurately simulating the spread of the solute and quantifying the mixing process. This also motivates us to develop another new numerical tool that incorporates the MW technique with the numerical tool presented in this study.

7 References

Alfonsi, G., 2009. Reynolds-averaged Navier-Stokes equations for turbulence modeling. Appl. Mech. Rev. 62, 1–20. https://doi.org/10.1115/1.3124648

Alvarez-Vázquez, L.J., Martínez, A., Vázquez-Méndez, M.E., Vilar, M.A., 2008. An optimal shape problem related to the realistic design of river fishways. Ecol. Eng. 32, 293–300. https://doi.org/10.1016/j.ecoleng.2007.10.008

Angeloudis, A., Stoesser, T., Falconer, R.A., 2014. Predicting the disinfection efficiency range in chlorine contact tanks through a CFD-based approach. Water Res. 60, 118–129. https://doi.org/10.1016/j.watres.2014.04.037

Angeloudis, A., Stoesser, T., Falconer, R.A., Kim, D., 2015. Flow, transport and disinfection performance in small- and full-scale contact tanks. J. Hydro-Environment Res. 9, 15–27. https://doi.org/10.1016/j.jher.2014.07.001

Arnold, U., Hottges, J., Rouve, G., 1989. Turbulence and mixing mechanisms in compound open channel flow, in: Proc., 23rd IAHR Congress. pp. A133–A140.

Ayog, J.L., Kesserwani, G., Shaw, J., Sharifian, M.K., Bau, D., 2021. Second-order discontinuous Galerkin flood model: Comparison with industry-standard finite volume models. J. Hydrol. 594, 125924. https://doi.org/10.1016/j.jhydrol.2020.125924

Ayyappan, T., Vengadesan, S., 2008. Three-dimensional simulation of flow past a circular cylinder by nonlinear turbulence model. Numer. Heat Transf. Part A Appl. 54, 221–234. https://doi.org/10.1080/10407780802084694

Badrot-Nico, F., Brissaud, F., Guinot, V., 2007. A finite volume upwind scheme for the solution of the linear advection-diffusion equation with sharp gradients in multiple dimensions. Adv. Water Resour. 30, 2002–2025. https://doi.org/10.1016/j.advwatres.2007.04.003

Baek, K.O., Seo, I.W., Jeong, S.J., 2006. Evaluation of Dispersion Coefficients in Meandering Channels from Transient Tracer Tests. J. Hydraul. Eng. 132, 1021–1032. https://doi.org/10.1061/(asce)0733-9429(2006)132:10(1021)

Balachandar, S., Mittal, R., Najjar, F.M., 1997. Properties of the mean recirculation region in the wakes of two-dimensional bluff bodies. J. Fluid Mech. 351, 167–199. https://doi.org/10.1017/S0022112097007179

Baldyga, J., Bourne, J.R., 1999. Turbulent Mixing and Chemical Reactions. John Wiley & Sons.

Baptist, M.J., Babovic, V., Uthurburu, J.R., Keijzer, M., Uittenbogaard, R.E., Mynett, A., Verwey,

A., 2007. On inducing equations for vegetation resistance. J. Hydraul. Res. 45, 435–450. https://doi.org/10.1080/00221686.2007.9521778

Behr, M., Liou, J., Shih, R., Tezduyar, T.E., 1991. Vorticity-streamfunction formulation of unsteady incompressible flow past a cylinder: Sensitivity of the computed flow field to the location of the outflow boundary. Int. J. Numer. Methods Fluids 12, 323–342. https://doi.org/10.1002/fld.1650120403

Bonetti, S., Manoli, G., Manes, C., Porporato, A., Katul, G.G., 2017. Manning's formula and Strickler's scaling explained by a co-spectral budget model. J. Fluid Mech. 812, 1189–1212. https://doi.org/10.1017/jfm.2016.863

Boussinesq, J., 1877. Essai sur la théorie des eaux courantes. Mémoires présentes par divers savantsa l'Académie des Sciences.

Bouteligier, R., Vaes, G., Berlamont, J., Flamink, C., Langeveld, J.G., Clemens, F., 2005. Advection-dispersion modelling tools: What about numerical dispersion? Water Sci. Technol. 52, 19–27. https://doi.org/10.2166/wst.2005.0057

Braza, M., Chassaing, P., Ha Minh, H., 1986. Numerical study and physical analysis of the pressure and velocity fields in the near wake of a circular cylinder. J. Fluid Mech. 165, 79–130. https://doi.org/10.1017/S0022112086003014

Brière, C., Abadie, S., Bretel, P., Lang, P., 2007. Assessment of TELEMAC system performances, a hydrodynamic case study of Anglet, France. Coast. Eng. 54, 345–356. https://doi.org/10.1016/j.coastaleng.2006.10.006

Caviedes-Voullième, D., Kesserwani, G., 2015. Benchmarking a multiresolution discontinuous Galerkin shallow water model: Implications for computational hydraulics. Adv. Water Resour. 86, 14–31. https://doi.org/10.1016/j.advwatres.2015.09.016

Cea, L., Puertas, J., Vázquez-Cendón, M.E., 2007. Depth averaged modelling of turbulent shallow water flow with wet-dry fronts. Arch. Comput. Methods Eng. 14, 303–341. https://doi.org/10.1007/s11831-007-9009-3

Chang, K., Constantinescu, G., 2015. Numerical investigation of flow and turbulence structure through and around a circular array of rigid cylinders. J. Fluid Mech. 776, 161–199. https://doi.org/10.1017/jfm.2015.321

Chow, V.., 1959. Open-Channel Hydraulics. McGraw-Hill, New York.

Cockburn, B., Karniadakis, G.E., Shu, C.W., 2000. The development of discontinuous Galerkin methods, in: Discontinuous Galerkin Methods: Theory, Computation and Applications.

Springer Berlin Heidelberg, pp. 3–50.

Cockburn, B., Shu, C.-W., 2009. Foreword. J. Sci. Comput. 40, 1–3. https://doi.org/10.1007/s10915-009-9298-9

Cockburn, B., Shu, C.W., 2001. Runge-Kutta Discontinuous Galerkin methods for convection-dominated problems. J. Sci. Comput. 16, 173–261. https://doi.org/10.1023/A:1012873910884

Cockburn, B., Shu, C.W., 1998. The Runge–Kutta Discontinuous Galerkin Method for Conservation Laws V. J. Comput. Phys. 141, 199–224.

Corredor-Garcia, J.L., 2023. Solute Transport in Flow Through Random Emergent Vegetation. PhD thesis. The University of Sheffield.

Corredor-Garcia, J.L., Delalande, A., Stovin, V., Guymer, I., 2020. On the Use of Surface PIV for the Characterization of Wake Area in Flows Through Emergent Vegetation, in: Recent Trends in Environmental Hydraulics. Cham: Springer International Publishing, pp. 43–52. https://doi.org/10.1007/978-3-030-37105-0_4

Dairay, T., Lamballais, E., Laizet, S., Vassilicos, J.C., 2017. Numerical dissipation vs. subgrid-scale modelling for large eddy simulation. J. Comput. Phys. 337, 252–274. https://doi.org/10.1016/j.jcp.2017.02.035

Darby, S.E., 1999. Effect of Riparian Vegetation on Flow Resistance and Flood Potential. J. Hydraul. Eng. 125, 443–454. https://doi.org/10.1061/(ASCE)0733-9429(1999)125:5(443)

Djordjevic, S., 1993. Mathematical model of unsteady transport and its experimental verification in a compound open channel flow. J. Hydraul. Res. 31, 229–248. https://doi.org/10.1080/00221689309498847

Duan, J.G., 2004. Simulation of Flow and Mass Dispersion in Meandering Channels. J. Hydraul. Eng. 130, 964–976. https://doi.org/10.1061/(ASCE)0733-9429(2004)130:10(964) CE

Duran, A., Marche, F., 2014. Recent advances on the discontinuous Galerkin method for shallow water equations with topography source terms. Comput. Fluids 101, 88–104. https://doi.org/10.1016/j.compfluid.2014.05.031

Elder, J., 1959. The dispersion of marked fluid in turbulent shear flow. J. Fluid Mech. 5, 544–560. https://doi.org/10.4324/9781003325796-4

Etminan, V., Lowe, R., Ghisalberti, M., 2017. A new model for predicting the drag exerted by vegetation canopies. Water Resour. Res. 53, 3179–3196. https://doi.org/10.1111/j.1752-1688.1969.tb04897.x

Fang, S., Ji, Y., Zhang, M., 2022. Numerical Modeling the Flood and Pollutant Transport Processes in Residential Areas with Different Land Use Types. Adv. Meteorol. 2022, 1–16. https://doi.org/10.1155/2022/9320089

Fernández-Pato, J., Morales-Hernández, M., García-Navarro, P., 2018. Implicit finite volume simulation of 2D shallow water flows in flexible meshes. Comput. Methods Appl. Mech. Eng. 328, 1–25. https://doi.org/10.1016/j.cma.2017.08.050

Fischer, H.B., 1979. Mixing in inland and coastal waters. Academic press.

Franke, R., Rodi, W., Schönung, B., 1990. Numerical calculation of laminar vortex-shedding flow past cylinders. J. Wind Eng. Ind. Aerodyn. 35, 237–257. https://doi.org/10.1016/0167-6105(90)90219-3

Fringer, O.B., Dawson, C.N., He, R., Ralston, D.K., Zhang, Y.J., 2019. The future of coastal and estuarine modeling: Findings from a workshop. Ocean Model. 143, 101458. https://doi.org/10.1016/j.ocemod.2019.101458

Gao, Y., Qu, X., Zhao, M., Wang, L., 2019. Three-dimensional numerical simulation on flow past three circular cylinders in an equilateral-triangular arrangement. Ocean Eng. 189, 106375. https://doi.org/10.1016/j.oceaneng.2019.106375

Gerrard, J.H., 1978. The wakes of cylindrical bluff bodies at low Reynolds number. Philos. Trans. R. Soc. London. Ser. A, Math. Phys. Sci. 288, 351–382.

Ghisalberti, M., Nepf, H., 2005. Mass transport in vegetated shear flows. Environ. Fluid Mech. 5, 527–551. https://doi.org/10.1007/s10652-005-0419-1

Ginting, B.M., 2019. Central-upwind scheme for 2D turbulent shallow flows using high-resolution meshes with scalable wall functions. Comput. Fluids 179, 394–421. https://doi.org/10.1016/j.compfluid.2018.11.014

Ginting, B.M., Ginting, H., 2019. Hybrid Artificial Viscosity–Central-Upwind Scheme for Recirculating Turbulent Shallow Water Flows. J. Hydraul. Eng. 145, 1–17. https://doi.org/10.1061/(asce)hy.1943-7900.0001639

Gioia, G., Bombardelli, F.A., 2001. Scaling and Similarity in Rough Channel Flows. Phys. Rev. Lett. 88, 014501. https://doi.org/10.1103/PhysRevLett.88.014501

Godunov, S.., 1959. A difference scheme for numerical solution of discontinuous solution of hydrodynamic equations. Math. Sb. 47, 271–306.

Golzar, M., 2018. CFD modelling of dispersion within randomly distributed cylinder arrays. PhD thesis. The University of Sheffield.

Golzar, M., Sonnenwald, F., Guymer, I., Stovin, V., 2018. A CFD based comparison of mixing due to regular and random cylinder arrays, in: Free Surface Flows and Transport Processes: 36th International School of Hydraulics. pp. 195–205. https://doi.org/10.1007/978-3-319-70914-7_11

Golzar, M., Sonnenwald, S., Guymer, I., Stovin, V., 2017. Transverse mixing coefficient in random cylinder arrays–A CFD validation study, in: 37th IAHR Word Congress, Kuala Lumpur, Malaysia.

Gualtieri, C., Angeloudis, A., Bombardelli, F., Jha, S., Stoesser, T., 2017. On the values for the turbulent schmidt number in environmental flows. Fluids 2, 17. https://doi.org/10.3390/fluids2020017

Hajihassanpour, M., Hejranfar, K., 2020. An implicit dual-time stepping high-order nodal discontinuous Galerkin method for solving incompressible flows on triangle elements. Math. Comput. Simul. 168, 173–214. https://doi.org/10.1016/j.matcom.2019.08.011

Hamidifar, H., Omid, M.H., Keshavarzi, A., 2015. Longitudinal dispersion in waterways with vegetated floodplain. Ecol. Eng. 84, 398–407. https://doi.org/10.1016/j.ecoleng.2015.09.048

Hervouet, J., 1999. TELEMAC , a hydroinformatic system. La Houille Blanche 3, 21–18.

Hinterberger, C., Fröhlich, J., Rodi, W., 2007. Three-Dimensional and Depth-Averaged Large-Eddy Simulations of Some Shallow Water Flows. J. Hydraul. Eng. 133, 857–872. https://doi.org/10.1061/_ASCE0733-9429_2007133:8_857

Horritt, M.S., Bates, P.D., 2001. Predicting floodplain inundation: Raster-based modelling versus the finite-element approach. Hydrol. Process. 15, 825–842. https://doi.org/10.1002/hyp.188

Hou, J., Liang, Q., Zhang, H., Hinkelmann, R., 2015. An efficient unstructured MUSCL scheme for solving the 2D shallow water equations. Environ. Model. Softw. 66, 131–152. https://doi.org/10.1016/j.envsoft.2014.12.007

Hou, J., Liang, Q., Zhang, H., Hinkelmann, R., 2014. Multislope MUSCL method applied to solve shallow water equations. Comput. Math. with Appl. 68, 2012–2027. https://doi.org/10.1016/j.camwa.2014.09.018

Hu, D., Zhu, Y., Zhong, D., Qin, H., 2017. Two-Dimensional Finite-Volume Eulerian-Lagrangian Method on Unstructured Grid for Solving Advective Transport of Passive Scalars in Free-Surface Flows. J. Hydraul. Eng. 143, 04017051. https://doi.org/10.1061/(asce)hy.1943-7900.0001371

Huang, G., Xing, Y., Xiong, T., 2022. High order well-balanced asymptotic preserving finite

difference WENO schemes for the shallow water equations in all Froude numbers. J. Comput. Phys. 463, 111255. https://doi.org/10.1016/j.jcp.2022.111255

Jiang, H., Cheng, L., 2021. Large-eddy simulation of flow past a circular cylinder for Reynolds numbers 400 to 3900. Phys. Fluids 33. https://doi.org/10.1063/5.0041168

Jiang, H., Cheng, L., 2017. Strouhal-Reynolds number relationship for flow past a circular cylinder. J. Fluid Mech. 832, 170–188. https://doi.org/10.1017/jfm.2017.685

Jiang, H., Cheng, L., Draper, S., An, H., Tong, F., 2016. Three-dimensional direct numerical simulation of wake transitions of a circular cylinder. J. Fluid Mech. 801, 353–391. https://doi.org/10.1017/jfm.2016.446

Katul, G., Wiberg, P., Albertson, J., Hornberger, G., 2002. A mixing layer theory for flow resistance in shallow streams. Water Resour. Res. 38, 32–1. https://doi.org/10.1029/2001wr000817

Kesserwani, G., 2013. Topography discretization techniques for Godunov-type shallow water numerical models: A comparative study. J. Hydraul. Res. 51, 351–367. https://doi.org/10.1080/00221686.2013.796574

Kesserwani, G., Ayog, J.L., Bau, D., 2018. Discontinuous Galerkin formulation for 2D hydrodynamic modelling: Trade-offs between theoretical complexity and practical convenience. Comput. Methods Appl. Mech. Eng. 342, 710–741. https://doi.org/10.1016/j.cma.2018.08.003

Kesserwani, G., Ayog, J.L., Sharifian, M.K., Baú, D., 2023. Shallow-Flow Velocity Predictions Using Discontinuous Galerkin Solutions. J. Hydraul. Eng. 149. https://doi.org/10.1061/jhend8.hyeng-13244

Kesserwani, G., Ghostine, R., Vazquez, J., Ghenaim, A., Mosé, R., 2008. Riemann Solvers with Runge–Kutta Discontinuous Galerkin Schemes for the 1D Shallow Water Equations. J. Hydraul. Eng. 134, 243–255. https://doi.org/10.1061/(ASCE)0733-9429(2008)134:2(243)

Kesserwani, G., Liang, Q., 2012. Locally limited and fully conserved RKDG2 shallow water solutions with wetting and drying. J. Sci. Comput. 50, 120–144. https://doi.org/10.1007/s10915-011-9476-4

Kesserwani, G., Liang, Q., 2011. A conservative high-order discontinuous Galerkin method for the shallowwater equations with arbitrary topography. Int. J. Numer. Methods Eng. 86, 47–69. https://doi.org/10.1002/nme

Kesserwani, G., Sharifian, M.K., 2023. (Multi)wavelet-based Godunov-type simulators of flood

inundation: Static versus dynamic adaptivity. Adv. Water Resour. 171, 104357. https://doi.org/10.1016/j.advwatres.2022.104357

Kesserwani, G., Sharifian, M.K., 2020. (Multi)wavelets increase both accuracy and efficiency of standard Godunov-type hydrodynamic models: Robust 2D approaches. Adv. Water Resour. 144, 103693. https://doi.org/10.1016/j.advwatres.2020.103693

Kesserwani, G., Wang, Y., 2014. Discontinuous Galerkin flood model formulation: Luxury or necessity? Water Resour. Res. 50, 6522–6541. https://doi.org/10.1002/2013WR014906

Kim, H.S., Kimura, I., Park, M., 2018. Numerical Simulation of Flow and Suspended Sediment Deposition Within and Around a Circular Patch of Vegetation on a Rigid Bed. Water Resour. Res. 54, 7231–7251. https://doi.org/10.1029/2017WR021087

King, A., 2006. Field Measurements of Bulk Flow and Transport Through a Small Coastal Embayment Having Variable Distributions of Aquatic Vegetation. Master dissertation. Cornell University.

Kubatko, E.J., Westerink, J.J., Dawson, C., 2006. hp Discontinuous Galerkin methods for advection dominated problems in shallow water flow. Comput. Methods Appl. Mech. Eng. 196, 437–451. https://doi.org/10.1016/j.cma.2006.05.002

Kvočka, D., Falconer, R.A., Bray, M., 2015. Appropriate model use for predicting elevations and inundation extent for extreme flood events. Nat. Hazards. https://doi.org/10.1007/s11069-015-1926-0

Landmann, B., Kessler, M., Wagner, S., Krämer, E., 2008. A parallel, high-order discontinuous Galerkin code for laminar and turbulent flows. Comput. Fluids 37, 427–438. https://doi.org/10.1016/j.compfluid.2007.02.009

Laroussi, M., Djebbi, M., Moussa, M., 2014. Triggering vortex shedding for flow past circular cylinder by acting on initial conditions: A numerical study. Comput. Fluids 101, 194–207. https://doi.org/10.1016/j.compfluid.2014.05.034

Lee, J.H., Paik, B.G., Cho, S.K., Jung, J.H., 2023. Visualization of Turbulent Flow Fields Around a Circular Cylinder at Reynolds Number 1.4×105 Using PIV? J. Ocean Eng. Technol. 37, 137–144. https://doi.org/10.26748/KSOE.2023.009

Lee, M.E., Kim, G., 2012. Influence of secondary currents on solute dispersion in curved open channels. J. Appl. Math. 2012. https://doi.org/10.1155/2012/781695

Legrand, S., Deleersnijder, E., Hanert, E., Legat, V., Wolanski, E., 2006. High-resolution, unstructured meshes for hydrodynamic models of the Great Barrier Reef, Australia. Estuar.

Coast. Shelf Sci. 68, 36–46. https://doi.org/10.1016/j.ecss.2005.08.017

Lei, C., Cheng, L., Kavanagh, K., 2000. A finite difference solution of the shear flow over a circular cylinder. Ocean Eng. 27, 271–290. https://doi.org/10.1016/S0029-8018(98)00050-X

Li, L., Yan, Z., Liu, Z., 2012. Numerical model for shallow wake behind cylinder. Appl. Mech. Mater. 212–213, 1205–1212. https://doi.org/10.4028/www.scientific.net/AMM.212-213.1205

Li, W., Ren, J., Hongde, J., Luan, Y., Ligrani, P., 2016. Assessment of six turbulence models for modeling and predicting narrow passage flows, part 2: Pin fin arrays. Numer. Heat Transf. Part A Appl. 69, 445–463. https://doi.org/10.1080/10407782.2015.1081024

Liang, D., Lin, B., Falconer, R.A., 2007. A boundary-fitted numerical model for flood routing with shock-capturing capability. J. Hydrol. 332, 477–486. https://doi.org/10.1016/j.jhydrol.2006.08.002

Liang, D., Wang, X., Falconer, R.A., Bockelmann-Evans, B.N., 2010. Solving the depth-integrated solute transport equation with a TVD-MacCormack scheme. Environ. Model. Softw. 25, 1619–1629. https://doi.org/10.1016/j.envsoft.2010.06.008

Lightbody, A.., Nepf, H.M., 2006. Prediction of velocity profiles and longitudinal dispersion in salt marsh vegetation. Limnol. Oceanogr. 51, 218–228.

Lin, B., Shiono, K., 1995. Numerical modelling of solute transport in compound channel flows. J. Hydraul. Res. 33, 773–788. https://doi.org/10.1080/00221689509498551

Liu, D., Diplas, P., Fairbanks, J.D., Hodges, C.C., 2008. An experimental study of flow through rigid vegetation. J. Geophys. Res. Earth Surf. 113, 1–16. https://doi.org/10.1029/2008JF001042

Liu, K., Haworth, D.C., 2011. Development and assessment of POD for analysis of turbulent flow in piston engines, in: SAE 2011 World Congress and Exhibition. https://doi.org/10.4271/2011-01-0830

Lu, J., Dai, H.C., 2018. Numerical modeling of pollution transport in flexible vegetation. Appl. Math. Model. 64, 93–105. https://doi.org/10.1016/j.apm.2018.06.039

Lu, J., Dai, H.C., 2016. Effect of submerged vegetation on solute transport in an open channel using large eddy simulation. Adv. Water Resour. 97, 87–99. https://doi.org/10.1016/j.advwatres.2016.09.003

Luhar, M., Nepf, H.M., 2013. From the blade scale to the reach scale: A characterization of aquatic vegetative drag. Adv. Water Resour. 51, 305–316.

https://doi.org/10.1016/j.advwatres.2012.02.002

Man, C., Tsai, C.W., 2008. A higher-order predictor–corrector scheme for two-dimensional advection–diffusion equation. Int. J. Numer. METHODS FLUIDS 56, 401–418. https://doi.org/10.1002/fld.152

Marjoribanks, T.I., Hardy, R.J., Lane, S.N., Tancock, M.J., 2017. Patch-scale representation of vegetation within hydraulic models. Earth Surf. Process. Landforms 42, 699–710. https://doi.org/10.1002/esp.4015

Mignot, E., Riviere, N., Dewals, B., 2023. Formulations and Diffusivity Coefficients of the 2D Depth-Averaged Advection-Diffusion Models: A Literature Review. Water Resour. Res. 59. https://doi.org/10.1029/2023WR035053

Mittal, S., 2005. Excitation of shear layer instability in flow past a cylinder at low Reynolds number. Int. J. Numer. Methods Fluids 49, 1147–1167. https://doi.org/10.1002/fld.1043

Murillo, J., García-Navarro, P., Burguete, J., Brufau, P., 2006. A conservative 2D model of inundation flow with solute transport over dry bed. Int. J. Numer. Methods Fluids 52, 1059–1092. https://doi.org/10.1002/fld.1216

Murphy, E., 2006. Longitudinal Dispersion in Vegetated Flow. PhD thesis. Massachusetts Institute of Technology.

Navas-Montilla, A., Juez, C., Franca, M.J., Murillo, J., 2019. Depth-averaged unsteady RANS simulation of resonant shallow flows in lateral cavities using augmented WENO-ADER schemes. J. Comput. Phys. 395, 511–536. https://doi.org/10.1016/j.jcp.2019.06.037

Neal, J., Villanueva, I., Wright, N., Willis, T., Fewtrell, T., Bates, P., 2012. How much physical complexity is needed to model flood inundation? Hydrol. Process. 26, 2264–2282. https://doi.org/10.1002/hyp.8339

Nepf, H.M., 2012. Flow and transport in regions with aquatic vegetation. Annu. Rev. Fluid Mech. 44, 123–142. https://doi.org/10.1146/annurev-fluid-120710-101048

Nepf, H.M., 1999. Drag, turbulence, and diffusion in flow through emergent vegetation. Water Resour. Res. 35, 479–489. https://doi.org/10.1029/1998WR900069

Nepf, H.M., Mugnier, C.G., Zavistoski, R.A., 1997a. The effects of vegetation on longitudinal dispersion. Estuar. Coast. Shelf Sci. 44, 675–684. https://doi.org/10.1006/ecss.1996.0169

Nepf, H.M., Sullivan, J.A., Zavistoski, R.A., 1997b. A model for diffusion within emergent vegetation. Limnol. Oceanogr. 42, 1735–1745. https://doi.org/10.4319/lo.1997.42.8.1735

Nguyen, T.T., Keupers, I., Willems, P., 2018. Conceptual river water quality model with flexible model structure. Environ. Model. Softw. 104, 102–117. https://doi.org/10.1016/j.envsoft.2018.03.014

Nishino, T., Roberts, G.T., Zhang, X., 2008. Unsteady RANS and detached-eddy simulations of flow around a circular cylinder in ground effect. J. Fluids Struct. 24, 18–33. https://doi.org/10.1016/j.jfluidstructs.2007.06.002

Noye, B.J., Tan, H.H., 1989. Finite difference methods for solving the two-dimensional advection–diffusion equation. Int. J. Numer. Methods Fluids 9, 75–98. https://doi.org/10.1002/fld.1650090107

O'Hare, M.T., 2015. Aquatic vegetation - A primer for hydrodynamic specialists. J. Hydraul. Res. 53, 687–698. https://doi.org/10.1080/00221686.2015.1090493

Okamoto, T., Nezu, I., 2010. Large eddy simulation of 3-D flow structure and mass transport in open-channel flows with submerged vegetations. J. Hydro-Environment Res. 4, 185–197. https://doi.org/10.1016/j.jher.2010.04.015

Paranthoën, P., Browne, L.W.B., Le Masson, S., Dumouchel, F., Lecordier, J.C., 1999. Characteristics of the near wake of a cylinder at low Reynolds numbers. Eur. J. Mech. B/Fluids 18, 659–674. https://doi.org/10.1016/S0997-7546(99)00105-3

Park, I., Seo, I.W., Do Kim, Y., Song, C.G., 2016. Flow and dispersion analysis of shallow water problems with Froude number variation. Environ. Earth Sci. 75, 1–12. https://doi.org/10.1007/s12665-015-4928-z

Pathirana, A., Maheng, M.D., Brdjanovic, D., 2011. A Two-dimensional pollutant transport model for sewer overflow impact simulation, in: Proceedings: 12th International Conference on Urban Drainage, Porto Alegre/Brazil. pp. 10–15.

Pokrajac, D., McEwan, I., Nikora, V., 2008. Spatially averaged turbulent stress and its partitioning. Exp. Fluids 45, 73–83. https://doi.org/10.1007/s00348-008-0463-y

Ponta, F.L., 2010. Vortex decay in the Kármán eddy street. Phys. Fluids 22. https://doi.org/10.1063/1.3481383

Prandtl, L., 1925. Über die ausgebildete turbulenz (investigations on turbulent flow). Z. Angew. Math. Mech 5, 136–139.

Qu, L., Norberg, C., Davidson, L., Peng, S.H., Wang, F., 2013. Quantitative numerical analysis of flow past a circular cylinder at reynolds number between 50 and 200. J. Fluids Struct. 39, 347–370. https://doi.org/10.1016/j.jfluidstructs.2013.02.007

Rajani, B.N., Kandasamy, A., Majumdar, S., 2009. Numerical simulation of laminar flow past a circular cylinder. Appl. Math. Model. 33, 1228–1247. https://doi.org/10.1016/j.apm.2008.01.017

Ramshaw, J.D., 1994. Numerical viscosities of difference schemes. Commun. Numer. Methods Eng. 10, 927–931. https://doi.org/10.1002/cnm.1640101108

Rauen, W.B., Angeloudis, A., Falconer, R.A., 2012. Appraisal of chlorine contact tank modelling practices. Water Res. 46, 5834–5847. https://doi.org/10.1016/j.watres.2012.08.013

Raupach, M.R., Antonia, R.A., Rajagopalan, S., 1991. Rough-wall turbulent boundary layers. Appl. Mech. Rev. 44, 1–25. https://doi.org/10.1115/1.3119492

Reddy, J.N., 1993. An introduction to the finite element method. New York: McGraw-Hill.

Reed, W.H., Hill, T.R., 1973. Triangular mesh methods for the neutron transport equation, in: No. LA-UR-73-479; CONF-730414-2. Los Alamos Scientific Lab., N. Mex.(USA). https://doi.org/10.1080/00091383.1977.10569251

Ricardo, A.M., Franca, M.J., Ferreira, R.M.L., 2016a. Turbulent Flows within Random Arrays of Rigid and Emergent Cylinders with Varying Distribution. J. Hydraul. Eng. 142, 04016022. https://doi.org/10.1061/(asce)hy.1943-7900.0001151

Ricardo, A.M., Koll, K., Franca, M.J., Schleiss, A.J., Ferreira, R.., 2014. The terms of turbulent kinetic energy budget within random arrays of emergent cylinders. Water Resour. Res. 50, 4131–4148. https://doi.org/10.1002/2013WR014979

Ricardo, A.M., Sanches, P.M., Ferreira, R.M.L., 2016b. Vortex shedding and vorticity fluxes in the wake of cylinders within a random array. J. Turbul. 17, 999–1014. https://doi.org/10.1080/14685248.2016.1212166

Rizzetta, D.P., Visbal, M.R., Morgan, P.E., 2008. A high-order compact finite-difference scheme for large-eddy simulation of active flow control. Prog. Aerosp. Sci. 44, 397–426. https://doi.org/10.1016/j.paerosci.2008.06.003

Rizzi, A., 1982. Mesh Influence on Vortex Shedding in Inviscid Flow Computations, in: Recent Contributions to Fluid Mechanics. Berlin, Heidelberg: Springer Berlin Heidelberg, pp. 213–221.

Rodi, W., 2017. Turbulence Modeling and Simulation in Hydraulics: A Historical Review. J. Hydraul. Eng. 143, 03117001. https://doi.org/10.1061/(asce)hy.1943-7900.0001288

Rodi, W., 1993. Turbulence models and their application in hydraulics: A state of the art review, 3rd Ed. ed. A.A. Balkema, Rotterdam, Netherlands.

Rodi, W., 1976. A new algebraic relation for calculating the Reynolds stresses, in: Gesellschaft Angewandte Mathematik Und Mechanik Workshop Paris France. p. 219.

Russell, T.F., Heberton, C.I., Konikow, L.F., Hornberger, G.Z., 2003. A finite-volume ELLAM for three-dimensional solute-transport modeling. Groundwater 41, 258–272.

Rutherford, J.C., 1994. River mixing. Wiley.

Schär, C., Smith, R.B., 1993. Shallow-Water Flow past Isolated Topography. Part I: Vorticity Production and Wake Formation. J. Atmos. Sci. 50, 1373–1400.

Seo, I.W., Song, C.G., 2012. Numerical simulation of laminar flow past a circular cylinder with slip conditions. Int. J. Numer. Methods Fluids 68, 1538–1560. https://doi.org/10.1002/fld

Serra, T., Fernando, H.J.S., Rodríguez, R. V., 2004. Effects of emergent vegetation on lateral diffusion in wetlands. Water Res. 38, 139–147. https://doi.org/10.1016/j.watres.2003.09.009

Shaw, J., Kesserwani, G., Neal, J., Bates, P., Sharifian, M.K., 2021. LISFLOOD-FP 8.0: The new discontinuous Galerkin shallow-water solver for multi-core CPUs and GPUs. Geosci. Model Dev. 14, 3577–3602. https://doi.org/10.5194/gmd-14-3577-2021

Shields, F.D., Coulton, K.G., Nepf, H., 2017. Representation of Vegetation in Two-Dimensional Hydrodynamic Models. J. Hydraul. Eng. 143, 1–9. https://doi.org/10.1061/(asce)hy.1943-7900.0001320

Shucksmith, J., Boxall, J., Guymer, I., 2007. Importance of advective zone in longitudinal mixing experiments. Acta Geophys. 55, 95–103. https://doi.org/10.2478/s11600-006-0042-7

Shucksmith, J.D., Boxall, J.B., Guymer, I., 2010. Effects of emergent and submerged natural vegetation on longitudinal mixing in open channel flow. Water Resour. Res. 46, 1–14. https://doi.org/10.1029/2008WR007657

Singh, S.P., Mittal, S., 2004. Energy spectra of flow past a circular cylinder. Int. J. Comut. Fluid Dyn. 18, 671–679. https://doi.org/10.1080/10618560410001730278

Smith, G.D., 1985. Numerical solution of partial differential equations: finite difference methods. Oxford university press.

Sonnenwald, F., Guymer, I., Stovin, V., 2019a. A CFD-Based Mixing Model for Vegetated Flows. Water Resour. Res. 55, 2322–2347. https://doi.org/10.1029/2018WR023628

Sonnenwald, F., Guymer, I., Stovin, V., 2018. Computational fluid dynamics modelling of residence times in vegetated stormwater ponds, in: Proceedings of the Institution of Civil Engineers-Water Management. Thomas Telford Ltd, pp. 76–86.

https://doi.org/10.1680/jwama.16.00117

Sonnenwald, F., Hart, J.R., West, P., Stovin, V., Guymer, I., 2017. Transverse and longitudinal mixing in real emergent vegetation at low velocities. Water Resour. Res. 53, 961–978. https://doi.org/10.1002/2016WR019937

Sonnenwald, F., Stovin, V., Guymer, I., 2019b. Estimating drag coefficient for arrays of rigid cylinders representing emergent vegetation. J. Hydraul. Res. 57, 591–597. https://doi.org/10.1080/00221686.2018.1494050

Sonnenwald, F., Stovin, V., Guymer, I., 2019c. A stem spacing-based non-dimensional model for predicting longitudinal dispersion in low-density emergent vegetation. Acta Geophys. 67, 943–949. https://doi.org/10.1007/s11600-018-0217-z

Sonnenwald, F., Stovin, V., Guymer, I., 2013. Correlation measures for solute transport model identification and evaluation, in: Experimental and Computational Solutions of Hydraulic Problems: 32nd International School of Hydraulics. pp. 389–401.

Spalart, P.R., Allmaras, S.R., 1992. One-Equatlon Turbulence Model for Aerodynamic Flows, in: 30th Aerospace Sciences Meeting & Exhibit. p. 439. https://doi.org/10.2514/6.1992-439

Sridharan, B., Bates, P.D., Sen, D., Kuiry, S.N., 2021. Local-inertial shallow water model on unstructured triangular grids. Adv. Water Resour. 152, 103930. https://doi.org/10.1016/j.advwatres.2021.103930

Stansby, P.K., 2006. Limitations of Depth-Averaged Modeling for Shallow Wakes. J. Hydraul. Eng. 132, 737–740. https://doi.org/10.1061/(ASCE)0733-9429(2006)132

Stoesser, T., Kim, S.J., Diplas, P., 2010. Turbulent Flow through Idealized Emergent Vegetation. J. Hydraul. Eng. 136, 1003–1017. https://doi.org/10.1061/(asce)hy.1943-7900.0000153

Stovin, V.R., Sonnenwald, F., Golzar, M., Guymer, I., 2022. The Impact of Cylinder Diameter Distribution on Longitudinal and Transverse Dispersion Within Random Cylinder Arrays. Water Resour. Res. 58. https://doi.org/10.1029/2021wr030396

Sumer, B.M., 2006. Hydrodynamics around cylindrical strucures. World scientific.

Sun, X., Kesserwani, G., Sharifian, M., Stovin, V., 2023. LISFLOOD-FP8.0: DG2 and FV2 SWE simulation files. https://doi.org/10.5281/ZENODO.8146884

Syme, W.J., 2008. Flooding in urban areas - 2D modelling approaches for buildings and fences, in: Engineers Australia, 9th National Conference on Hydraulics in Water Engineering, Darwin Convention Centre, Australia. pp. 23–26.

Tanino, Y., 2008. Flow and Solute Transport in Random Cylinder Arrays: a Model for Emergent Aquatic Plant Canopies. PhD thesis. Massachusetts Institute of Technology.

Tanino, Y., Nepf, H.M., 2009. Laboratory investigation of lateral dispersion within dense arrays of randomly distributed cylinders at transitional Reynolds number. Phys. Fluids 21. https://doi.org/10.1063/1.3119862

Tanino, Y., Nepf, H.M., 2008a. Lateral dispersion in random cylinder arrays at high Reynolds number. J. Fluid Mech. 600, 339–371. https://doi.org/10.1017/S0022112008000505

Tanino, Y., Nepf, H.M., 2008b. Laboratory Investigation of Mean Drag in a Random Array of Rigid, Emergent Cylinders. J. Hydraul. Eng. 134, 34–41. https://doi.org/10.1061/(ASCE)0733-9429(2008)134

Teng, J., Jakeman, A.J., Vaze, J., Croke, B.F.W., Dutta, D., Kim, S., 2017. Flood inundation modelling: A review of methods, recent advances and uncertainty analysis. Environ. Model. Softw. 90, 201–216. https://doi.org/10.1016/j.envsoft.2017.01.006

Tezduyar, T.E., Shih, R., 1991. Numerical experiments on downstream boundary of flow past cylinder. J. Eng. Mech. 117, 854–871. https://doi.org/10.1061/(ASCE)0733-9399(1991)117:4(854)

Tinoco, R.O., Cowen, E.A., 2013. The direct and indirect measurement of boundary stress and drag on individual and complex arrays of elements. Exp. Fluids 54. https://doi.org/10.1007/s00348-013-1509-3

Tominaga, Y., Stathopoulos, T., 2012. CFD Modeling of Pollution Dispersion in Building Array: Evaluation of turbulent scalar flux modeling in RANS model using LES results. J. Wind Eng. Ind. Aerodyn. 104–106, 484–491. https://doi.org/10.1016/j.jweia.2012.02.004

Tong, F., 2014. Numerical Simulations of Steady and Oscillatory Flows around Multiple Cylinders. PhD thesis. The University Of Western Australia.

Tong, F., Cheng, L., Zhao, M., 2015. Numerical simulations of steady flow past two cylinders in staggered arrangements. J. Fluid Mech. 765, 114–149. https://doi.org/10.1017/jfm.2014.708

Tong, F., Cheng, L., Zhao, M., Zhou, T., Chen, X.B., 2014. The vortex shedding around four circular cylinders in an in-line square configuration. Phys. Fluids 26. https://doi.org/10.1063/1.4866593

Toro, E.F., 2001. Shock-capturing methods for free-surface shallow flows. Wiley and Sons Ltd.

Toro, E.F., Garcia-Navarro, P., 2007. Godunov-type methods for free-surface shallow flows: A review. J. Hydraul. Res. 45, 736–751. https://doi.org/10.1080/00221686.2007.9521812

Tsai, T.-L., Yang, J.-C., Huang, L.-H., 2002. Hybrid Finite-Difference Scheme for Solving the Dispersion Equation. J. Hydraul. Eng. 128, 78–86. https://doi.org/10.1061/(asce)0733-9429(2002)128:1(78)

Tsai, T.-L., Yang, J.-C., Huang, L.-H., 2001. An accurate integral-based scheme for advection–diffusion equation. Commun. Numer. Methods Eng. 17, 701–713. https://doi.org/10.1002/cnm.442

Tsavdaris, A., Mitchell, S., Williams, J.B., 2015. Computational fluid dynamics modelling of different detention pond configurations in the interest of sustainable flow regimes and gravity sedimentation potential. Water Environ. J. 29, 129–139. https://doi.org/10.1111/wej.12086

Uzun, A., Yousuff Hussaini, M., 2012. An application of delayed detached eddy simulation to tandem cylinder flow field prediction. Comput. Fluids 60, 71–85. https://doi.org/10.1016/j.compfluid.2012.02.029

Vater, S., Beisiegel, N., Behrens, J., 2017. Comparison of wetting and drying between a RKDG2 method and classical FV based second-order hydrostatic reconstruction, in: Finite Volumes for Complex Applications VIII-Hyperbolic, Elliptic and Parabolic Problems: FVCA 8, Lille, France. Springer International Publishing, pp. 237–245. https://doi.org/10.1007/978-3-319-57394-6_26

Versteeg, H.K., 2007. An introduction to computational fluid dynamics: the finite volume method, 2/E. ed. Pearson Education India.

Waltham, N.J., Barry, M., McAlister, T., Weber, T., Groth, D., 2014. Protecting the Green Behind the Gold: Catchment-Wide Restoration Efforts Necessary to Achieve Nutrient and Sediment Load Reduction Targets in Gold Coast City, Australia. Environ. Manage. 54, 840–851. https://doi.org/10.1007/s00267-014-0330-y

Wang, W., Chen, W., Huang, G., Liu, J., Zhang, D., Wang, F., 2023. A hybrid shallow water approach with unstructured triangular grids for urban flood modeling. Environ. Model. Softw. 166, 105748. https://doi.org/10.1016/j.envsoft.2023.105748

Wang, Y., Liang, Q., Kesserwani, G., Hall, J.W., 2011. A 2D shallow flow model for practical dam-break simulations. J. Hydraul. Res. 49, 307–316. https://doi.org/10.1080/00221686.2011.566248

West, P.O., Wallis, S.G., Sonnenwald, F.C., Hart, J.R., Stovin, V.R., Guymer, I., 2021. Modelling transverse solute mixing across a vegetation generated shear layer. J. Hydraul. Res. 59, 621–636. https://doi.org/10.1080/00221686.2020.1818307

White, B.L., Nepf, H.M., 2003. Scalar transport in random cylinder arrays at moderate Reynolds number. J. Fluid Mech. 487, 43–79. https://doi.org/10.1017/S0022112003004579

Willman, C., Scott, B., Stone, R., Richardson, D., 2020. Quantitative metrics for comparison of in-cylinder velocity fields using particle image velocimetry. Exp. Fluids 61, 1–16. https://doi.org/10.1007/s00348-020-2897-9

Wilson, C.A.M.E., Horritt, M.S., 2002. Measuring the flow resistance of submerged grass. Hydrol. Process. 16, 2589–2598. https://doi.org/10.1002/hyp.1049

Wirasaet, D., Kubatko, E.J., Michoski, C.E., Tanaka, S., Westerink, J.J., Dawson, C., 2014. Discontinuous Galerkin methods with nodal and hybrid modal/nodal triangular, quadrilateral, and polygonal elements for nonlinear shallow water flow. Comput. Methods Appl. Mech. Eng. 270, 113–149. https://doi.org/10.1016/j.cma.2013.11.006

Wissink, J.G., Rodi, W., 2008. Numerical study of the near wake of a circular cylinder. Int. J. Heat Fluid Flow 29, 1060–1070. https://doi.org/10.1016/j.ijheatfluidflow.2008.04.001

Wu, W., 2004. Depth-Averaged Two-Dimensional Numerical Modeling of Unsteady Flow and Nonuniform Sediment Transport in Open Channels. J. Hydraul. Eng. 130, 1013–1024. https://doi.org/10.1061/(asce)0733-9429(2004)130:10(1013)

Wu, W., Rodi, W., Wenka, T., 2000. 3D numerical modeling of flow and sediment transport in open channels. J. Hydraul. Eng. 126, 4–15. https://doi.org/10.1061/(ASCE)0733-9429(2000)126:1(4)

Yan, C., Nepf, H.M., Huang, W.X., Cui, G.X., 2017. Large eddy simulation of flow and scalar transport in a vegetated channel. Environ. Fluid Mech. 17, 497–519. https://doi.org/10.1007/s10652-016-9503-y

Ye, J., McCorquodale, J.A., 1997. Depth-Averaged Hydrodynamic Model in Curvilinear Collocated Grid. J. Hydraul. Eng. 123, 380–388. https://doi.org/10.1061/(asce)0733-9429(1997)123:5(380)

Young, P., Jakeman, A., McMurtrie, R., 1980. An instrumental variable method for model order identification. Automatica 16, 281–294. https://doi.org/10.1016/0005-1098(80)90037-0

Zampiron, A., Cameron, S.M., Stewart, M.T., Marusic, I., Nikora, V.I., 2023. Flow development in rough-bed open channels: mean velocities, turbulence statistics, velocity spectra, and secondary currents. J. Hydraul. Res. 61, 133–144. https://doi.org/10.1080/00221686.2022.2132311

Zdravkovich, M.M., 1997. Flow Around Circular Cylinders: Volume 1: Fundamentals. Oxford

University Press.

Zhang, C., Tang, H., Kang, H., Choi, S., 2009. Turbulence modeling of solute transport in open-channel flows over submerged vegetation., in: Proceedings of 16th IAHR-APD Congress and 3rd Symposium of IAHR-ISHS. pp. 674–679.

Zhang, K., Katsuchi, H., Zhou, D., Yamada, H., Han, Z., 2016. Numerical study on the effect of shape modification to the flow around circular cylinders. J. Wind Eng. Ind. Aerodyn. 152, 23–40. https://doi.org/10.1016/j.jweia.2016.02.008

Zhang, M., Shu, C.W., 2005. An analysis of and a comparison between the discontinuous Galerkin and the spectral finite volume methods. Comput. Fluids 34, 581–592. https://doi.org/10.1016/j.compfluid.2003.05.006

Zhang, W., 2011. A 2-D numerical simulation study on longitudinal solute transport and longitudinal dispersion coefficient. Water Resour. Res. 47, 1–13. https://doi.org/10.1029/2010WR010206

Zhang, X., Shu, C.W., 2011. Maximum-principle-satisfying and positivity-preserving high-order schemes for conservation laws: Survey and new developments, in: Proceedings of the Royal Society A: Mathematical, Physical and Engineering Sciences. pp. 2752–2776. https://doi.org/10.1098/rspa.2011.0153

Zhou, T., Li, Y., Shu, C.W., 2001. Numerical comparison of WENO finite volume and Runge-Kutta discontinuous Galerkin methods. J. Sci. Comput. 16, 145–171. https://doi.org/10.1023/A:1012282706985

Zong, L., Nepf, H., 2012. Vortex development behind a finite porous obstruction in a channel. J. Fluid Mech. 691, 368–391. https://doi.org/10.1017/jfm.2011.479

Appendix A. The implementation of the DG2-SWE and FV2-SWE solvers

This appendix summarises the implementation of the DG2-SWE and FV2-SWE solvers. The DG2 solver is formulated based on the "slope-decoupled" simplified stencil (Kesserwani et al., 2018), which is 2.6 times faster to run than the standard DG2 solver formulated on a full tensor-product stencil, without compromising the accuracy and convergence. The FV2-SWE solver adopts the Monotonic Upstream-centred Scheme for Conservation Laws (MUSCL) and is formulated on a computational stencil similar to that of the DG2-SWE solver. Technical aspects of the DG2-SWE and FV2-SWE solvers are detailed in Ayog et al. (2021), and the corresponding codes are available at the University of Sheffield local repository of the LISFLOOD-FP 8.0 (The University of Sheffield, 2021). In the following, only a brief overview of the solvers is presented.

The DG2-SWE and FV2-SWE solvers discretise the conservative vectorial form of the full SWE:

$$\partial_t \boldsymbol{U} + \partial_x \boldsymbol{F}(\boldsymbol{U}) + \partial_y \boldsymbol{G}(\boldsymbol{U}) = \boldsymbol{S_b}(\boldsymbol{U}) + \boldsymbol{S_f}(\boldsymbol{U}) \qquad (A.1)$$

where ∂ represents a partial derivative operator and $\boldsymbol{U}(x, y, t) = [h, q_x, q_y]^{\mathrm{T}}$ is the vector of flow variables at time t and location (x, y), which includes water depth h and the discharge per unit width, $q_x = hu$ and $q_y = hv$, involving the depth-averaged longitudinal and transverse velocities u and v, respectively. $\boldsymbol{F} = [q_x, q_x^2/h + gh^2/2, q_x q_y/h]^{\mathrm{T}}$ and $\boldsymbol{G} = [q_y, q_x q_y/h, q_y^2/h + gh^2/2]^{\mathrm{T}}$ are vectors representing the components of physical flux field, and g is the gravity acceleration. $\boldsymbol{S_b} = [0, -gh\partial_x z, -gh\partial_y z]^{\mathrm{T}}$ is the source term vector representing topography gradients and $\boldsymbol{S_f} = [0, -C_f u\sqrt{u^2 + v^2}, -C_f v\sqrt{u^2 + v^2}]^{\mathrm{T}}$ is the source term vector representing the friction effects expressed as function of roughness coefficient $C_f = gn_M^2/h^{1/3}$ in which n_M is the Manning's resistance parameter.

The solvers assume a 2D domain discretized into N non-overlapping and uniform square grids Q_c ($c = 1, \ldots, N$), the centred at (x_c, y_c) with horizontal dimensions ($\Delta x = \Delta y$), over which the discrete flow vector $\boldsymbol{U_h}(x, y, t)$ and topography $z_h(x, y)$ will be approximated.

A.1 DG2-SWE solver

In the DG2-SWE solver, $\boldsymbol{U_h}(x, y, t)$ and $z_h(x, y)$ are represented by local piecewise-planar solutions expanded onto a simplified and scaled Legendre basis $\boldsymbol{P}$ (Kesserwani and Sharifian, 2020; Shaw et al., 2021). Hence, $\boldsymbol{U_h}(x, y, t)$ consists of an averaged coefficient $\boldsymbol{U_c^0}$ and two directionally independent slope coefficients, $\boldsymbol{U_c^{1x}}$ and $\boldsymbol{U_c^{1y}}$; such that each of its physical components can be written in the form of an equation of a plane, as follows,

$$\boldsymbol{U_h}(x, y, t) = \mathbf{U_c} \cdot \boldsymbol{P} = \begin{bmatrix} h_c^0 & h_c^{1x} & h_c^{1y} \\ q_{x_c}^{\ 0} & q_{x_c}^{\ 1x} & q_{x_c}^{\ 1y} \\ q_{y_c}^{\ 1x} & q_{y_c}^{\ 1x} & q_{y_c}^{\ 1y} \end{bmatrix} \cdot \begin{bmatrix} 1 \\ 2\sqrt{3}(x - x_c)/\Delta x \\ 2\sqrt{3}(y - y_c)/\Delta y \end{bmatrix} \qquad (A.2)$$

where $\mathbf{U_c}$ is a matrix of flow coefficients and "·" stands for the scalar product. Each row of matrix $\mathbf{U_c}$ includes the average and slope coefficients that span the piecewise-planar representation of each component of the flow variables after projection onto the basis $\boldsymbol{P}$. As the discharge gradients are available in Eq. (A.2) as the respective slope coefficients of discharges q_x and q_y, the longitudinal and transverse velocity gradients in x and y directions can be directly obtained within each grid, which provides a straightforward way to calculate the vorticity W, defined as $W = \partial v/\partial x - \partial u/\partial y$. Namely, the numerical vorticity W_c for each grid element is obtained as $W_c = q_{y_c}^{\ 1x}/h_c^0 - q_{x_c}^{\ 1y}/h_c^0$.

Topography $\boldsymbol{z_h}$ is expressed in a similar way, using the average and slope coefficients as follows:

$$\boldsymbol{Z_h}(x, y) = \boldsymbol{z_c} \cdot \boldsymbol{P} = \begin{bmatrix} z_c^0 & z_c^{1x} & z_c^{1y} \end{bmatrix} \cdot \begin{bmatrix} 1 \\ \frac{2\sqrt{3}(x - x_c)}{\Delta x} \\ \frac{2\sqrt{3}(y - y_c)}{\Delta y} \end{bmatrix} \qquad (A.3)$$

where $\boldsymbol{z_c}$ is a vector that includes the average and slope coefficients of topography, for spanning the piecewise-planar representation of the topography after projection onto the same basis $\boldsymbol{P}$ (Shaw et al., 2021). The time-dependent flow coefficients $\mathbf{U_c}$ are initialized from a given initial condition, while the time-invariant topography coefficients $\boldsymbol{z_c}$ are projected based on the cylinders' diameter and location (Shaw et al., 2021).

Eq. (A.1) is discretized by an explicit second-order two-stage Runge-Kutta (RK2) scheme with the time step Δt calculated based on the Courant-Friedrichs-Lewy (CFL) condition with a maximum stable Courant number C_r of 0.33 (Cockburn and Shu, 2001; Kesserwani et al., 2018). The matrix $\mathbf{U_c}$ evolved from time level n to n+1, by solving three independent ordinary differential equations, $\partial_t \mathbf{U_c^K}(t) = \boldsymbol{L_c^K}$, where $\boldsymbol{L_c^K}$ (K = 0, 1x, 1y) are DG2 spatial operator vectors defined as:

$$\boldsymbol{L_c^0} = -\left(\frac{(\tilde{\boldsymbol{F}}_{eas} - \tilde{\boldsymbol{F}}_{wes})}{\Delta x} + \frac{(\tilde{\boldsymbol{G}}_{nor} - \tilde{\boldsymbol{G}}_{sou})}{\Delta y} + \begin{bmatrix} 0 \\ \frac{2\sqrt{3} g \bar{h}_c^0 \bar{z}_c^{1x}}{\Delta x} \\ \frac{2\sqrt{3} g \bar{h}_c^0 \bar{z}_c^{1y}}{\Delta y} \end{bmatrix} \right) \qquad (A.4a)$$

$$\boldsymbol{L}_{\boldsymbol{c}}^{1\boldsymbol{x}} = -\frac{\sqrt{3}}{\Delta x}\left(\widetilde{\boldsymbol{F}}_{\boldsymbol{eas}} + \widetilde{\boldsymbol{F}}_{\boldsymbol{wes}} - \boldsymbol{F}(\overline{\boldsymbol{U}}_{\boldsymbol{c}}^{0} - \overline{\boldsymbol{U}}_{\boldsymbol{c}}^{1\boldsymbol{x}}) - \boldsymbol{F}(\overline{\boldsymbol{U}}_{\boldsymbol{c}}^{0} + \overline{\boldsymbol{U}}_{\boldsymbol{c}}^{1\boldsymbol{x}}) + \begin{bmatrix} 0 \\ 2g\overline{h}_{c}^{1x}\overline{z}_{c}^{1x} \\ 0 \end{bmatrix}\right) \qquad (A.4b)$$

$$\boldsymbol{L}_{\boldsymbol{c}}^{1\boldsymbol{y}} = -\frac{\sqrt{3}}{\Delta y}\left(\widetilde{\boldsymbol{G}}_{\boldsymbol{nor}} + \widetilde{\boldsymbol{G}}_{\boldsymbol{sou}} - \boldsymbol{G}(\overline{\boldsymbol{U}}_{\boldsymbol{c}}^{0} - \overline{\boldsymbol{U}}_{\boldsymbol{c}}^{1\boldsymbol{y}}) - \boldsymbol{G}(\overline{\boldsymbol{U}}_{\boldsymbol{c}}^{0} + \overline{\boldsymbol{U}}_{\boldsymbol{c}}^{1\boldsymbol{y}}) + \begin{bmatrix} 0 \\ 0 \\ 2g\overline{h}_{c}^{1y}\overline{z}_{c}^{1y} \end{bmatrix}\right) \qquad (A.4c)$$

in which the terms $\widetilde{\boldsymbol{F}}_{\boldsymbol{wes}}$, $\widetilde{\boldsymbol{F}}_{\boldsymbol{eas}}$, $\widetilde{\boldsymbol{G}}_{\boldsymbol{sou}}$, and $\widetilde{\boldsymbol{G}}_{\boldsymbol{nor}}$ are fluxes across the western, eastern, southern and northern interfaces of each grid Q_c. These fluxes are computed using the Harten, Lax and van Leer (HLL) approximate Riemann solver, based on the two limits of the piecewise-planar solutions at either side of each interface. For instance, the limits at the eastern interface centre, are expressed as: $\boldsymbol{U}_{\boldsymbol{eas}}^{-} = \boldsymbol{U}_{\boldsymbol{c}}^{0}(t) + \boldsymbol{U}_{\boldsymbol{c}}^{1\boldsymbol{x}}(t)$ and $\boldsymbol{U}_{\boldsymbol{eas}}^{+} = \boldsymbol{U}_{\boldsymbol{nei}_{\boldsymbol{eas}}}^{0}(t) - \boldsymbol{U}_{\boldsymbol{nei}_{\boldsymbol{eas}}}^{1\boldsymbol{x}}(t)$, where '$nei_{eas}$' is the index of the direct neighbour from the eastern side. These limits are modified to maintain well-balancedness and non-negative water depths around cylinders (Kesserwani et al., 2018). The friction source term $\boldsymbol{S}_{\boldsymbol{f}}$ is not explicitly included in the spatial operators, rather it is discretized using a split implicit scheme applied at the beginning of each time step.

Local slope limiting is adopted based on the shock detector ZZ and a generalised minmod limiter (Cockburn and Shu, 2001), as demonstrated by the analysis of Ayog (2022); the local slope limiter should be activated to avoid noise which may possibly appear around the steep obstacles when DG2-SWE is applied on a submeter grid resolution.

A.2 FV2-SWE solver

In the FV2-SWE solver, $\boldsymbol{U}_{\boldsymbol{h}}(x, y, t)$ and $\boldsymbol{z}_{\boldsymbol{h}}(x, y)$ are represented by local piecewise-constant solutions by setting the basis $\boldsymbol{P}$ to unity. By doing so, each physical component of $\boldsymbol{U}_{\boldsymbol{h}}(x, y, t)$ takes the form of a flat plane that is only spanned by an average coefficient given by:

$$\boldsymbol{U}_{\boldsymbol{h}}(x, y, t) = \boldsymbol{U}_{\boldsymbol{c}}^{0} \cdot P = \begin{bmatrix} h_c^0 \\ q_{x_c}^{\ 0} \\ q_{y_c}^{\ 0} \end{bmatrix} \cdot 1 = \begin{bmatrix} h_c^0 \\ q_{x_c}^{\ 0} \\ q_{y_c}^{\ 0} \end{bmatrix} \qquad (A.5)$$

where $\boldsymbol{U}_{\boldsymbol{c}}^{0}$ denotes a vector of average flow coefficients. Unlike the DG2-SWE solver that adopts the local slope coefficients to directly calculate W_c, the FV2-SWE solver uses the piecewise-constant coefficients of the neighbouring grids to derive each grid's velocity gradients and

associated W_c. W_c is calculated as $W_c = (q_{y_{nei_{eas}}}^{0} / h_{nei_{eas}}^{0} - q_{y_{nei_{wes}}}^{0} / h_{nei_{wes}}^{0})/2\Delta x - (q_{x_{nei_{nor}}}^{0} / h_{nei_{nor}}^{0} - q_{x_{nei_{sou}}}^{0} / h_{nei_{sou}}^{0})/2\Delta y$.

Similarly, $\boldsymbol{z_h}(x, y)$ is represented by an average coefficient as,

$$\boldsymbol{Z_h}(x, y) = \boldsymbol{z_c} \cdot P = z_c^0 \cdot 1 = z_c^0 \tag{A.6}$$

The FV2-SWE solver only involves a $\boldsymbol{L_c^0}$ vector, which is updated via Eq. (A.4a) using the RK2 time integration scheme with C_r equal to 0.5. For each grid element Q_c, the fluxes at each interface are also evaluated using the HLL Riemann solver, but the MUSCL linear interpolation approach is applied to reconstruct the solution limits with the aid of neighbouring grids' information. For instance, at the eastern interface, the solution limits are evaluated as $\boldsymbol{U_{eas}^{-}} = \boldsymbol{U_c^0}(t) + 0.5\nabla_{\boldsymbol{c}}^{1\boldsymbol{x}}$ and $\boldsymbol{U_{eas}^{+}} = \boldsymbol{U_{nei_{est}}^0}(t) - 0.5\nabla_{\boldsymbol{nei_{est}}}^{1\boldsymbol{x}}$, where ∇_c^{1x} is the x-directional gradient term, expressed as:

$$\nabla_c^{1x} = \phi\left(\frac{\boldsymbol{U_c^0}(t) - \boldsymbol{U_{nei_{wes}}^0}(t)}{\boldsymbol{U_{nei_{eas}}^0}(t) - \boldsymbol{U_c^0}(t)}\right)\left(\boldsymbol{U_c^0}(t) - \boldsymbol{U_{nei_{wes}}^0}(t)\right) \tag{A.7}$$

In Eq. (A.7), ϕ is a slope limiter function that avoids spurious oscillations around sharp discontinuities to obtain a stable second-order accuracy. Informed by the work of Ayog, Kesserwani, Shaw, et al. (2021), the Sweby symmetric limiter with the β parameter value equal to 1.25 is adopted herein.

Appendix B. Grid resolution selection

This section is aimed to justify the grid resolution selected for running the DG2-SWE and FV2-SWE solvers. For the scope of this study, the aim was to choose a resolution that is appropriate for a solver to trigger periodical shedding of vortices, while keeping the simulation within the GPU memory capacity and within a runtime of less than a day in order to support the needs for larger scale simulations, including the case study in Sec. 3.3.2. This choice was done diagnostically by applying both solvers to run the flow past a single cylinder of diameter d = 4 mm for R_{ed} = 250 (Sec.3.3.1). The simulations were investigated on grids starting with a resolution of 0.25d, equivalent to 1 mm, and the finest resolution possible was 0.025d, equivalent to 0.1 mm. The capability of a solver to capture periodical vortex shedding was evaluated based on the predicted Strouhal number S_t values and instantaneous scaled vorticity contours (with respect to the maximum vorticity) as compared to value of 0.205 and reference vorticity distribution from the reference prediction (Rajani et al., 2009). Also, the computational cost (or called runtime efficiency) of each solver at different grid resolutions was measured by considering the overall GPU runtime cost needed to complete 50 shedding cycles and the relative runtime cost per grid element. The latter was obtained by first dividing the overall GPU runtime cost by the number of elements and then scaling it with respect to the runtime cost per element of a baseline simulation. The baseline simulation was taken to be the DG2-SWE solver run at the coarsest resolution that could trigger the vortex shedding (i.e., at the grid resolution of 0.25d). Table B.1 lists the predicted S_t values, GPU runtime costs and the relative runtime costs per element for the DG2 and FV2 solvers at different grid resolutions.

Table B.1 Flow past one cylinder at R_{ed} = 250: S_t values predicted by the DG2 and FV2 solvers at grid resolutions between 0.25d and 0.025d, and the associated number of elements, overall GPU runtime costs as well as relative runtime cost per element. Reference S_t number is 0.205 (Rajani et al., 2009)

Resolution	No. of elements	S_t (-)		Overall GPU runtime costs		Relative runtime costs per element	
		DG2	FV2	DG2	FV2	DG2	FV2
0.25d (1 mm)	15,616	0.155	-	11 mins	-	1×	-
0.125d (0.5 mm)	62,464	0.19	-	2 hours	-	2.7×	-
0.0625d (0.25 mm)	249,856	0.21	-	5 hours	-	1.7×	-
0.025d (0.1 mm)	1.56 million	-	0.105	-	16.5 hours	-	0.9×

'-' indicates no such data was obtained.

The FV2-SWE solvers fail to predict any S_t values except using a grid resolution of 0.025d. Relative to the baseline simulation, the FV2-SWE solver at this grid resolution has a slightly lower relative runtime cost per element (0.9 times) but requires 90 times higher overall GPU runtime cost, taking about 16.5 hours to complete the simulation. Moreover, the predicted S_t value of 0.105 is lower than that predicted by the baseline of 0.155, showing less accuracy. Note that better accuracy could not be achieved since a finer grid resolution could not be afforded for this simulation. In contrast, the DG2-SWE solver is able to predict S_t values regardless of the grid resolutions used, except for the grid resolution of 0.025d which could not be performed due to high GPU memory cost. Also, finer grid resolutions lead to predictions that approach the reference S_t value of 0.205.

To further analyse the DG2-SWE solver's performance. Figure B.1 compares the instantaneous vorticity contours using DG2-SWE simulation under the different grid resolution with the reference vorticity contour presented in Rajani et al. (2009). Under the coarse grid resolution (0.25d), the DG2-SWE is seen to reproduce the vortices which are periodically shed behind the cylinders, as observed in the reference vorticity prediction. However, using the medium (0.125d) and fine grid (0.0625d) resolutions, although can lead to a better estimation of S_t values, distort the evolution of vortices in the region far away from the cylinder. This may result from grid

resolution refinement, causing the DG2-SWE simulated flow field to converge to a state with increasingly less numerical diffusion, which then diverges from the state obtained from the viscous turbulence model incorporating the kinematic and eddy viscosity terms. Such spurious asymmetrical pattern of the vortex street was also observed in the third order FV (FV3) solver (Macias et al. 2020) but it can be mitigated by incorporating the eddy viscosity terms into the SWE (Collecutt and Syme 2017; Navas-Montilla et al. 2019). The most recent research ("Discontinuous Galerkin simulator of shallow vortical flow with turbulence", submitted, *Advances in Water Resources*) also proved that, when incorporating the kinematic and/or eddy viscosity terms, the DG2 solver to RANS using the medium and fine resolution is able to accurately capture the vortical structures behind the cylinder without spurious eddy asymmetricity.

In term of the computational cost, compared to the baseline simulation, the grid resolutions of $0.125d$ and $0.0625d$ lead to more expensive GPU runtime costs (2 hours and 5 hours, respectively) and higher relative runtime costs per element (2.7 and 1.7 times, respectively). These in turn result in simulation runtimes longer than one day and exceed GPU memory limits, for the laboratory-scale case study in Sec 3.3.2 and 3.3.3. Therefore, the grid resolution used in the baseline, $0.25d$, is found to be adequate for meeting the needs of the simulations for this study.

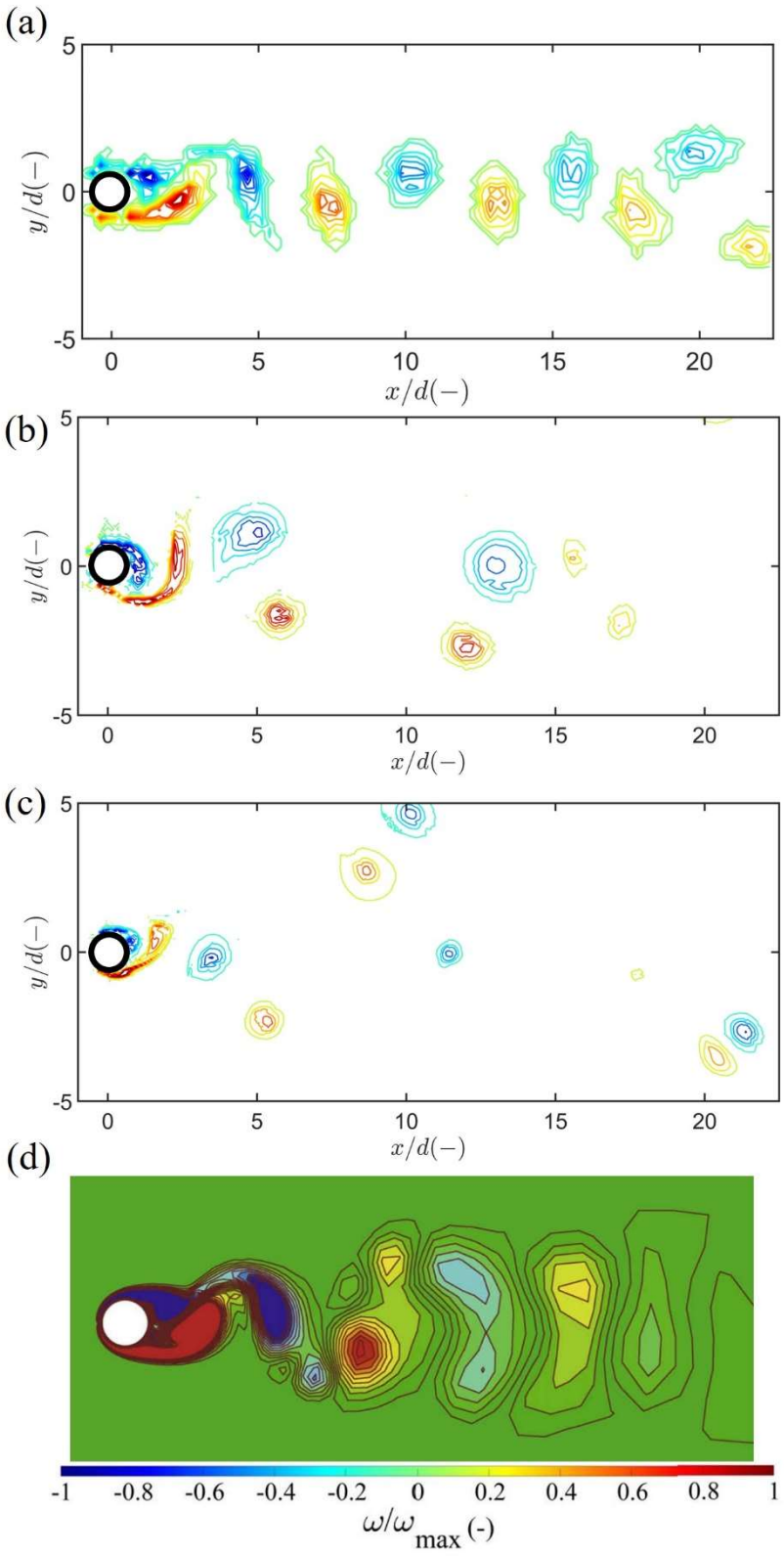

Figure B.1. Flow past one cylinder at R_{ed} = 250: instantaneous scaled vorticity contours from the DG2-SWE simulation using (a) coarse grid resolution of 0.25*d* (equivalent to 1 mm), (b) medium grid resolution of 0.125*d* (equivalent to 0.5 mm), (c) fine grid resolution of 0.125*d* (equivalent to 0.25 mm), and reference vorticity contours at R_{ed} = 250 (Source: Rajani et al. 2009).

Appendix C. Impact of simulation time on flow fields within different reaches

This appendix aims to investigate the impact of simulation time on shedding frequency and prediction accuracy within different locations for both flow cases at R_{ed} = 53 and 220. Three different zones were considered to compare the effects due to the developing flow with the fully developed flow. These three zones are located within three sequential reaches and share the same cylinder distribution. The first zone (within the first reach) represents where flow was believed to be under the developing stage, and the last two zones (within the last two reaches) represent where flow was believed to be fully developed. The third zone is also where SPIV data was collected (Corredor-Garcia et al., 2020). Coordinates of these three zones are, respectively, $x \in [82.5d, 210d]$, $[697.5d, 835d]$ and $[1332.5d, 1460d]$, where d denotes the cylinder diameter.

For each test case, when the vortex initially generated behind the first cylinder exited at the outlet, the simulation was set to terminate after 100 more additional shedding cycles because 100 additional cycles are typically sufficient (Rajani et al., 2009; Qu et al., 2013). The simulation time t was scaled to be dimensionless time unit t^*, which is defined as $t^* = tU_\infty/d$ where U_∞ is the imposed steady inflow velocity (Laroussi et al., 2014). Once the vortex was generated, t^* was also converted to the number of cycles N_{cyc} by multiplying t^* and Strouhal number S_t of the first cylinder. The reason for choosing the S_t of the first cylinder is that such value is constant with time and is not affected by flow interactions from other cylinders. The quasi-steady state convergence is first studied by deriving the L^1-norm error in the difference between each two adjacent water depth maps (Kesserewani et al., 2023). The impact of N_{cyc} on shedding frequency is then investigated by calculating the mean value of S_t within cylinder arrays over different locations. Finally, the impact of N_{cyc} on prediction accuracy is also explored. The time-averaged longitudinal velocity over different locations and cycles are extracted to be analysed with respect to the SPIV velocity data, quantitatively via the L^1- norm error.

Figure B1 shows the time history of the L^1- norm error in water depth between two subsequent time units at different R_{ed}. In the figure, the bottom x-axis denotes the time unit t^* and the top x-axis represents the number of shedding cycles N_{cyc}. N_{cyc} = 0 means that the vortex starts to be generated, N_{cyc} = 350 represents the cycles required to guarantee the initially generated vortex exited the outlet, and the simulations stopped at N_{cyc} = 450.

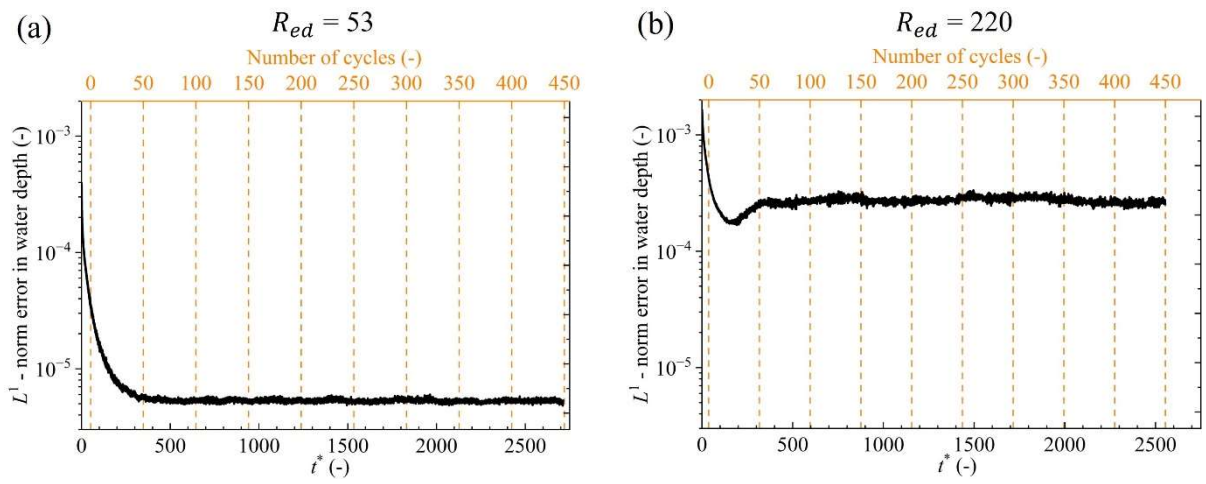

Figure B1. L^1- norm error in water depth for Re_d = (a) 53 and (b) 220 test cases.

At R_{ed} = 53 (Figure B1a), the L^1- norm error in water depth decreases with time as expected, becoming converged and varying between 3 x 10^{-6} and 5 x 10^{-6} after $900t^*$ (equivalent to 150 cycles). It can also be found that the first vortex was generated at $51.45t^*$ and exited the outlet around $2121.8t^*$. After $2756.3t^*$, 450 quasi-periodic shedding cycles occurred.

For the case of R_{ed} = 220 (Figure B1b), the L^1- norm error in water depth becomes stable in the range of 2 × 10^{-4} and 3 × 10^{-4} after $1150t^*$ (equivalent to 200 cycles), and there is a small decrease in L^1- norm error after $2000t^*$ (equivalent to 350 cycles). The comparison between different R_{ed} reveals that as the R_{ed} increases, the L^1- norm error in water depth and the time required to converge to quasi-steady state also increase. This is owing to the fact that flow disturbance is more pronounced at higher R_{ed} (Sumer et al., 2006). However, in contrast to the case of Re_d = 53, the case of R_{ed} = 220 requires less time unit ($37.2t^*$) to generate the first vortex generation, as identified in Sec. 3.3.1 that the lower R_{ed}, the more challenging for exciting vortex shedding. Moreover, at R_{ed} = 220, it takes $2000t^*$ and $2553.6t^*$ to complete 350 and 450 shedding cycles, which are less than that at R_{ed} = 53.

According to the water depth, quasi-steady states appear to be reached after 150 and 200 cycles for the cases of R_{ed} = 53 and 220, respectively. In the further investigations, the instantaneous flow fields are extracted at the intervals of 50 cycles for analysing shedding frequency and prediction accuracy within different locations and times. A sequence of these flow fields starting from the 150th cycle was used for R_{ed} = 53, and from the 200th cycle was used for R_{ed} = 220.

Figure B2 shows the mean S_t values within cylinder arrays over different locations and time periods for both cases. The black square markers represent the mean S_t values of the cylinder array in the first zone over 50 shedding cycles, with the black line indicating the mean S_t values within the first zone under the quasi-steady state. Similarly, the pink and blue ones refer to the mean S_t values of the

cylinder array in the second and third zones, respectively. The red line denotes the estimates of mean S_t values from the SPIV data.

In Figure B2a, at R_{ed} = 53, the mean S_t values within the developing zone (i.e. the first zone) over 50 cycles are always higher than those within the fully developed zone (i.e., the second zone and the third zone). For the latter, the mean S_t values are close to each other over the same time period. Looking at the mean S_t values between the 150th and the 450th cycles, the value within the developing zone is closely aligned with the one from the SPIV measured data, whereas the values within the fully developed zones are lower than the measurement. This might be attributed to the significantly higher velocities near the sidewalls within the fully developed zone, exceeding the expected values. Such overpredicted velocities may exert an influence on the wake flow evolution and thereby distort the shedding frequency.

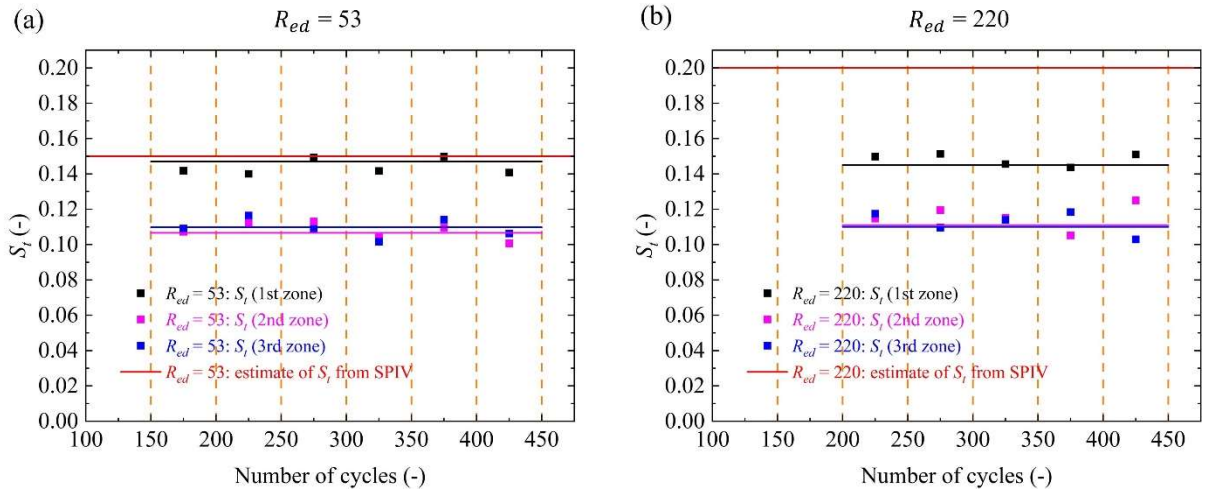

Figure B2. S_t values within different locations and times periods for Re_d = (a) 53 and (b) 220 test cases. Black marker represents mean S_t values within the first zone, while pink and blue markers denote S_t values within the second and third zones, respectively.

At R_{ed} = 220 (Figure B2b), the mean S_t values within the developing zone, although higher than those within the fully developed zone, is lower than the SPIV measurement. This is also in line with the findings in Sec. 3.3.1: the DG2-SWE solver tends to predict S_t values that are lower than the reference values at high R_{ed}. Still, the mean S_t values within the fully developed zones between the 150th cycles and the 450th cycles remain close to each other but are also lower than the measurement. However, despite being under the quasi-steady state, the mean S_t values over different time periods do not converge to a constant value for both R_{ed} cases.

To further analyse impact of N_{cyc} on prediction accuracy of velocity, Figure B3 shows the L^1-norm error in time-averaged longitudinal velocity ($\bar{u}$) within different locations and times. At R_{ed} = 53 (Figure B3a), the L^1- norm error in $\bar{u}$ within the developing zone (the black circular markers) is lower

than the errors within the fully developed zone (the pink circular markers representing the second zone and the blue circular markers representing the third zone). The higher L^1- norm error may still be due to the larger discrepancy in velocities near the sidewalls within the fully developed zone. However, it is worth noting that the L^1- norm error within the third zone between the 350th and 400th cycles is 0.2004, which is close to the error between the 400th and 450th cycle, also measured at 0.20. This may imply that the DG2-SWE solver tends to yield more converged flow fields after the initially generated vortex exited the outlet (equivalent to 350 cycles).

In comparison to the case of R_{ed} = 53, the L^1- norm error in $\bar{u}$ at Re_d = 220 is much lower (Figure B3b), indicating a better performance for DG2-SWE at this Re_d. The difference in L^1- norm error in $\bar{u}$ between the developing and the fully developed zones at Re_d = 220 is not as obvious as that as Re_d = 53. Again, the L^1- norm error in $\bar{u}$ within the third zone between the 350th and 400th cycles is close to the one between the 400th and 450th cycle.

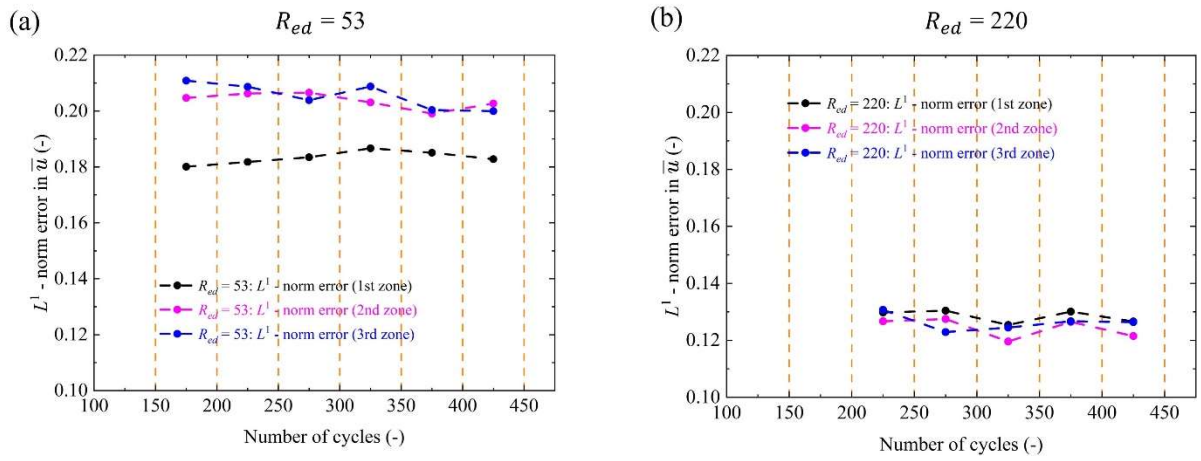

Figure B3. L^1-error in time-averaged longitudinal velocity within different locations and times for Re_d = (a) 53 and (b) 220 test cases. Black marker represents L^1- norm error in $\bar{u}$ within the first zone, while pink and blue markers denote L^1- norm errors in $\bar{u}$ within the second and third zones, respectively.

Furthermore, either S_t values or L^1- norm errors in $\bar{u}$ within the third zone are close to those within the second zone. Such similarity confirms that the flow within the second and third zones (or reaches) is fully developed (Zampiron et al. 2023), while the flow within the first zone (or reach) is under the developing stage.

Overall, these results indicates that, once the initially generated vortex has exited the outlet, flow fields over next additional 50 cycles within the third zone can be used for the analysis in the following investigation.

Appendix D. Instructions for running the DG2-ADE solver

This appendix introduces the instructions for running the DG2-ADE solver integrated into LISFLOOD-FP 8.0, taking the example of the Warwick test case (filename: Warwick). To run the DG2-ADE solver, users should first compile LISFLOOD-FP 8.0, following the same instruction process as the DG2-SWE solver. After successful compilation, users should go to the directory where the executable file lisflood.exe is located. Then, users should prepare the input files in raster format and specify the parameter file with extension of .par (i.e. Warwick.par) in the same directory. The required input files are presented in Table D.1, and the list of items needed to be specified in the parameter file are given in Table D.2. Once these files are ready, user can run the code by typing ..\lisflood.exe Warwick.par in Command Prompt window. DG2-ADE solver will produce the output files in the directory specified in the file of Warwick.par. Outputs include the average and two slope coefficients of concentration saved at specified time interval, time series of concentration at specific points and mass-balance errors. For further information on running instructions, visit https://www.seamlesswave.com.

Table D.1. Required input files with the extensions for the DG2-ADE solver and description of these input files. Examples are also provided.

Input files	Extensions	Description	Example
Velocity distribution	.vx and .vy	Longitudinal and transverse velocity components. Note that velocities should be set as NaN where the cylinders are located.	Warwick.vx Warwick.vy
Initial condition of concentration field	.c0, .c1x and .c1y	Average and two directional slope coefficients of initial concentration field.	Warwick.c0 Warwick.c1x Warwick.c1y
Turbulent diffusivity coefficient	.Dx and .Dy	*x*-directional and *y*-directional diffusivity coefficients. If turbulent diffusivity is assumed to be isotropic (such as this work), the data of these two files are the same. Note that diffusivity coefficients should be set as zero where the cylinders are located.	Warwick.Dx Warwick.Dy
Boundary condition	.bci and .bdy	Time invariant and time varying boundary conditions. The setting for specifying boundary conditions in LISFLOOD-FP 8.0 DG2-ADE solver is same as that in the LISFLOOD-FP 8.0 DG2-SWE solver.	Warwick.bci Warwick.bdy
Time series of concentration at specific points	.stage	Location of the specific points where users wish the DG2-ADE solver to record the time series of concentration	Warwick.stage

Table D.2. Required items name in .par file, and their description. Examples are also provided.

Item name	Description	Example
advdiff	Select the DG2-ADE solver	advdiff
cuda	Run the DG2-ADE solver on a Nvidia graphics card with CUDA support	cuda
startfile	The file name of the initial condition of concentration field, excluding the extensions of .c0, .c1x and .c1y	Warwick
velfile	The file name of the longitudinal and transverse velocity components, excluding the extensions of .vx and .vy	Warwick
visfile	The file name of turbulent diffusivity coefficients, excluding the extensions of .Dx and .Dy	Warwick
bcifile	The file name of the boundary conditions	Warwick.bci
saveint	Interval in seconds at which 2D concentration maps are saved	0.05
sim_time	Total length of the simulation time, in seconds	100
initial_tstep	Initial time step (unit: seconds)	0.0001
stagefile	The file name of the time series of concentration at specific points	Warwick.stage
resroot	Root name based on which result files are to be named	Warwick_res
dirroot	Name of the directory where the result files are to be saved	Warwick_dir